Final Report to

Gas Production Forecasting From Tight Gas Reservoirs: Integrating Natural Fracture Networks and Hydraulic Fractures

07122-44 FINAL REPORT

Date: February 8, 2013

Milind D. Deo, Principal Investigator

Department of Chemical Engineering, University of Utah, Salt Lake City, UT 84112

Authors

Milind Deo, Rasoul Sorkhabi, John McLennan, Ravi Bhide and Nan Zhao,

University of Utah

Ryan Sonntag and James Evans, Utah State University

Craig Morgan and Stephanie Carney, Utah Geological Survey

Paul LaPointe, Golder and Associates

Subcontractors

Utah State University, Department of Geology, Logan, Utah 84322; (435)797-1267

Utah Geological Survey, 1594 West North Temple, Utah 84114, (801)537-3300

Golder and Associates, 18300 NE Union Hill Road, Suite 200, Redmond, Washington, USA 98052, (425)883-0777

Itasca Incorporated, 10701 Corporate Dr Ste 310, Stafford, Texas 77477, (832) 532-77474

LEGAL NOTICE

This report was prepared by University of Utah as an account of work sponsored by the Research Partnership to Secure Energy for America, RPSEA. Neither RPSEA members of RPSEA, the National Energy Technology Laboratory, the U.S. Department of Energy, nor any person acting on behalf of any of the entities:

a. MAKES ANY WARRANTY OR REPRESENTATION, EXPRESS OR IMPLIED WITH RESPECT TO ACCURACY, COMPLETENESS, OR USEFULNESS OF THE INFORMATION CONTAINED IN THIS DOCUMENT, OR THAT THE USE OF ANY INFORMATION, APPARATUS, METHOD, OR PROCESS DISCLOSED IN THIS DOCUMENT MAY NOT INFRINGE PRIVATELY OWNED RIGHTS, OR

b. ASSUMES ANY LIABILITY WITH RESPECT TO THE USE OF, OR FOR ANY AND ALL DAMAGES RESULTING FROM THE USE OF, ANY INFORMATION, APPARATUS, METHOD, OR PROCESS DISCLOSED IN THIS DOCUMENT.

THIS IS A FINAL REPORT. THE DATA, CALCULATIONS, INFORMATION, CONCLUSIONS, AND/OR RECOMMENDATIONS REPORTED HEREIN ARE THE PROPERTY OF THE U.S. DEPARTMENT OF ENERGY.

REFERENCE TO TRADE NAMES OR SPECIFIC COMMERCIAL PRODUCTS, COMMODITIES, OR SERVICES IN THIS REPORT DOES NOT REPRESENT OR CONSTIITUTE AND ENDORSEMENT, RECOMMENDATION, OR FAVORING BY RPSEA OR ITS CONTRACTORS OF THE SPECIFIC COMMERCIAL PRODUCT, COMMODITY, OR SERVICE.

ABSTRACT

As the name of the project implies, "Gas Production Forecasting From Tight Gas Reservoirs: Integrating Natural Fracture Networks and Hydraulic Fractures", this research effort developed a software system that predicts gas production while considering the interaction of induced hydraulic fractures with the natural fracture system in the reservoir. The reservoir simulator and workflow required was developed on an existing platform at the University of Utah built to model and simulate reservoirs with discrete-fracture networks. The simulator titled ARTS (Advanced Reactive Transport Simulator) is capable of simulating different physical processes (oil and gas recovery, water flooding, steam flooding, etc.) in complex fractured domains.

Several different tools were used to place and validate the hydraulic fracture created in the presence of natural fractures. Fracman was used to integrate all of the fracture and geologic information to create a conceptual geologic model. Fracman is not a geomechanics simulator. A rule based module within Fracman was used to generate the hydraulic fracture. A simplified discrete fracture network model was used in 3-DEC (an Itasca product) to place the hydraulic fracture in the natural fracture network. Flow simulations in this combined system were performed using ARTS. A geomechanics module was later developed for use within ARTS. The combined simulations were performed using soft coupling, where the geomechanical simulator and ARTS were coupled using a series of look-up tables. Hard coupling was also built into ARTS where the geomechanical and flow equations were solved within the same framework. The use of hard coupling was demonstrated on a system consisting of a number of fractures. The delineation and characterization of natural fracture systems in tight gas reservoirs is the most important step in development of these plays because of the ultralow matrix permeability. Ultimate exploitation of these reservoirs and their economic fate depends on how well the natural fracture systems are developed, and how well they are recognized, characterized and ultimately connected to the production system – usually by hydraulic fracturing.

The project team consisted of University of Utah, Utah State University, Utah Geological Survey, Golder and Associates and Itasca Incorporated. Data from Tract 21 in the Natural Buttes Field in the Uinta Basin was used for the modeling (T. 9 S., R. 21 E., section 21 and the E1/4 of section 20). A cohesive natural fractures map of the reservoir was made by integrating geologic information such as data from seismic , outcrop, log, geophysical, etc. Detailed fracture characterization showed that sedimentologic and diagenetic characteristics influence the fracture distribution and development of the Mesaverde Group on a regional, mesoscopic and microscopic scale. Dominant fracture sets and densities were established. Anadarko Petroleum contributed well data for wells in Tract 21. Microseismic information was not available for any of the wells in Tract 21. Hence, microseismic information from a well in the nearby section was used to validate the geometry and the extent of the hydraulic fracture created.

The main outcomes of this project were methodologies of characterizing fractures, creating discrete fracture networks, generating hydraulic fractures and performing multiphase flow simulations of the integrated system. These methodologies can be used in any system where fractures are important in establishing reservoir production. The software system can be accessed by working with University of Utah. The researchers at the University of Utah will provide guidelines for supplying a data set or will work with interested parties in creating appropriate data sets and the workflow required.

Table of Contents

ABSTRACT 3

EXECUTIVE SUMMARY 18

GREATER NATURAL BUTTES FIELD GEOLOGY 20

Gas Production in Natural Buttes 20

Stratigraphy 22

Paleogeography 25

Source and Reservoir Rocks 26

Gas Characteristics 29

Initial Area Selected for Detailed Modeling 29

NBU 253 Core Analysis 30

Tract 21 Site 30

NBU 921-21L Core Analysis 30

Reservoir Quality in Tract 21 31

Production Decline Analysis in Tract 21 31

General Description of Fractures and Faults in the Basin 32

DETAILED FRACTURE CHARACTERIZATION 35

Data Collection Methods 35

Outcrops 35

Fracture Mapping 36

Core, Well and Image Logs 36

Petrography 37

Field Locations 37

Analytical Methods 37

Orientation Analysis 37

Fracture Spacing and Density *38*

Statistical Analysis *38*

Fracture Characterization Results 38

Fractures in Outcrop *38*

Regional Fracture Sets *39*

Sandstone Texture and Lithofacies *39*

Subsurface Analysis 40

Drill Core Description *40*

Fracture Orientation and Spacing Based on Image Log Analysis *40*

Fracture Stratigraphy from Core, Image and Well Logs *41*

Petrography 41

Outcrops *41*

Drill Core *42*

Comparison of Outcrop and Core Petrography *42*

Data Analysis and Interpretation 43

Structural Control on Fracture Geometry *43*

Bed Thickness and Stratigraphic Architecture of Sandstone Units *43*

Influence of Mudstone/Shale Thickness on the Mechanical Interface *44*

Degree and Cement Type *44*

Lithofacies Fracture Characteristics *45*

Fracture Characterization Discussion 46

Relative Timing of Fracture Set and Development *46*

Sedimentologic and Diagenetic Controls on Fracture Distribution *47*

Analysis from Outcrop to the Subsurface *48*

Implications for Developing Well-log: Fracture Stratigraphy *48*

Implications for Fracture Distribution Prediction Based on Depositional Environment and Sandstone Diagenesis *49*

Implications for Improving Hydraulic Fracture Design within the Greater Natural Buttes Field *49*

Main Conclusions Concerning Fracture Characterization *49*

Creation and Validation of Discrete Fracture Network Models 50

Development of the Geological Conceptual Model 51

Antelope Ridge Scanline Site *52*

Blue Mountain Scanline Site *53*

Snake John Ridge Scanline Site *53*

Summary of Outcrop Observations & Development of the GCM *54*

DFN Model Development 55

Implementation of GCM for Tract 21 56

Mechanical Layering *56*

Creation of the Tract 21 DFN Model *57*

Calibration *58*

INCORPORATING GEOMECHANICS IN RESERVOIR SIMULATION 60

Mathematical Formulation 60

Governing Equation of Reservoir Model 62

Coupling Schemes 62

Hard Coupling 64

Hard coupling schemes *70*

Model Verification 71

INTEGRATED MODELING OF NATURAL AND HYDRAULIC FRACTURES 74

Injection Calculations 75

Effect of injection rate *75*

Effect of fluid viscosity *75*

Effect of fluid loss *75*

Soft Coupling 75

Effect of Proppant *77*

One more example of soft coupling 77

Representation of Reservoir Fabric *79*

Hydraulic Fracturing *79*

Representation of Production into the Fracture Network *81*

The Hydraulic Fracturing *83*

Production Modeling *83*

Water Blocking and Conductivity *83*

Conclusions Concerning Soft Coupling *84*

Realistic Discrete Fracture Networks 84

Impact to Producers 86

Technology Transfer Efforts 86

BIBLIOGRAPHY 87

List of Acronyms and Abbreviations 97

Greater Natural Buttes Geology 99

Detailed Fracture Characterization 104

Creation and Validation of Discrete Fracture Models 106

Incorporating Geomechanics in Reservoir Simulation 108

Integrated Modeling of Natural and Hydraulic Fractures 111

General Natural Buttes Geology 114

Natural Fracture Characterization 143

Creation of Discrete Fracture Networks and Validation 169

Integration of Geomechanics in Reservoir Simulation 182

Integrating Hydraulic Fractures and Natural Fractures and Simulation 184

List of Tables

Table 2-1. Description of fractures in the NBU 253 core, section 10, T. 9 S., R. 21 E., Uintah County, Utah. See figure 11 for fracture location in core. 99

Table 2-2. Tight rock analysis results from the NBU 253 core, section 10, T. 9 S., R. 21 E., Uintah County, Utah. See figure 11 for sample location in core. 100

Table 2-3. Description of fractures in the NBU 921-21L core, section 21, T. 9 S., R. 21 E., Uintah County, Utah. See figure 16 for fracture location in core. 101

Table 2-4. Tight rock analysis results from the NBU 921-21L core, section 21, T. 9 S., R. 21 E., Uintah County, Utah. See figure 16 for sample location in core. 102

Table 2-5. Triaxial compression results for sample taken from 921-21L core, section 21, T. 9 S., R. 21 E., Uintah County, Utah. See figure 16 for sample location in core. 103

Table 3-1. Table listing the structural setting, stratigraphic units sampled and number of lithofacies sampled at each field locality. 104

Table 3-2. Mean distribution and length data for each regional fracture set. Fracture density is defined as the number of fractures per m. Sstdv/ Savg is the standard deviation of spacing divided by the average spacing. 104

Table 3-3. Description of the 7 lithofacies identified and sampled. 105

Table 4-1. Uncorrected mean fracture intensity measured from scanlines. 106

Table 4-2. Terzaghi-corrected mean fracture intensity and mean spacing values measured from scanlines. 107

Table 5-1. Parameters used in the verification of the geomechanics code using the 1-D analytical solution. 108

Table 5-2. Parameters used in verifying the geomechanics code using the 2-D analytical solution. 109

Table 5-3. Parameters used in verifying the 3-dimensional implementation of the geomechanics code using the STARS - simulator from Computer Modeling Group. 110

Table 6-1. Tabulation of important properties used in the soft-coupling case studies. 111

Table 6-2. Properties used in the case study to study the impact of keeping the main fracture system open with proppant. 112

Table 6-3. Table of properties used in simulating flow through an extensive natural fracture network with geomechanics incorporated. 113

List of Figures

Figure 2-1. Regional location of Uinta Basin and the Greater Natural Butte (GMB0 field (after USGS Uinta-Piceance Assessment Team, 2003) 114

Figure 2-2. North-south cross section of the Uinta Basin (modified after Fouch et al., 1992; Osmond, 2003). Strata dip not true angles. 114

Figure 2-3.Oil and gas field map of the Uinta Basin showing the location of the Greater Natural Buttes gas field. 115

Figure 2-4. West-East chronostratigraphic chart across the Uinta-Piceance basins (Johnson and Roberts, 2003). 116

Figure 2-5. Vertical distribution of gas production from eight wells completed in the Mesaverde Group in eastern Uinta Basin 117

Figure 2-6. Paleogeography of North America during the mid-Cretaceous (about 100 Ma) (from Wicander and Monoroe, 1989). 118

Figure 2-7. Facies distribution and dispositional environments of the Mesaverde formations (White et al., 2008). 119

Figure 2-8. Three snapshots of the paleofacies map showing the changing depositional environments of the Mesaverde formations from A through B to C through time during Campanian (80-70 Ma) (after Fouch et al., 1992). 120

Figure 2-9. Structure on top of the Dark Canyon Conglomerate; contour interval 1000 feet and datum is mean sea level 121

Figure 2-10. Wells in section 10, T. 9 S., R. 21 E., the area of detailed study and modeling. 122

Figure 2-11. Cross-section of the Mesaverde Group in section 10, T. 9 S., R. 21 E., showing the discontinuous nature of the sand bodies. 123

Figure 2-12. Percentage of sandstone beds with 6% or more density/neutron porosity in wells drilled in section 10, T. 9 S., R. 21 E. 124

Figure 2-13. Percentage of sandstone beds with 6 to <8%, 8 to <10%, and 10% or more porosity in wells drilled in section 10, T. 9 S., R. 21 E. 124

Figure 2-14. Decline curves for the three wells in Tract 21 125

Figure 2-15. Geophysical well log of the NBU 253 well, section 10, T. 9 S., R. 21 E., Greater Natural Buttes field, Uintah County, Utah. The Sego and Castlegate Sandstones of the Mesaverde Group were cored in this well. 126

Figure 2-16. Graphical core description of the Sego and Castlegate Sandstones from the NBU 253 well, section 10, T. 9 S., R. 21 E., Greater Natural Buttes field, Uintah County, Utah. 127

Figure 2-17. Examples of lithology and depositional features identified in the NBU 253 core, section 10, T. 9 S., R. 21 E., Uintah County, Utah. 128

Figure 2-18. Examples of fractures found in the NBU 253 well, section 10, T. 9 S., R. 21 E., Uintah County, Utah. Top of each photograph is oriented towards the top of the core. 129

Figure 2-19. Wells in section 21 and eastern ¼ of section 20, T. 9 S., R. 21 E.. 130

Figure 2-20. Cross section A to A' of the Mesaverde Group in section 20 and section 21, T. 9 S., R. 21 E., showing discontinuous nature of the sand bodies (shown in yellow). 131

Figure 2-21. Graphical core description of the NBU 921-21L well, section 21, T. 9 S., R. 21 E., Greater Natural Buttes field, Uintah County, Utah. 132

Figure 2-22. Examples of fractures found in the NBU 921-21L well, section 21, T. 9 S., R. 21 E., Uintah County, Utah. Top of each photograph is oriented towards the top of the core..... 133

Figure 2-23. Graphs showing bed thickness and distance between beds in wells penetrating the Mesaverde Group in the Tract 21 site. See Figure 2-19 for well locations. 134

Figure 2-24. Graphs showing the bed thickness with 10% or more density porosity. 135

Figure 2-25. Production decline curves for four wells from section 21, T. 9 S., R. 21 E., that are producing from the Wasatch Formation..... 136

Figure 2-26. Production decline curves for the CIGE 288 and NBU 300 wells, both with commingled production from the Wasatch Formation and Mesaverde Group. 137

Figure 2-27. Production decline curve for NBU 921-21L well..... 138

Figure 2-28. Regional structural map of the Uinta-Piceance basins (Johnson and Roberts, 2003). 139

Figure 2-29. Gas migration model in the Mesaverde sediments. 140

Figure 2-30. (A) Bedding parallel and bedding perpendicular joints in a tilted section of the Mesaverde sandstone, Douglas Creek Arch. (B) Fractures in a core of Mesaverde sandstone, Natural Buttes Well #85433, Anadarko (photos by Rasoul Sorkhabi)..... 141

Figure 2-31. Structural map of the Greater Natural Buttes (compiled from Fouch et al., 1992; Osmond et al., 1992; Verbeek and Grout, 1992; Bader, 2009)..... 142

Figure 2-32. Cretaceous-Cenozoic event-chart for the Mesaverde petroleum system in the Greater Natural Buttes Field. 142

Figure 3-1. Location of the Greater Natural Buttes Gas Field along with the geologic map showing the outcrop exposures of the stratigraphic units within the Uinta Basin. 143

Figure 3-2. Azimuthal distribution of fracture sets at each field locality shown in Figure 3-1.144

Figure 3-3. Photographs of fractures..... 145

Figure 3-4. Stereonets showing poles to planes of all measured fractures from each locality 146

Figure 3-5. Mapped fracture sets on a Google Earth image of Asphalt Ridge (Locailty 1) (top) and a low – angle oblique air photo of "Blue Mountain Ridge" (Locality 3) (bottom) of outcrops of upper Mesaverde Group..... 147

Figure 3-6. Photographs of the seven sampled lithofacies..... 148

Figure 3-7. (A.) Multiple calcite filled fractures penetrating a fluid escape structure within core from well NBU 921 – 21L at 3,250 meters depth. (B.) Shear fracture terminating into a mud parting and splaying out near the bottom of the core off setting finely laminated sandstone (on left) against a more massive sandstone (on right) at 3,231 meters depth. 149

Figure 3-8. Left photograph is of core from well NBU 921 – 21L from the Price River Formation at 2349 meters deep with an extensional fracture with coarse calcite mineralization with an open, unfilled fracture penetrating the edge of the calcite mineralized fracture..... 150

Figure 3-9. Rose diagrams comparing fracture orientations from the subsurface and outcrop.... 151

Figure 3-10. Fracture stratigraphy of well NBU 921-21L core compared with wireline log curves.. 152

Figure 3-11. The figure displays the gamma ray (GR), static and dynamic resistivity image logs, sonic porosity (SPHI) and neutron porosity (NPHI) logs for well NBU 921-21L from 2587 – 2616 meters depth. 153

Figure 3-12. Photomicrographs of typical thin sections samples from lithofacies 1 – 7 sampled in outcrop taken in plane polarized light (left) and cross-polarized light (right)..... 154

Figure 3-13. Photomicrograph of outcrop samples with the left photos being in plane polarized light and the right photos are in cross polarized light. A & B) Medium-grained, moderately soted, quartz arenite with quartz cement..... 155

Figure 3-14. Photomicrographs of outcrop (photo C & D) and core (photo A &B) samples taken at 2.5x magnification with the left photos being in plane polarized light and the right photos are in cross polarized light. 156

Figure 3-15. Contoured stereonets of poles to planes of joints from each scanline at Snake John Reef (Locality 2) overlain on a Google Earth image.. 157

Figure 3-16. Plots of bed thickness versus fracture spacing for the four regional fracture sets identified in the basin..... 158

Figure 3-17. Crossplots of bed thickness versus fracture spacing. 159

Figure 3-18. A. Photo and interpretative drawing illustrates typical bed thickness control on fracture distribution. 160

Figure 3-19. Histograms of average fracture distribution data 161

Figure 3-20. Cross plot of fracture density of through-going fractures (y-axis) and thickness of shale that bounds the mechanical unit (x-axis) the scanline was taken in. 162

Figure 3-21. A & B. Photographs are taken of a vertical face.. 162

Figure 3-22. A. Photo of a bedding plane of a well indurated, carbonate cemented sandstone... 163

Figure 3-23. A) Histogram of average fracture density for poorly and well-cemented samples of similar bed thicknesses from 90 cm – 105 cm thick. 164

Figure 3-24. A) Histogram of average fracture densities for different cement types identified in thin sections. Fracture densities are from continuous sandstone beds with thicknesses from 305 cm – 550 cm thick. B) Cross plot of raw data with cement type versus fracture density.. 165

Figure 3-25. Photographs exhibiting fracture character in different lithofacies sampled..... 166

Figure 3-26. A & C) Histogram of the average fracture spacing and average fracture density for each lithofacies. B & D) Plot of raw data for each scanline station of fracture spacing and fracture density versus lithofacies type..... 167

Figure 3-27. Schematic 3D box diagram showing different sandstone reservoirs present within the GNB field.. 167

Figure 3-28. Schematic illustration of a lateral wellbore penetrating through lithofacies 4. Hydraulic fractures (blue lines) are shown to intersect the WNW-striking fracture set and the NE fracture set connecting the two fracture sets and potentially connecting the two fracture sets and potentially connecting the fracture systems allowing for increased drainage of the reservoir. 168

Figure 4-1. Primary outcrop locations for GCM development and fracture data acquisition. GPS station numbers are indicated by numbers. 169

Figure 4-2. Photo of Antelope Ridge scanline site, including stereoplots of fractures measured at each of the five scanlines. The black line in each small stereoplot shows the trend of the scanline used to acquire the data. 170

Figure 4-3. Stereoplot for all Antelope Ridge scanlines. 170

Figure 4-4. Blue Mountain outcrop area scanline locations. Numbers indicate GPS locations..... 171

Figure 4-5. Stereoplots for the Blue Mountain scanline site. 171

Figure 4-6. Relation of fracture orientation and termination style. 172

Figure 4-7. CCN plot for doubly censored and doubly truncated fractures from all outcrops.173

Figure 4-8. CFI plot for NBU921_21L, along with intervals of mechanical layering and their P10 values. 173

Figure 4-9. Visualization of mechanical layers derived from the CFI plot shown in Figure 4-8. 174

Figure 4-10. Stereoplot of open fractures for NBU21_21L. 175

Figure 4-12. ISIS analysis of open fracture data from the NBU21_21L well. 176

Figure 4-13. Fracture generation grids for Tract 21 model based on CFI plots for NBU21_21L open fracture data. 176

Figure 4-14. Generation of fractures from the fracture generation grids. 177

Figure 4-15. Visualization of fractures generated in the preliminary DFN model for Tract 21. 177

Figure 4-16. Validation of fracture orientations in the Tract 21 DFN model, comparing measured fractures with fractures intersected by well in the DFN model. 178

Figure 4-17. Compartmentalization analysis of the preliminary Tract 21 DFN model. 179

Figure 4-18. Compartment formation in the preliminary Tract 21 DFN model. 179

Figure 4-19. Visualization of fractures connected to the wellbore in the preliminary Tract 21 DFN model. 180

Figure 4-20. Microseismic response from Chapita Wells hydrofracturing and comparison with model results. 181

Figure 5-1. The University of Utah reservoir simulator framework – ARTS – Advanced Reactive Transport Models – that couples reservoir geomechanics with flow. 182

Figure 5-2. Comparison of the analytical and numerical solutions for a one-dimensional compression problem showing that the numerical implementation of the code in ARTS is verified. 182

Figure 5-3. Comparison of the analytical and numerical solutions for the two-dimensional compression problem (Mandel problem) showing that the numerical implementation of the code in ARTS is verified. 183

Figure 5-4. Comparison of various simulation output attributes between STARS and ARTS. The agreement is excellent once again validating the implementation of geomechanics in ARTS. ... 183

Figure 6-1. The fracture network used in 3-DEC simulations to create hydraulic fractures in the presence of natural fractures. 184

Figure 6-2. Pressures in the fracture system after 866 and 1624 seconds respectively. Injection rate was 50 barrels per minute. Pressures are in psi. 184

Figure 6-3. Injection pressure increase as a function of injection rate..... 185

Figure 6-4. Pressure in the fracture system at 2 cp fluid injection at 50 bpm. Left panel shows the pressure at 849 seconds and the right panel at 1931 seconds. Pressures are in psi. 186

Figure 6-5. Pressure as a function of injection fluid viscosity. 186

Figure 6-6. Snapshot of fluid pressure in the fracture system after 587 and 1054 seconds of injection at 50 bpm with fluid loss coefficient of 0.001 ft/min1/2. 187

Figure 6-7. Time profile for injection pressure with different leakoff coefficients. 187

Figure 6-8. Time profile for injection pressure for a 20 min injection, period followed by shut-in. This plot is extremely important. Many interpretations of in-situ behavior are based on shut-in behavior that is predicated by assumptions of a single planar fracture. These numerical simulations allow simulation of closure of complex fracture networks, and representation of the associated pressure decay. 188

Figure 6-9. The soft coupling scheme used for the implementation of geomechanics in reservoir simulation and the geometry employed (right)..... 188

Figure 6-10. Gas pressures and saturations in the fractured reservoir – no geomechanical coupling..... 189

Figure 6-11. Gas pressures and saturations in the fractured reservoir – case 1 simple geomechanical coupling where same geomechanical attributes are expected to affect all features. 189

Figure 6-12. Gas pressures and saturations in the fractured reservoir – case 2 complex geomechanical coupling where different geomechanical attributes are expected to affect all features. 189

Figure 6-13. Cumulative gas production for the three cases of no geomechanical coupling, simple coupling and complex coupling. All use the soft coupling scheme. 190

Figure 6-14. Gas saturation profiles with (right) and without (left) the presence of proppant. With the proppant, the drawdown limits permeability reduction. 190

Figure 6-15. Gas production rates with and without proppant. 191

Figure 6-16. A simplified view of a naturally fractured reservoir, subjected to in-situ stresses. 191

Figure 6-17. This is a cutout from the overall simulation (with dimensions of 1060 feet by 970 feet by 132 feet) showing inflated apertures. All apertures are in inches. All penetration into numerous natural fractures is evident to occur rapidly – and since there is finite initial width it can occur below fracturing pressure. Different panels show the evolution of the complex hydraulic fracture at various times. 192

Figure 6-18. End of Job (EOJ) geometries for the hydraulic fracture modeling at 0.254 m3/minute injection rate..... 193

Figure 6-19. Pore pressure (in psi) distribution profile at the end of hydraulic stimulation treatment (plan view) showing influence of the fracture network. In the first quadrant where natural fractures are closely spaced, injection fluid tends to follow the paths of least resistance, and no longer results in a simple elliptical pressure diffusion front as assumed by analytical models..... 193

Figure 6-20. Comparison of aperture of the hydraulic fracture at the end of injection treatment using different rates. Joint displacement vectors shown in inches are a proxy for apertures. Doubling the injection rate from 0.264 m3/min (above) to 0.528 m3/min (below) helps increase the hydraulic fracture aperture by ~30%-50% at the well and 2-10 times at the fracture tips. For tight gas and gas shales, this large increase in fracture conductivity may justify the cost of higher hydraulic power. 194

Figure 6-21. Gas saturations after 100 days of multiphase simulations using the University of Utah discrete-fracture network multiphase simulator. It is seen that the areas around the large-aperture fractures are drained effectively, while the remainder of the reservoir with poorly connected large-aperture fractures remains at high gas saturation. 194

Figure 6-22. Demonstration of the water-block concept in a simpler domain. It is seen that the gas is locked out of the flow system. 195

Figure 6-23. The realistic fracture network used to demonstrate the coupling of geomechanics and reservoir flow simulation. 195

Figure 6-24. Pressures and gas saturations in a simulation where the geomechanics is coupled with flow. The gas saturation variation is minimal since the gas is basically redistributed in the system. 196

Figure 6-25. Reservoir average pressure difference between coupled and uncoupled geomechanics simulations. The difference in pressure is not significant. 196

Figure 6-26. This figure shows the difference in cumulative gas production between the coupled and the uncoupled cases in the left panel. The differences are not discernible at this scale. The actual differences on an expanded y-scale are plotted in the right panel. There are some differences, but not significant due to the diffuse nature of the fracture system. 197

Figure 6-27. The difference between the initial and permeabilities at 2800 days in the fractures (left) and in the matrix (right) are shown in this figure. The differences between the permeabilities are not significant. But the permeability change is uneven dictated by the nature of the fracture system. 197

Figure 6-28. Volumetric and displacement changes in the reservoir at 2800 days. 198

EXECUTIVE SUMMARY

It is believed that the presence and characteristics of the natural fractures are important in the production of gas from tight sandstones. The objectives of this project were to first establish a methodology to characterize these natural fracture systems. It is common to complete wells using hydraulic fracturing in the tight gas formations in the Uinta Basin. The interaction between hydraulic fractures and the existing natural fractures governs the production behavior of these systems. In this project, we examined two different tools to see how hydraulic fractures propagate in this environment. The FRACMAN tool (from Golder and Associates) was used to characterize the natural fractures. A rule based method was employed in creating a hydraulic fracture in Fracman. The shape and extent of the hydraulic fracture created was validated using microseismic data on a nearby well. Fracman is not a geomechanics simulator. In a second method, a commercial geomechanics simulator (3DEC) was used to evaluate which of the natural fractures are activated during stimulation. The flow simulations with combined natural and hydraulic fractures were performed using a simulator developed at the University of Utah – Advanced Reactive Transport Simulator (ARTS). A geomechanics module was first developed in ARTS. This geomechanical module is able to use fracture characteristics data from an external simulator or is able to compute differences in fracture properties as production continues. A number of case studies and sensitivity analyses were performed. Main findings of the projects were as follows:

1. It is possible to integrate various types of geologic data to map out natural fractures and create discrete fracture network models.

2. Tools to create hydraulic fractures in the presence of natural fractures are effective and can be validated using microseismic data.

Multiphase simulations can be performed on DFN based models to study the interaction of natural and hydraulic fractures. A number of case studies were performed to show the applicability of the methodology and impact on production.

The Greater Natural Buttes (GNB) gas field was used to support this study. It covers about 400 square miles in Townships 8 to 12 S., and Ranges 18 to 24 E., Uintah County, Utah. Cumulative production from the GNB field has been about 2.1 trillion cubic feet of gas. A generalized geologic conceptual model was developed using field and other geologic data, and was applied to Tract 21, a section in the field. The Discrete Fracture Model (DFN) thus developed was validated using pressure and pumping data during hydraulic fracturing and the observed microseismic cloud from a nearby well. A series of sensitivity studies of the effect of fracture properties on hydraulic fracture creation were undertaken using 3-DEC, a commercial hydraulic fracture creation tool. These simulations employed a simple domain consisting of five fractures. Fracture orientations and dip had a significant impact as did injection rates and spacing.

The effect of flow rate and fluid viscosity on the fracture morphology was documented. Higher viscosity fluids affect a smaller region, but create more effective open fractures. A method to study leak-off was also developed and demonstrated. Because of leak-off, fracture conductivity is reduced by 10-20%. These changes in fracture characteristics are seen in increased production in fracture networks with higher conductivity. The outputs of 3-DEC in the form of lookup tables were implemented into the Utah Advanced Reactive Transport Model code (ARTS), and the impact of using geomechanics on flow simulations was examined.

The geomechanical hard coupling algorithm was implemented within ARTS. This was achieved by using the fundamental geomechanics equations. In this manner, the changes in fracture properties on injection and production were calculated within ARTS, so that input from an external geomechanical tool was not required.

The focus of this study is the Mesaverde Group, which consists of Tuscher, Farrer, Bluecastle (tongue of the Castlegate), Neslen, Sego, Castlegate, and Blackhawk Formations. The project team selected section 10 (T. 9 S., R. 21 E.) (referred to as Tract 10 Site) in the north-central portion of GNB for detailed study based on initial recommendations by Anadarko Petroleum, the operator. Detailed geologic and production analysis of this section were reported. Due to a decrease in natural gas prices, drilling in section 10 did not occurred as was originally anticipated. As a result, the location for modeling was changed to section 21 (T. 9 S., R. 21 E.) and the E1/4 of section 20 (referred to as Tract 21 Site), where core and formation imaging logs were available from the productive portion of the Mesaverde Group. Petrophysical measurements showed that sands of the Mesaverde Group have very low porosity (0.43 % to 8.64 %) and low permeability (0.0001 to 0.031 mD). These results were used in production modeling. Triaxial compression testing was conducted on a sandstone sample and graphs of the stress and strain data were prepared. The measured stresses appeared higher than expected for these types of rock. These mechanical properties were used in the geomechanical modeling. Detailed fracture characterization was performed. The bedding strike was north-south. The results also indicated that the fractures in the Mesaverde on the margin of the Uinta Basin were formed primarily due to folding of the rock. However, at Blind Draw, about 10 km away, smaller and larger joints strike obliquely to the bedding strike and dip. These joints do not show the geometric relation to bedding that occurs if they were formed through folding. These findings of joints consistent with folding and those that are not were found at other locations as well suggesting that the fracture sets in the Mesaverde may be characterized by sets related to folding and a set in some locations that is dictated by regional effects.

Core description (from the NBU 253 core) shows that the Castlegate and Sego Sandstones have similar lithology and consist mostly of sandstone interbedded with black, bioturbated, and carbonaceous shale. Individual sandstones range from very fine to fine grained and have low-angle cross-bedding, small ripples, sparse burrows, and moderate bioturbation. The Castlegate was deposited in a marginal marine to lower coastal plain environment, whereas the Sego is a marginal marine deposit.

GREATER NATURAL BUTTES FIELD GEOLOGY

The Uinta basin of northern Utah has an area of about 93,000 square miles (24,000 sq. km) in a strict sense (roughly 90 miles north-south and 100 miles east-west) (Anders et al., 1992) although the USGS Uinta-Piceance Assessment Team (2003) extends the "Uinta assessment province" some thirty miles south of Book Cliffs to include the petroleum resources in the "transitional area" as well, thus resulting in an area of 120,000 square miles (roughly 120 miles long and 100 miles wide) for the basin (Figure 2-1). The Douglas Creek Arc separates the Uinta basin from the Piceance basin of western Colorado although these two basins share similarities in their tectonostratrigraphy including the presence of the Upper Cretaceous Mesaverde Group in both basins. Sedimentary rocks in the Uinta basin date back to the Cambrian (Lodore Sandstone and Ophir Shale); however its current basinal framework as a Rocky Mountain foreland basin was fashioned during two orogenic events affecting the western USA: (1) The Cretaceous Sevier orogeny which supplied sediments to the basin in fluvial-coastal-shallow marine depositional environments; and (2) the Paleogene Laramide orogeny which was responsible for the uplift of the Uinta Mountains to the north and other basement uplifts to the south of the Uinta basin. About 32,000 ft of Phanerozoic sedimentary rocks probably occur in the Uinta basin. Of these, the Upper Cretaceous rocks are 5,000-10,000 ft thick, and Paleocene and Eocene alluvial and lacustrine sediments account for as much as16,000-22,000 ft, which provide a significant overburden for the Upper Cretaceous sediments (Anders et al., 1992; Spencer, 1995).

The Uinta basin is an asymmetrical foreland basin with deepest parts to the north where the Precambrian clastic rocks of Uinta Mountains have upthrust; the basin gradually thins toward south where Cretaceous sedimentary rocks crop out along Book Cliffs (Figure 2-2). In this manner, the Late Cretaceous and Paleogene strata dip 4°-6° toward the Uinta Mountains in the north. To the west, the Uinta Basin is separated from the Wasatch Mountains by the Charleston-Nebo Thrust, which originated during the Cretaceous Sevier Orogeny. To the southwest, south, and southeast of Uinta Basin lie respectively the Wasatch Plateau, San Rafael Swell, and Uncompahgre Uplift, all of which formed during the Laramide orogeny. On the eastern boundary, as mentioned above, the Douglas Creek Arch separates the Uinta basin from the Piceance basin (Figure 2-1) (Osmond, 2003). The Green River originating in Wyoming is the predominant river presently draining the Uinta basin; the river cuts through the basin in a NE-SW direction (small rivers such as the White River also drain the basin).

The Greater Natural Buttes (GNB) gas field covers about 400 square miles in T. 8 to 12 S., and R. 18 to 24 E., Salt Lake Baseline and Meridian, Uintah County, Utah (Figure 2-3). The field was discovered in 1955 and produces mostly from the Tertiary Wasatch Formation and the Cretaceous Mesaverde Group. The Utah Division of Oil, Gas, and Mining (DOGM, 2012) reported 4620 active wells produced 23.9 billion cubic feet of gas (BCFG) from GNB field during the month of July 2012, and the cumulative production is 2.6 trillion cubic feet of gas.

Gas Production in Natural Buttes

In the 19th century, gilsonite found abundantly in vertical veins on the surface topography of the Uinta basin was mined for non-fuel purposes (gilsonite mining still continues in the region). In 1925, gas was discovered in the Ashley Valley anticline in the Uinta basin; the gas flowed

from shallow sandstone of the Jurassic Morrison Formation (Spencer, 1995). In 1949, oil was discovered in the Ashley Valley field, which is a small-scale version of the giant Rangely field a few miles to the east in Colorado. Both fields produce oil from the Pennsylvanian-age Weber Sandstone. Also in 1949, oil was discovered in the paleo-lake sediments of the Green River Formation at Roosevelt field; oil from the same Eocene sediments was discovered at Duchesne field in 1951 and at Red Wash field in 1951 (Osmond, 2003).

Osmond (2003) has divided the post-World War II history of exploration in the Uinta basin into three phases:

1. Phase 1 (1945-67) during which surface and aerial photographic mapping was initially used to locate anticlinal traps and was supplemented in the 1950s by seismic surveys. More drillings found that hydrocarbon accumulations were mainly controlled by stratigraphic traps (sand channels not structural anticlines) in the central part of the basin. During this period, as more gas was produced, the first gas pipeline was constructed in 1963.

2. Phase 2 (1968-86) began with the discovery of the over-pressured, basin-center Altamont-Bluebell oil and gas field in 1970, which to this day remains the largest field in the Uinta basin. This phase witnessed a remarkable growth in drilling activities, mainly due to the oil shocks of 1973 and 1979.

3. Phase 3 (1987-present) was initially motivated by the fact that the Wasatch-Mesaverde reservoirs in the GNB gas field was qualified for tight-gas formation tax credits, and this gave companies financial incentives to drill numerous wells into these formations before the tax credit expires. In 1993, two news gas pipelines were built in the Uinta basin.

In the GNB field proper, the first gas discovery was made in December 1952 by the Continental Oil Co. No. 1 Chapita Wells Unit (SW NW Sec. 16, T9S R23E); the well was completed in the Mesaverde Formation but was depleted in a few months and was thus abandoned. The Continental Oil Co. No. 2 Chapita Wells Unit (NW SE Sec. 28 T9S R23E) in February 1952 was completed in the Eocene Wasatch formation (porosity of 6-20% and permeability of nearly 1 mD) and proved to be a discovery well. Later drillings identified the underlying Cretaceous Mesaverde sands (with porosity of 6-13% and permeability of 0.01 to 0.1 mD) as a significant gas reservoir (Cuzella and Stancel, 2006). Major gas field discoveries that put the GNB field in spotlight during the 1950s-70s are listed below (from Osmond, 1992).

FIELD	LOCATION	DISCOVERY YEAR
Chapita Wells	T9S, R22-23E	1952-1955
Ute Trail	T9-10S, R20-23E	1956
Southman Canyon	T10S, R23-24E	1956
Uinta	T10S, R20-21E	1959
Rock House-Rainbow	T11S, R23-24E	1960
Bitter Creek	T9-120S, R20-23E	1961
Buck Canyon	T12S, R21E	1961
Island/River Bend	T10S, R18-19E	1961
Oil Springs	T12S, R21E	1962
Stagecoach	T8S, R21-22E	1965
Devils Playground	T9S, R24E	1973
Love	T11S, R21E	1974
Ouray	T9S, R20E	1979

A 2003 USGS report estimated the total natural gas reserves of the Mesaverde system to be 5.9 tcf (at 95% probability) 8.5 tcf (at 50% probability), 14.2 tcf (at 5% probability), and 8.96 tcf (mean value), of which only 66.4 bcf is "conventional" gas accumulated at shallow levels while the bulk of the gas reserves are "unconventional" (basin-centered continuous) gas accumulations (USGS Uinta-Piceance Assessment Team, 2003).

Stratigraphy

The Mesaverde Group are clastic (alluvial, deltatic and coastal plain) sediments, ranging in thickness from 2200 to 2900 ft (670-885 m) in the GNB field, and are Late Cretaceous (Campanian) in age. The Mesaverde overlies the Mancos "Shale" Group (equivalent of the Indianola Group in San Pitch Mountains and Sanpete Valley in central Utah) although a distinct separation between the two groups is not always clear, especially at the GNB field where the lower Mesaverde formations interfinger with the uppermost Mancos sediments. The Mesaverde is separated from the overlying Paleocene-Eocene Wasatch Formation along a major unconformity (2 to 20 million year old gap), which increases from west to east toward the Douglas Creek Arch. The Mesaverde Group, studied mainly at outcrops on the mountains surrounding the Uinta basin, consists of several formations with (sometimes) varying stratigraphic names and/or sedimentologic character from one area to another (Figure 2-4). Early stratigraphic work on the Mesaverde was done by Spieker et al. (1925) and Fisher (1936, 1960) followed by Fouch et al. (1983), Pitman et al. (1987), Franczyk et al. (1990), White et al. (2008), and many others.

In the Price Canyon, the Mesaverde Group is divided into four formations, which are briefly described below from bottom upward (Fisher, 1960):

1. Star Point Sandstone Formation, lowermost sandstone, primarily littoral marine, about 350 ft in thickness;

2. Blackhawk Formation, the main coal-bearing unit, over 900 ft in thickness;

3. Castlegate Sandstone Formation, an upward coarsening delta plain sandstone, 250-500 ft thick;

4. Price River Formation, about 600 ft thick, consists of interbedded sandstone beds (each 20-90 ft thick) and siltstone beds (each 7-30 ft thick). The sandstones are medium sized and cross bedded (Guiseppe and Heller, 1998). The Price River Formation is unconformably overlain by the North Horn Formation (latest Maastrichtian to Eocene) consisting of reddish sandstone and limestone beds. The unconformity on the top of the Price River Formation is estimated to be about 2 million years.

In the GNB field, Osmond (1992) divided the 2200-2900 ft (670-885 m) thick Mesaverde Group into the following formations described from older to younger strata:

1. Castlegate Sandstone Formation, 350 ft thick, is an upward coarsening, very fine to coarse-grained sandstone of delta plain. Castlegate Sandstone overlies the dark-gray marine shale of the Mancos Group (about 5000 ft thick) and is overlain (due to interfingering) by the 100 ft thick Buck Tongue formation of the Mancos Shale Group.

2. Nelson Formation, accounting for almost one-third of the thickness of the Mesaverde, contains coal and carbonaceous shale interbedded with siltstone and fine-grained quart-rich sandstone typical of deltaic environments.

3. The undifferentiated Tuscher and Farrer Formations consist of tight sands, siltstone, gray shale and coal, with thicknesses reaching up to more than 1000 ft, and represent a change from deltaic (Nelson Formation) to alluvial plain conditions. The top of the Mesaverde is marked by a regional unconformity and is overlain by the Wasatch Formation, which is about 3000 ft (915 m) thick in the western GNP and thins to about 1000 ft (305 m) in the eastern part (Osmond, 1992). (The Wasatch Formation is equivalent to the Colton Formation to the west of GNB.)

In a recent study, White et al. (2008) documented outcrop characteristics of the Tuscher-Farrar Formations along the Tuscher and Sego canyon roads at Book Cliffs. White et al. (2008) used sandstone content (net-to-gross ratio) and outcrop relief as criteria to distinguish between the Farrar and Tuscher formations. According these authors, the Tuscher is characterized by massive cliffs (50 to 200 ft high) consisting of 75 to 95% sandstone, whereas the Farrer is less cliff prone and has lower (50-75%) sandstone. The Farrar Formation is generally a 410-800 ft thick package of fluvial sandstone interbedded with non-carbonaceous mudrock; the Tuscher Formation is 200-600 thick, amalgamated fluvial sandstone with small amounts of non-carbonaceous mud. Paleocurrent directions from the Farrer and Tuscher formations exhibit a generally NE channel trend toward the GNB field (While et al., 2008).

At the subsurface reservoir scale, Longman and Koepsell (2005), using image logs from 10 wells in the GNB field, divided the Mesaverde Group into the Lower, Middle and Upper parts as follows (listed from younger to older strata) (Figure 2-5):

(3) Upper Mesaverde, 500 ft. thick, consist mainly of:

Blocky braided stream sandstone

(2) Middle Mesaverde, about 1100 ft thick, consist of:

Upper fluvial fining-up channel sandstones

Laterally persistent blocky braided stream sandstones

Fining-up fluvial channel sandstone (lowermost part)

(1) Lower Mesaverde, over 700 ft thick, consist of:

Upper coal-bearing interval

Middle Nelson interval

Lower Nelson coal-bearing interval

Upper Sego transition interval

Blocky Sego sandstone (marine shoreline)

Black Tongue marine shale

Castlegate sandstone (marine shoreline) (lowermost part)

Of these strata, fluvial channel sandstone bodies (each ranging in thickness from a few to over 25 ft) and braided stream sandstone bodies (each up to 100 ft thick) lying above the Lower Nelson coal-bearing interval, provide the bulk of gas production in the GNB field, while Castlegate and Blocky Sego sandstone units are mainly wet sands (Longman and Koepsell, 2005).

To summarize the above discussion, the following stratigraphic framework is given for the Mesaverde Group in the GNB field:

- Uinta Formation (Late Eocene, 40-34 Ma, alluvial sediments, 1700 ft)
- Green River Formation (Middle Eocene, 49-40 Ma, mainly lacustrine shale and marl, 2200-3800 ft)
- Wasatch Group (Late Paleocene-Middle Eocene, 60-49 Ma and the Dark Canyon rocks of Early Paleocene age), 3000 ft thick
- Unconformity (Maastrichtian-Early Paleoce, 70-60 Ma)
- Mesaverde Group (Campanian, 80-70 Ma), 2200-2900 ft thick
- Tuscher and Farrer Formations (mainly sandstone), 450-1000 ft
- Nelson Formation (mainly sandstone), 700-1000 ft

- Sego Sandstone Formation, ~100 ft
- Buck Tongue Formation (of the Mancos "Shale" Group interfingering with the Mesaverde), ~100 ft
- Castlegate Sandstone Formation, 350 ft
- Blackhawk Formation (main coal-bearing formation), 300-500 ft
- Mancos "Shale" Group (Cenomonian-Campanian, 95-80 Ma), 5000 ft thick

The entire Phanerozoic sediments in the GNB field range from 15,000 ft in southeast to 20,000 ft to the northwest of the field (Cuzella and Stancel, 2006).

Paleogeography

Deposition of the Mesaverde clastic sediments during the Late Cretaceous was due to (1) an Interior Seaway (marine incursion) that spanned from Canada in the north through the mid-western USA to Mexico in the south; and (2) the formation of the Rocky Mountains by Sevier orogeny on the western side of the Cretaceous Interior Seaway. Sea-level changes as well as lateral variation (proximity to or remoteness from Sevier uplands) caused facies changes in the Mesaverde Group spatially from the Uinta to Piceance basins and temporally through Late Cretaceous times (Figure 2-6). The Cretaceous Interior Seaway in the Utah and Colorado sections has been referred by some geologists to as Mancos Sea (Ryer and McPhillips, 1983; White et al., 2008).

White et al. (2008) identified the following depositional environments for the various formation of the Mesaverde Group (Figure 2-7):

- Blackhawk Formation and Sego Sandstone Formation:
  Marginal-marine environment
- Castlegate Sandstone and Nelson Formation:
  Marginal-marine to lower coastal plain environments
- Tuscher and Farrer Formations:
  Upper coastal plain and alluvial-plain environments

White et al. (2008) also classified various types of "sand bodies" from the producing Nelson, Farrer and Tuscher formations based on channel pattern, sediment load, and grain size.

On a basinal scale and focusing on certain marine fossil zones within the Campanian-age Mesaverde Group, Fouch et al. (1992) constructed several paleofacies maps for the Mesaverde sediments depicting the changing geography of marginal marine, coastal plain and braided-stream plain environments in the Uinta basin (Figure 2-8). These paleogeographic maps show that overall braided stream plains progressively cover a larger tract of the basin through time. These paleo-environmental changes explain why coal-bearing and carbonaceous shales (the Blackhawk Formation) dominate the lower part of the Mesaverde while sand-rich alluvial

sediments dominate the uppermost part of the Mesaverde. Regression and transgression of the shoreline-produced deposition of various sand bodies across the Uinta-Piceance basins during late Cretaceous times. This was followed by the Laramide orogeny, which deformed the flat-lying mid-continental foreland basin into a terrain of basement uplifts and structural depressions, filled with Paleogene fluvial and lacustrine sediments.

Source and Reservoir Rocks

Information on the Mesaverde petroleum systems is given in Fouch et al. (1992), Anders et al. (1992), Nuccio et al. (1992), Rice et al. (1992), Osmond (1992), Johnson and Roberts (2003), Nuccio and Roberts (2003), Osmond (2003), and Cuzella and Stancel (2006). Coal seams and carbonaceous shale beds are present within the Mesaverde Group and were accumulated in mires, swamps, and marshes associated with deltaic and coastal environments which generally prograded in a west to east direction. In the Uinta basin, these gas-bearing source rocks occur in the Nelson Formation (250-500 ft thick) but more prominently in the underlying Blackhawk Formation (about 900 ft thick). Total net coal thickness in the Nelson Formation is as much as 29 ft while that of the Blackhawk Formation reaches up to 80 ft. It is also conceivable that gas-prone coal and mudstone beds in the underlying Mancos "Shale" Group have generated gas now accumulated in the sandstone units of the Mesaverde (Johnson et al., 2003). Given the abundant coal beds and the gas accumulations in the Mesaverde, type III kerogen (organic matter) must be the dominant type in these sediments. Nevertheless, in a geochemical study from the Piceance basin Johnson and Rice (1990) found that gas in the lowermost part of the Mesaverde is chemically wet gas and is associated with minor amounts of oil, indicating the presence of both type II and III kerogen in the source rocks at the lowermost part of the Mesaverde and in the underlying Mancos Shale.

The base of the Mesaverde Group/top of the Mancos Group yield maximum burial depths ranging from 6,500 to 25,000 ft. Values of Vitrinite Reflectance (Ro) from the lower Mesaverde coal and shale samples measured from the Uinta basin vary depending on depth, reaching up to 2.0% in the deepest parts of the basin. The Ro values of the Mesaverde in the GNB field range from 0.6% in the east to over 1.3% in the west. Geothermal gradient in the GNB field ranges from 1.4 to 1.9 °F/ft (Anders et al., 1992); Osmond (1992) reports an average gradient of 1 °F/49 ft (1 °C/27 m) based on data from 28 wells at the GNB. Maturity modeling indicates that the onset of thermogenic gas from Mesaverde source rocks in the Uinta basin began at about 42 Ma, with peak gas generation during 26-17 Ma (Johnson and Roberts, 2003; Nuccio and Roberts, 2003) while Osmond (1992), based on relatively higher geothermal gradient in the Mesaverde intervals compared to that of the Wasatch Group, argues for the ongoing generation of thermogenic gas in the Mesaverde Group.

Gas generated from the coals and carbonaceous shales migrated upward and filled the nearby sandstone beds of the Mesaverde Group which were deposited by meandering to braided rivers in deltaic, coastal and alluvial plain environments (Johnson and Roberts, 2003). These sandstone rocks are, however, tight reservoirs. Sandstone units as thick as 70 ft, have porosities up to 18%, but generally 8-12% (based on density and neutron logs as well as core analyses) and producing zones lie at depths of 4500 ft in the southeastern GNB to 8600 ft in the northwestern part of the field (Osmond, 1992). Cuzella and Stancel (2006) report average porosity of 11% and

permeability of 0.01 mD, water saturation of 43%, and pressure gradient of 0.43 to 0.52 psi/ft for the GNB Mesaverde sandstones with an average net pay thickness of 157 ft (maximum 404 ft thick), and a gross thickness of 3,800 to 5,600 ft.

A detailed investigation of the petrographic and petrophysical properties of the Mesaverde sandstones in both Uinta and Piceance basins was conducted by Byrnes et al. (2009) as part of the DOE Mesaverde Petrophysical Project (DE-FC26-05NT42660)/Kansas Geological Survey. They analyzed 539 core samples from 8 wells (Flat Mesa 2-7, KM1022-1A, KM State 920-360, RBU 11-17F, LAMCO 4-54, LAMCO 3-24, USGS BC-3, and USGS BC-4) in the Uinta basin. Their results are summarized below:

1. In the Mesaverde Group, sandstone samples contain more than 50% of quartz and lithic fragments. Samples from Uinta are more quartz rich than those from Piceance because the Uinta basin was filled with more fluvial sands. Quartzose samples are preferentially subject to quartz growth cementation while feldspathic sandstones suffer compaction and clay cementation.

2. Grain density of the Mesaverde sands in the Uinta basin is 2.30-2.80 g/cc, with a mean value of 2.639 g/cc.

3. Porosity: 6.1% (mean), 5.9% (median); Maximum 23.8%

4. Permeability: 0.0022 mD (mean), 0.0014 mD (median), Minimum 0.000005 mD, maximum 76.2 mD,

5. Empirical relationship between Klinkenberg permeability and porosity:

   $K_{klinki} = 10^{(0.3\varphi - 4.75)}$

6. In-situ Klinkebberg permeability for gas in the Mesaverde sandstones:

   $K_{gasi} = K_{liquid}\,(1 + 4cL/r) = K_{liquid}\,(1 + b/P)$

   where Kgasi= gas permeability at pore pressure; Kliquidi= liquid permeability; c = proportionality constant (about 1); L = mean free path of gas molecules at pore pressure; r = pore radius; b = proportionality constant (=f(c, L, r)) is empirically found to be 0.851 Kklink -0.34; P = pore pressure (atm).

7. Low-permeability Mesaverde sandstones are stress sensitive; the following empirical relationship was found for the in-situ Kinkenberg permeability (in mD).

   $\log K_{klinki} = --0.0088\,(\log K_{air})^3 - 0.072\,(\log K_{air})^2 + 1.37 \log K_{air} - 0.46$

8. Power-law relationship between pore volume compressibility and net effective confining pressure

   Log_{10} ß = C $\log_{10}$ Pe + D

   The slope and intercept of the pore volume compressibility relations is given by

   C = -1.035 + 0.106/$\varphi^{0.5}$ D = 4.857 φ-0.038

9. The relationship between in-situ Archie cementation exponent (m) and Mesaverde sandstone porosity is given by the following empirical equation:

   m = 0.676 log φφ+ 1.22 +

   R22= 0.63

   Limit of m = 1.9

   No increase in m above the porosity of 12%. RMA)

   Note that m is related to tortuosity (length of the flow path, or the electrical efficiency of the path).

   For dual porosity (where the sandstone behaves a mixture of matrix porosity and fractures):

   m = log [φ-φ2)^{m1} + φ2 ^{m2}] / logφ

   φ2 is fracture porosity = 0.35%; m1 = 2, m1 = 1

10. Relationship between the principal pore throat diameter (Pd in microns) and the in-situ Klinkenberg permeability (Kklink in mD):

    Pd = 2.6 $K_{klink}^{0.445}$ R^2 = 0.93

11. Relationship between threshold entry pressure (air-mercury threshold entry, Ts, in psi) and Klinkenberg permeability (Kklink in mD):

    Ts = 64.66 $K_{klink}^{-0.44}$ R^2 = 0.82

The following geomechanical rock parameters have been reported from one well for the Mesaverde in the GNB field (EGG Resources, 2007, reported in Guiterrez, 2007): Pressure gradient = 0.43 b/ft; pore pressure = 179 bars (for sandstone depth of 6300 ft); Poisson ratio = 0.22; Young's Modulus = 39024.32626 Pa; density = 2480 kg/m^3.

Gas Characteristics

The following data on the quality of the Mesaverde gas come from Osmond (1992) and Cuzella and Stancel (2006):

BTU: 1066 Btu (300 kg-cal) to 1179 Btu (297 kg-cal), averaging 1114 Btu (280 kg-cal)

WGR (average): 100 bbl/mcfg

Associated Water (RW): 20,000 ppm

Specific Gravity (average): 0.63 g/cc

CO2 Content: Less than 2%

Average composition: 92% CH4; 4.18% C2; 1.74% C3; 0.48% C4, 0.15% C5, 0.46% CO2, 0.15% N2

The focus of this study is the Mesaverde Group, which consists of, in descending order, the Tuscher, Farrer, Bluecastle (tongue of the Castlegate), Nelson, Sego, Castlegate, and Blackhawk Formations (Figure 2-4). The Tuscher and Farrer are combined in the western part of the Uinta Basin, into the Price River Formation. The Mesaverde is overlain by the Paleocene Dark Canyon Conglomerate. Although not part of the Mesaverde, the Dark Canyon is relatively thin compared to the Wasatch and Mesaverde, and most operators include it in the Mesaverde. GNB field lies in an area of gentle northwest dip on the southeast flank of the Uinta Basin. Thickness of the Mesaverde in GNB field ranges from 2200 to 2900 feet (670-880 m) (Osmond, 1992), and drill depths to the base of the Mesaverde can range from 6000 to 12,000 feet (1800-3600 m).

Cole (2008) summarized the Blackhawk and Sego as marginal marine deposits; the Nelson and Castlegate as marginal marine to lower coastal plain; and the Bluecastle, Farrer, and Tuscher as upper coastal-plain to alluvial-plain deposits. Many of the deposits are lenticular channel sandstones with limited lateral extent, resulting in a vertically extensive but highly compartmentalized set of reservoirs. Cole (2008), working in Sego Canyon south of GNB, described Nelson sand bodies as 1.4 to 12.9 feet (0.43-3.9 m) thick with a width of 52 to 1222 feet (16-373 m), and lower Farrer sand bodies as 1.5 to 27.0 feet thick (0.5-8 m) with a width of 92 to 2556 feet (28-780 m). The sandstones are tight (low permeability) with some natural fractures. Longman and Koepsell (2005) showed the vertical distribution of gas production from the Mesaverde Group . Massive hydraulic fracture treatments are necessary to establish economic gas production.

Initial Area Selected for Detailed Modeling

The project team initially selected section 10, T. 9 S., R. 21 E. (Figure 2-9) in the north-central portion of GNB for detailed modeling. The area was selected after consultation with Anadarko Petroleum Corporation, our industry partner, because it has several potential locations for drilling to the Mesaverde Group, providing an opportunity to obtain new data during the study. Currently, only three wells have been completed in the Mesaverde in section 10 (Figure

2-10). The cross section of the three wells shows the highly lenticular nature of the sand bodies (Figure 2-11). Only one well, Natural Buttes Unit (NBU) 253, was drilled through the Blackhawk Formation; the other two wells (NBU 406 and NBU 921-10H) were drilled to a total depth in the Nelson Formation. The density and neutron logs of the three wells show the NBU 921-10H has the highest percentage of sandstone beds with 6% or more porosity. In the NBU 921-10H well the Farrer has the highest percentage of beds with 6% or more porosity, whereas in the NBU 406 and NBU 253 wells the Farrer and Tusher Formations have the highest percentage of beds with 6% or more porosity. In all three wells, most beds have 6 to 8% porosity (Figures 2-12 and 2-13). Overall, the NBU 406 well has the best porosity distribution and is the best gas producer of the three wells over the first four years of production (Figure 2-14). This quick-look analysis does not take into account many other factors that can influence the production.

NBU 253 Core Analysis

Cores of the Sego and Castlegate sandstones were taken in the NBU 253 well (Figure 2-15). Over 200 feet (61 m) of slabbed core is housed at the Utah Geological Survey's Utah Core Research Center in Salt Lake City, Utah. Core analysis shows that the Castlegate and Sego sandstones have similar lithology and consist mostly of sandstone interbedded with black bioturbated and carbonaceous shale. Individual sandstone beds range from very fine to fine grained and have low-angle cross-bedding, small ripples, sparse burrows, and moderate bioturbation (Figures 2-16 and 2-17). Twenty-six fractures were described and photographed (Figure 2-18 and Table 2-1). Most are natural fractures between 2 and 9 inches (8-20 cm) long, closed or slightly open with no discernable mineralization. Several appear to be drilling induced and are nearly vertical and very long (~ 2.5 ft [0.75 m]) with no mineralization. Eight samples were taken for tight rock analysis (Table 2-2). Porosity values range from 2.06 to 7.74 %, and permeability values range from 0.007 to 0.068 milidarcies (mD).

Tract 21 Site

Due to a decrease in natural gas prices, drilling in section 10 did not occur as anticipated. As a result, the location for modeling was changed to section 21, T. 9 S., R. 21 E. and the E1/4 of section 20 (Figure 2-19) (referred to as Tract 21 Site), where core and formation imaging logs are available from the productive portion of the Mesaverde Group. Three wells are completed as gas wells in the Mesaverde Group in section 21. The NBU 300 well was drilled only into the uppermost portion of the Mesaverde, whereas the NBU 921-21L and CIGE 288 wells drilled more than 1000 feet (300 m) of Mesaverde. A close offset to the NBU 921-21L well is the NBU 921-20P well, which was drilled in the SWSW section 20, and is included in this study. The cross section (Figure 2-20) of the three wells shows the highly lenticular nature of the sand bodies in the Mesaverde.

NBU 921-21L Core Analysis

One hundred and eleven feet (34 m) of core from the NBU 921-21L well was loaned to the project team by Anadarko for detailed core description and analyses. The cored interval is within the Price River Formation, which is equivalent to the Tuscher and Farrer Formations, in the upper Mesaverde Group. Like the Castlegate and Sego sandstones, the Price River Formation is mostly fine-grained sandstone interbedded with carbonaceous shale and silty mudstone (Figure 2-21).

Sedimentary structures include low-angle cross-bedding, flaser bedding, small ripples, sparse burrows, and moderate bioturbation. Twenty-eight fractures were identified, and all appear to be natural, many with mineralization (Figure 2-22 and Table 2-3). Most are inclined to vertical in orientation, but there is also an abundance of horizontal fractures. Forty samples were taken for tight-rock analysis, and the results show very low porosity (0.43 to 7.65 %) and permeability (0.002 to 0.031 mD) (Table 2-4). A core plug through a fracture was taken at 9405 feet (2869 m) for triaxial compression analysis (Table 2-5).

Reservoir Quality in Tract 21

The reservoir quality of the three Mesaverde wells in the Tract 21 Site was evaluated using the same parameters that were used in evaluating the Mesaverde wells in section 10. Sandstone bed thickness was determined using a gamma-ray value of 65 API units or less and a minimum thickness of 4 feet (1.2 m). The three wells have similar sandstone thickness; CIGE 288 has 494 feet (150.6 m) total sandstone from 42 beds, NBU 921-21L has 504 feet (153.6 m) total sandstone from 46 beds, and NBU 921-20P has 541 feet (164.9 m) total sandstone from 52 beds. The majority of the beds are 4 feet (1.2 m) (minimum criteria) to less than 10 feet (3.0 m) in all three wells. The vertical distance between the beds is often less than 19.5 feet (5.9 m) and rarely greater than 50 feet (15 m) (Figure 2-23).

The distance of porous sandstone was determined using the density porosity data with 6%, 8%, and 10% cutoffs. NBU 921-21L has 152 feet (46.3 m) of sandstone with 10% or more porosity from 28 beds, NBU 921-20P has 117 feet (35.7 m) of sandstone with 10% or more porosity from 30 beds, and CIGE 288 has 59 feet (17.9 m) of sandstone with 10% or more porosity from 17 beds. In all three wells the thickness of the porous sandstones beds is mostly less than 10 feet (3.0 m) per bed (Figure 2-24).

Production Decline Analysis in Tract 21

Production decline curves were created for 14 wells in section 21, T. 9 S., R. 21 E. Eleven wells produce from the Wasatch Formation; two wells have commingled production from the Wasatch and Mesaverde Group (NBU 300 and CIGE 288), and one well (NBU 921-21L) produced 214,370 thousand cubic feet of gas (MCFG) from the Mesaverde before the production was commingled with the Wasatch (see Figure 2-19 for well locations).

Each curve, created using PETRA™ software, is a plot of yearly production versus time. The productive period is extrapolated 20 years beyond the last reported yearly production. Each curve was manually "fit" using the hyperbolic method. Individual curves show the predicted rate at which gas production will decline and intercept a specified economic limit [quantity final (Qf)]. The Qf selected for each curve is 750 MCFG/year. When predicted production reaches this limit, the well is no longer considered economical. Some wells have a very short production history, and therefore the estimated parts of the curves produced for these wells are highly speculative.

Based on the production decline curves, the wells in section 21 that produce solely from the Wasatch Formation have an estimated ultimate recovery (EUR) of 1.1 to 1.9 BCFG (Figure 2-25).

The EUR for wells with commingled production from the Wasatch and Mesaverde Group are 2.8 BCFG for NBU 300 and 3.6 BCFG for CIGE 288 (Figure 2-26). Subtracting out the EUR of 1.1 to 1.9 BCFG from the Wasatch, the calculated Mesaverde contribution to the EUR for each well is 0.9 to 1.7 BCFG for NBU 300 and 1.7 to 2.5 BCFG for CIGE 288.

For a brief time NBU 921-21L produced (0.2 BCFG) solely from the Mesaverde Group; then the Wasatch Formation was perforated and production was commingled. Decline curve analysis from the initial Mesaverde period indicates an EUR from the Mesaverde only of 1.2 BCFG (Figure 2-27A). The analysis of the commingled decline curve indicates an EUR of 2.9 BCFG (Figure 2-27B); adding the initial Mesaverde production brings the EUR to 3.1 BCFG.

General Description of Fractures and Faults in the Basin

The Uinta basin is surrounded by major tectonic features formed during the Sevier-Laramide orogenies: Uinta Mountains to the north, Wasatch Mountains and Wasatch Plateau to the west, San Rafael Swell, Book Cliffs, and Uncompahgre Uplift to the south, and Douglas Creek Arch to the east. The Cretaceous Sevier orogeny, which formed the Wasatch Range as part of the Central Rocky Mountains, was a NNW-SSE-trending event producing W-NW-dipping thrust faults in parallel with the principal maximum, horizontal compressional stress. The Charleston-Nebo thrust fault of the Wasatch Mountains is a remnant of the Sevier event. During the Laramide orogeny, the principal maximum, horizontal compressional stress was rotated by various degrees in the region. Reverse faults and anticlines in the Uinta Mountains in the north are almost west-east trending structures, while the Douglas Creek Arch, 75 km long and 35 km wide, is a north-south trending faulted anticline, and the Uncompahgre Uplift is a NW-SE trending structure extending to a series NW-SE striking anticlines which have deformed the southeastern part of the Uinta basin (Figure 2-28). According the World Stress Map, the principal horizontal stress in Utah is oriented 115°-285° (SE-NW)

The origin, orientation, and density, and populations of faults and fractures in the subsurface Uinta basin in view of various deformation phases are poorly understood; nevertheless faults and fractures have played a significant role in the fluid flow and reservoir characteristics of the basin. If the major period of gas generation in the Mesaverde Group occurred in the Miocene (as maturity models of Nuccio and Roberts, 2003, suggest), i.e. well after the deposition of the Eocene age Wasatch-Uinta overburden sediments, it is conceivable that the Mesaverde sandstones were already tight reservoirs and could not perform as effective carrier beds for the migration of gas. The migration was thus probably through rock fractures and tectonic faults already present in the basin as well as tensile fractures produced in the source rocks by the generation of hydrocarbons and associated overpressures. Rice et al. (1992) noted that in the GNB field gases present in the Mesaverde sandstone reservoirs at depths of 4,210 to 9,332 ft are chemically identical. Furthermore, gas accumulations are found to be continuous in the reservoirs with no discrete gas-water contacts (Cuzella and Stancel, 2006). Johnson et al. (1994, 2003) also noted that gas generated in the Cretaceous rocks have found their way to the Lower Tertiary reservoirs in the Uinta basin. These observations imply that (1) the volume of gas generated in the Mesaverde source rocks was so massive that it overcharged the Mesaverde sandstone beds and spilled into the younger, shallower reservoirs, and (2) an effective and extensive network of fractures and faults was present in the basin for a long period of time,

and thus utilizing these natural fractures (probably still open or only partially healed) in the production of the Mesaverde gas is a significant technological and financial opportunity for the operating companies.

Cumella and Scheevel (2008) have emphasized the role of gas generation and overpressures in the fracturing of the Mesaverde rocks (Figure 2-29). Indeed, various studies have shown that open fractures are more common within the overpressured strata than outside the overpressured rocks in the Uinta basin (e.g., Narr and Currie, 1982; Wesley, 1990). Verbeek and Grout (1992) interpreted the abundant NW-SE striking gilsonite dikes as hydraulic extension fractures generated by high pore-fluid pressures in the Green River source beds during post-Laramide times when the horizontal compressive stress was reduced. These authors also observed that widespread gilsonite sills indicate that fluid pressures during intrusion often exceeded lithostatic load.

Fractures (faults and joints) have been documented in the Uinta basin by different methods and at various scales (Figure 2-30). Byrnes et al. (2009) even noted that microfractures were present on some grains in the thin sections of the Mesaverde they studied.

Verbeek and Grout (1992) mapped gilsonite dikes and major joints in several key locations in eastern Uinta basin and categorized the following fracture sets:

SET	STRIKE	ABUNDANCE
F1 (oldest)	N 15°-30° W	Sparse
F2	N 55°-85° W	Very abundant
F3	N 60°-80° E	Moderate
F4	N 15°-40° E	Very abundant
F5 (youngest)	N 65°-85° W	Sparse

Bates et al. (1999), as part of the U.S. Department of Energy (DOE) Project #DE-AC21-92MC28135, conducted a study of natural fractures in the upper Green River Formation, which is a tight-gas reservoir in the Bluebell-Altamont field in northern Uinta basin. Gas production comes from depths of 1980-2590 m from tight sandstone with matrix porosity of less than 8% and permeability of less than 1 mD.

From the nearby outcrops of the rocks (Duchesne River Formation), Bates et al. (1999) recorded two populations of vertical fractures: N20°–40°W and N60°-70°E. From the imaging logs of rocks at depths of 2000–3320 m, they also identified two fracture populations: N20°–30°W and east-west. The NW-striking fractures are consistent with the trend of gilsonite dikes in the area and also with the maximum horizontal stress (N30°W) on the World Stress Map (Zobak and Zobak, 1991).

Focusing on the Douglas Creek Arch and the eastern Uinta basin, Bader (2009) compiled 104 fracture strike data and noted that they broadly fall into two populations: NE (40°-60°) and NW (290°-310°). The former, dominantly present in the Douglas Creek Arch area range from 3-14 km in length, have high dip angles (over 60°) and are arrayed in an en echelon fault pattern (Bader, 2009).

Gutierrez (2007) mapped major fractures in the Uinta basin and concluded the following remarks:

1. Seismic interpretation indicates that the major faults in the region strike N70°E, W-E, and N50°-70°W.

2. Curvature seismic attribute analysis showed orientations of negative curvature at three different levels: At the basement level W-E, N60°E, N25°E, and N-S; at intermediate levels (including the Mesaverde) N75°W, N-S to N35°E, N60°E and W-E; and at shallower levels W-E, N25°-60°E, N-S, and N50°-80°W (which is the predominant group).

3. Using the elastic dislocation method, the fractures were generated at different stratigraphic levels: at the basement level N40°-85°E, N45°-75°W, with minor N-S and W-E populations; at the intermediate (including the Mesaverde) level N25°-65°E and N40°-75°W, with minor W-E fractures; and at the shallow (Wasatch Formation) level W-E, N25°-70°W, N40°-65°E, and rare N-S fractures.

4. An examination of a 900-ft core exhibited only a few fractures including mainly joints in sandstones, break-outs in mudstones, and irregular fractures with residual oil.

5. According to the dipole sonic log data, present-day direction of maximum horizontal stress is 101°-281° and a large population of partially healed fractures strike 110°-290°.

Well data do not often show faults in the Mesaverde sandstones mainly because of the discontinuing of sandstone bodies (Osmond, 1992). Nevertheless, various studies show that two major populations of fractures, one NW-SE trending and the second NE-SW trending, are present in the subsurface sedimentary rocks of the Uinta basin. In general, the NW-SE striking fractures are more prominent because they cut through the younger Eocene sediments. Osmond (1992) reports NW-SE striking normal faults with throws up to 170 ft that have displaced the lower part of the Eocene Green River Formation. The NW-SE trending fractures also include the famed NW gilsonite dikes, the maximum concentration of which is found in the GNB field. These gilsonite veins are vertical and vary from a few inches to 30 ft (mostly 5 ft) in width, and range from less than 2 km to 36 km in length (Osmond, 1992; Bader, 2009). According to Verbeek and Grout (1992), the gilsonite dikes are mainly extensional joints with no offsets. Bader (2009), on the other hand, highlights the presence and importance of slickenlines in the gilsonite dikes and the fact that the veins are characterized by en echelon and left-stepping pattern in map view. These authors associate the kinematic origin of the gilsonite dikes with that of the NW-striking, high-angle faults in the Douglas Creek Arc area and postulate the role of post-Laramide strike-slip faults in their genesis, concurrent with the regional Basin-and-Range extension in the

southwest US. Bader (2009) also map a right-lateral wrench fault, the Douglas Creek shear zone, to the southeast of the GNB field.

Figure 2-31 shows a fracture map of the GNB field compiled from several sources. Figure 2-32 provides a geologic time-event chart for the GNB field.

DETAILED FRACTURE CHARACTERIZATION

Fracture characterization and the effect of lithofacies on fracturing has been reproduced from a Master of Science Thesis by Ryan Sonntag working under the direction of Professor James Evans at Utah State University.

Data Collection Methods

Outcrops

Low-altitude oblique air reconnaissance surveys and photos were taken in 2009-2010 to locate suitable locations for sampling. Sandstone lithofacies were identified and classified based on grain size, sedimentary structures, bed thickness, bed geometry, bed continuity, and sandstone color (e.g. Aschoff, 2010). Sandstone type, grain roundness, sorting and the cement type(s) were also characterized in the field and with optical microscopic petrography. Sandstone lithofacies with different grain size, bed thickness, geometry, and sedimentary structures were targeted for study of fracture characterization. Mechanical units are defined based on the nature of fracture terminations observed within the Mesaverde Group by the presence of mudrock beds and partings between sandstone units.

Fracture characteristics were measured and described at outcrops using scanline surveys (Sonntag, 2012). Quantifiable fracture data including trace length, orientation, spacing, presence and type of mineralization were measured, and qualitative characteristics including termination styles, termination relationships and fracture type were noted. The fracture termination style describes the nature of how fractures terminate in outcrop. Termination styles observed include censored (no visible termination), blind (stops at a point within the rock), "T" termination into another fracture (fracture forms a "T" into another fracture or bedding plane) and asymptotic (fracture gently curves into another fracture) (La Pointe and Hudson, 1985). Scanline sampling involves measuring fracture intersections along a sample line placed approximately normal to a fracture set to measure and collect the aforementioned fracture characteristics. The scanline length varies based on the outcrop exposure but were typically at least 30.5 meters in length. For horizontal or low-angle dip slope (pavement) surfaces, the trace lengths of the fractures were measured, and terminating relationships were recorded. Due to the nature of the outcrops, terminating relationships between fracture sets and trace lengths for sub-vertical fractures are only observed on pavement outcrops. Trace lengths represent minimum values because the ends of large fractures are frequently censored by the exposure limitations of the outcrops. Fractures with similar attributes are grouped together into fracture sets. A fracture set is a number of approximately parallel fractures of the same type and presumable same age (Committee on Fracture Characterization and Fluid Flow, 1996). In addition, the thickness of shale intervals above and below sandstone beds was recorded along with the nature of the fracture terminations into these intervals.

Outcrop fracture patterns can provide insight into the potential character of the fracture pattern in the subsurface; therefore, it is important to distinguish them from surface-related joints and polygonal cracks. Polygonal cracks are interpreted to develop during uplift due to rock dilation associated with change in temperature (Ortega and Marrett, 2000). Scanline surveys were designed to avoid jointing related to surface- related processes.

Every visible fracture that the scanline survey intersected was noted. Fractures were ranked. The highest grade (A) consisted of a through-going, linear fracture where fracture terminations were generally not visible and the fracture cut through an entire vertical outcrop or has trace length longer than 10 meters on horizontal outcrops. A failing grade is assigned when fractures are curved, with a short trace lengths (< 5-10 cm), terminated randomly into the host rock (blind termination) and did not penetrate through a significant part of the mechanical unit. Fractures with failing grades were considered surface – related and therefore not used in calculating fracture spacing and density. In addition, local fracture sets were also distinguished from regional fracture sets. Regional fracture sets have little variation in orientation (15-20°), have a relatively large spacing, are perpendicular to bedding and are present over an extremely large area (Nelson, 2001). Regional fracture sets were considered rather than local sets since this is a basin-wide study.

Fracture Mapping

Detailed fracture maps were constructed from outcrop photos, low-altitude oblique aerial photos and Google Earth® images in order to delineate regional and local fracture sets. Three-dimensional (3D) outcrop models were created using terrestrial digital photogrammetry (Haneburg, 2008). These models provide an additional analysis tool to sample fracture orientations and distributions of vertical outcrops that are difficult to sample via traditional scanline methods. Photogrammetry uses overlapping images to create a 3D surface on which an image can be draped over, and orientation measurements can be made using the Sirovision® software suite (Haneburg, 2008). Images are obtained with a digital single-lens reflex camera with a GPS unit and input into the Sirovision® software suite to produce geo-referenced, oriented and scaled outcrop models. With these models, fractures within the outcrop were mapped, and fracture orientations and distributions were generated.

Core, Well and Image Logs

Open fractures in outcrops and cores were examined. Characterizing and understanding the controls of open fractures at depth is vital to accurately model subsurface fluid flow. Characterization of natural fractures within cores and image logs allowed correlation of subsurface fractures to those in outcrop. Core, well logs, and interpreted image logs provided by Anadarko Petroleum Corporation were used to evaluate fracture set orientation and spacing within the GNB field. Fractures were noted within core and image logs for two wells, NBU 253 and NBU 921-21L, from the GNB field. Along with noting what depth the fractures occur at the corresponding lithology and well log characteristics are also noted. Fracture stratigraphies have been interpreted for the cored intervals of wells NBU 253 and NBU 921-21L. An additional fracture stratigraphy has been interpreted for well NBU 921-21L by comparing fractures identified in image logs to gamma ray (GR), sonic porosity (SPHI), neutron porosity (NPHI) and density porosity (DPHI) well logs.

Fracture stratigraphy is the identification of the presence and distribution of fractures in the subsurface and their relationship to lithologic characteristics of the rock derived from core observations and well logs (Laubach, 2009; Nelson, 2001). Fracture occurrences were compared to different porosity log values in order to examine relationships that may exist between porosity log values and the occurrence of fractures within different sandstone lithofacies that define mechanical units at depth.

Petrography

Samples collected from scanline stations and core were described in detail using an optical petrographic microscope. Fractured rocks from outcrop and core were sampled to examine microscopic fracture properties (i.e. mineralization, terminations, etc.) in thin section. Due to the friable nature of the Mesaverde Group in outcrop, samples with fractures were only collected in lower porosity, well-cemented sandstones. Friable sandstones with fractures were not able to be preserved from the field to the lab.

Field Locations

The five outcrop localities from where the samples were collected are shown in Figure 3-1. Three localities are on the northern, southward dipping limb of the basin (Figure 3-1). At these localities, the Mesaverde Group is divided and mapped into an upper and lower unit (Figure 3-2; Sprinkel, 2007). The upper unit of the Mesaverde Group consists of the Tuscher, Farrer and Nelson formations and the lower unit of the Mesaverde Group consists of the Sego and Castlegate sandstone and the Buck Tongue of the Mancos Shale (Figure 3-2; Sprinkel, 2007). Two localities are identified on the southern, gently northerly dipping limb, which defines the Book Cliffs. At these localities, the Mesaverde Group is subdivided into the Blackhawk Formation, Castlegate Formation, Buck Tongue of the Mancos Shale, Sego Sandstone, Nelson Formation, Bluecastle Tongue, Farrer Formation and Tuscher Formation (Witkind, 1988; Gualtieri, 1988). Structural setting of the field localities and sample descriptions are summarized in Table 3-1. Average fracture distributions calculated for each regional fracture set is summarized in Table 3-2. Seven lithofacies (Table 3-3) from the Mesaverde Group were sampled. Five 3D outcrop models and twenty-two photo fracture maps were constructed to supplement scanline data. Dominant fractures set orientations present at each scanline station are plotted on the geologic maps of each field locality (Figure 3-2).

Analytical Methods

Orientation Analysis

Structural analysis of fracture orientation data is accomplished using Orient® to electronically plot the fracture planes on Stereonet. The best-fit eigenvector for each fracture set is calculated based on stereonets from each scanline station. Eigenvectors for each station are the mean orientation for each fracture set to represent the mean strike of each fracture set for each locality. Orientations of regional fracture sets are calculated based on mean eigenvector orientations from scanline stations from all localities. The variance of the mean eigenvector orientations for each regional fracture set is also presented.

Fracture Spacing and Density

Fracture spacing was evaluated for each fracture set as well as the total fracture population for each scanline. Fracture spacing is measured by recording the perpendicular distance between neighboring fractures of the same set on a scanline and calculated by taking the average of the measurements for each set. The regularity for fracture distributions can be evaluated by using the relationship between average fracture spacing (Savg) and the standard deviation of spacing (Sstdv) (Odling and Gillespie, 1999). An even, perfectly regular pattern is indicated when the ratio Sstdv/ Savg = 0, and a random distribution is indicated if Sstdv/ Savg = 1. As this relationship increases higher than 1, the tendency of clustering increases (Wennberg et al., 2007). Fracture density is defined here as the number of fractures per meter. Average fracture density has been calculated for each fracture set and the total fracture population for each scanline station. Fracture density can be related to fracture spacing of the same fracture set by 1/ Savg (Narr et al., 2006).

Statistical Analysis

The relationships between fracture distribution data and sedimentologic/ lithofacies characteristics were evaluated using a number of statistical tests. Simple linear regression analysis (Zar, 2010) was used to evaluate the relationship between dependent variables (i.e., fracture density and spacing) with independent variables (i.e. bed thickness and grain size). The Wilcoxon-Mann-Whitney test was used in order to evaluate the existence of significant differences between fracture distribution data and sedimentologic/lithofacies characteristics for two samples. The Kruskal-Wallis ANOVA test was used in order to determine if a significant relationship exists between fracture density/spacing and cement types of sandstone. Statistical tests are calculated with a significance level of 0.1 indicating a 90% probability. Statistical tests were run using XLSTAT® 2011.

Fracture Characterization Results

Fractures in Outcrop

Seven fracture sets were documented. Four fracture sets are regional in extent and are documented at all field localities. In addition to regional fracture sets, three local fracture sets are observed at one or two of the field localities. Fractures at each scanline station are primarily open mode I extensional fractures (joints) oriented normal to bedding with no visible shear offsets. Typically, multiple fracture sets were present at each scanline station. However, all regional fracture sets are not present at every scanline station. Horse tail splays (Twiss and Moores, 2007) at fracture terminations are observed indicating the possibility that some fractures developed in shear (Figure 3-3). Abundant plumose markings are observed on fracture surfaces at many stations (Figure 3-3).

Plumose structures correspond with well-indurated sandstone units at these localities. Fractures tend to terminate vertically within sandstone beds or at mudstone/shale boundaries. Typically, fracture heights correspond to mechanical unit thickness however, through-going extension fractures have been observed to penetrate multiple mechanical units. Fracture set distributions within outcrop range from being moderately even to randomly distributed (Sstdv/ Savg values ranging from 0.4 – 1.5) with no apparent fracture swarms observed in outcrop.

Regional Fracture Sets

The regional fracture sets include four sets: N-S-striking (006° - 015°), NE- striking (045° - 059°), NNW-striking (326° - 342°) and a WNW-striking (271° - 286°) (Figure 3-4). The WNW-striking fracture set is the most pervasive, through-going fracture set (Figure 37) with the longest mean trace length (Table 3-2). Typical terminations of the WNW-striking fracture set include censored (no visible termination) and blind (stops at a point within the rock) terminations (Figure 3-5). Trace length of the WNW-striking fracture set shortens from east to west from Blue Mountain Ridge (Locality 3) to Asphalt Ridge (Locality 1) and is less pervasive with shorter trace lengths in the southern localities. The WNW-striking fracture set has wider fracture spacing at Asphalt Ridge (Locality 1) than at Blue Mountain Ridge (Locality 3) and is more pervasive in the northern part of the basin than the southern. The N-S-striking fracture set often terminates into the WNW-striking fracture set and seldom terminates into the NNW-striking fracture set. The N-S-striking fracture set occasionally cross-cuts WNW- striking and NNW-striking fractures. The N-S-striking set does not vary in relation to bedding curvature at the field localities. Trace length of the N-S-striking fracture set lengthens from east to west (Blue Mountain Ridge [Locality 3] to Asphalt Ridge [Locality 1]) and shortens from south (Tusher Canyon [Locality 4]) to the north. The NNW-striking set has the longest average trace length (Table 3-2) and primarily terminates into the WNW- and N-S- striking sets. The fracture density of the NNW-striking set decreases from west to east in the basin. The NE-striking fracture set is generally the shortest fracture set (Table 3-2) and commonly terminates into the NNW-striking fracture set as well as the WNW-striking set. The average trace length of the NE-striking set is longer in the south (Tusher Canyon [Locality 4]) than at other localities with average of 4.3 meters long. Values from the Sstdv/ Savg relationship indicate that all regional fracture sets are close to random distributions (Table 3-2).

Sandstone Texture and Lithofacies

The seven identified lithofacies are listed in Table 3-3. The sandstone lithofacies vary from thin-bedded, discontinuous sandstone units to thick-bedded, continuous sandstone units (Figure 3-6). The seven lithofacies include quartz and lithic arenite that are typically fine- to medium-grained with coarse-grained samples corresponding to lithofacies 6. The grains are generally sub-rounded to sub-angular and poorly to well sorted. Degree of cementation can vary from well-cemented, indurated sandstones to friable sandstones within the same lithofacies. With the exception of Lithofacies 1, lithofacies are comprised of individual sandstone beds/bodies. Sandstone thicknesses range from 0.15 to 5 meters thick (Table 3-3). Bedding continuity is defined based on the scale of the outcrop. Laterally discontinuous beds terminate within the outcrop, which are typically 20 to 30 meters in lateral extent. Laterally continuous beds are continuous for the entire outcrop sampled, which is typically at least 35 meters in length. Three dimensional photogrammetric models and two-dimensional (2D) photographic maps were used in order to help evaluate the continuity of identified lithofacies (Sonntag, 2012). Continuous beds of Lithofacies7 have been traced via 3D photogrammetric models, 2D terrestrial photographic maps, aerial photos and Google Earth® images to be greater than 125 meters in length (Sonntag, 2012). Little to no primary organic material was identified within any of the lithofacies identified.

Subsurface Analysis

Drill Core Description

Core from two producing wells in the Natural Buttes Field are sampled. Well NBU 253 (APL #43-047-32917) samples the Price River Formation (equivalent to the Farrer and Tuscher formations of the Upper Mesaverde Group) from 3,197 – 3,267 meters depth. NBU 921 – 21L (APL #43-047-39256) samples the Castlegate and Sego Sandstones (Lower Mesaverde Group) from 2,842 – 2,875 meters depth. These units consist of sandstone interbedded with carbonaceous shale and silty mudstone. Individual sandstone beds consist of very fine- to fine-grained sand and have low-angle crossbedding, with ripples, flaser bedding, sparse burrows, and moderate bioturbation (Carney et al., 2011).

Calcite mineralization fills some fractures. Along with extension fractures, shear fractures were identified based on offset bedding and slickenlines on fracture surfaces (Figure 3-7). Open and closed natural fractures are more common in sandstone lithologies than in the mudrocks (Figure 3-8). Slickenlines were only observed within carbonaceous shale of well core NBU 921-21L. Natural fractures within core from NBU 253 are more commonly open and unmineralized, whereas the fractures identified within core NBU 921-21L are more often filled with calcite. Two of the twenty-six identified natural fractures in well core NBU 253 are mineralized with calcite while fourteen of the twenty-eight natural fractures identified within well core NBU 921-21L are mineralized with calcite. Fractures often terminate at shale and clay partings as well as terminate into other sedimentologic features (i.e. mud drapes, stylolites and cross laminations/bedding) (Figure 3-9). Fractures are also present at other sedimentologic features such as soft sediment deformation structures (Figure 3-7). Several fracture tips blindly terminate within sandstone beds indicating that subsurface, extensional fractures do not only terminate at mechanical unit boundaries.

Fracture heights within well core NBU 921-21L vary with 17 fractures ranging from 0.03 to 0.09 meters in height and the tallest two fractures measured at 0.18 and 0.21 meters (Carney et al., 2011). Fracture heights within core from NBU 253 are taller relative to well core NBU 921-21L. Fracture heights within core NBU 253 vary with the shortest fracture measured at 0.09 meters tall to the tallest fracture measured at 0.37meters. Fracture height appears to be a function of sandstone bed thickness. The sandstone beds are thicker in NBU 253 than in NBU 921-21L, therefore the fractures are taller. Several fractures within core are interpreted to have undergone several episodes of fracturing with calcite mineralization sealing an open fracture during an earlier episode of fracturing followed by a later episode of fracturing re-opening the same fracture (Figure 3-8).

Fracture Orientation and Spacing Based on Image Log Analysis

Analysis of three image logs provided by Anadarko Petroleum from wells in the GNB field reveals several open and cemented fracture sets. The dominate fracture set identified is a west-northwest trending fracture set with a Terzhagi corrected spacing from 3.35 m to 7.01 m. Other fracture orientations observed are a ~NNW, ~N-S, and ~NE orientations. Orientations of subsurface fractures are of similar orientations to those observed in outcrop (Figure 3-9). Depths of fracture occurrences observed from the core were correlated to sonic porosity (SPHI),

density porosity (DPHI), neutron porosity (NPHI) and gamma ray (GR) signatures of the section (Figure 3-10). Zones of relatively higher fracture densities within sandstones correspond to low porosity zones (Figure 3-10 and 3-11). Fracture depths were matched with well log values to examine the average well-log values of the sandstone units where fractures were observed. Where fractures are observed, the sonic porosity log appears to have the most consistent values (with an average of 0.15 μsec/ft) on the well logs examined.

Fracture Stratigraphy from Core, Image and Well Logs

Fracture stratigraphy was further interpreted for well NBU 921-21L based on comparing fractures identified from image logs to density porosity (DPHI), neutron porosity (NPHI), sonic porosity (SPHI) and gamma ray (GR) logs (Figure 3-11). The image log is from 2436-3039 meters deep encompassing much of the upper Mesaverde Group. Fifty-nine fractures were identified in the image log. Fifty-one fractures are interpreted to be in sandstone with the remaining eight fractures interpreted to be in shale. Fracture occurrences generally appear to be related to low porosity sandstone. The sonic porosity log values are consistent when fractures are present in sandstones (Figure 3-11).

Petrography

Outcrops

Thirty-eight thin sections from outcrop were analyzed to describe the sandstone lithologies and fracture characteristics in detail (Sonntag, 2012). Samples were taken within each lithofacies from each locality at which it was present. Eighteen samples were taken from the two southern localities (Tusher Canyon and San Arroyo Canyon), and twenty samples were taken from the three northern localities (Asphalt Ridge, Snake John Reef and Blue Mountain Ridge). Sandstone lithofacies consist of poorly to well-sorted, fine- to coarse- grained, quartz and lithic arenites (Figure 3-12). Sandstone porosity ranges from low (with intergranular pore space occupied by clay/calcite cement or with clay matrix) to high (little intergranular matrix present) (Figure 3-12). Irregularly distributed hematite mineralization is observed in many of the samples. Clay minerals are abundant throughout many of the samples and coat the sand grains as well as fill pore space. Calcite and clay replacement of feldspar grains is commonly observed. All cement types identified in thin section have been documented within each lithofacies type.

The degree and type of cement varies between each sample (Figure 3-13). Intergranular pressure solution boundaries are observed at quartz grain boundaries within many thin sections (Figure 3-12: I and J). Cement types identified include syntaxial quartz overgrowth, carbonate (fine-grained calcite and poikilotopic calcite) and clay mineral cement (Figure 3-13). Most samples consist of several types of cementing agents therefore the samples are characterized based on the most prevalent cement type throughout the thin sections. Syntaxial quartz overgrowths are present in every thin section (Figure 3-13: A and B). Typically syntaxial quartz overgrowths cements are less pervasive cementing agents with carbonate or clay cements occurring more commonly and often surrounding the quartz overgrowths in some areas. Some quartz grains exhibit overgrowths that do not grow into any neighboring grains. This is most likely evidence of deposition of reworked quartz grains within the Mesaverde Group. Thin sections described with syntaxial quartz overgrowth cement typically have high porosity, with numerous "floating"

grains apparently not in contact with other grains/matrix/cement. Samples described with syntaxial quartz overgrowths consistently have a high porosity relative to carbonate cemented sandstones. Carbonate cement is the dominant cement type identified in most low porosity samples. Fine-crystalline calcite cement (Figure 3-13: C and D) and poikilotopic calcite cement (Figure 3-13: G and H) is observed. Poikilotopic calcite cement consists of sparry calcite that completely engulfs grains within the sandstone samples leaving very little pore space. Poikilotopic calcite cement accounts for the highest fracture densities of all scanlines taken. Sandstone units with clay mineral cement have the highest variation in porosity. Several samples have relatively low to moderate porosity while most of the clay mineral cemented sandstones have a high porosity.

Samples described with clay cement typically have thin films of clay coating sand grains (Figure 3-13: E and F). Clay minerals have been observed to coat quartz grains with and without overgrowths. This is evidence of pre- and post-quartz overgrowth diagenetic events. Clay mineral cements are interpreted to be primarily authigenic based on the crystalline morphology, occasional radially aligned clay minerals around grains and clay coatings covering overgrowths (Wilson and Pittman, 1977). Hematite mineralization is not observed to behave as a cementing agent. Fractures sampled from outcrop are generally open and unmineralized; however, calcite mineralization has been identified in several samples (Figure 3-13).

Drill Core

Fifty-eight thin sections were described from two cores from 2,842 – 3,261 meters deep (Sonntag, 2012). Samples from core are very fine- to fine-grained, poorly to well sorted, sub-angular to rounded, quartz and lithic arenites. Siltstone and shale that contain fractures have also been examined in thin section. All sandstones sampled have low porosity and are highly compacted with intergranular pressure solution boundaries. Clay minerals and sparry calcite commonly occupy available pore space within the sandstones and greatly reduce any porosity that was present. Sparry calcite is more numerous near open fractures indicating they precipitated from fluid flow through the host rock. Cement types include syntaxial quartz overgrowth, carbonate (fine-crystalline calcite), and clay cements. Quartz overgrowths are observed in most thin sections and are a dominant cement type. Carbonate cemented sandstones have the lowest porosity of the samples. Carbonate cemented samples consist of fine-crystalline calcite (Figure 3-13: C and D). Clay cements typically consist of clay mineral coatings around grains. Clay mineral coatings around grains with and without quartz overgrowth are observed. Calcite mineralization is present within fractures from core however; open, un-mineralized fractures are most commonly observed. Open fractures sampled often provide for the only pore space visible in many thin sections (Figure 3-14).

Comparison of Outcrop and Core Petrography

Thin-section samples from outcrop and core exhibit very similar characteristics with regards to composition, grain size, sorting, roundness and cement types . All cement types defined within the outcrop samples are observed in the core samples except poikilotopic calcite cement. Fine crystalline sparry calcite is commonly observed within core samples filling pore space between grains while fine crystalline sparry calcite grains are less common in outcrop samples.

Primary differences between outcrop and core samples are the degree of cementation, degree of compaction and porosity. Outcrop samples are typically more porous, unless cemented by carbonate and sometimes clay cement, with sand grains generally not in contact each other. Core thin section samples consistently have very little porosity and are very well cemented. Pressure solution boundaries are much more commonly observed in core samples than in the outcrop samples. Core samples are more commonly cemented by syntaxial quartz overgrowths with more pressure solution boundaries observed than the outcrop samples. In addition to the quartz cementation and pressure solution boundaries between grains a higher degree of compaction and very low porosity is observed in core samples. Pervasive poikilotopic calcite cement is present in outcrop samples but not in core samples. While poikilotopic calcite cement leaves very little pore space, it is also probably evidence of near-surface fluid flow.

Data Analysis and Interpretation

Structural Control on Fracture Geometry

At some localities, local tectonic folds are superposed on regional fracture sets thereby influencing their orientations. Strikes of fractures orthogonal to bedding systematically vary as bedding geometry varies. This is illustrated by the "fanning" of fracture azimuths at Snake John Reef from the eastern limb of the syncline to the western limb (Figure 3-15). Tectonic folding also controls local fracture sets, which may have developed due to the formation of the structure, as well as regional fracture sets that have formed prior to the development of the local structure. Regional fracture sets that develop after the formation of a structure have strikes that are independent of bedding curvature and local structures. Fracture sets that have a consistent orientation across a fold are interpreted to have formed after the formation of the structure. Therefore, bedding curvature due to tectonic folds is interpreted to control fracture orientations of fractures that have formed prior or during the tectonic event.

Bed Thickness and Stratigraphic Architecture of Sandstone Units

Bed thickness is often invoked as a primary control on fracture spacing (Figure 3-16; Narr et. al., 2006). In this study, fracture spacing for individual fracture sets are strongly controlled by the bed thickness of sandstone units (Figure 3-16). Thin beds correspond to lower fracture spacing and thicker beds correspond to higher fracture spacing.

The lateral extent of sandstone units is also an important influence on fracture spacing. When fracture spacing from each scanline station are plotted versus bed thickness a weak statistical relationship exists (R2 = 0.11) (Figure 3-17A). However, when discontinuous sandstone bodies are removed a stronger statistical relationship (R2 = 0.59) exists (Figure 49B). Therefore, the fracture spacing for discontinuous sandstone bodies appear to be more randomly distributed and are not controlled as strongly by the thickness of the sand body. Thus, bed thickness is more of an influence on fracture spacing for continuous, tabular, blanket-like sandstone beds than discontinuous sandstone bodies (Figure 3-17). Discontinuous sandstone bodies sampled are described as sandstones with laterally inconsistent bed thicknesses with visible terminations in the outcrop. Discontinuous sandstone bodies vary in bedding geometry but are most commonly lenticular (Figure 3-18B). Discontinuous sandstone bodies act as mechanical layers where fractures terminate at the boundaries of sandstone units (Figure 3-18) and have a higher

fracture density when compared with continuous sandstone bodies (Figure 3-19). In addition, discontinuous sandstone bodies have a higher average Sstdv/ Savg ratio (0.87; Figure 3-19) indicating that the fracture distributions are more randomly distributed than in continuous sandstone beds. While there is no significant statistical difference with respect to fracture spacing between continuous, sandstone beds and discontinuous sandstone bodies, a statistical significant relationship does exist between fracture density and sandstone architecture.

Influence of Mudstone/Shale Thickness on the Mechanical Interface

Fractures typically terminate at the edges of mudstone/shale beds and partings within beds (Figure 3-18) defining mechanical units that are 0.3 to 5 meters high within the Mesaverde Group. Mudrock bed thicknesses that act as mechanical unit boundaries around sandstone units were measured to evaluate the influence on fracture propagation through multiple mechanical units (Figure 3-18). A statistically significant relationship shows through-going fracture densities increase with thicker mudrock boundaries (Figure 3-20). This relationship may be due to the sandstone bodies above and below thin shale beds accommodating strain, accounting for fewer fractures within the thin shale beds, while thicker shale beds have to accommodate strain because there are no nearby brittle lithologic units to accommodate the strain.

Fractures often terminate into mudstones or shale stringers present within sandstone units. Mudstone/shale stringers are typically thin, laterally discontinuous mudstone/shale deposits that "split" a unit from top to bottom which notably change fracture patterns of a sandstone bed (Figure 3-21). These stringers create "sub"-mechanical units within larger mechanical units. Fractures rarely penetrate these stringers and only terminate at the mechanical unit boundaries when no mudstone/shale stringer is present. These "sub"-mechanical units are often present within many of the discontinuous sandstone bodies and less common in the tabular, continuous beds. These "sub"- mechanical units may contribute to the more randomly spaced nature of fractures that exist within discontinuous sandstone bodies.

Degree and Cement Type

In addition to parameters discussed above, the degree of cementation and type of cement of the sandstone unit also influences fracture distribution. Highly indurated, well- cemented sandstones have a higher fracture density than friable sandstones. Well- cemented sandstones are defined by a pervasive, continuous cementing agent within the sandstones that typically have little pore space. High fracture density systematically corresponds to highly indurated, well-cemented sandstones indicating that the better indurated the sandstone the more brittle it behaves (Figure 3-22 and 3-23).

Cement type is a control on fracture distribution for sandstone units with similar bed thicknesses and geometries (Figure 3-24). Carbonate-cemented samples generally have a higher fracture density while clay and syntaxial overgrowth cemented samples have a lower fracture density (Figure 3-24).

Relatively high fracture density in samples corresponds to low porosity samples and carbonate cement. Low porosity clay-cemented samples correspond to higher fracture densities than

samples cemented by syntaxial quartz overgrowth. However, clay-cemented and syntaxial quartz overgrowth cemented samples systematically correspond to lower fracture densities when compared to carbonate cemented samples (Figure 3-24).

Carbonate cemented sandstones are generally less porous than the samples with syntaxial quartz overgrowth and clay cement. The higher average fracture densities within carbonate cemented samples can potentially be due to higher porosity in the samples. However, based on thin sections from core samples, carbonate cement appears to almost completely destroy porosity within sandstones while syntaxial quartz overgrowth and clay cemented samples typically have more of a clay matrix within the pore space. Thus, it is likely that these sandstones at depth may have equally low porosity but could exhibit different fracture characteristics. Therefore, the nature of the dominant cement type is still interpreted to be an important and separate control on fracture distribution.

High porosity and poorly cemented samples correspond with friable sandstones present within Mesaverde Group outcrops. Sandstone units dominated with syntaxial quartz overgrowth cement exhibit high porosity relative to carbonate and clay mineral cemented sandstone units from outcrop and to all sandstone units sampled from core. Due to the lack of high-porosity samples from core, the porosity that is present in these samples most likely developed as these rocks were being uplifted. Sandstones observed in core are well-cemented with very low porosity. The existence of high-porosity within these sandstone units in outcrop likely developed as the sandstone either lost previous cementing agents that were present at depth (due to fluids dissolving the cement (possibly calcite) or weathering clay cement out at the surface) or gained significant porosity due to being decompacted. Many of the samples exhibit multiple cement types. These observations suggest that the Mesaverde Group has experienced multiple diagenetic phases imparting different types of cementing agents. Uplift of the Mesaverde Group sandstones could potentially remove some of these cementing agents while leaving behind the more resistant cementing agents behind such as syntaxial quartz overgrowth.

Lithofacies Fracture Characteristics

At many scanline stations, the fracture character and distribution varies markedly between the different sandstone lithofacies (Figure 3-25). The lowest average fracture spacing is within Lithofacies 1 while the two highest fracture spacing are in Lithofacies 6 and 7 (Figure 3-26). Highest average fracture densities occur within Lithofacies 1 and 2, and the lowest average fracture density is in Lithofacies 7 (Figure 3-26). Control on fracture distribution can be attributed to the multiple sedimentologic characteristics that define the lithofacies classification scheme used. The thinly bedded, discontinuous sandstone units of Lithofacies 1 have the lowest fracture spacing and one of the highest average fracture densities while massively bedded, continuous sandstones such as Lithofacies 7 have high fracture spacing and low fracture density (Figure 3-26).

Grain size, degree of cementation and cement type influence the fracture distribution within different lithofacies. While most of the lithofacies are fine- to medium- grained sandstones, Lithofacies 6 is medium- to coarse- grained and has the highest fracture spacing (347.6 cm/fracture) and one of the lowest average fracture densities (0.64 fractures/meter). Lithofacies 6

is similar to Lithofacies 4 and 5 with respect to bed thickness but is more continuous in nature. Differences between the fracture distributions of other lithofacies from lateral extent are not as drastic as the fracture distribution difference between Lithofacies 4, 5 and that of 6. Therefore, we interpret the discontinuous nature of this unit in conjunction with the larger grain size to contribute to the much higher fracture spacing and lower fracture density. Lithofacies 2 has the highest average fracture density and one of the lowest fracture spacings. This is most likely due to several of the scanlines being taken within poikilotopic calcite cemented (Figure 3-13: G and H) sandstones within this lithofacies. While poikilotopic calcite cement is present in all lithofacies, Lithofacies 2 has a higher number of scanlines (3) than the other lithofacies, potentially skewing the fracture density to a higher average and lower average fracture spacing. Large differences observed in fracture distributions within the same lithofacies type are often attributed to the degree of cementation and the cement type of the sandstone.

In addition to systematic fracture patterns that are observed within all the lithofacies, the thickly bedded, white and tan, fine to medium – grained, discontinuous and continuous sandstones are typically found with a high amount of polygonal fracturing (Sonntag, 2012). Pervasive polygonal fracturing within these lithofacies is mostly observed at Asphalt Ridge (Locality 1) and Snake John Reef (Locality 2).

Fracture Characterization Discussion

Relative Timing of Fracture Set and Development

Based on twelve pavement outcrops and low-angle aerial photography, the relative timing of fracture set development for the regional fracture sets has been determined (Sonntag, 2012). The WNW-striking is the most pervasive fracture set at most field localities and rarely terminates into any other fracture set. This is interpreted to be the oldest fracture set, due to the lack of observed systematic terminations into other fracture sets. The NNW-striking set and the NE set commonly terminate into the WNW-striking at many of the scanline stations indicating that they are younger sets. The NNW- and NE-striking fracture sets are interpreted to be orthogonal fracture sets with the NNW- striking set being the systematic fracture set and the NE-striking fracture set being a non- systematic set with a higher fracture density and lower spacing (Table 3-2). The N-S- striking fracture set is typically observed to terminate into WNW-striking and, less often, NNW-striking fractures. Therefore, N-S-striking set is probably the youngest fracture set (Figure 3-5).

The Mesaverde Group in the Uinta Basin has experienced a complex stress history due to several phases of horizontal tectonic compression, as well as stresses imparted from overburden, increased heat with depth and by internal pore pressure. Numerous authors have advanced hypotheses for the development of regional fracture sets in the Cretaceous to Tertiary strata within the Uinta and the Piceance Basins (Narr and Currie, 1982; Verbeek and Grout, 1983, 1984, 1992, 1993, 1997, 1998; Lorenz and Finley, 1991; Condon, 2003). Regional fracture sets may have developed in response to horizontal compressional stresses due to tectonic events (Condon, 2003), uplift and reduction of lithostatic loads (Narr and Currie, 1982; Verbeek and Grout, 1997), the onset of Basin and Range extension to the west (Verbeek and Grout, 1997), from high formation pore pressure due to organic maturation at maximum burial depth and

buoyant or delaminating mantle below (Pitman and Sprunt, 1986; Lorenz et al., 1991; Wells and Hoisch, 2008). A potential explanation for the orientation of the WNW-striking fracture set is late thrusting of the Sevier fold-and-thrust belt (Lorenz and Finley, 1991); however, similarly oriented WNW-striking fractures within the Tertiary strata in east-central Utah are interpreted by Verbeek and Grout (1992, 1993) to have probably formed due to the strongest period of post-Laramide extensional deformation. Lorenz and Finley (1991) suggest that the WNW-striking regional set observed in the subsurface developed "under conditions of high pore pressure and anisotropic, tectonically created, horizontal stress." In the Piceance Basin, the more deeply buried Mesaverde Group strata in the central parts of the basin were at optimum conditions for fracturing and the WNW-striking fractures present in the subsurface are interpreted to have developed due to the tectonic stresses imparted by the Sevier Orogeny (Lorenz and Finley, 1991). In situ stress measurements within the Mesaverde Group sandstones within the Piceance Basin shows a west-northwest compressive stress that is interpreted to be a residual stress that was "locked in during grain-to-grain cementation under Sevier/Laramide compression" (Lorenz and Finley, 1991). The WNW-striking fracture set at Locality 3 varies in orientation (from WNW – WNW-E-W) remaining parallel to the strike of the bedding as it changes with gentle folds that are present there. These observations are most consistent with fracture set development prior to the bending of the bedding related to the formation of the Douglas Creek Arch due to the Laramide Orogeny. The terminating relationships of the regional sets identified from this study are not wholly consistent with the younger regional fracture sets identified in the Tertiary strata by Verbeek and Grout (1983, 1984, 1992, 1993). We suggest that the WNW-striking fracture set identified in outcrop and in the subsurface first developed at maximum burial depth with high pore pressure due to organic maturation along with enhanced west-northwest compression similar to the same striking set within the Piceance Basin (Lorenz and Finley, 1991) which may have been reactivated during the Tertiary due to similar stress fields. The development of the WNW-striking fracture set present in the subsurface within the Piceance Basin formed at about 36-40 Ma (Lorenz and Finley, 1991).

The NNW- and NE- striking fracture sets are interpreted to be orthogonal to one another. The sequence of development for orthogonal open-mode fractures can be explained when one joint set develops and relieves the extensional stress normal to their trend causing the stress directed parallel to their strike to become the minimum principal stress leading to the formation of a second orthogonal fracture set (Narr and Currie, 1982). Lastly, the N-S-striking set is the youngest set and is correlative to the Verbeek and Grout (1983, 1984, 1992, 1993) F4 fracture set. This fracture set is interpreted to be stress relief features that formed during uplift. The NNE-striking orientation is interpreted to be controlled by the Laramide, WNW oriented stresses that are locked into the Mesaverde Group sandstones during cementation and lithification which were re- oriented by uplift and removal of strata during uplift (Lorenz and Finley, 1991).

Sedimentologic and Diagenetic Controls on Fracture Distribution

Sedimentologic controls on fracture distribution are interrelated and complex but can be delineated. We observe a hierarchy of sedimentologic controls on fracture distribution. First-order controls are defined as sedimentologic characteristics that exhibit a direct influence on the character and distribution of natural fractures while second-order controls are only observed when the first-order controls are held constant. First-order controls include bed thickness and

sandstone architecture. Second-order controls include the degree of cementation and the type of cement. In addition, grain size and porosity appear to serve as a control on fracture distribution. However, while grain size and porosity of the Mesaverde Group varies, it typically consists of very fine- to medium- grained sandstone with very low porosity. There are coarse-grained sandstone lithofacies observed in the field; therefore, it is assumed the coarse- grained sandstones are present at depth but were not sampled and are not commonly reported (Johnson and Roberts, 2003). Therefore, the influence of porosity and grain size on fracture distribution is not considered to be a primary factor among most sandstone units in the Mesaverde Group. A schematic 3D block model has been developed to show the expected fracture character of sandstone reservoirs at depth with varying bed thicknesses, architecture/geometries, degree of cementation and cement types (Figure 3-27).

Analysis from Outcrop to the Subsurface

No porous sandstones were sampled in the subsurface within the Mesaverde Group; therefore, careful consideration is needed when comparing fracture characteristics of porous, poorly-cemented sandstones in outcrop to non-porous, well-cemented sandstones in the subsurface. Fracture characteristics of friable sandstones, regardless of cement type, are most likely not representative of the fracture patterns in the subsurface and should not be considered when predicting fracture characteristics of these tight-gas sandstone reservoirs at depth.

Clay mineral and fine grained, crystalline calcite-cemented sandstone units sampled in the outcrop are typically low porosity and similar to what is observed from core. Since these samples are consistent to what is observed at depth, fracture characteristics and patterns observed in outcrop are more representative of what can be in the subsurface. From the outcrop, we see that there is a significant difference in fracture distribution between carbonate and clay mineral cemented sandstones. Thus, it would be a relatively safe assumption to use this relationship between cement type and fracture density in the subsurface for modeling purposes.

Sedimentologic and fracture characteristics observed in outcrop serve as an excellent analog for subsurface characterization and should be a strong basis when developing subsurface discrete fracture network models. Fracture characteristics observed in core such as termination styles, fracture heights, mineralization, spacing, and orientations are all similar to what has been documented in outcrop. By evaluating the Mesaverde Group on the surface and in the subsurface we can understand where to better focus the outcrop analysis and how to develop better DFN models.

Implications for Developing Well-log: Fracture Stratigraphy

It was documented that well indurated, well-cemented sandstones correspond to higher fracture densities in outcrop. Core and image log observations indicate that low-porosity sandstones fracture more commonly than higher porosity sandstone units as well as other lithologies. In addition, well-indurated, well-cemented sandstones correspond to high compressional velocities (Vp), which are represented as low values from a sonic log (μsec/ft). Therefore, zones of high fracture density can potentially be predicted based on sonic porosity logs with low values. Sonic log values from wells NBU 253 and NBU 921-21L are not statistically different where fractures were identified indicating that, a potential relationship could exist between low sonic log values and the occurrence of natural fractures at depth.

Implications for Fracture Distribution Prediction Based on Depositional Environment and Sandstone Diagenesis

Significant statistical relationships exist between fracture distribution and sedimentologic characteristics defined within sandstone units of the Mesaverde Group. The sedimentologic characteristics defining lithofacies within the Mesaverde Group can be used to interpret depositional environments as well as predict the character of fractures. From this, we can begin to develop predictions of relative fracture densities based on the depositional environments of sandstone units. Lithofacies consisting of tabular, continuous sandstone beds, sampled within the Castlegate and Tuscher formations of the Mesaverde Group, are interpreted to be deposited in braided stream environments while the lithofacies with discontinuous, channel sandstone bodies, sampled within the Sego Sandstone and Nelson and Farrer formations, are interpreted to be deposited in meandering stream environments (Lawton, 1986; Franczyk et al., 1989, 1990; Hettinger and Kirschbaum, 2002). Based on the different fracture characteristics of these sandstone lithofacies, which reflect depositional environments of the sandstone units, we can potentially predict fracture patterns on a more regional scale.

Implications for Improving Hydraulic Fracture Design within the Greater Natural Buttes Field

By understanding the different fracture characteristics of the different sandstone reservoirs that can be encountered in a lateral wellbore, hydraulic fracture designs can be better designed to optimally stimulate each sandstone reservoir that is intersected. Lateral wellbores can be designed to penetrate through multiple types of discontinuous, channel sandstone reservoirs and stimulate each reservoir differently in order to optimize production (Figure 3-27). As induced hydraulic fractures propagate WNW (parallel to the maximum principal horizontal stress and the dominant open fracture set at depth) the NE- striking fracture set can potentially be reactivated (Figure 3-28) providing better connectivity between the natural fracture system, resulting in increased drainage of the reservoir.

In addition, if lateral wellbores are designed to intersect multiple channel sandstone reservoirs with different geometries and sedimentologic characteristics (Figure 3-27), the hydraulic fracture design can be developed to anticipate different densities of natural fractures, which results in different contributions of flow of hydrocarbons to the wellbore. When lithofacies that are similar to Lithofacies 1, 2 and 3 are identified, higher fracture densities can be expected; therefore, potentially smaller hydraulic fracture treatments are needed as the natural fracture system can be expected to contribute more to the flow of hydrocarbons to the wellbore. When sandstone lithofacies similar to Lithofacies 6 and 7 are encountered larger hydraulic fracture treatments may be considered due to relatively lower fracture densities, which potentially results in less flow contribution from the natural fracture system. By being able to develop custom hydraulic fracture treatments, volumes of water and proppant can potentially be saved, which will result in lower completion costs.

Main Conclusions Concerning Fracture Characterization

Sedimentologic and diagenetic characteristics influence the fracture distribution and development of the Mesaverde Group on a regional, mesoscopic and microscopic scale. The fracture distributions within the Mesaverde Group sandstone units are complexly controlled by a

hierarchy of sedimentologic and diagenetic characteristics. The sedimentologic and diagenetic controls include first order controls (e.g. bed thickness and bedding geometry) and second-order controls (e.g. degree of cementation and cement type) on the fracture development within the Mesaverde Group. A dominant WNW fracture set that is documented in outcrop and in the subsurface is approximately perpendicular to the N-S depositional trends of the Mesaverde Group in the Uinta Basin. Higher fracture densities are related to discontinuous, channel sand bodies interpreted to be deposited from meandering river environments that have a general northwesterly orientation. Thus, the observed regional WNW fracture swarms are likely controlled by the distribution of discontinuous, channel sand bodies. Therefore, the depositional environment controls the development of the fracture network within the Mesaverde Group, which helps to explain the WNW-trending zones of increased hydrocarbon productivity within the GNB field.

Understanding the sedimentologic, diagenetic and lithofacies controls on the natural fracture network within the Uinta Basin can result in more efficient and increased natural gas production from the tight-gas, fluvial sandstone reservoirs in the Mesaverde Group. In order to maximize the natural gas production within these sandstone reservoirs within the GNB field, hydraulic fracture treatments can be designed to exploit the sandstone lithofacies that have higher natural fracture densities due to favorable bed thicknesses, sandstone architecture, high degree of cementation and cement types that are prone to fracture more thoroughly. Outcrop and subsurface fracture analysis suggests that well-cemented, discontinuous sandstones (> 1.5 m thick) have a higher fracture density relative to other sandstones. Targeting these lithofacies will increase connectivity of hydraulic fractures with the natural fracture system and allow for more efficient draining of these tight-gas reservoirs and provide higher production volumes of natural gas at minimal completion costs.

Creation and Validation of Discrete Fracture Network Models

This section describes the team's work on taking the detailed fracture characterization described in Section 3 to create quantitative fracture network models for simulations. The goal for this project was to develop a validated fracture model that could be used or abstracted for numerical hydrofracture modeling codes.

The need to develop a realistic, testable model that could be used as input to hydro-mechanical numerical models requires that the model be based on the geological causes for the observed regional variation of fracture geometry and flow properties. Only through the development of an accurate conceptual basis for the natural fractures in the Uinta Basin is it possible to construct a realistic model because many of the parameters needed to construct the model need to be inferred from a variety of different measurements and tests that rarely occur at a single well location. There must be a basis for this inference or interpolation. This basis is termed the Geological Conceptual Model (GCM) and is the first step in the workflow.

Once the GCM has been developed, the next step is to implement and test the conceptual model. The GCM is like a recipe for how to make fractures at any location in the Uinta Basin. The recipe can be implemented in many ways; for this project the conceptual model was implemented as a Discrete Fracture Network (DFN) model. A DFN model represents fractures as polygons that

have shape, size, orientation, aperture, intrinsic flow and mechanical properties, and relations with other fractures.

The DFN is more than a visualization of the natural fracture system; it can also be converted into a finite element model in which the fractures are discretized into triangles. The model can then be input to a variety of numerical codes to carry out a wide variety of simulations. This makes it possible to validate the DFN model by simulating, for example, Drill Stem Tests (DSTs) or other transient flow tests, tracer experiments and the microseismicity associated with hydrofracturing. If the model reproduces the flow or mechanical deformation at a well, then there is increased confidence that the model is geologically realistic, that its implementation is appropriate, and that it is useful for well-scale modeling in other codes.

Thus the workflow follows three major steps:

1. Development of a GCM to explain/predict fracture characteristics in the Uinta Basin;
2. Implement the GCM as a well-scale DFN model at a location with adequate data support and potential for validation; and
3. Validate the DFN model.

Development of the Geological Conceptual Model

From a fracture creation standpoint, the following parameters are important.

- Orientations
  - How many sets?
  - Are set orientations regionally consistent or do they vary according to structural context?
  - Are presence/absence of sets dependent to any meaningful extent on lithology or stratigraphy?
  - What insights might be gained for subsequent mathematical parameterization as a DFN?
- Intensity
  - Is intensity a function of stratigraphy and/or lithology?
  - Is intensity related to bed thickness or mechanical unit thickness?
  - How spatially variable or consistent is intensity?
  - Mathematical Parameterization

- Size
  - Can it be derived from heavily censored trace lengths in outcrop
  - Is size a function of lithology, orientation, structural history, or?
  - What insights might be gained for subsequent mathematical parameterization as a DFN?

The primary locations for detailed outcrop studies are shown in Figure 4-1 (this is a Google Earth image). One or more scanlines were set up at each location. The lines were positioned to be as long as possible given the outcrop geometry, accessibility and safety protocols. Some outcrops were well suited because of their accessibility, extent, orientation and well-developed fracturing to collect a wide variety of data; others were suitable for collecting only a subset of parameters. The superset of parameters recorded consisted of:

- Location along scanline
- 3D orientation
- Visible/measureable trace length
- Termination style on each end of trace
- If terminated against another set, orientation of set
- Qualitative aspects such as mineralization
- Some outcrops were subhorizontal; others were subvertical faces. Outcrops in different orientations were included where possible.

Antelope Ridge Scanline Site

Both the Upper and Lower Mesaverde are present at the Antelope Ridge locale. Scanlines AR1, AR2, AR4 and AR5 were situated in the Lower Mesaverde, while AR3 was located on a vertical exposure in the Upper Mesaverde (Figure 4-2). The large stereoplot in this figure is a composite of all five of the individual scanlines.

Overall, there appear to be two characteristic orientations. One orientation, which dominates the composite stereoplot, is northeast and subvertical. This is perpendicular to the bedding strike in the area. The other orientation is subvertical and roughly parallel to bedding strike. Often the northeasterly striking fractures (NE set) terminate against the northwesterly striking fractures (NW set). The northwest set is very common on many of the scanlines. The NE set (black arrow) has a smaller spacing than the NW set (red arrow). However, the NW fractures tend to be much longer and the NE set often (but not always) terminates against the NW set. The joint sets may not be extensive in the cross-bedded units. These joints frequently terminate against the boundaries of the cross-bedding packages.

The same elements of the fracture pattern observed in the other sites is also present at the AR5 site: two sets, one striking NE and typically terminating into a second that strikes NW to NNW. Overall, the pattern gives the impression of their being two well-developed sets, both orthogonal to bedding (Figure 4-3). One strikes parallel to bedding (NW to NNW at this location), while the other strikes northeasterly, perpendicular to bedding. The NE joints often terminate against the NW set, although the reverse termination style is also seen as well, but is much less frequent. The joints do not always look to be through-going but may terminate on internal boundaries in the cross-bedded units. AR3, however, showed fractures that had vertical extent of several meters or more.

Blue Mountain Scanline Site

The Blue Mountain scanline site is the easternmost of all the scanline sites (Figures 4-4 and 4-5). It is northeast of the Rangely Field. The bedding strikes to the east-northeast at this location. There are two dominant sets present at this locale: a NNW set and a NE set. The NNW set dominates the BMR2 and BMR3 locations; it is also found at BMR1, but the NE set dominates at BMR1. The NNW set is approximately perpendicular to bedding strike at this location.

Snake John Ridge Scanline Site

The Snake John Ridge site is a long series of outcrops between the Dinosaur, CO and Vernal, UT. Snake John Ridge is an important outcrop because of its changing strike. The observations at the Antelope and Blue Mountain sites show two joint sets parallel and perpendicular to bedding strike, which just happen to be northeast or northwest. This makes it impossible to determine if the NE and NW sets are regional or whether they are related to the folding of the rock. Scanlines were set up at several different locations along the ridge, but exposures where the outcrop trends almost east-west were either inaccessible or inadequate for acquiring systematic scanline measurements.

The western end of the Snake John Ridge outcrop belt was the location for four scanlines. These scanlines were on near-vertical outcrop faces, and as such, were only useful for collecting data on fractures that had strikes perpendicular to the outcrop faces. At this location, the outcrop (and bedding) strike to the ENE. The dominant fracture set seen along the vertical faces is a NNW set.

At the eastern end of the outcrop belt, the bedding strikes to the WNW. Joints measured in the outcrops show strikes parallel and perpendicular to bedding strike. As in the other locations, joints are orthogonal to bedding. The NE set dominates and is approximately perpendicular to bedding strike. The NW set is actually slightly oblique to bedding strike.

Unfortunately, it was not possible at Snake John Ridge to resolve the question as to whether the joints are regional, and just happen to align with the bedding strikes, or are in fact related to the folding of the rock. However measurements made just to the west in the overlying Dakota Sandstone provided evidence that at least one set is likely to be regional.

The outcrop and scanlines are located in Blind Draw to the west of Snake John Ridge. The stereoplots and more importantly, the yellow dashed lines that show major fractures cutting

across the outcrop suggest that the NW set maybe regional, rather than simply related to the local fold axis geometry, as they are not parallel or perpendicular to the bedding strike, but cut obliquely to it. All of the Snake John Ridge scanline results and stereoplots are available in the previous annual reports.

Orientations and Termination Style. The termination style of all fractures measured along scanlines was recorded. Fractures can terminate in several ways:

- Censored, which means that the end is not observed due to outcrop limitations;
- Blind, which means that the end of the fractures just ends in the rock, and not against another fracture;
- T-termination, in which a fracture intersects another fracture almost perpendicularly;
- Asymptotic, where the fracture approaches another fracture at a high angle, but changes orientation and terminates subparallel to the other fracture; and
- Hooking, in which one or both fractures that are subparallel and separated by a few centimeters hook into one another.

Fractures that are censored tend to be large, or at least larger than the outcrop dimension in the direction of their strike. Fractures that terminate, especially on both ends, against other fractures tend to be small. Stereoplots were constructed from all of the fractures in all of the scanlines in which both ends were censored, and in which both ends terminated against other fractures (Figure 4-6). Interestingly, the doubly terminated fractures strike dominantly to the NE, while the fractures that extend beyond the ends of the outcrops dominantly strike NNW. The few NE-striking doubly censored fractures are exclusively from scanline BMR1 north of Rangely. This suggests that while there may be many more NE fractures, they typically terminate against the NNW fractures, which may be longer and more widely spaced.

From a hydraulic standpoint, this suggests that the NNW set is more important, while the NE set connects the NNW sets together.

Summary of Outcrop Observations & Development of the GCM

There is always one set that is subvertical and nearly perpendicular to bedding strike, and sometimes a second set steeply dipping and subparallel to bedding strike.

- These observations would be consistent with a simple plate-bending model in which joints would form in these two orientations
- Because of the orientation of the bedding at most of the Mesaverde outcrops on which fracture data was gathered along scanlines, this model would produce and northwest set and a northeast set that might appear regionally consistent, and hence be attributed to regional stress controls, rather than local structural controls
- However, a few scanline sites suggest that the northwest set is a regional set and not related to local structure. These scanlines include the Dakota sandstone sites (SJR1

and SJR2), and the Antelope Ridge scanline sites AR1 and AR5. All of these sites show evidence of a northwest to north-northwest set that is oblique to bedding strike.

- Moreover, the dominant NNW and NE sets are not orthogonal or really even very close to it, suggesting that these two sets are not both related to simple plate bending.
- The NNW set may be the dominant set in terms of fluid flow, as the NE set typically terminates against it. It may also be the longer set, but termination styles alone are insufficient to determine this.
- Thus, it is likely that there are two, and possibly a third, fracture set. The dominant set subparallels the in-situ stress direction, and strikes E-W to NW, depending upon the location in the Basin. Additional sets relate to local structure, in particular, folds that were formed during Basin formation. Joints develop parallel and perpendicular to the fold axes. In many locations, the fold axis trends north-northwesterly, and so it may be difficult to find evidence of stress control vs. a plate-bending origin for the joints observed in the field.

DFN Model Development

Fracture Size Determination. The only method for estimating fracture size from the outcrop data is the size-number scaling plot, referred to as the Complementary Cumulative Number (CCN) plot. In this type of plot, the Y-axes plots the number of fracture traces greater than or equal to a given length, while the X-axis is the trace length. Plots are typically posted on doubly logarithmic axes to test for fractal scaling behavior. A fractal or power law model will plot as a straight line on such axes. Given the previous observations, fractures were divided into NNW and NE sets, and then the fractures with a doubly terminating or doubly censored termination styles were plotted on the CCN plots (Figure 4-7). This was done to be consistent with the orientation and termination models thus far developed.

Best-fit power law models for the All-NNW, XX-NNW and XX-NE sets show a remarkable consistency and a reasonable power law fit (the departure from linearity at low and high values is due to censoring effects). The slope of the line for these sets is about -1.02. The best fit power law models for TT-NE and All-NE show a good consistency and a reasonable power law fit (the departure is due to truncation effects most likely). The slope of the line for these subsets is -1.04. The offset in the two lines indicates that the respective subsets have different sizes. The fact that the NNW group is higher than the NE group indicates that the NNW group is larger. Both sets can be well-modeled by a power law distribution.

Fracture Intensity. Fracture intensity is another parameter that is needed for generating a DFN model. The outcrop scanline data was analyzed to determine if there were characteristic spacings for different units in the Mesaverde and what order of magnitude facture intensity or spacing is reasonable. The workflow was:

- P10 values (number of fractures per foot) were tabulated for each set at each scanline locale;

- The P10 values were corrected for scanline orientation relative to the set orientation using the modal set values previously presented;
- The corrected P10 values were then converted to spacing values; and
- Table 4-1 and Table 4-2 summarize the mean intensity and spacing values. These tables show that:
    - The NNW set has spacings on the order of 15 ft to 25 ft, with most of the spacings between 15 and 20 ft;
    - The NE set has spacing values that are much smaller: 1 – 5 ft is a typical range;
    - For a prototype DFN, the mean spacing for the NNW set is 15 ft (with some variation), while the NE set is 5 ft (with some variation); and
    - The variation for each set is assumed to follow a normal distribution with a CV of 0.5.

Implementation of GCM for Tract 21

The preliminary GCM developed in the previous section provided the basis for generating fracture models elsewhere in the Basin. The GCM implies that there will likely be two sets of joints, one of which strikes parallel to the orientation of the present day maximum in-situ stress, while the other makes a high angle and strikes parallel or perpendicular to bedding strike. The set that is related to the stress direction should be larger, and in general, the other set should terminate against it. The fracture sizes follow power laws, and it is assumed that the exponents determined from the outcrop data will apply elsewhere in the Basin. These implications, however, need to be evaluated carefully at any new location to assess their validity.

Data was made available by Anadarko from some wells in the Tract 21 region. Additional data was obtained from public sources.

Mechanical Layering

The fracturing observed in outcrop shows strong visual evidence of mechanical layering. These layers contain joints that extend from the top and bottom of the layer for the most part, and tend to have characteristic spacing values. A Cumulative Fracture Intensity (CFI) plot (La Pointe, 2010) was created for the NBU21-21L data using only the open fractures (Figure 4-8). Also shown are the mechanical intervals selected from the CFI plot, and the values of the P10 fracture intensity in terms of the number of fractures per foot. Figure 4-9 shows a visualization of the mechanical layers inferred from the CFI plot.

Analyses of the fracture orientations (Figure 4-10) shows that there are two sets. The two sets are steeply dipping and nearly orthogonal to one another. The primary set strikes EW to WNW, while the secondary set strikes NS to NNE. Induced hydrofracture orientations (Figure 4-11) indicate that the minimum in situ horizontal stress is approximately NS to NNE, and the maximum in-situ horizontal stress is EW to WNW. This is consistent with the GCM developed from the outcrop studies in that:

- There are two sets, orthogonal to bedding and steeply dipping;
- The dominant set strikes parallel to the direction of maximum in-situ horizontal stress (perpendicular to the minimum in-situ horizontal stress);
- The secondary set strikes orthogonal to bedding strike; and
- The fractures form mechanical layers separated by unfractured or weakly fractured units.

Figure 4-12 presents the results of a more detailed analysis of the fracture orientations. In these analyses, the ISIS (Interactive Set Identification System) module in FracMan was used to find the best-fit statistical model for the orientations of each fracture set. The analyses showed that the best fitting model for the EW/WNW set is the Fisher model with mean pole 189/8.2. The best fitting model for the NS/NNE set is a virtual tie between the Fisher and Bivariate Bingham models. The Fisher model with mean pole 276.4/1.8 will used for its mathematical simplicity.

Note that the relative intensity between the two sets is about 2. This compares favorably with the intensity ratio of about 2.5 found in the size models derived from outcrop work (Figure 4-13), further validating another geometric aspect of the Tract 21 DFN model.

Creation of the Tract 21 DFN Model

The preliminary Tract 21 DFN model was generated based on the mechanical layering identified from the CFI plots (Figure 4-14). This generation process was carried out by defining fracture generation grids for each mechanical layer (Figure 4-15). The recipe for generating the fractures in each grid was based on the following observations, inferences and data:

- Two sets were generated. The orientations were based on the ISIS analysis of the FMI data for NBU21-21L;
- Fracture sets in outcrop followed powerlaw distribution with very similar exponents (D = 2.02 & 2.04). Thus, both sets in the Tract 21 model are given powerlaw size models. The EW set is assumed to be the counterpart of the outcrop doubly-censored (the "XX" set in the following slides), as both are parallel or subparallel to local in situ stress directions. The NS set is assumed to be the counter part of the "TT" set. Therefore, DEW = 2.02, DNS = 2.04. The minimum size is unconstrained, but will be obtained later through hydrofracture simulation calibration;
- Global volumetric intensity: EW Set P32 = 0.01; NS Set P32 = 0.005 based on matching total number of fractures in 9 intervals and maintaining 2:1 ratio in relative set intensity seen in FMI data (Figure 4-12) and the 2.5 ratio shown in the CCN plots for outcrop traces (Figure 4-7);
- Fractures are generated in mechanical layers identified from the CFI plots for Tract 21 (Figure 4-8);
- NNW-NS set terminates 50% of the time against EW set (based on qualitative appraisal of terminations in outcrop studies);

- Elongation (horizontal:vertical) = 20:1 (qualitative appraisal of mechanical layer thickness and horizontal trace lengths in outcrop);

Figure 4-14 and Figure 4-15 show visualizations of the preliminary DFN model based on these considerations. Figure 4-16 provides a partial validation of the implementation of the model. This figure compares the orientations of fractures measured from the FMI data with the orientations of fractures intersected by a synthetic well in the same orientation placed into the preliminary DFN model. This figure shows a good match between the DFN model data and the measured FMI data.

Figure 4-17 through Figure 4-19 illustrate aspects of the connectivity of the fracture model. Figure 4-17 and Figure 4-18 show reservoir compartments that develop in the fracture model. Each compartment consists of color-coded fractures. Those with the same color are connected to one another, but not to other fractures or compartments in the model. In a reservoir, these represent the potential volume of matrix that could be drained by the fracture network when matrix permeability is low, as it is in the Mesaverde. Note that not all layers have the same sized compartments. In this model, thicker layers tend to develop larger compartments.

Figure 4-19 shows the fractures connected to the well. The importance of this figure is the potential variability in layer productivity. The bottom layer, because it is thickest, has the most extensive connected fracture network. Thin layers are much more poorly connected.

Calibration

The final steps for calibrating and validating the Tract 21 DFN model require the specification of the hydro-mechanical properties and the validation of these properties. This was done by simulating a hydrofracture in the preliminary Tract 21 model. In particular the validation consisted of comparing the microseismic response in the model to the microseismic response of the nearby Chapita Wells hydrofracture. Using the microseismic response as a validation/calibration case provided and intergrated test of the model geometry, hydraulic and mechanical properties assigned to the model. There is uncertainty in the hydro-geomechanical properties of the model, as described below. With an acceptable match, DFN model geometry and properties are within the range of uncertainty, and the model can be used as input for the more advanced hydrofracturing simulators with confidence. Moreover, a successful match will have demonstrated how other operators in the Basin can take the CGM and implement it and validate it for their own local use.

In-situ stress orientations have been inferred from the induced hydrofractures and assigned to the fracture generation grids. The magnitudes have not been directly measured in the vicinity of Tract 21. The vertical stress can be calculated from the overburden. For the validation exercise, the following were assumed for the horizontal stress magnitudes:

- sv from lithostatic
- Assume mild anisotropy:
    - $s_{Hmax} = 0.46$ sv

  - s_{Hmin} = 0.42 sv
- Depth = 9800 ft below surface

The hydraulic parameters could be inferred from transient well tests, but such tests do not exist in the Tract 21 region. Hydraulic fracture pumping parameters provided by Anadarko were used to adjust the model input. Important properties were:

- Aperture
  - Correlated to size (radius)
  - Aperture = Radius/6143.875
  - Matches aperture range determined from proprietary analyses of data elsewhere in Uinta Basin
- Intrinsic Fracture Permeability
  - Correlated to size (radius)
  - Kf = Size*80
  - Matches intrinsic permeability data determined from proprietary analyses of data elsewhere in the Uinta Basin

As in the case of the horizontal stress magnitudes, these are preliminary values and were changed to match the geometry of the microseismic response.

Mechanical properties are also needed for the fractures themselves. These consist of the frictional sliding (Mohr-Coulomb) parameters of cohesion and shear strength, and the elastic moduli. There is no published geomechanical data for the Mesaverde in the Tract 21 area. A survey of literature on the Mesaverde and Piceance Basins suggests that the following values are possible starting points:

- Mohr-Coulomb properties of fractures;
  - Cohesion = 0.0; and
  - Friction Angle = 30 degrees.
- Elastic properties;
  - Shear modulus 3.0e+6 psi; and
  - Poisson's ratio = 0.20.

These values are uncertain, and like the stress magnitudes and hydraulic fracture properties, were adjusted in order to achieve an acceptable match to the Chapita Wells microseismic cloud geometry.

The microseismic events computed using the hydraulic fracturing module in Fracman for the Chipeta well are shown in Figure 4-20. This is a horizontal view. Orientation of microseismic clouds are nearly identical. Length and width of microseismic clouds are very similar (600 ft vs. 480 ft. horizontal half-length extent; 300 ft vs. 365 ft width of affected zone perpendicular to hydraulic fracture.)

INCORPORATING GEOMECHANICS IN RESERVOIR SIMULATION

The project team enhanced the DFN model and reservoir simulation. The Utah Finite Element Simulator (UFES) has been under development with continuous contribution from group members (Yang, 2003; Fu, 2007; Balasubramanian, 2007). The Control Volume Finite Element (CVFE) discretization method was developed for reservoir simulation (Fu et al., 2005; Yang and Deo, 2006) this method has the advantage to model unstructured fracture and complex fluid flow behavior in the reservoir. A transmissibility-based finite volume method was also developed to integrate the UFES with other reservoir simulators. A 3-D black oil model and Compositional K value Thermal (CKT) model were developed to simulate conventional and unconventional oil and gas recovery. A geochemical reactive transport model was also introduced for modeling CO2 sequestration and enhanced oil recovery (Gu, 2010). Modularization implementation was applied to the CKT model development (Huang, 2009). A variety of simulations have been performed previously to evaluate the UFES and to show the advantages of the DFN model in simulating conventional reservoir recovery processes. In summary, the UFES originally developed under previous research has proved to be effective and accurate in modeling a conventional reservoir with complex fractures.

Based on these previous developments, a generalized reservoir simulator with geomechanics (Advanced Reactive Transport Simulator (ARTS)) was developed to model the oil and gas recovery process in this research (Figure 5-1). DFN is used as the default fracture representation method, and several submodels have been implemented in ARTS to improve the computational efficiency and to extend the capability.

Mathematical Formulation

Only the very basic aspects of the development of incorporating geomechanics into reservoir simulation are discussed here. Details are available in a Ph.D. dissertation by Nan Zhao at the University of Utah (Zhao, 2012).

The governing equation for the geomechanical model is based on the force balance or momentum balance of a small control volume (REV). In general we can write it as:

$$\nabla \cdot \sigma + \rho \vec{b} = 0$$

Where, σ is a tensor, which represents the symmetric stress matrix.

$$\begin{bmatrix} \sigma_{x,x} & \sigma_{x,y} & \sigma_{x,z} \\ \sigma_{y,x} & \sigma_{y,y} & \sigma_{y,z} \\ \sigma_{z,x} & \sigma_{z,y} & \sigma_{z,z} \end{bmatrix}$$

Different models can be used to treat the stress like the linear elastic model, linear poroelastic model and so on.

$$\sigma = \sigma' - \alpha\delta_{i,j}P$$

Where σ′ is the effective stress, and P is an averaged pore pressure of all fluids in the system.

$$P = \sum_{i=1}^{n} s_i p_i$$

In the simulator, a saturation weighted pore pressure is used, and then the governing equation can be written as:

$$\nabla \cdot (\sigma' - \alpha\delta_{i,j}P) + \rho\vec{b} = 0$$

The density is defined as the "average" of solid and fluid density:

$$\rho = (1 - \phi^*)\rho_s + \phi^*\rho_f$$

In the simulation, a poroelastical model is used.

$$\sigma_{i,j} = 2G\varepsilon_{i,j} + 2G\frac{\nu}{1-2\nu}\varepsilon_{k,k}\delta_{i,j} - \alpha p\delta_{i,j}$$

In this equation, G is the shear modulus, v is the drained Poisson ratio, and α is the Biot coefficient.

Governing Equation of Reservoir Model

For a two-phase black-oil reservoir model, the governing equation is:

$$\nabla \cdot (\frac{Kk_{rl}}{B_l \mu_l} \nabla \varphi_l) = \frac{\partial}{\partial t}(\phi \frac{S_l}{B_l}) + q_l$$

Φ_l is the potential of the fluid l:

$$\varphi_l = p + \gamma Z$$

q is the source term of the fluid. The model can be single or multiphase flow, this depends on the problem. A control volume finite element method is used in the flow calculation, in which the fracture of the reservoir is discretized one order lower in dimension than the matrix. All the properties and calculations are node based, which makes the flow model consistent with the traditional finite element method (geomechanical model).

Coupling Schemes

In general, there are two types of coupling schemes, soft coupling and hard coupling. Soft coupling means the geomechanical effect is not directly built into the reservoir simulation. The hard coupling method integrates the geomechanical model into the reservoir simulator. Both of these two methods need some parameters to connect the geomechanical model and reservoir model. In this approach, reservoir true porosity and permeability are chosen as coupling parameters.

First the true porosity of the reservoir is computed. (Chin, 2002):

$$\phi^* = 1 - (1 - \phi_0)e^{-\varepsilon_v}$$

Or, in a linear form:

$$\phi = (\frac{1 - \phi_0}{1 - \phi^*})\phi^*$$

The basis for the above is the continuity equation.

$$\frac{\partial \rho_s (1 - \phi)}{\partial t} + \nabla((1 - \phi)v_s) = 0$$

In the above equation, ε_v is the volumetric strain of the rock, and Vs is the velocity of the rock. The permeability can be related to the geomechanic factor (Ran and Li 1997):

$$\frac{k}{k_0} = \frac{1 + \frac{\varepsilon_v}{\phi_0}}{1 + \varepsilon_v}$$

The volumetric strain is:

$$\varepsilon_v = \frac{\delta V}{V} = \varepsilon_{xx} + \varepsilon_{yy} + \varepsilon_{zz}$$

The strain is:

$$\varepsilon_{ij} = \frac{1}{2}\left(\frac{\partial u_i}{x_j} + \frac{\partial u_j}{x_i}\right)$$

Through this information, the impact of geomechanics is introduced in the reservoir model. The geomechanical model is related to the reservoir model by the effective stress formulation. Further the geomechanical model is assumed to be at equilibrium all the time through the reservoir life.

To take into account of the geomechanical effect without much change in the reservoir model, the updated permeability and porosity can be used in the soft-coupling scheme. In this way, the reservoir permeability and porosity is set to be a function of pressure (and/or saturation) based on the mechanical information of this reservoir. This external information can include real data and pure mechanical simulation results for the reservoir. In order to integrate two different simulations, a matching scheme needs to be chosen. In the soft coupling code, the pore pressure of the reference phase is set to be a parameter to integrate the two simulations.

The procedure for this type of soft coupling is to generate the same reservoir model for the two simulations. The flow properties and other well operating parameters are also set to be the same. The procedure requires the two simulations to be run simultaneously. From this geo-type calculation, a locus of pressure and deformation or aperture information is obtained, and a table containing pressure and difference in the mechanical properties between the old and new is constructed for the purpose of using in the flow simulation. Finally, the flow simulation is re-initiated with integrated pressure-permeability-porosity table.

A soft-coupling scheme was developed based on the Itasca 3-DEC for the multiphase-flow simulation. In the simulator, the updated permeability and porosity is obtained from a look-up table generated from the geomechanical information of 3-DEC. The pore pressure is the link between the two simulators.

Hard Coupling

The geomechanical model is integrated into the reservoir simulator with hard coupling. The geomechanical equation set and flow equation set can be solved "explicitly" or "implicitly" depending on the geomechanical importance of the problem.

For the geomechanical model, a general virtual work formulation can be derived.

$$\int_{\Omega} \delta\vec{\varepsilon}^T \Delta\sigma' d\Omega - \alpha \int_{\Omega} \delta\vec{\varepsilon}^T \Delta p d\Omega - \int_{\Gamma_\sigma} \delta\vec{u}^T \Delta\vec{t} d\Gamma = 0$$

After applying the effective stress law the equation reduces to:

$$(\int_{\Omega} B^T D B d\Omega)(\Delta\vec{u}) - \alpha(\int_{\Omega} B^T \vec{m} N d\Omega)(\Delta p) - \int_{\Gamma_\sigma} \delta\vec{u}^T \Delta\vec{t} d\Gamma = 0$$

For the finite element discretization:

$$\vec{u} = \begin{bmatrix} N_1 & 0 & 0 & N_2 & 0 & 0 & N_3 & 0 & 0 & \dots \\ 0 & N_1 & 0 & 0 & N_2 & 0 & 0 & N_3 & 0 & \dots \\ 0 & 0 & N_1 & 0 & 0 & N_2 & 0 & 0 & N_3 & \dots \end{bmatrix} \begin{bmatrix} u_1 \\ v_1 \\ w_1 \\ u_2 \\ v_2 \\ w_2 \\ u_3 \\ v_3 \\ w_3 \\ \vdots \end{bmatrix} = N\vec{u^e}$$

and

$$\varepsilon = \begin{bmatrix} \frac{\partial}{\partial x} & 0 & 0 \\ 0 & \frac{\partial}{\partial y} & 0 \\ 0 & 0 & \frac{\partial}{\partial z} \\ \frac{\partial}{\partial y} & \frac{\partial}{\partial x} & 0 \\ 0 & \frac{\partial}{\partial z} & \frac{\partial}{\partial y} \\ \frac{\partial}{\partial z} & 0 & \frac{\partial}{\partial x} \end{bmatrix} \begin{bmatrix} N_1 & 0 & 0 & N_2 & 0 & 0 & N_3 & 0 & 0 & \dots \\ 0 & N_1 & 0 & 0 & N_2 & 0 & 0 & N_3 & 0 & \dots \\ 0 & 0 & N_1 & 0 & 0 & N_2 & 0 & 0 & N_3 & \dots \end{bmatrix} (\vec{u^e}) = B(\vec{u^e})$$

$$B = [B_1, B_2, B_3, \dots]$$

$$B_i = \begin{bmatrix} \frac{\partial N_i}{\partial x} & 0 & 0 \\ 0 & \frac{\partial N_i}{\partial y} & 0 \\ 0 & 0 & \frac{\partial N_i}{\partial z} \\ \frac{\partial N_i}{\partial y} & \frac{\partial N_i}{\partial x} & 0 \\ 0 & \frac{\partial N_i}{\partial z} & \frac{\partial N_i}{\partial y} \\ \frac{\partial N_i}{\partial z} & 0 & \frac{\partial N_i}{\partial x} \end{bmatrix}$$

In order to simplify, the vector form of the stress tensor is introduced, and the stress tensor can be reduced to six component vector as it is symmetric.

$$\vec{\sigma} = \begin{bmatrix} \sigma_{xx} \\ \sigma_{yy} \\ \sigma_{zz} \\ \sigma_{xy} \\ \sigma_{yz} \\ \sigma_{zx} \end{bmatrix}$$

The effective stress rule and the stress model can be used.

$$\vec{\sigma} = D\vec{\varepsilon} - \alpha\vec{m}P$$

where:

$$\vec{\varepsilon} = \begin{bmatrix} \varepsilon_{xx} \\ \varepsilon_{yy} \\ \varepsilon_{zz} \\ \varepsilon_{xy} \\ \varepsilon_{yz} \\ \varepsilon_{zx} \end{bmatrix} \quad \vec{m} = \begin{bmatrix} 1 \\ 1 \\ 1 \\ 0 \\ 0 \\ 0 \end{bmatrix}$$

The geomechanical model can be simplified by applying the divergence theorem and Galerkin method:

$$\nabla \underline{\underline{\sigma}} + \underline{b} = 0$$

We obtain the following after multiplying a "constant" displacement vector on both sides of the equation:

$$\vec{u}(\nabla \underline{\underline{\sigma}} + \underline{b}) = 0$$

applying integration by part:

$$\vec{u}\nabla \underline{\underline{\sigma}} = \nabla(\vec{u}\underline{\underline{\sigma}}) - \underline{\underline{\sigma}}\nabla\vec{u}$$

Then integrating over the whole volume of one element (REV):

$$\int_V (\nabla(\vec{u}\underline{\underline{\sigma}}) - \underline{\underline{\sigma}}\nabla\vec{u} + \vec{u}b)dV = 0$$

Applying the Gaussian-Green theorem.

$$\oint_S \vec{u}\underline{\underline{\sigma}}\vec{n}dS - \int_V \underline{\underline{\sigma}}\nabla\vec{u}dV + \int_V \vec{u}bdV = 0$$

Once a multiplication matrix is introduced,

$$S^T = \begin{bmatrix} \frac{\partial}{\partial x} & 0 & 0 & \frac{\partial}{\partial y} & 0 & \frac{\partial}{\partial z} \\ 0 & \frac{\partial}{\partial y} & 0 & \frac{\partial}{\partial x} & \frac{\partial}{\partial z} & 0 \\ 0 & 0 & \frac{\partial}{\partial z} & 0 & \frac{\partial}{\partial y} & \frac{\partial}{\partial x} \end{bmatrix}$$

The integration can be written as:

$$\oint_S \vec{u}\underline{\underline{\sigma}}\vec{n}dS - \int_V \vec{u}S^T\underline{\underline{\sigma}}dV + \int_V \vec{u}bdV = 0$$

Notice that u is assumed to be finite "constant" displacement vector:

$$\oint_S \underline{\underline{\sigma}}\vec{n}dS - \int_V S^T\underline{\underline{\sigma}}dV + \int_V bdV = 0$$

The Galerkin-weighted residual method is applied to the equation.

$$\oint_S N^T\vec{t}dS - \int_V B^T\underline{\underline{\sigma}}dV + \int_V N^T\vec{b}dV = 0$$

The effective stress relationship and stress model can now be applied, and the final equation set is derived as follows.

$$\oint_S N^T\vec{t} - \int_V B^T DBu^e + \int_V B^T\alpha\vec{m}\vec{p} + \int_V N^T\vec{b} = 0$$

All the terms can be expressed in the form of trial function N, and the formula becomes:

$$\oint_S N^T N t^e - \int_V B^T D B u^e + \int_V B^T \alpha \vec{m} N p^e + \int_V N^T N b^e = 0$$

For the volume integration term

$$\int_V B^T D B u^e dV \approx \int_V B^T D B dV u^e = V_e B^T D B u^e$$

This is based on the isotropic assumption.

Other terms in the integration are obtained as follows.

The pressure term:

$$\int_V B^T \alpha \vec{m} N p^e dV = \alpha B^T \vec{m} \int_V N p^e dV = \alpha B^T \vec{m} \int_V N_1, N_2, N_3, N_4 p^e dV$$

The integration is calculated through a one-point Gaussian quadrature for a linear basis function. If more points are needed, the trial function needs to be of higher order.

$$\int_V N_1 dV = \frac{1}{4} V_e$$

Other terms follow the same methodology.

The surface traction term needs to be calculated only on the boundary. Because when assembling the global system, equations are added element by element and then the surface traction term is canceled out (because of the direction of the traction force). Thus, the traction term only appears in the boundary element.

Volumetric strain can be used as a coupling parameter. The original mass balance equation for fluid in porous media is:

$$-\nabla \cdot \frac{\vec{v_l}}{B_l} = \frac{\partial}{\partial t}(\phi^* \frac{S_l}{B_l}) + q_l$$

The velocity is changed to relative velocity,

$$\vec{v_{ls}} = \vec{v_l} - \vec{v_s}$$

and the equation becomes:

$$-\nabla \cdot \frac{\vec{v_l} - \vec{v_s}}{B_l} = \frac{\partial}{\partial t}(\phi^* \frac{S_l}{B_l}) + q_l$$

$$-\nabla \cdot \frac{\vec{v_l}}{B_l} + \nabla \cdot \frac{\vec{v_s}}{B_l} = \frac{\partial}{\partial t}(\phi^* \frac{S_l}{B_l}) + q_l$$

$$\nabla \cdot \vec{v_s} = \nabla \cdot \frac{D\vec{u_s}}{Dt} = \frac{D(\nabla \cdot \vec{u_s})}{Dt} = \frac{D\varepsilon_v}{Dt}$$

The governing equation becomes:

$$\nabla \cdot (\frac{K k_{rl}}{B_l \nu_l} \nabla \varphi_l) + \frac{D}{Dt}(\frac{\varepsilon_v}{B_l}) = \frac{\partial}{\partial t}(\phi^* \frac{S_l}{B_l}) + q_l$$

Using the continuity of the solid,

$$\frac{\partial}{\partial t}((1 - \phi^*)\rho_s) + \nabla \cdot ((1 - \phi^*)\rho_s \vec{v_s}) = 0$$

the density of the solid is assumed to be constant:

$$\frac{\partial(1 - \phi^*)}{\partial t} + (1 - \phi^*)\nabla \cdot \vec{v_s} + \vec{v_s} \cdot \nabla(1 - \phi^*) = 0$$

$$\frac{D(1-\phi^*)}{Dt} + (1-\phi^*)\frac{D(\frac{\varepsilon_v}{B_l})}{Dt} = 0$$

The term above serves as another accumulation term if we assume the total derivative is almost the same with partial differential term.

$$\nabla \cdot (\frac{Kk_{rl}}{B_l \nu_l}\nabla\varphi_l) + \frac{\partial}{\partial t}(\frac{\varepsilon_v}{B_l}) = \frac{\partial}{\partial t}(\phi^* \frac{S_l}{B_l}) + q_l$$

The volume-strain coupling method is consistent with the true porosity and true permeability model chosen. If some other porosity and permeability model is applied, the artificial accumulation part needs to be adjusted.

Hard coupling schemes

The geomechanical calculation using a pure finite element method is generally slow. Consequently for hard coupling, there are two ways to set up the coupling procedure. One is solving the geomechanical equation at each time step, and the other is only solving the geomechanical model at "specific" times and positions. The reason for doing this is to obtain a reasonable result at a reasonable cost.

Iterative coupling. For this type of method, the geomechanical part is treated "separately" as an individual model. The flow model only takes the information at certain times and in certain spatial locations. The mechanical effect is not always significant during reservoir operations.

In the simulator, the user can define the time to consider geomechanical calculation. At this time, the geomechanical update is applied after the flow calculation is updated (this can be after nonlinear iteration or linear iteration). In the new flow calculation iteration, the new porosity, permeability and extra accumulation is considered. The geomechanical model always takes the current pressure as an input.

Implicit coupling. For the implicit coupling, the geomechanical model is calculated together with the flow model through the system like:

$$\begin{bmatrix} A_g & A^{g-f} \\ A^{f-g} & A_f \end{bmatrix} \begin{bmatrix} x_g \\ x_f \end{bmatrix} = rhs$$

The f-g and g-f are the coupling matrices of two models. This system can be solved in Schur's form in order to "separately" handle the information of two models and reduce some of the

overlapping calculation. However, generally speaking, the system is difficult to construct and compute.

The hard coupling method used in this project is implemented in a single method with an option of turning full coupling on and off. This allows reuse of information from the geomechanical model.

Model Verification

The first verification case is a 1-D consolidation problem with linear poroelasticity. The analytical solution to this problem is provided by Jaeger and Cook (2007). This is actually a 1-D Terzaghi problem (Tergazhi and Peck, 1996; Znidarcic and Schiffman, 1983), in which a layer of porous media was subjected to a normal external load at the surface. Analytical solutions of this problem have been derived from the original research work done by Terzaghi in 1923, but the original solution was restricted to the problem where the vertical strain is small. To extend the limitation of the problem, several researches (Fox, 1999; Hanrahan, 1982; Korn and Korn, 2000_ have modified the original formulations.

A fluid-filled poroelastic layer of soil extending from the surface z = 0 down to the depth z = h is under a normal traction load p at time t = 0 on the upper surface. The analytical solutions of pore pressure and vertical displacement can be derived if the linearized theory is applied. Details of the analytical solution are provided by Zhao, 2012. The parameters used in the comparison are shown in Table 5-1. Comparisons for one-dimensional consolidation for pressure and displacement are shown in Figure 5-2. The analytical solution is reproduced by the numerical implementation described.

The second verification case study is a 2-D rock under pressure load. This problem comes from the reversion of Mandel's problem. Mandel (1953) presented one of the first solutions for the three dimensional consolidation of Biot's problem which demonstrates the nonmonotonic pore pressure effect. The effect of Poission's ratio on the magnitude of pore pressure development and dissipation was illustrated by later research, which is based on Mandel's original research (Cryer, 1963). The nonmonotonic pressure effect has been referred to as the Mandel-Cryer effect (Gibson et al., 1989; Selvadurai and Shirazhi, 2004; McKinley, 1998). The physical phenomenon has been confirmed in the field as the Noordbergum effect (Kim, 1997). Hence, the solution of Mandel's problem has been used as a benchmark problem for testing the validity of numerical code for poroelasticity (Christian and Boehmer, 1970; Coussy, 2004). In this research, Mandel's problem is also used as a verification case study but with some modifications to simplify the original problem.

The original Mandel problem involves an infinitely long rectangular specimen, sandwiched at the top and the bottom by two rigid plates with no friction (Cheng et al., 1996). Figure 5.3 shows the basic geometry of Mandel's problem.

The specimen contains incompressible solid saturated single phase fluid. The initial pore pressure is p0. The lateral sides are free from normal and shear stress, and the top and bottom of the specimen have an external force load which is 2F per unit thickness at time t = 0+.

The lateral boundary surfaces S1 and S2 perpendicular to x direction are traction free and exposed to the surrounding environment, which also has the pressure p0. According to the Skempton effect (Skempton, 1994), a pressure rise will be observed inside the specimen as the force starts to be applied on the boundary. Drainage will occur at the side surfaces, and pressure dissipation will also happen. The pressure depletion will later propagate to the inner region of the specimen. Once the pressure rise vanishes, the drainage will stop. This is a fairly simple physical process, but obtaining the analytical solution is not easy.

The original solution provided by Mandel only includes pore pressure. Cheng et al. (1996) revisited the problem and extended the solution to compressible fluids and skeletons, and the material behavior was generalized from isotropy to transverse isotropy. Indeed, the complete solutions of stress, displacement and pore pressure are provided (Cui et al., 1996; Nguyen and Abousleiman, 2010; Wheeler and Gai, 2007).

For the particular verification problem, the rock media is assumed to be isotropic, and the original solution is modified to meet this assumption. The modified analytical solutions of this problem are shown by Zhao, 2012. The comparison of analytical solution with the numerical model is shown in Figure 5-3. Parameters used in the model are shown in Table 5-2.

As discussed in the previous section, verification with commercial software is necessary to verify ARTS framework. This is also called index method for verifying and validating a computational code. In this case study, the reservoir simulator, STARS from the Computer Modeling Group (CMG), is used for verification purposes with ARTS.

STARS is a widely used compositional reservoir simulator in the oil and gas industry. A geomechanical model has been integrated in recent years [Dennis et al, 2001; Tran et al., 2009]. However, there is no industry standard for geomechanical reservoir simulations as a result of some unsolved difficulties involved in coupling geomechanics with reservoir simulation, such as running speed and adaptability. The comparison of ARTS and STARS is just to show the agreement between these two simulators and that ARTS has the potential to be applied in solving real field problems.

The reservoir model in STARS has a K-value based compositional model with a geomechanical model that has nonlinear elasticity and plasticity models. Some parameters are adjusted in STARS to enforce the linear poroelasticity model, which is used in ARTS. Indeed, the black oil simulation data is converted to a data set, which meets the requirements of a K value thermal model, some important properties are listed in Table 5-3.

This case study models a reservoir with a relatively soft rock in the production process with the coupling of geomechanics and reservoir simulation. The comparisons of pressure, subsidence, and the production rate are discussed. From these results, we can see a reasonable agreement between ARTS and STARS. This proves the validity of ARTS, and shows the potential of applying ARTS in real field problems.

The block at the center of the top surface is chosen to be the check area for comparing pressure, subsidence, volumetric change in this case study. Figure 5-4 shows the comparison of pore pressure, subsidence, volumetric change and production rate. The results from STARS and ARTS match closely and the maximum difference between ARTS and STARS is around 9%. The trend of the pressure change is the same for both simulators and it clearly shows the pressure depletion procedure after production begins. During the 300-day study period, the pressure declines as the fluid is producing from the reservoir. The reason for choosing a relatively short time in this case is to ensure the volumetric change is small and the linear poroelasticity model is used. The close match of pressures verifies the coupling scheme applied in ARTS solves the coupled system correctly. Although the match is not prefect, it is still enough to show the validity of pressure calculation in the coupled model in ARTS. The coupling scheme used is iterative coupling in STARS, and the same kind of coupling scheme is applied in ARTS.

With respect to subsidence, the reservoir has a trend to move downwards after the production begins and the pressure starts to decline. This trend is displayed from the results from both simulators. The results for subsidence between ARTS and STARS are close but not identical as shown in Figure 5-4. One possible reason is the difference for stress modeling. In ARTS, a linear poroelasticity model is applied, but an elastic plastic model is used in STARS. Although some parameters have been set to enforce the linear elasticity in STARS, the stress models in these two simulators are not the same. Despite the difference for stress models, the physical phenomenon modeled in these two simulators are the same and similar mechanical response of rocks during the production process are observed. This proves the validity of ARTS in calculating the geomechanical property change caused by pressure depletion.

In STARS, the compressible force is defined as positive and sign conversion is made in ARTS to reflect this change. The volume of rock at the check area shrinks as the production begins. Both the results of ARTS and STARS capture this trend, which has a huge impact on the reservoir simulation. The agreements seen in the volumetric change and production rate show that ARTS solves the coupled system correctly. Overall, the verification results between ARTS and STARS are reasonable and it shows the validity of ARTS in solving the coupled system. After a series of case studies from 1-D, 2-D, and benchmark, the conclusion can be drawn that ARTS solves the governing equations of the coupled system correctly. This is a remarkable result and shows that ARTS can be applied to solve real field problems. In order to verify and validate ARTS in a more rigorous way, validation with field data is needed.

INTEGRATED MODELING OF NATURAL AND HYDRAULIC FRACTURES

3-DEC (3-Dimensional Distinct Element Code), developed by Itasca Consulting Group (3-DEC, 2010), was used for simulations of hydraulic fracturing. This numerical tool can perform three dimensional, hydromechanical analyses of soil and rock that are subjected to static or dynamic loading. It can also model fluid flow through fractured impermeable rock bodies. The methodology adopted here is based on the following assumptions:

Fracture propagation does not occur into the matrix. Extensive pre-existing fractures are initially water saturated and will further open up due to fluid pressurization.

- Single-phase fluid flow is modeled.
- The rock matrix in 3-DEC is impermeable. The permeability of the rock matrix was represented by artificially imposing fluid loss within fractured internal domain. The surrounding domain deformed only.
- Total fluid loss due to various physical processes is numerically represented by the so-called Carter's equation (3-DEC, 2010). This is done for computational expediency. The rate of fluid loss from the fracture due to filter-cake resistance is considered here. Other resistances to fluid loss due to compression of reservoir fluid, fracture-fluid invasion are similarly incorporated in the numerical coding scenarios.

The reservoir domain and pre-existing, vertical fractures in two directions were established using a representative discrete fracture network developed (discussed in detail previously). The naturally fractured domain is shown in Figure 6-1.

The properties for the fractured matrix and fluid are also specified. The model has dimensions of 800 m by 800 m by 100 m, consisting of an isotropic rock matrix with a bulk density of 128 lb/ft3. The bulk and shear moduli are 33.61 GPa (487,4723 psi) and 12.04 GPa (182,7477 psi), respectively. The interior of this overall domain (250 m by 250 m by 40 m) is where the fractured volume is simulated. Dimensions of the reservoir are relatively large so that boundary effects are negligible. The normal and shear stiffness for the joints were calculated as given below.

$$k = \frac{M_i M_m}{L(M_i - M_m)}$$

where M represents rock modulus (in tension/compression or shear), L is the mean fracture spacing, and subscripts 'i' and 'm' represents intact and porous rock matrix. A pre-injection initial aperture of 0.1 mm is used for all fractures in these calculations. Far-field in plane stresses of σxx = 37.71 MPa (5469 psi) and σyy = 32.41 MPa (4700 psi) were imposed with a corresponding vertical stress of σzz = 46.21MPa (6702 psi). The treating fluid was assumed to be a water-based formulation with a density of 66 lb/ft3. The natural fractures were assumed to be initially water saturated, at a reservoir pore pressure of 2800 psi.

Injection Calculations

Since there is no complete analytical theory to estimate rate of fluid loss for such a complex fractured domain, numerical calculations were carried out to evaluate the effect of injection hydraulic fracturing treatment on this fractured reservoir. The parameters considered were pumping rate, fluid viscosity and pumping schedule.

Effect of injection rate

Fluid with a Newtonian viscosity of 1 cP was injected at three different rates for a relatively short time, 30 min. The pumping rates used were 25, 50 and 75 bpm. A fluid loss coefficient of 0.001 ft/√min was used to represent the fluid loss from the fractures. Figure 6-2 shows fluid pressure evolution in the fractures for a pumping rate of 50 bpm. Figure 6-3 shows the bottom-hole injection pressure, clearly demonstrating an increase in the injection pressure of 50% when the pumping rate is doubled. This is analogous to rate effects in a single planar fracture with finite initial hydraulic aperture. The low injection rate was characterized by fractures taking fluid at pressures below the normal stress acting on them.

Effect of fluid viscosity

Similarly, increase in the fluid pressures was observed when fluid with a higher viscosity was injected into the fractured domain. Figure 6-4 shows the evolution of aperture for pumping a fluid with a viscosity of 2 cp at an injection rate of 50 bpm. Higher shear resistance for fluid flow gives rise to higher pore pressures (Figure 6-5). Despite the short scale of the model run, the results seen in Figure 6-5 suggest the potential of the viscosity of the injected fluid to change the morphology of the created fracture systems. Higher viscosity characteristically leads to more tightly aligned fracture propagation trends.

Effect of fluid loss

The effect of fluid loss on aperture evolution was deduced by varying the leakoff coefficient, as seen from the snapshots shown in Figure 6-6. Figure 6-7 presents a comparison of injection pressures with various fluid-loss coefficients. Figure 6-8 describes a scenario where fluid was pumped for 20 min and then shut-in; fluid loss led to the post-shut-in pressure decline.

Soft Coupling

A soft-coupling scheme is created to extend the capability of ARTS in working with other geomechanical simulators. In this research, 3-DEC (Itasca, Inc.) is used as the external geomechanical simulator for obtaining geomechanical properties, then all these properties are passed to ARTS to perform reservoir simulation. In this way, the geomechanical effect is integrated in the flow simulation, and the work flow of this particular scheme is shown in Figure 6-9. In this application, the geometry of the reservoir and fractures comes from real field data with some simplifications. Initially, thousands of natural fractures were generated, but only 16 major fractures are considered in this case. Figure 6-9 also shows the geometry of the reservoir. The geometry was a simplified version of the DFN network generated using geologic inputs. Some of the major properties are listed in Table 6-1. The reservoir geometry and fracture location in the ARTS simulation are the same as those in 3-DEC simulation, and this guarantees

the consistency of the geomechanical properties between these two simulators. Three sets of simulations are studied based on the geomechanical information provided by 3-DEC. The first simulation is performed without geomechanical coupling (no coupling). The second simulation (coupled case 1) is performed with identical look-up table input information based on the major fracture's aperture change from 3-DEC. The third simulation (coupled case 2) is performed with various look-up tables for individual fracture sets. The first simulation is designed as a reference case study, and the second simulation is designed to be the upper limit of the geomechanical impact as the geomechanical information from the fracture with the largest aperture change is used. The third simulation is set up to reflect the reality of the 3-DEC simulation.

In Figure 6-10, the gas pressure and saturation distributions are displayed in a x-y plane view (no coupling). The impact of the fracture network is seen in the results as the gas transport mainly happens near the fracture, and the fractures in the far field are not fully activated because the pressure depletion in that area is relatively small.

Figure 6-11 illustrates the gas pressure and saturation for the case (coupled case 1) in which a uniform table input is used. When comparing these figures with Figure 6-10, we can see the gas pressure depletion is faster and reaches more area in the reservoir if geomechanics is considered. This results in production increases of 10-15%. From the comparison of the pressure and saturation distribution, we can see that the geomechanical effect is an important factor for predicting production in the reservoir system with low permeability.

In this particular case, the major conductivity path for the gas flow is the fractures, which have been modeled dynamically by using the input from 3-DEC. The apertures of fractures are increasing due to the injection of hydraulic fracturing fluid in the geomechanical simulator (3-DEC), and this information is integrated in the ARTS simulation by adjusting the fracture permeability. A uniform table that comes from the fracture that has the largest aperture (near the injection location in 3-DEC) is applied to the whole reservoir. This brings about a significant change to the reservoir simulation, as evidenced in the gas pressure and saturation distributions. Overall, the geomechanical effect results in enhanced permeability causing higher production.

Figure 6-12 shows the gas pressure and saturation distributions for coupled case 2. In this case, various geomechanical inputs are applied to different fractures in the reservoir. In the 3-DEC simulation, fractures have diverse apertures and some of the fractures in the far field have much less aperture than the ma jor fractures near injection locations. These heterogeneous properties have been fully integrated in ARTS simulation in this case study. The gas flow is also enhanced as a result of geomechanical effect, but the enhancement is at a lower magnitude compared with coupled case 1. The less activated fractures in left corner of the reservoir (x-y plane view) are clearly shown in the gas-pressure depletion figures. In the heterogeneous set studied, increase in permeability in some fractures is negated by decrease in permeability in others. A complex set of fractures with a distribution of permeabilities and apertures smears out the geomechanical effect.

Figure 6-13 shows the comparisons of cumulative gas production for these three case studies. Coupled case 1 has the largest cumulative rate, which is almost 25% more than the case without

geomechanical coupling. The gas production from coupled case 2 is less than coupled case 1, but is still about 7% more than the case without geomechanical coupling. The instantaneous rate shows the same trend, and it also shows the well-control method changing as a result of the smart well-control module designed in ARTS.

In this application, the geomechanical effect is a key factor. Enhancement of gas production is observed from the comparisons of the three case studies. We can conclude that the increased permeability in the fractures is important for gas production, but this effect may differ as fractures have different mechanical responses to the hydraulic fracturing process. Overall, soft coupling is a powerful tool, which has almost the same computational cost as a conventional reservoir simulation. Furthermore, the effect of proppant can be simulated by using the soft coupling scheme. If we have knowledge of where the proppant goes, the fracture containing the proppant can be assumed to have some minimal permeability, which is implemented in the look-up table in ARTS. In this way, the reservoir simulation would reflect the impact of proppant. A demonstration case study of this kind of application is discussed later.

Effect of Proppant

In order to show the impact of proppant, another case study is performed with the soft-coupling scheme. The same fluid properties and geometry information are used as the previous application, but the number of fractures and the well-control method are changed. The properties and parameters used in this case study are summarized in Table 6-2.

Figure 6-14 illustrates the effect of proppant on the gas production; we can see that production declines slowly when the proppant exists in certain fractures. Production rate comparison is shown in Figure 6-15. The two major fractures with proppant can be identified from the comparison in Figure 6-14. This case study clearly shows the effect of proppant and the potential capability of the soft-coupling scheme.

In summary, the soft-coupling scheme is applied to a series of case studies to understand the geomechanical effect in the reservoir simulation. This coupling scheme is a powerful tool with a good computing speed. However, it is still an approximation of the geomechanical effect, and the decoupled approach may not be appropriate in certain conditions. As a result, the hard-coupling scheme was developed in ARTS, and some of the applications using that method are discussed in the following sections.

One more example of soft coupling

Modeling hydraulic fractures has its roots in semi-analytical calculations that simplified the fracturing system to a planar feature propagating symmetrically away from a line source of injection. These are summarized and manipulated in numerous publications (for example, Economides and Nolte, 1989). Frictional pressure losses in the planar fracture were coupled with basic fracture mechanics considerations to allow a rational method for propagation in relatively stiff, brittle materials. With time, geometrical predictions were supplemented with one- and two-dimensional mass balance corrections associated with fluid loss, and were pseudo-analytically or numerically allowed to grow vertically in the same plane.

It has progressively become more accepted that fracture growth, particularly in extremely low permeability, naturally fractured reservoirs cannot be reliably represented by such conventional planar simulations. Pressure-dependent leakoff and complexities in fracture geometry were suggested by Nolte and Smith (1981) and Perkins and Gonzalez (1985), among many others. Microseismic signal acquisition has since convinced many that the fracture network complexity can be substantial (for example, Warpinski, 2009). There have been various attempts in the last few decades to numerically represent the complicated network of fractures that exist/dominate in certain situations. The earliest attempts were made in the middle 1980s, in response to minebacks (Curran and Vandamme, 1984; Jeffrey et al., 1987; Vandamme et al., 1988) using finite element or discrete element simulations.

Minebacks and anomalous treating pressures in coalbed methane treatments suggested fracture complexity – at least T-shaped situations. Some realistic efforts have been made to represent these. Jeffrey et al. (1998), presented a new hydraulic fracture design model that included pressure-dependent nonlinear leakoff, multiple interacting fractures, and failure in the coal near a "parent" fracture plane, as a result of changes in effective stress.

Some time ago, investigators reported that supplementary fracturing could also occur. As early as 1981, Smith and Nolte described supplementary fracture complexity and predisposed the industry to later quantification of pressure-dependent leakoff. Two decades later, alternative methods and computational capability were starting to allow fabric-impacted hydraulic systems to be represented. Fabric is taken to encompass discontinuities; including faults, fractures, lithologic boundaries, etc. Bruno (2001) used discrete particle models, which explicitly simulate interparticle mechanical interaction to represent fracturing in a weakly cemented medium. Bruno demonstrated a multiplicity of fractures and dilation during slurry injection. On another front, the enhanced geothermal systems (EGS) momentum in Australia also led to fracture simulation developments. Hossain et al. (2002) described a model that stochastically simulates field-representative natural fractures that regulate hydraulic fracturing in low-permeability environments. Deformation of these fractures was formulated as functions of fluid pressure inside the fractures and the in-situ stresses. The permeability enhancement and reservoir-growth pattern are then formulated as functions of fracture deformations. Koutsabeloulis and Zhang (2009) described finite-element approaches. There have also been renewed efforts to build on decades-old inferences and to numerically appreciate hydraulic-fracture behavior proximal to natural fractures and interfaces (de Pater, 2005; Jeffrey et al., 2009).

An increasingly important segment of the industry is currently stimulating naturally fractured formations (e.g. tight sands and shales); where the assumptions of linear elasticity, simple fluid leakoff, and planar geometry fail to hold. Furthermore, the physics of the interaction between the hydraulically induced fracture(s) and the natural fractures in the rock is often disregarded. Finding modeling alternatives is relevant for economically producing these naturally fractured reservoirs

This section describes a workflow, methodology and simulation techniques for representing the existing complex fracture network, and predicting growths of both existing and hydraulically induced fractures, and associated production. There are three stages in this protocol. The first

is a representation of the fracture networks. The second is importing this DFN into a coupled geomechanical simulator and representation of fracture evolution. The final step is importing this resultant conductive system into a multiphase DFN reservoir simulator for the prediction of production rates and the generation of pressure and saturation maps. These stages and a practical demonstration of our workflow are presented next.

Representation of Reservoir Fabric

Characterizing the evolution of multiple, non-planar, interconnected and possibly non-vertical hydraulic fractures requires hydraulic and mechanical characterization of the nominally intact matrix as well as existing latent or healed fracture networks. One starts by developing a static model. This incorporates devising the conceptual basis, mathematical description and numerical implementation of a model that describes the geometry, flow, storage and geomechanical properties of the natural fractures and faults in the target reservoir formations. Such a model is developed from outcrop studies, subsurface data, and well-testing information, and is periodically subjected to various confidence-building and validation exercises. Some of the required properties, including aperture, infill, and strength properties, and abutting relationships and fracture dimensions (lengths and unstressed apertures) are difficult to obtain from subsurface data alone. Field work can characterize discontinuities in the target formations and produce data on the number and chronology of fracture sets, the mechanical stratigraphy/fracture facies description, lateral variability of fracture intensity, potential of larger joints and faults to vertically connect mechanical layers, height/length distribution of natural fractures, and possible geologic causes of fracturing.

In addition to traditional field site analyses, newer methods such as ground-based laser mapping (LiDAR) can elucidate fractured outcrops (Pollard et al., 2007). Available subsurface data is used to refine the static fracture model. Analyses of these data will produce additional constraints on the number of fracture sets, the orientation of the fractures in each set, both in different mechanical layers and laterally within layers. Additional refinement of the mechanical stratigraphy for stratigraphic units studied in outcrop and extension to other portions of the reservoir section (not available in outcrop exposures) can also be ascertained. The aperture distribution of fractures by set and mechanical layer, fracture surface morphology, mineral infill, and the relation of structural position and/or curvature to variations in fracture intensity and orientation should also be deduced.

Lastly, available suitable pressure transient analyses are used to determine the types of fracture network geometries, permeability structures and matrix properties required to match the transient response. Validation of this conceptual model through transient, well-scale DFN models can be used to derive fracture-flow parameters such as fracture permeability, flow aperture and fracture compressibility.

Hydraulic Fracturing

In ultra-low permeability scenarios where existing, latent or healed natural fractures, faults and other discontinuities (including lithologic boundaries) govern hydraulically related fracture morphology it is desirable to use the model of reservoir fabric and infer how complex, non-planar, hydraulic fracture growth will occur, to optimize stimulation and to provide direct input for a DFN reservoir simulation that will reliably represent the fracture system.

The approach is to carry out a hydraulic fracturing simulation that:

- Combines inputs such as complex geologic features, including natural and incipient fractures, with conventionally accepted stress and mechanical properties data.
- Simulates coupled geomechanical growth of a non-planar fracture system during hydraulic fracturing.
- Passes results to a reservoir simulation methodology that can account for production through natural and hydraulically induced or enhanced fractures.

The total fracture system (conductive natural and hydraulically induced) will be represented as a modification of the original system, and these will both be exported to the reservoir simulator. The reservoir simulations will represent the actual complex fracture network. The hydraulic fracturing simulator, 3-DEC (Cundall, 1990; Cundall and Hart, 1993), is a numerical modeling code for advanced geotechnical analysis of soil, rock, and structural support in three dimensions. The code simulates the response of discontinuous media (such as jointed and fractured rock) that are subject to either static or dynamic loading. It is used to model fluid flow through the fractures of a system of impermeable blocks. A fully coupled mechanical-hydraulic analysis is performed, in which fracture conductivity is dependent on mechanical deformation and, in return in-fracture pressure affects the mechanical computations.

This is a weakly coupled system. This means:

1. Fracture and reservoir information are imported into a third-party simulator such as 3-DEC.
2. A simulated fracture treatment is pumped. Pressure and fracture characteristics are recorded from the simulations in the adopted model.
3. This information is fed into a DFN reservoir simulator – natural fracture geometries, induced fracture geometries, fracture apertures, formation pressures.
4. Ultimately there could be incremental feedback to the fracture simulator to account for pressure dependent permeability (permeability as a function of fracture aperture).

This is an off-the-shelf numerical hydraulic fracturing simulation. There are advantages and disadvantages associated with these simulations. Some advantages are:

- Multiple lithologies can be represented
- Multiple fractures with any dip or dip direction and with various native apertures, infill and strength can be simulated.
- Fluid pressure in the fractures is coupled with the aperture of the fractures and the deformability of the matrix.

There are however some challenges with the off-the-shelf code that mandate creativity:

- The matrix is impermeable. Consequently, to represent fluid loss an artifact was introduced into the model. This was a very stiff, horizontal plane with a finite aperture that took fluid as a proxy for fluid loss. It extended across the entire domain. The high stiffness mitigated vertical load increase but muted the degree of pressure dependency. Fracture propagation will not occur into the matrix. This can be overcome by very fine gridding, by remeshing as appropriate or by prescribing latent fracture systems. The later approach is the most easily implemented. Extensive (long) preexisting fractures are specified, but they are "sewn shut." This means that the pre-existing features are prescribed in segments and the segments are initially specified as non-conductive and will open up according to a propagation criterion when an adjacent segment is pressurized.
- Constant height modeling is assumed in this demonstration.
- Single-phase flow only is afforded. Otherwise, geomechanically coupled hydraulic fracturing and production simulation could conceivably be done from this one commercial platform.
- Currently, only neat fluids can be injected.
- Computational times are significant.

Representation of Production into the Fracture Network

The control volume finite element method (CVFE) is used to represent complex, irregular domains and complicated fracture networks (Fu et al., 2005). In this method, fractures are discretely represented (Kim and Deo, 1999; Yang and Deo, 2001). Fundamental aspects of fracture flow mechanics, such as imbibition, water bypassing, etc. are more easily examined using these simulators. Capillary pressure functions in matrix and fractures are very important in determining recovery behavior, and with the model different combinations of capillary pressures in matrix and fractures can be examined.

A realistic fracture network was used to demonstrate the utility of modeling protocol. A variety of different initial stress conditions and treatments were simulated. The objective of this modeling included:

1. Assessing the effects that operational parameters (such as injection rate and treating fluid viscosity) have on the volumetric extent of the fracture system or domain and the extent of fluid penetration in the natural fractures; and

2. Using DFN reservoir simulation to appreciate the degree of water blocking and loss of conductivity in the fracture system.

Both of these issues are crucial for treatments in shale-gas systems.

The team characterized a portion of the GNB field in Utah as described earlier. For illustrative purposes, simplifications have been made in the simulations. A reservoir domain was established, and vertical fractures in two orthogonal directions were assumed. The fractured domain is shown in Figure 6-16. The basic reservoir and fracture properties are also specified. These were as follows.

Dimensions (x, y, z) of 805m by 800m by 100m, the center of which (321m by 294m by 40m) is where the fracture system is stimulated. Dimensions for the reservoir and simulation area are by necessity relatively large so that boundary effect is negligible, and there is enough pore volume for fluid flow. As mentioned in the previous section, flow into an artificial fracture was used to mimic imbibition by the matrix.

A fluid density of 1000 kg/m3 was used. It was assumed that the natural fractures were initially water saturated. It is recognized that this is a limitation of this particular model. The treating fluid was assumed to be a low-viscosity, water-based formulation, slickwater or similar.

A fluid viscosity of 1 cP was selected, as discussed above. The bulk density was 2000 kg/m3 (125 lb/ft3). This is the bulk density assumed for the matrix material. The matrix is deformable.

The bulk modulus was 1.378 x 109 Pa (199,862 psi), and the shear modulus was 0.827 x 109 Pa (120,062 psi). It can be inferred from Young's modulus and Poisson's ratio. Isotropy was assumed in this simulation.

Fractures normal stiffness was 1 x 109 Pa (145,037 psi). The transformational consideration for many is that it is necessary to prescribe mechanical properties for fractures and joints that exist in-situ., recognizing that these are deformable during injection and during production. The normal stiffness of a fracture or a joint is given by (Barton, 1972):

$$k_n = \frac{E_i E_m}{L(E_i - E_m)}$$

where Ei is the intact rock modulus, Em is the rock mass modulus, and L is the mean fracture or joint spacing. Infill characteristics can alternatively be used to infer stiffness.

Fractures shear stiffness was 1 x 109 Pa (145,037 psi). For shear stiffness, with G indicating shear modulus, the analogous relationship is:

$$k_s = \frac{G_i G_m}{L(G_i - G_m)}$$

Fracture initial aperture was 1 x 10-4 m. The initial aperture (pre-stimulation) is approximated. One can imagine the difficulty in inferring this and the two preceding properties. The civil engineering community (Barton, 1972) has been considering mechanical properties of weaknesses for some time.

Far-field stresses were sx=s2=37 MPa (5366 psi); sy=s3=32.41 MPa (4700 psi); sz=s1=46.21 MPa (6702 psi).

The Initial reservoir pore pressure was 2800 psi.

Strength (tensile and shear) properties are also provided for the intact rock and for the fractures/ joints.

The Hydraulic Fracturing

Two treatments were simulated. A treating fluid with a Newtonian viscosity of 1 cP was injected at two different rates. Only a relatively small treatment was pumped (40 minutes). The treatment rates used in the two scenarios considered were 0.264 m3/minute (9.33 ft3/min), and 0.528 m3/minute (18.66 ft3/min) respectively.

Figure 6-17 shows snapshots of aperture evolution for the situation with a treatment rate of 0.264 m3/minute (9.33 ft3/min). Figure 6-18 shows the final geometries for one of the simulations – geometries imported to a DFN reservoir simulator. The pore pressure distribution profile is shown in Figure 6-19, clearly affected by the presence of the fracture network. Moreover, the fracture aperture of the whole network is found to be dependent on the injection treatment rate. When the rate is doubled in the second scenario, the final fracture aperture increases from 30%-50% at the point of maximum aperture to 3 to 10 times at the fracture tips (Figure 6-20).

Other parameters being considered in the simulations include relative geometry, the viscosity of the treating fluid, the stress field and mechanical formation properties.

Production Modeling

The domain shown in Figure 6-18 was input into the multiphase DNF simulator at the University of Utah. The matrix permeability was assumed to be 0.001 md. A two-phase simulation for a period of 100 days was performed. The gas saturation profiles after 100 days are shown in Figure 6-21. It is seen that the area of the reservoir with large aperture fractures in Figure 6-18 (pink) is drained effectively, while rest of the reservoir still holds significant amount of gas.

Water Blocking and Conductivity

In tight gas and shale reservoirs, production after hydraulic fracturing is often greatly impaired, by invasion of fracturing fluid into the matrix and fractures and poor cleanup efficiency (Ghahri et al., 2009). Invasion of aqueous fracturing fluids can reduce the relative permeability to gas and cause a water block. High capillary pressure in low permeability reservoirs compounds cleanup difficulties. The hysteresis of gas and water relative permeabilities has a strong impact on the rate of water removal. Water displacement is hindered by a relative permeability hysteresis induced by the imbibition of the fracturing fluid. Sufficiently high pressure draw down is crucial to overcome capillary forces - the ratio of drawdown to capillary pressure has a significant effect on cleanup. Even at high drawdown, water removal is difficult and gas-return permeability reaches a plateau because of the very low relative permeability to water when the gas saturation increases. Water cannot be expelled even by maximizing the drawdown (Bazin et al., 2009).

Treating fluids are quickly recovered during flowback if drawdown greatly exceeds the capillary forces. In depleted and/or heterogeneous, low-permeability reservoirs, this can be problematic, and cleanup is inefficient and/or prolonged (Parekh and Sharma, 2004). They observed that Holditch (Holditch, 1979) accounted for capillary pressure and relative permeability in his numerical study of formation damage around a hydraulic fracture in a tight-gas reservoir. Results presented in the study show that reservoir properties such as capillary pressure and relative permeability in low-permeability reservoirs are important in determining the behavior of a fractured well during cleanup. He also observed that the damaged-zone permeability must be reduced by several orders of magnitude before a serious water block to gas flow will occur. "Even if the reservoir rock permeability is not reduced, gas production can be severely curtailed if the pressure drawdown does not exceed the formation capillary pressure."

To test this concept, a smaller domain with similar properties was simulated in the multiphase simulator. Preliminary results with this simple domain are shown in Figure 6-22. As water fills the fractures the gas remains locked out of the flow channels.

Conclusions Concerning Soft Coupling

1. A workflow for realistic modeling of complex fractures is provided – simulating the creation of and production from multiple fractures.

2. The impact of water block is illustrated.

3. Shear displacements were recorded at fracture intersections. From a theoretical point of view this is reassuring, justifying why microseismic activity is seen even in situations where the natural fractures are parallel to the principal stresses.

4. Post-shut-in fracture extension (contact with injected fluid) is anticipated to be relatively large in situations where there are pre-existing fractures, since fracture flow is anticipated in conductive, non-zero apertures, as long as there is a pressure gradient (irrespective of closure stress).

5. Additional simulations, or site specific simulations, can be used to calibrate Diagnostic Fracture Injection Test DFIT signatures.

Realistic Discrete Fracture Networks

In previous case studies, the fracture network in the reservoir is relatively simple. However, the real reservoir is always assumed to have complex fracture networks, and the impact of geomechanical coupling in those systems is an interesting problem. The goal of this case study is to show the capability of ARTS in simulating complex fracture networks with coupled geomechanics, and some preliminary conclusions of the geomechanical effect in a reservoir with complex fracture networks are drawn. In this case study, a reservoir model, which has 44 fractures with different dip angles, is created, the basic geometry of the fractured reservoir is shown in Figure 6-23.

As shown in Figure 6-23, the fractures existing in the reservoir are highly connected. This means that more areas with higher permeability exist in the reservoir, and it will have a significant impact on the coupled simulation. The reservoir is assumed to have water and gas in place initially. Some important properties used in this case study are listed in Table 6-3. The matrix permeability is extremely low (0.00001 md), and the fractures have much higher permeability (100 md). Nine production wells are located at the top of the reservoir, and the production continues for 3000 days.

Two sets of simulations are performed. The first simulation is coupled with geomechanics, and the second is not. The results from these two simulations are compared to see the geomechanical effect. As we seen in the previous case studies, a positive geomechanical effect is expected in this case study. However, the highly connected fracture networks may change the characteristics of geomechanical coupling. For example, one possible reason for the increasing pressure seen in previous case studies is the relatively low permeability and limited fracture area in the reservoir. This is not valid due to the highly connected fracture networks, and the area of fractures may be large enough to make the reservoir more permeable overall. Furthermore, the geomechanical coupling in these types of reservoirs add another level of heterogeneity to a heterogeneous system. This makes the system behavior even harder to predict. This case study is an excellent showcase for evaluating the advantage of ARTS in modeling complex fracture network with geomechanical coupling, and we expect a fundamentally different result compared with previous cases.

Figure 6-24 displays the gas pressures and saturation distributions at 2800 days after production (coupled geomechanics) in a x-y plane view. The gas pressure and saturation for the uncoupled case is almost the same compared with the coupled case. In order to illustrate the pressure difference between uncoupled and coupled simulations clearly, the variation of average reservoir pressure is shown in Figure 6.-25. The pressure differences shown in the result are relatively small, and have both positive and negative values. This is totally different from the results previous case studies, and a similar production is expected for these two cases. Figure 6.26 shows the cumulative gas production for coupled and uncoupled cases. The comparisons of average pressure and cumulative production also illustrate the heterogeneity in the system as the differences observed have both positive and negative values.

The difference between the initial and the final permeabilities at 2800 days is shown in Figure 6.27. Once again, over the entire domain, the differences in permeabilities, both plus and minus are only about two percentage points at most. The nature of the fracture system makes it so that the change is heterogeneous. The volumetric changes and displacements are shown in Figure 6.28. The greatest volumetric changes are at the edges of the reservoir, but because of the heterogeneous nature of the reservoir, the x and y displacements are uneven. In summary, this case study demonstrates the capability of ARTS in modeling complex fracture networks with coupled geomechanics. The geomechanical coupling brings heterogeneity to the reservoir system, and the combined effect of geomechanics and fracture networks governs the system. The geomechanical effect in a reservoir with complex fracture networks is fundamentally different from a normal reservoir.

Impact to Producers

Methods developed in this project would be applicable for the characterization of any fractures, leading to an improved understanding the morphology of the fractures created and simulation of multiphase flow through the combined network of natural and hydraulic fractures.

Technology Transfer Efforts

The University of Utah created a technology transfer plan, which included a website hosted at Utah Geological Survey (http://geology.utah.gov/emp/tightgas/). The Project Team made a number of presentations at RPSEA Forums and at national and international meetings, including the Utah Geological Survey (UGS) booth at the American Association of Petroleum Geologists (AAPG) Annual Convention in Houston, Texas (April 2011) and at the Rocky Mountain Section Meeting (RMS-AAPG) in Cheyenne, Wyoming (June 2011). Posters were presented by UGS at both the AAPG Annual Convention (Carney and others, 2011) and RMS-AAPG meeting (Carney and others, 2010). A poster was presented at the Rocky Mountain Section of the Geological Society of America in Logan, Utah (Laine and Dempster, 2011). The UGS along with the Research Partnership to Secure Energy for America (RPSEA) and the University of Utah sponsored a Petroleum Technology Transfer Council (PTTC) workshop titled "Shale-gas and tight-gas-sand reservoirs of Utah-Core workshop and field trip." The workshop included oral presentations by Craig Morgan (UGS), John McLennan U of U), and Paul LaPointe (Golder and Associates); and a poster presentation by Stephanie Carney (UGS) and a core display from the NBU 921-21L well.

BIBLIOGRAPHY

3-DEC 4.10. Theoretical Background, 2010, Itasca Incorporated.

Anadarko Petroleum Corporation. 2010. Anadarko Petroleum Corporation Investor Conference. www.anadarko.com/sitecollectiondocuments/investor%20 conferences/2010/2010i rconf.pdf

Anders, D.E., and Gerrild, P.M., 1984, Hydrocarbon generation in lacustrine rocks of Tertiary age, Uinta Basin, Utah—Organic carbon, pyrolysis yield, and light hydrocarbons. In: Woodward, Jane, Meissner, F.F., and Clayton, J.L. (eds.), Hydrocarbon Source rocks of the Greater Rocky Mountain Region, Rocky Mountain Association of Geologists, p. 513–529.

Anders, D.E., Palacas, J.G., and Johnson, R.C., 1992, Thermal maturity of rocks and hydrocarbon deposits, Uinta Basin, Utah. In: Fouch, T.D., Nuccio, V.F., and Chidsey, T.C., Jr. (eds.), Hydrocarbon and Mineral Resources of the Uinta Basin, Utah and Colorado, Utah Geological Association Publication 20, p. 53-76.

Anderson, P., 2005, Mesaverde Gas of Southeastern Utah. UGS Open File Report 460.

Aschoff, J.L., 2010, Preliminary Regional Sequence Stratigraphic Framework and Characterization of Potential Fluvial Reservoirs of the Upper Mesaverde Group, Uinta Basin, Utah. Utah Geologic Survey Open-File Report 569. http://geology.utah.gov/online/ ofr/ofr-569.pdf.

Bader, J.W., 2009, Structural and tectonic evolution of the Douglas Creek Arch, the Douglas Creek fault zone, and environs, northwestern Colorado and northeastern Utah: Implications for petroleum accumulation in the Piceance and Uinta basins. Rocky Mountain Geology, v. 44, no. 2, p. 121-145.

Balasubramanian, S., 2007, A Compositional Model For Fractured Reservoir Simulation, Ph.D. dissertation, University of Utah, 2007.

Barb, C.F., 1945, The origin of the hydrocarbons in the Uinta Basin. Mines Magazine, v. 35, no. 10, p. 555-557.

Barb, C.F., and Ball, J.O., 1944, Hydrocarbons of the Uinta Basin of Utah and Colorado. Colorado School Mines Quarterly, v. 39, no. 1, 115 p.

Bates, C.R., Lynn, H.B., and Simon, M., 1999, The study of a naturally fractured gas reservoir using seismic techniques. AAPG Bulletin, v. 83, no. 9, p. 1392–1407.

Boardman, C.R., and Knutson, C.F., 1980, Reservoir Characteristics in Uinta Basin Gas Wells. U.S. Department of Energy Report DOE/ET/11399-1, 89 p..

Bryant, Bruce, Naeser, C.W., Marvin, R.F., and Mehnert, H.H., 1989, Upper Cretaceous and Paleogene sedimentary rocks and isotopic ages of Paleogene tuffs, Uinta Basin, Utah. U.S. Geological Survey Bulletin 1787-J, 22 p.

Burchfiel, B.C., Cowan, D.S. & Davis, G. A. 1992. Tectonic overview of the Cordilleran orogen in the western United States: The Geology of North America. In: Burchfiel, B.C., Lipman, P.W., & Zoback, M.L. (eds) The Cordilleran Orogen: Conterminous U.S.

Geological Society of America. The Geology of North America, G-3, 407-480.

Bureau of Land Management. July 2010. Greater Natural Buttes Draft Environmental Impact Statement, DES 10-31.

Byrnes, A.P., Cluff, R.M., Webb, J.C., Krygowski, D.A., and Whittaker, S.D., 2009, Lithofacies and Petrophysical Properties of Mesaverde Tight-Gas Sandstones in Western U.S. Basins: A Short Course. 2009 AAPG Annual Convention, Short Course No. 1, June 6, 2009, Denver, Colorado, 222 p.

Carney, S. M., Morgan, C.D., Chidsey Jr., T.C. & Laine, M.D. 2011. Tight Gas Sands and Natural Fractures in the Cretaceous Mesaverde Group, Greater Natural Buttes Field, Uinta Basin, Utah. Abs. American Association of Petroleum Geologists Annual Conference, Houston, TX. http://geology.utah.gov/emp/tightgas/pdf/poster_aapg_2011.pdf

Catacosinos, P.A., 1968, Upper Cretaceous-lower Tertiary relations west of Raven Ridge, Uintah County, Utah. AAPG Bulletin, v. 52, no. 2, p. 343-348.

Cheng, H.D., Y. Abousleiman, E. Detournay, L. Cui, and J.C. Roegiers, 1996, Mandel's problem revisited, G´eotechnique, vol. 46, no. 2, pp. 187–195, 1996.

Chidsey, T.C., Jr., and Laine, M.D., 1992, The fractured Green River and Wasatch formations of the Uinta basin, Utah: Targets for horizontal drilling. In; Fouch, T.D., Nuccio, V.F., and Chidsey, T.C., Jr., (eds.), Hydrocarbon and Mineral Resources of the Uinta Basin, Utah and Colorado. Utah Geological Association Guidebook 20, p. 123-134.

Cole, R., Kirschbaum, M. and Young, R., 2005, Stratigraphy, sedimentology, and energy resources of Cretaceous rocks in the Book Cliffs area, Western Colorado and eastern Utah. In: Guidebook for the Rocky Mountain Section of the Geological Society of America Annual Meeting, Grand Junction Geological Society, 76 p.

Cole, R., 2008, Characterization of fluvial sand bodies in the Nelson and lower Sego Canyon, Utah. In: Longman, M.W. and C.D. Morgan (eds.) Hydrocarbons Systems and Production in the Uinta Basin, Utah. RMAG-UGA Publication 37 p. 81-100.

Condon, S.M. 2003. Fracture network of the Ferron Sandstone Member of the Mancos Shale, east-central Utah, USA. International Journal of Coal Geology, 56, 111-139.

Coussy, O., 2004, Poromechanics. John Wiley & Sons Ltd, 2004.

Christian, J. T. and J. W. Boehmer, 1970, Plane Strain Consolidation by Finite Elements, Journal of the Soil Mechanics and Foundations Division,, vol. 96, no. 4, 1970.

Cryer, C. W., 1963, A Comparison of the Three-Dimensional Consolidation Theories of Biot and Terzaghi, The Quarterly Journal of Mechanics and Applied Mathematics, vol. 16, no. 4, pp. 401–412, 1963.

Cui, L., A. H. D. Cheng, V. N. Kaliakin, Y. Abousleiman, and J.-C. Roegiers, 1996, Finite Element Analyses of Anisotropic Poroelasticity: A Generalized Madel's Problem and An Inclined Borehole Problem, International Journal for Numerical and Analytical Methods in Geomechanics, vol. 20, no. 6, pp. 381–401, 1996.

Cumella, S.P., and Scheevel, J., 2008, The influence of stratigraphy and rock mechanics on Mesaverde gas distribution, Piceance basin, Colorado. In: Cumella, S.P., Shanley, K.W., and Camp, W.K. (eds.) Understanding, Exploring, and Developing Tight-Gas Sands, AAPG Hedberg Series No. 3, pp. 147-155.

Currie, J.B., 1974, Study examines fracture porosity and permeability in stratigraphic traps. Oil and Gas Journal, 72, 178-181.

Cuzella, J.J., and Stancel, S.G., 2006, Greater Natural Buttes field, Uinta basin, Utah. 2006 Rocky Mountain Natural Gas Geology and Resources Conference, The Mountain Geologist, v. 43, p. 213-218.

Dennis, C., Bernard, T. and T. David, T., 2001, Coupled Hydro-Geomechanical Modelling of the Cold Production Process, presented at SPE International Thermal Operation and Heavy Oil Symposium, 2001.

Dickinson, W.R., Klute, M.A., Hayes, M.J., Janecke, S.U., Lundin, E.R., McKittrick, M.A. & Olivares, M.D. 1988. Paleogeographic and paleotectonic setting of Laramide sedimentary basins in the central Rocky Mountain region. Geological Society of America Bulletin, 100, 1023-1039.

Fisher, D.J., 1936, The Book Cliffs coal field in Emery and Grand Counties, Utah. USGS Bulletin 852, 104 p.

Fisher, D.J., Erdman, C.E., and Reside, J.B., Jr., 1960, Cretaceous and Tertiary formations of the Book Cliffs, Carbon, Emery, and Grand Counties, Utah and Garfield and Mesa Counties, Colorado. U.S. Geological Survey Professional Paper 332, p. 80.

Fisher, D.J., Erdmann, C.E., and Reeside, J.B., Jr., 1960, Cretaceous and Tertiary formations of the Book Cliffs, Carbon, Emery, and Grand counties, Utah, and Garfield and Mesa counties, Colorado. U.S. Geological Survey Professional Paper 332, 80 p.

Fouch, T.D., 1975, Lithofacies and related hydrocarbon accumulations in Tertiary strata of the western and central Uinta Basin, Utah. In: Bolyard, D.W. (ed.) Symposium on Deep Drilling Frontiers in the Central Rocky Mountains, Rocky Mountain Association of Geologists Special Publication, p. 163-173.

Fouch, T.D., 1981, Distribution of rock types, lithologic groups, and interpreted depositional environments for some lower Tertiary and Upper Cretaceous rocks from outcrops at Willow Creek-Indian Canyon through the subsurface of Duchesne and Altamont oil fields, southwest to north-central parts of the Uinta Basin, Utah. U.S. Geological Survey Oil and Gas Investigations Map, Chart OC-81, 2 sheets.

Fouch, T.D., 1985, Oil and gas-bearing upper Cretaceous and Paleogene fluvial rocks in central and northeast Utah. Society of Economic Paleontologists and Mineralogists Short Course Notes 19, p. 241-271.

Fouch, T.D., and Cashion, W.B., 1979, Preliminary chart showing distribution of rock types, lithologic groups, and depositional environments for some lower Tertiary, Upper and Lower Cretaceous, and Upper and Middle Jurassic rocks in the subsurface between Altamont oil field and San Arroyo gas field, north-central to southeastern Uinta Basin, Utah. U.S. Geological Survey Open-File Report 79-365, 2 sheets.

Fouch, T.D., Lawton, T.F., Nichols, D.J., Cashion, W.B., and Cobban, W.A. 1983. Patterns and timing of synorogenic sedimentation in Upper Cretaceous rocks of central and northeast Utah. In: Dolly, E.D., and Reynolds, M.W. (eds.) Mesozoic Paleogeography of West-central United States. Rocky Mountain Section SEPM Symposium 2, p. 305-336.

Fouch, T.D., Nuccio, V.F., Osmond, J.C., MacMillan, L., Cashion, W.B., and Wandrey, C.G., 1992, Oil and gas in uppermost Cretaceous and Tertiary rock, Uinta basin, Utah. In: Fouch, T.D., Nuccio, V.F., and Chidsey, T.C. (eds.), Hydrocarbon and Mineral Resources of the Uinta Basin, Utah and Colorado. Utah Geological Association Guidebook 20, p. 9-47.

Fouch, T.D., Wandrey, C.J., Pitman, J.K., Nuccio, V.F., Schmoker, J.W., Rice, D.D., Johnson, R.C., and Dolton, G.L., 1992, Natural gas accumulations in low-permeability Tertiary, and Cretaceous (Campanian and Maastrichtian) rock, Uinta Basin, Utah. Final Report to the U.S. Department of Energy NTIS no. DE92001132, 81 p.

Franczyk, K.J., 1991, Stratigraphic and time-stratigraphic cross sections of Phanerozoic rocks along line C-C′, Uinta and Piceance Basin area, southern Uinta Mountains to northern Henry Mountains, Utah. U.S. Geological Survey Miscellaneous Investigations Series Map I-2184-C, 2 sheets, scale 1:500,000.

Franczyk, K.J., Pitman, J.K., and Nichols, D.J., 1990, Sedimentology, mineralogy, palynology, and depositional history of some uppermost Cretaceous and lowermost Tertiary rocks along the Utah Book and Roan Cliffs east of Green River. U.S. Geological Survey Bulletin, 1787-N, 27 p., 16 figs., 3 plates.

Franczyk, K.J., Fouch, T.D., Johnson, R.C., Molenaar, C.M., and Cobban, W.A., 1992, Cretaceous and Tertiary paleogeographic reconstructions for the Uinta-Piceance Basin study area, Colorado and Utah. U.S. Geological Survey Bulletin 1787-Q, 37 p.

Franczyk, K.J., Pitman, J.K., Cashion, W.B., Dyni, J.R., Fouch, T.D., Johnson, R.C., Chan, M.A., Donnell, J.R., Lawton, T.F., and Remy, R.R., 1989, Evolution of resource-rich foreland and intramontane basins in eastern Utah and western Colorado. In: Hanshaw, P.M. (ed.) 28th International Geological Congress Field Trip Guidebook T324, American Geophysical Union, 53 p.

Fu, Y., 2007, Multiphase Control Volume Finite Element Simulation of Fractured Reservoirs, Ph.D. dissertation, University of Utah, 2007.

Fu, Y. Yang, Y.K.., and Deo, M.D., 2005, Three-Dimensional, Three-Phase Discrete-Fracture Reservoir Simulator Based on Control Volume Finite Element (CVFE) Formulation, presented at SPE Reservoir Simulation Symposium, 2005.

Gibson, R.E., Gobert, A. and Schiffman, R.L., 1989, On Cryer's Problem with Large Displacements, International Journal for Numerical and Analytical Methods in Geomechanics, vol. 13, no. 3, pp. 251–262, 1989.

Gu, Z., 2010, A Geochemical Compositional Simulator for Modeling C O2 Sequestration in Geological Formations, Ph.D. dissertation, University of Utah, 2010.

Guiseppe, A.C., and Heller, P.A., 1998, Long term river response to regional doming in the Price River Formation, central Utah. Geology, v. 26, p. 239-242.

Guiterrez, G. (2007) Analysis of Faults and Fractures, and Their Impact on a Tight Gas Sand Resource Play in the Uinta Basin. M.S. thesis, Colorado School of Mine, Golden, Colorado, 174 p.

Gualtieri, J.L. 1988. Geologic Map of the Westwater 30′ x 60′ Quadrangle Grand and Uintah Counties Utah and Garfield and Mesa Counties Colorado. USGS Map I-1765.

Haneburg, W.C., 2008. Using close range terrestrial digital photgrammetry for 3-D rock slope modeling and discontinuity mapping in the United States. Bulletin of Engineering Geology and the Environment, 67, 457-469.

Huang, C.K., 2009, Development of A General Thermal Oil Reservoir Simulator Under A Modularized Framework," Ph.D. dissertation, University of Utah, 2009.

Jaeger, J.C., Cook, N.G.W., and Zimmerman, R.W., 2007, Fundamentals of Rock Mechanics, 4th ed. Blackwell, 2007.

Johnson, R.C., and Rice, D.D., 1990, Occurrence and geochemistry of natural gases, Piceance basin, northeast Colorado. AAPG Bulletin, v. 74, no. 6, p. 805-829.

Johnson, R.C., Rice, D.D., and Fouch, T.D., 1994, Evidence for gas migration from Cretaceous basin-centered accumulations into lower Tertiary reservoirs in Rocky Mountain basins. Rocky Mountain Association of Geologists and Colorado Oil and Gas Association First Biennial Conference, Oct. 17–18, 1994, Natural Gas in the Western United States Proceedings.

Johnson, R.C., and Roberts, S.B., 2003, The Mesaverde total petroleum system, Uinta- Piceance Province, Utah and Colorado, Chapter 7. In: Petroleum systems and geologic assessment of oil and gas in the Uinta-Piceance Province, Utah and Colorado. USGS Uinta-Piceance Assessment Team, compilers: U.S. Geological Survey Digital Data Series DDS-69-B, Version 1.0, 68 p. [CD-ROM]. http://pubs.usgs.gov/dds/dds-069/dds-069-b/REPORTS/Chapter_7.pdf

Kim, J., 1997, Numerical Simulation of the Noordbergum Effect Resulting from Ground- water Pumping in a Layered Aquifer System, Journal of Hydrology, vol. 202, no. 1-4, pp. 231–243, 1997.

La Pointe, P.R., and Hudson, J.A., 1985, Characterization and interpretation of rock mass joint patterns. Geological Society of America Special Paper, 199, no. 31.

Laubach, S. E., Olson, J. E. & Gross, M. R. 2009. Mechanical and fracture stratigraphy. American Association of Petroleum Geologists Bulletin, 93, no. 11, 1413-1426.

Lawton, T.F., 1986, Fluvial systems of the Upper Cretaceous Mesaverde Group and Paleocene North Horn Formation, central Utah—A record of transition from thin-skinned to thick-skinned deformation in the foreland region. In: Peterson, J. A. (ed.), Paleotectonics and Sedimentation in the Rocky Mountain Region, United States. AAPG Memoir 41, p. 423–442.

Longman, M., and Koepsell, R., 2005, Defining and Characterizing Mesaverde and Mancos Sandstone Reservoirs Based on Interpretation of Formation MicroImager (FMI) Logs, Eastern Uinta Basin, Utah. Kerr McGee, EOG Resources, Questar, and

Schlumberger Corporations (Colorado) contributed to the project. UGS Open-File Report 458, 122p.

Lorenz, J.C., 1994, Subsurface fracture spacing - comparison of inferences from slant/horizontal and vertical cores. Society of Petroleum Engineers Formation Evaluation, v. 9, no. 1, p. 66-72.

Lorenz, J.C. & Finley, S.J. 1991. Regional Fractures II: Fracturing of Mesaverde Reservoirs in the Piceance Basin, Colorado. American Association of Petroleum Geologists Bulletin, 75, 1738-1757.

Mandel, J., 1953, Consolidation Des Sols (E´ tude Math´ematique), G´eotechnique, vol. 3, no. 7, pp. 287–299, 1953.

McKinley, J., 1998, Coupled Consolidation of a Solid, Infinite Cylinder using a Terzaghi Formulation, Computers and Geotechnics, vol. 23, pp. 193–204, 1998.

Narr, W.N., 1977, The origin of fractures in Tertiary strata of the Altamont field, Uinta Basin, Utah. M.S. University of Toronto, 132 p.

Narr, W.N., and Currie, J.B., 1982, Origin of fracture porosity - example from Altamont field, Utah. AAPG Bulletin, v. 66, no. 9, p. 1231-1247.

Narr, W., Schechter, D.W. & Thompson, L.B. 2006. Naturally Fractured Reservoir Characterization. Society of Petroleum Engineers, Houston, TX.

Nelson, R.A. 2001. Geological Analysis of Naturally Fractured Reservoirs, 2nd edition. Gulf Publishing Co., Houston, TX.

Nguyen V. K. and Y. N. Abousleiman, 2010, Poromechanics Solutions to Plane Strain and Axisymmetric Mandel-Type Problems in Dual-Porosity and Dual-Permeability Medium, Journal of Applied Mechanics, vol. 77, no. 1, 2010.

Nuccio, V.F. and Fouch, T.D., 1992, Thermal maturity of the Mesaverde Group, Uinta Basin, Utah. In: Magoon, L.B. (ed.) The Petroleum System- Status of Research and Methods 1992. U.S. Geological Survey Bulletin 2007, p. 70-78.

Nuccio, V.F., and Johnson, R.C., 1986, Thermal maturity map of the lower part of the Upper Cretaceous Mesaverde Group, Uinta Basin, Utah. U.S. Geological Survey Miscellaneous Field Studies Map MF-1842, one plate.

Nuccio, V.F., and Roberts, L.N.R., 2003, Thermal maturity and oil and gas generation history of petroleum systems in the Uinta-Piceance province, Utah and Colorado. Chapter 4 of Petroleum Systems and Geologic Assessment of Oil and Gas in the Uinta-Piceance Province, Utah and Colorado. U.S. Geological Survey Digital Data Series DDS-69-B, 35 p.

Nuccio, V.F., Schmoker, J.W., and Fouch, T.D., 1992, Thermal maturity, porosity, and lithofacies relationships applied to gas generation and production in Cretaceous and Tertiary low-permeability (tight) sandstones, Uinta basin, Utah. In: Fouch, T.D., Nuccio, V.F., and Chidsey, T.C., Jr. (eds.), Hydrocarbon and Mineral Resources of the Uinta Basin, Utah and Colorado, Utah Geological Association Guidebook 20, p. 77–93.

Odling, N.E., and Gillespie, P. 1999. Variations in fracture system geometry and their implications for fluid flow in fractured hydrocarbon reservoirs. Petroleum Geosciences 5, 373-384.

Ortega, O., and Marrett, R., 2000, Prediction of macrofracture properties using microfracture information, Mesaverde Group sandstones, San Juan basin, New Mexico; Journal of Structural Geology, 22, 571-588.

Osmond, J.C., 1992, Greater Natural Buttes gas field, Uintah County, Utah. In: Fouch, T.D., Nuccio, V.F., and Chidsey, T.C. (eds.), Hydrocarbon and Mineral Resources of the Uinta Basin, Utah and Colorado. Utah Geological Association Guidebook 20, p. 143-163.

Osmond, J.C., 2005, History of oil and gas exploration in the Uinta basin, Utah. The Mountain Geologist, v. 40, p. 101-110.

Osmond, J.C., 1964, Tectonic history of the Uinta Basin, Utah. In: Sabatka, E.F. (ed) Guidebook to the Geology and Mineral Resources of the Uinta Basin. Intermountain Association of Petroleum Geologists, 13th Annual Field Conference, 47-58.

Pitman, J.K., and Sprunt, E.S., 1986, Origin and distribution of fractures in lower Tertiary and Upper Cretaceous rocks, Piceance Basin, Colorado, and their relation to the occurrence of hydrocarbons. In: Spencer, C.W., and Mast, R.F. (eds.) Geology of Tight Gas Reservoirs. AAPG Studies in Geology, No. 24, p. 221-233.

Pitman, J.K., Francsyk, K.J., and Anders, D.E., 1987, Marine and nonmarine gas-bearing rocks in Upper Cretaceous Blackhawk and Nelson Formations, eastern Uinta Basin, Utah: Sedimentology, diagenesis, and source rock potential. AAPG Bulletin, v. 71, no. 1, p. 76-94.

Heidbach, O., Tingay, M., Barth, A., Reinecker, J., Kurfeß, D., and Müller, B., The World Stress Map database release 2008 doi:10.1594/GFZ.WSM.Rel2008, 2008. World Stress Map Project (2008) maintained by Helmholtz Centre Potsdam - GFZ German Research Centre for Geosciences (http://dc-app3-14.gfz-potsdam.de/pub/introduction/introduction_frame.html)

Rice, D.D., Fouch, T.D., and Johnson, R.C., 1992, Influence of source rock type, thermal maturity, and migration on composition and distribution of natural gases, Uinta Basin, Utah. In; Fouch, T.D., Nuccio, V.F., and Chidsey, T.C., Jr., (eds.), Hydrocarbon and Mineral Resources of the Uinta Basin, Utah and Colorado. Utah Geological Association Guidebook 20, p. 95–110.

Roberts, L.N.R., and Kirschbaum, M.A., 1995, Paleogeography of the Late Cretaceous of the Western Interior of Middle North America – coal distribution and sediment accumulation. United States Geological Survey Professional Paper 1561, 115.

Ryer, T.A., and McPhillips, M., 1983, Early Late Cretaceous paleogeography of east-central Utah. In: Reynolds M.W., and Dolly, E.D. (eds.), Mesozoic Paleogeography of the West-Central United States. Rocky Mountain Section, SEPM Symposium, Denver, Colo., p 253-272.

Selvadurai, A,. and Shirazi, A., 2004, MandelCryer Effects in Fluid Inclusions in Damage-susceptible Poroelastic Geologic Media, Computers and Geotechnics, vol. 31, no. 4, pp. 285–300, 2004.

Skempton, A.W., 1954, The Pore-Pressure Coefficients A and B, G´eotechnique, vol. 4, no. 4, 1954.

Spencer, C.W., 1987, Hydrocarbon generation as a mechanism for overpressuring in Rocky Mountain region. AAPG Bulletin, v. 71, no. 4, p. 368-387.

Spencer, C.W., 1989, Review of characteristics of low-permeability gas reservoirs in the western United States. AAPG Bulletin, v. 73, p. 613–629.

Spencer, C.W., 1995, Unita-Piceance Basin Province (020), United States Geological Survey, 29 p. (http://certmapper.cr.usgs.gov/data/noga95/prov20/text/prov20.pdf)

Spieker, E.M., Reeside, J.B. Jr., 1925, Cretaceous and Tertiary formations of the Wasatch Plateau, Utah. Geological Society of America Bulletin, v. 46, no. 3, p. 435-454.

Sprinkel, D.A., 2004, Map of the Vernal 30′ x 60′ Quadrangle, Utah and Colorado, Utah Geological Survey Open-File Report.

Sprinkel, D.A., 2007, Interim Geologic Map of the Dutch John 30′ x 60′ Quadrangle, Daggett and Uintah Counties, Utah, Moffat County, Colorado, and Sweetwater County, Wyoming. Utah Geological Survey Open-File Report 491 DM.

Stancel, S.G., Cuzella, J.J., MacMillan, L., and Ragas, A., 2008, Controls on Gas Production along the Southern Flank of Greater Natural Buttes Field: A Case Study of the Love Area, Uinta Basin, Utah. In: Longman, M. W. and Morgan, C.D. (eds.) Hydrocarbon Systems and Production in the Uinta Basin, Utah, Rocky Mountain Association of Geologists and Utah Geological Association Publication 37, p. 237-266.

Terzaghi K. and Peck, R. B., 1996, Soil Mechanics in Engineering Practice. John Wiley, 1996.

Tran, D., Shrivastava, V. and Nghiem, L., 2009, Geomechanical Risk Mitigation for CO2 Sequestration in Saline Aquifers, presented at SPE Annual Technical Conference and Exhibition, 2009.

Twiss, R.J., and Moores, E.M., 2007, Structural Geology, 2nd edition. W.H. Freemann and Company, New York, NY.

Untermann, G.E., and Untermann, B.R., 1968, Geology of Uintah County. Utah Geological and Mineralogical Survey Bulletin 72, 98 p.

USGS Uinta-Piceance Assessment Team (2003) Executive summary – assessment of undiscovered oil and gas resources of the Uinta-Piceance province of Utah and Colorado, 2002. Chapter 1 of Petroleum Systems and Geologic Assessment of Oil and Gas in the Uinta-Piceance Province, Utah and Colorado. U.S. Geological Survey Digital Data Series DDS-69-B, 6 p.

Verbeek, E.R., and Grout, M.A., 1983, Fracture history of the northern Piceance Creek Basin, northwestern Colorado. In: Gary, J.H. (ed) 16th Oil Shale Symposium, Proceedings: Golden, Colo., Colorado School of Mines Press.

Verbeek, E.R., and Grout, M.A. 1984. Fracture studies in Cretaceous and Paleocene strata in and around the Piceance Basin, Colorado-Preliminary results and their bearing on a fracture-controlled natural-gas reservoir at the MWX site: U.S. Geological Survey Open-File Report 84-156.

Verbeek, E.R., and Grout, M.A., 1992, Structural evolution of gilsonite dikes, eastern Uinta Basin, Utah, In: Fouch, T.D., Nuccio, V.F., and Chidsey, T.C., Jr. (eds) Hydrocarbon and Mineral Resources of the Uinta Basin, Utah and Colorado. Utah Geological Association Guidebook, 20, 237-255.

Verbeek, E.R., and Grout, M.A., 1993, Geometry and structural evolution of gilsonite dikes in the eastern Uinta basin, Utah, chapter HH of Evolution of sedimentary basins—Uinta and Piceance Basins: U.S. Geological Survey Bulletin, 1787-HH, HH1- HH42.

Verbeek, E.R., and Grout, M.A., 1997, Joint Networks in Reservoir Rocks: Case Studies of Prediction at Depth: In: Hoak, T., Klawiter, A. I., and Blomquist, P. K., (eds) Fractured Reservoirs: Characterization and Modeling. Rocky Mountain Association of Geologists Guidebook,115-130.

Verbeek, E.R., and Grout, M.A., 1998, Relation Between Basement Structures and Fracture Systems in Cover Rocks, Northeastern and Southwestern Colorado Plateau. In: Friedman, J. D., and Huffman, A.C., Jr. (eds) Laccolith Complexes of Southeastern Utah: Tectonic Control and Time of Emplacement-Workshop Proceedings: U.S. Geological Survey Bulletin 2158, 111-149.

Wesley, J.B., 1990, Finite Difference Modeling of Present Day Overpressures Maintained by Hydrocarbon Generation, and Regional Fluid Flow in the Green River Formation, Uinta Basin, Utah. M.S. Thesis, Colorado School of Mines, 139 p.

Wilson, M.D., and Pittman, E.D., 1977. Authigenic clays in sandstones; recognition and influence on reservoir properties and paleoenvironmental analysis. Journal of Sedimentary Petrology, 47, 3-31.

Witkind, I.J., 1988, Geologic map of the Huntington 30′ x 60′ quadrangle, Carbon, Emery, Grand and Uintah counties, Utah. Utah Geological Survey Open-File Report 440DM.

Wheeler, M.F., and Gai, X., 2007, Iteratively Coupled Mixed and Galerkin Finite Element Methods for Poroelasticity," Numerical Methods for Partial Differential Equations, vol. 23, no. 4, pp. 785–797, 2007.

White, H., Cole, R., Stancel, S., Lee, C., and MacMillan, L., 2008, "Window" Outcrop Analogs for Greater Natural Buttes Field, Uinta Basin, Utah. In: Longman, M. W. and Morgan, C.D. (eds.) Hydrocarbon Systems and Production in the Uinta Basin, Utah, Rocky Mountain Association of Geologists and Utah Geological Association Publication 37, p. 209-235.

Wicander, R., and Monroe, J.S., 1989, Historical Geology, Brook Cole.

Yang, Y.K. 2003, Finite-Element Multiphase Flow Simulator, Ph.D. dissertation, University of Utah, 2003.

Yang Y. K. and M. D. Deo, 2006, Modeling of Multilateral and Maximum Reservoir Contact Wells in Heterogeneous Porous Media, 2006 SPE IOR Symposium.

Zar, J.H. 2010. Biostatistical Analysis, 5th edition. Pearson Prentice-Hall, Upper Saddle River, NJ.

Zhao, N., McLennan, J., Deo, M.D. 2011, Morphology and Growth of Fractures in Unconventional Reservoirs, CSUG/SPE 147509, Canadian Unconventional Resources Conference held in Calgary, Alberta, Canada, 15-17 November 2011.

Zobak, M. L., and M. D. Zobak, 1991, Tectonic stress field of the continental United States. In: L. Pakiser and W. Mooney (eds.) Geophysical Framework of the Continental United States, Geological Society of America Memoir 172, p. 523–539.

List of Acronyms and Abbreviations

3-DEC	A discrete-element geomechanics simulator developed by Itasca, Inc.
A	Surface area of the control volume
ARTS	Advanced Reactive Transport Simulator – A reservoir simulator at the University of Utah
BCFG	Billions of Cubic Feet of Gas
C_p	Pore volume compressibility
D	Coefficient matrix for stress strain relationship
DFN	Discrete Fracture Network
F	External force load
DPHI	Density porosity – usually for a log
$F_{convective}$	Convective flow term
$F_{diffusive}$	Diffusive flow term
G	Shear modulus
GNB	Greater Natural Buttes
K	Usually means permeability, subscripts indicating types of permeability – air or Klinkenberg. In some cases, as indicated below the symbol is used for other notations.
K_b	Drained bulk modulus of the rock
K_g	Bulk modulus of the rock
$K_{p1\text{-}p2,\,i}$	Thermodynamics equilibrium constant of the i component
K_{req}	Chemical equilibrium constant for reaction req
K_{wb}	Permeability perpendicular to well
mD	Milli Darcies
NBU	Natural Buttes Unit – A natural gas field in the Uinta Basin, Utah
N_c	Maximum number of components
N_e	Maximum number of thermal equilibrium relationships
N_f	Maximum number of fluid phases
N_v	Total number of finite volumes in the reservoir discretization model
NPHI	Neutron porosity
P_p	Pore pressure of phase p
P_{avg}	Average pore pressure
Q_p	Source/sink/ well molar flow rate of phase p
$Q_{Source\ sink}$	Source or sink term of the property C

Q_e	Heat flow through wells
Q_{loss}	Heat loss to over/under burden
R	Residual term of the generalized governing equation
R_{Acc}	Residual term for the accumulation
$R_{F\ low}$	Residual term for flow related terms
SPHI	Sonic porosity
S_p	Saturation of phase p
$S_{req\ i}$	Stoichiometry coefficient of i component for req chemical equilibrium
T	Temperature
TCF	Trillions of Cubic Feet
$T_{i\ J}$	Transmissivity between finite volumes I and J
U_p	Energy per unit volume
V	Volume of a arbitrary control volume
Z	Elevation
k_{rp}	Relative permeability of phase
m_p	Relative mobility
p_{ter}	Water pressure in Terzaghi's experiment
q_p	Source and sink term for phase p
t	time
u_i	Deformation in the i direction
z_{ter}	Distance along the soil column
Φ	Potential term
ρ	Density of the porous medium
α	Biot coefficient

Greater Natural Buttes Geology

Table 2-1. Description of fractures in the NBU 253 core, section 10, T. 9 S., R. 21 E., Uintah County, Utah. See figure 11 for fracture location in core.

Fracture #	Depth Top (ft)	Depth Base (ft)	Fracture Length (ft)	Orientation	Aperture	Mineral-ization?
1	10532.0	10532.2	0.2	Sub-vertical	Open	No
2	10565.7	10565.9	0.2	Sub-vertical	Closed	No
3	10575.5	10575.7	0.2	Sub-vertical	Closed	No
4	10579.4	10579.9	0.5	Vertical	Closed	No
5	10580.7	10581.2	0.5	Vertical	Open	No
6	10584.0	10584.6	0.6	Vertical	Closed	No
7	10584.8	10585.4	0.6	Sub-vertical	Closed	No
8	10590.0	10590.7	0.7	Vertical	Open	No
9	10596.1	10596.3	0.2	Vertical	Closed	No
10	10600.7	10600.9	0.2	Sub-vertical	Closed	No
11	10606.2	10606.5	0.3	Sub-vertical	Closed	No
12	10607.7	10607.9	0.2	Sub-vertical	Closed	No
13	10608.5	10608.7	0.2	Vertical	Open	No
14	10617.7	10617.7	0.2	Horizontal	Closed	No
15	10631.5	10631.9	0.4	Sub-vertical	Closed	No
16	10634.7	10634.9	0.2	Sub-vertical	Closed	No
17	10657.4	10657.9	0.5	Vertical	Closed	Possible
18	10671.7	10672.2	0.5	Vertical	Closed	No
19	10671.8	10672.0	0.2	Sub-vertical	Closed	No
21	10676.2	10676.4	0.2	Vertical	Closed	No
22	10679.1	10679.6	0.5	Vertical	Open	No
23	10686.3	10686.5	0.2	Vertical	Open	No
24	10688.0	10688.7	0.7	Vertical	Open	No
25	10711.5	10714.0	2.5	Vertical	Open	Yes
26	10718.0	10718.7	0.7	Vertical	Closed	No

Table 2-2. Tight rock analysis results from the NBU 253 core, section 10, T. 9 S., R. 21 E., Uintah County, Utah. See figure 11 for sample location in core.

Depth (ft)	Sample Description	As Received Bulk Density (g/cc)	As Received Grain Density (g/cc)	Dry Grain Density (g/cc)	Effective Porosity (% of BV*)	Water Saturation (% of PV**)	Gas Saturation (% of PV)	Mobile Oil Saturation (% of PV)	Gas Filled Porosity (% of BV)	Bound Hydrocarbon Saturation (% of BV)	Bound Clay Water (% of BV)	Steady-State Permeability (mD)
10,532.0	Fine-grained sandstone with fracture	2.655	2.705	2.710	2.06	2.86	88.55	8.59	1.82	0.07	2.80	162.238***
10,572.0	Cross-bedded sandstone	2.518	2.660	2.667	5.69	2.13	93.79	4.09	5.34	0.09	0.74	0.068
10,580.0	Laminated, fine-grained sandstone	2.535	2.667	2.671	5.13	0.18	96.53	3.28	4.95	0.07	0.83	0.007
10,612.0	Massive sandstone	2.513	2.657	2.663	5.74	1.62	94.33	4.05	5.41	0.00	0.51	0.042
10,650.5	Bioturbated, sandstone	2.562	2.653	2.662	3.88	4.88	89.03	6.09	3.45	0.00	2.65	0.007
10,677.0	Laminated, fine-grained sandstone	2.538	2.676	2.682	5.43	0.86	94.81	4.32	5.15	0.00	0.42	0.007
10,700.0	Low-angle cross bedding in sandstone	2.533	2.677	2.684	5.72	2.46	94.59	2.95	5.41	0.07	0.75	0.007
10,706.5	Sandstone with contorted bedding	2.477	2.670	2.681	7.74	3.66	93.38	2.96	7.23	0.00	0.82	0.054

* BV = bulk volume

** PV = pore volume

*** Sample contained artificial induced fracture

Table 2-3. Description of fractures in the NBU 921-21L core, section 21, T. 9 S., R. 21 E., Uintah County, Utah. See figure 16 for fracture location in core.

Depth Top (ft)	Depth Base (ft)	Fracture Length (ft)	Orientation	Aperture	Mineral-ization?	Notes
9323.9	9324.2	0.3	Vertical	Open	No	
9347.9	9348.7	0.6	Vertical	Closed	Yes	
9348.0	9348.2	0.2	Vertical	Closed	Yes	
9348.4	9348.8	0.4	Vertical	Closed	Yes	
9348.8	9349.9	0.2	Vertical	Open	No	
9357.1	9357.4	0.3	Vertical	Open	?	
9362.4	9362.5	0.1	Inclined	Open & Closed	No	
9363.2	9663.4	0.2	Vertical	Open	Yes	
9367.3	9367.3	0.3	Horizontal	Open	No	
9379.2	9379.5	0.3	Vertical	Closed	Yes	
9386.5	9386.6	0.1	Vertical	Open	No	
9389.1	9389.2	0.1	Vertical	Closed	Yes	
9399.6	9399.6	0.3	Horizontal	Open	No	
9399.8	9399.9	0.1	Vertical	Closed	Yes	
9401.1	9401.3	0.2	Vertical	Closed	Yes	
9401.3	9401.5	0.2	Vertical	Closed	Yes	
9401.1	9401.5	0.4	Vertical	Closed	Yes	
9402.6	9402.8	0.2	Vertical	Closed	Yes	
9405.0	9405.7	0.7	Vertical	Open & Closed	No	
9407.9	9407.9	0.2	Horizontal	Open	No	
9408.3	9408.3	0.4	Horizontal	Closed	No	
9408.4	9408.4	0.1	Horizontal	Closed	No	
9413.1	9413.1	0.4	Horizontal	Closed	Yes	
9417.0	9417.4	0.4	Vertical	Open	No	Slickenlines
9428.0	9428.5	0.5	Vertical	Closed	Yes	
9433.0	9433.0	0.4	Horizontal	Open	No	
9433.2	9433.2	0.4	Horizontal	Closed	No	
9434.6	9435.0	0.4	Vertical	Closed	Yes	

Table 2-4. Tight rock analysis results from the NBU 921-21L core, section 21, T. 9 S., R. 21 E., Uintah County, Utah. See figure 16 for sample location in core.

Depth (ft)	Sample Description	Net Confining Stress (psig)	Porosity (%)	Klinkenberg Permeability (mD)	Kair Permeability (mD)	Oil Saturation (% PV*)	Water Saturation (% PV*)	Grain Density (g/cm^3)
9325.60	Carbonaceous siltstone with rooting disruptions	1820	5.79	.005	.011	0.0	91.4	2.602
9327.90	Carbonaceous shale with coaly stringers	1820	4.22	.001	.002	0.0	92.4	2.629
9333.60	Silty mudstone with plant and woody debris	1820	3.33	.0003	.001	0.0	92.8	2.620
9341.25	Siltstone with thin lenses of very fine-grained sandstone	1820	2.53	.0004	.001	0.0	78.6	2.680
9343.00	Very fine grained sandstone with flaser bedding	1820	2.03	.0002	.001	0.0	83.1	2.673
9349.70	Fine-grained sandstone with bioturbation and open fractures	1820	2.30	.0004	.001	0.0	84.9	2.670
9352.50	Fine-grained sandstone with flaser bedding and silt/mud laminae	1820	2.15	.002	.005	0.0	60.6	2.666
9354.70	Silty sandstone with muddy laminae and burrows	1820	1.62	.001	.002	0.0	72.5	2.674
9356.70	Very fine grained sandstone with burrows	1820	2.26	.0002	.001	0.0	71.9	2.674
9358.70	Very fine grained sandstone with ripples and rip-up clasts	1820	5.29	.002	.005	0.0	41.2	2.672
9360.90	Very fine grained sandstone with flaser bedding	1820	4.13	.001	.002	0.0	41.6	2.684
9362.70	Siltstone with mudchip rip-ups	1820	4.07	.006	.014	0.0	94.6	2.678
9364.70	Mudstone	1820	4.04	.001	.003	0.0	68.8	2.689
9366.60	Siltstone with rootlets	1820	0.57	.0003	.001	0.0	84.6	2.667
9368.60	Laminated siltstone	1820	1.04	.0002	.001	0.0	66.0	2.726
9372.50	Siltstone with soft sediment deformation	1820	2.84	.001	.003	0.0	71.3	2.662
9374.50	Mudstone	1820	2.68	.001	.002	0.0	70.7	2.674
9376.60	Very fine grained sandstone with rip-ups	1820	2.39	.002	.004	0.0	36.0	2.687
9378.40	Mudstone	1820	2.90	.004	.009	0.0	77.9	2.676
9380.00	Very fine grained sandstone with laminations	1820	1.94	.001	.002	0.0	68.5	2.691
9382.40	Very fine grained sandstone with soft sediment deformation	1820	2.51	.000	.001	0.0	57.5	2.615
9384.30	Very fine grained sandstone	1820	3.13	.002	.005	0.0	72.9	2.643
9388.20	Very fine grained sandstone with ripples and clay drapes	1820	5.29	.003	.007	0.0	TBD	2.644
9390.30	Siltstone	1820	4.37	.001	.002	0.0	53.3	2.646
9394.30	Very fine grained sandstone with carbonaceous debris	1820	3.73	.000	.001	0.0	68.9	2.629
9396.45	Very fine grained sandstone with laminations	1820	5.59	.001	.004	0.0	45.0	2.651
9398.40	Very fine grained sandstone with laminations	1820	4.58	.001	.002	0.0	50.6	2.657
9400.10	Very fine grained sandstone with soft sediment deformation	1820	2.25	.001	.002	0.0	77.0	2.648
9402.00	Very fine grained sandstone with multiple, filled fractures	1820	2.95	.001	.003	0.0	53.3	2.671
9403.95	Very fine grained sandstone with soft sediment deformation	1820	5.55	.006	.008	0.0	TBD	2.650
9405.60	Fine-grained sandstone with flaser bedding	1820	7.65	.010	.014	0.0	TBD	2.653
9406.50	Fine-grained sandstone with flaser bedding	1820	8.64	.015	.020	0.0	TBD	2.654
9407.50	Fine-grained sandstone with laminations	1820	8.36	.013	.019	0.0	TBD	2.656
9409.50	Fine-grained sandstone with flaser bedding	1820	6.11	.004	.009	0.0	TBD	2.651
9412.20	Carbonaceous mudstone	1820	3.46	.031	.031	0.0	64.6	2.622
9414.00	Very fine grained sandstone with soft sediment deformation	1820	1.85	.0002	.0006	0.0	85.9	2.664
9424.85	Very fine grained sandstone	1820	0.43	.0001	.0003	0.0	62.3	2.662
9427.95	Very fine grained sandstone with injection structure	1820	2.27	.0001	.0003	0.0	75.0	2.698
9429.70	Very fine grained sandstone with rooting	1820	1.83	.0001	.0003	0.0	85.7	2.664
9433.45	Mudstone with rooting	1820	1.54	.0001	.0002	0.0	53.7	2.643

* PV = Pore volume

Table 2-5. Triaxial compression results for sample taken from 921-21L core, section 21, T. 9 S., R. 21 E., Uintah County, Utah. See figure 16 for sample location in core.

Depth(ft)	Core Length(in)	Core Diameter(in)	Bulk Density (g/cc)	Effective Confining Pressure (psi)	Effective Compressive Strength (psi)	Quasi Static Young's Modulus (psi)	Quasi Static Poisson's Ratio (psi)
9405	1.4085	0.9955	2.415	5000	58,685	5,271,000	0.14

Detailed Fracture Characterization

Table 3-1. Table listing the structural setting, stratigraphic units sampled and number of lithofacies sampled at each field locality.

Number	Locality Name	Structural Setting	Stratigraphic units sampled	Number of lithofacies sampled
1	Asphalt Ridge	Northwest-trending hogback	Upper & Lower Mesaverde Group	5
2	Snake John Reef	Southward-plunging syncline	Upper & Lower Mesaverde Group	5
3	"Blue Mountain Ridge"	Northern limb of an east-west trending syncline	Iles Formation (laterally equivalent to the Farrer Formation)	3
4	Tusher Canyon	Within the Book Cliffs with a structural dip from 2° - 8° NW	Castlegate and Sego sandstones, Neslen, Farrer, and Tuscher formations	7
5	San Arroyo Canyon	Within the Book Cliffs with a structural dip from 4° - 9° N	Neslen, Farrer and Tuscher formations	3

Table 3-2. Mean distribution and length data for each regional fracture set. Fracture density is defined as the number of fractures per m. Sstdv/ Savg is the standard deviation of spacing divided by the average spacing.

Fracture set	Sample Number	Fracture Spacing (m)	Fracture Density (m)	S_{stdv}/ S_{avg}	Average fracture length (m)
WNW	15	3.17 ± 0.55	0.71 ± 0.12	0.83 ± 0.12	4.29 ± 0.53
N-S-NNE	24	1.8 ± 0.44	0.56 ± 0.09	0.89 ± 0.15	4.51 ± 0.56
NNW	20	2.79 ± 0.49	0.51 ± 0.08	0.81 ± 0.09	6.15 ± 0.74
NE	25	1.86 ± 0.45	0.84 ± 0.19	0.93 ± 0.16	2.07 ± 0.39

Table 3-3. Description of the 7 lithofacies identified and sampled.

Lithofacies	Description
1	Thin-bedded (5 – 30 cm thick), white to tan, laterally discontinuous, low-angle cross-laminated to planar laminated, very fine- to fine-grained sandstones interbedded with mudstones and shales. Lateral lengths of beds range from ~ 2 – 6 meters.
2	Medium-bedded (31 – 100 cm thick), brown to tan and gray, laterally discontinuous, often lenticular, cross-bedded, fine- to medium- grained sandstone. Lateral continuity ranges from ~ 5 – 9 meters.
3	Medium-bedded (31 – 100 cm thick), brown and tan, sharp-based, laterally continuous, tabular, cross laminations sometimes present, fine- to medium- grained sandstone.
4	Thick-bedded (101 – 300 cm thick), white and tan, laterally discontinuous, lenticular, sharp-based, structureless, fine- to medium- grained sandstone. Lateral continuity ranges from ~7 – 12 meters.
5	Thick-bedded (101 – 300 cm thick), white to tan, laterally discontinuous, broadly lenticular, cross bedded, erosional-based, upward-fining, fine- to medium- grained, stacked, amalgamated sandstones. Rip- up clasts are common at base of sandstone units. Lateral continuity ranges from ~ 8 – 23 meters.
6	Thick-bedded (101 - 300 cm thick), white to tan, laterally continuous, cross bedded, medium- to coarse- grained sandstone
7	Massively-bedded (≥ 300 cm thick),often cliff-forming, tan to brown – red, laterally continuous, sharp-based, cross-bedded, fine- to medium- grained sandstone

Creation and Validation of Discrete Fracture Models

Table 4-1. Uncorrected mean fracture intensity measured from scanlines.

Scanline	NNW p10	NEp10	Total P10	Formation	Comments
AR1	0.030	0.020	0.050	LMV	
AR2	0.049	0.010	0.059	UMV	
AR3	0.061	0.000	0.061	UMV	
AR4	0.164	0.295	0.459	LMV	
AR5	0.070	0.320	0.390	LMV	
BMR1	0.270	0.160	0.430	LMV	Castlegate Brown
BMR2	0.291	0.000	0.291	LMV	Castlegate Brown
BMR3	0.060	0.000	0.060	LMV	Castlegate Grey
SJR1	0.054	0.027	0.081	Dakota	
SJR2	0.040	0.150	0.190	Dakota	
SJR3	0.120	0.000	0.120	LMV	
SJR4	0.100	0.000	0.100	LMV	
SJR5	0.060	0.012	0.072	LMV	
SJR6	0.068	0.000	0.068	LMV	Only Big
SJR7	0.010	0.198	0.208	LMV	

Table 4-2. Terzaghi-corrected mean fracture intensity and mean spacing values measured from scanlines.

Scanline	TZP10NNW	TZP10NE	TotalTzP10	NNW Spacing	NE Spacing	Total Spacing
AR1	0.058	0.020	0.078	17.2	49.6	12.8
AR2	0.050	0.017	0.067	20.1	57.2	14.9
AR3	0.067	0.000	0.067	15.0		15.0
AR4	0.189	0.365	0.554	5.3	2.7	1.8
AR5	0.114	0.330	0.443	8.8	3.0	2.3
BMR1	0.278	0.921	1.200	3.6	1.1	0.8
BMR2	0.291	0.000	0.291	3.4		3.4
BMR3	0.060	0.000	0.060	16.7		16.7
SJR1	0.055	0.048	0.103	18.2	20.7	9.7
SJR2	0.040	0.330	0.370	25.0	3.0	2.7
SJR3	0.120	0.000	0.120	8.3		8.3
SJR4	0.102	0.000	0.102	9.8		9.8
SJR5	0.061	0.054	0.115	16.3	18.7	8.7
SJR6	0.068	0.000	0.068	14.6		14.6
SJR7	0.020	0.199	0.219	49.0	5.0	4.6

Incorporating Geomechanics in Reservoir Simulation

Table 5-1. Parameters used in the verification of the geomechanics code using the 1-D analytical solution.

Discretization Method	CVFE
Domain Dimensions (one dimension)	300 feet
Porosity	0.2
Compressibility (1/psi)	2.2×10^{-6}
Permeability (md)	150
Biot Coefficient	0.6
Shear modulus (psi)	8.7×10^{5}
Lame's parameter (psi)	5.8×10^{5}
Water viscosity (cp)	1
Initial pressure (psi)	15
Water saturation	0.3

Table 5-2. Parameters used in verifying the geomechanics code using the 2-D analytical solution.

Discretization Method	CVFE
Domain Dimensions (two dimensions)	330 feet by 200 feet
Porosity	0.2
Pore Compressibility (1/psi)	0
Permeability (md)	150
Biot Coefficient	1.0
Shear modulus (psi)	6×10^5
Young's Modulus (psi)	1.45×10^6
Poisson's Ratio	0.2
Water viscosity (cp)	1
Surface pressure (psi)	1,450
Water saturation	1.0

Table 5-3. Parameters used in verifying the 3-dimensional implementation of the geomechanics code using the STARS - simulator from Computer Modeling Group.

Discretization Method	CVFE
Domain Dimensions (three dimensions)	2200 feet by 2000 feet by 200 feet
Porosity	0.25
Pore Compressibility (1/psi)	3×10^{-6}
Initial Permeability (md)	100
Initial Depth (feet)	4010
Biot Coefficient	1.0
Shear modulus (psi)	6×10^{5}
Young's Modulus (psi)	1×10^{4}
Poisson's Ratio	0.3
Water viscosity (cp)	1
Initial Pressure (psi)	3010
Bottom hole production pressure (psi)	500
Water Saturation	1.0

Integrated Modeling of Natural and Hydraulic Fractures

Table 6-1. Tabulation of important properties used in the soft-coupling case studies.

Discretization Method	CVFE								
Domain Dimensions (three dimensions)	820 feet by 820 feet by 132 feet								
Number of fractures	16								
Number of elements	40612								
Porosity	0.3								
Initial matrix permeability (md)	0.001								
Initial fracture permeability (md)	10								
Initial pressure (psi)	3000								
Initial water saturation	0.3								
Initial gas saturation	0.7								
Bottom hole production pressure (psi)	1800								
Maximum production rate constraint (mscf)	2000								
Rock Fluid Data									
Water saturation	0.2	0.3	0.4	0.5	0.6	0.7	0.8	0.9	1.0
Relative permeability to gas	1	0.8	0.6	0.46	0.34	0.1	0.05	0.022	0
Relative permeability to water	0	0.07	0.15	0.24	0.33	0.55	0.65	0.83	1.0

Table 6-2. Properties used in the case study to study the impact of keeping the main fracture system open with proppant.

Discretization Method	CVFE
Domain Dimensions (three dimensions)	820 feet by 820 feet by 132 feet
Number of fractures	20
Number of elements	46449
Porosity	0.3
Initial matrix permeability (md)	0.1
Initial fracture permeability (md)	100
Initial pressure (psi)	3000
Initial water saturation	0.3
Initial gas saturation	0.7
Bottom hole production pressure (psi)	1000

Table 6-3. Table of properties used in simulating flow through an extensive natural fracture network with geomechanics incorporated.

Discretization Method	CVFE
Domain Dimensions, in feet (three dimensions)	1200 X 1200 X 1200
Number of fractures	44
Number of elements	52517
Porosity	0.2
Initial matrix permeability (md)	0.00001
Initial fracture permeability (md)	100
Pore Compressibility (1/psi)	4×10^{-6}
Initial Depth (feet)	4010
Biot Coefficient	1.0
Young's Modulus (psi)	1×10^{5}
Poisson's Ratio	0.35
Rock density (lb/ft3)	156
Water viscosity (cp)	1
Initial Pressure (psi)	4000
Initial water saturation	0.2
Initial gas saturation	0.8
Bottom hole production pressure (psi)	1000
Confinement	All surface displacements set to zero and top surface not confined

General Natural Buttes Geology

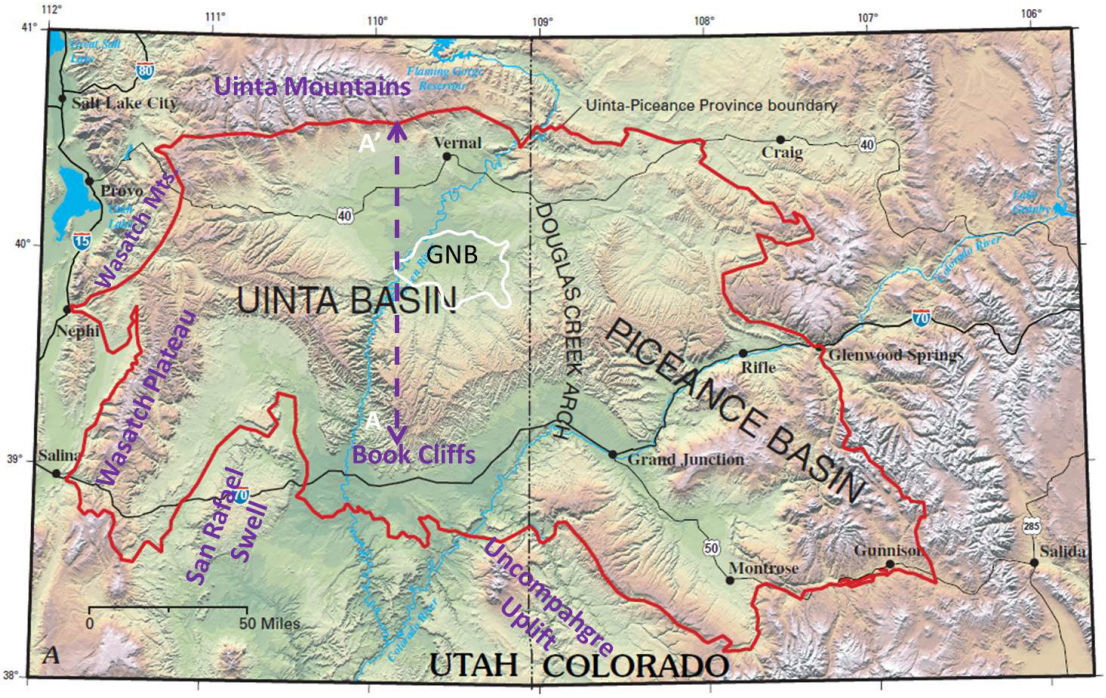

Figure 2-1. Regional location of Uinta Basin and the Greater Natural Butte (GMB0 field (after USGS Uinta-Piceance Assessment Team, 2003)

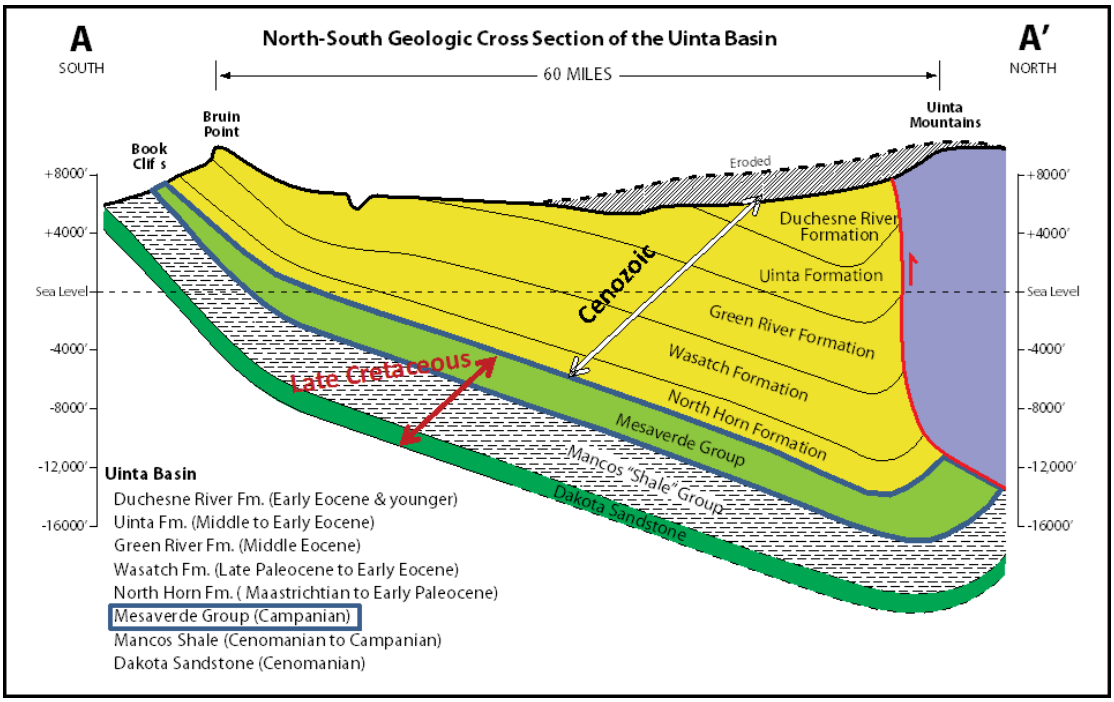

Figure 2-2. North-south cross section of the Uinta Basin (modified after Fouch et al., 1992; Osmond, 2003). Strata dip not true angles.

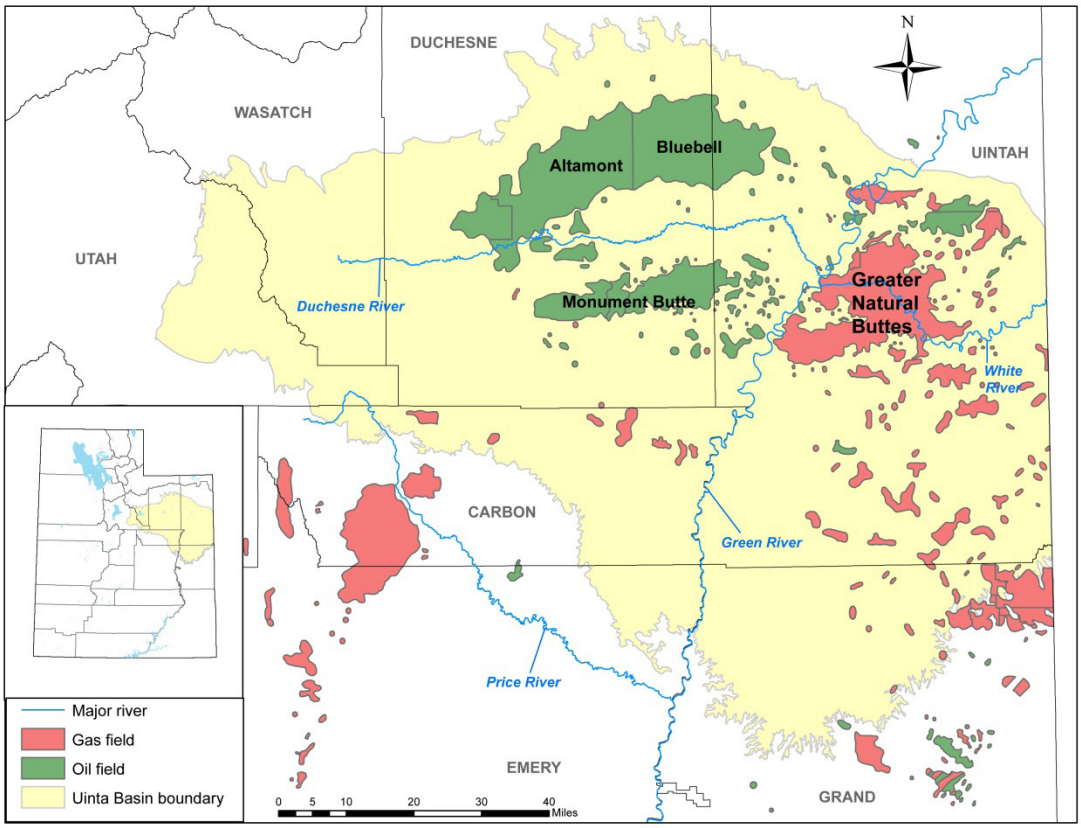

Figure 2-3.Oil and gas field map of the Uinta Basin showing the location of the Greater Natural Buttes gas field.

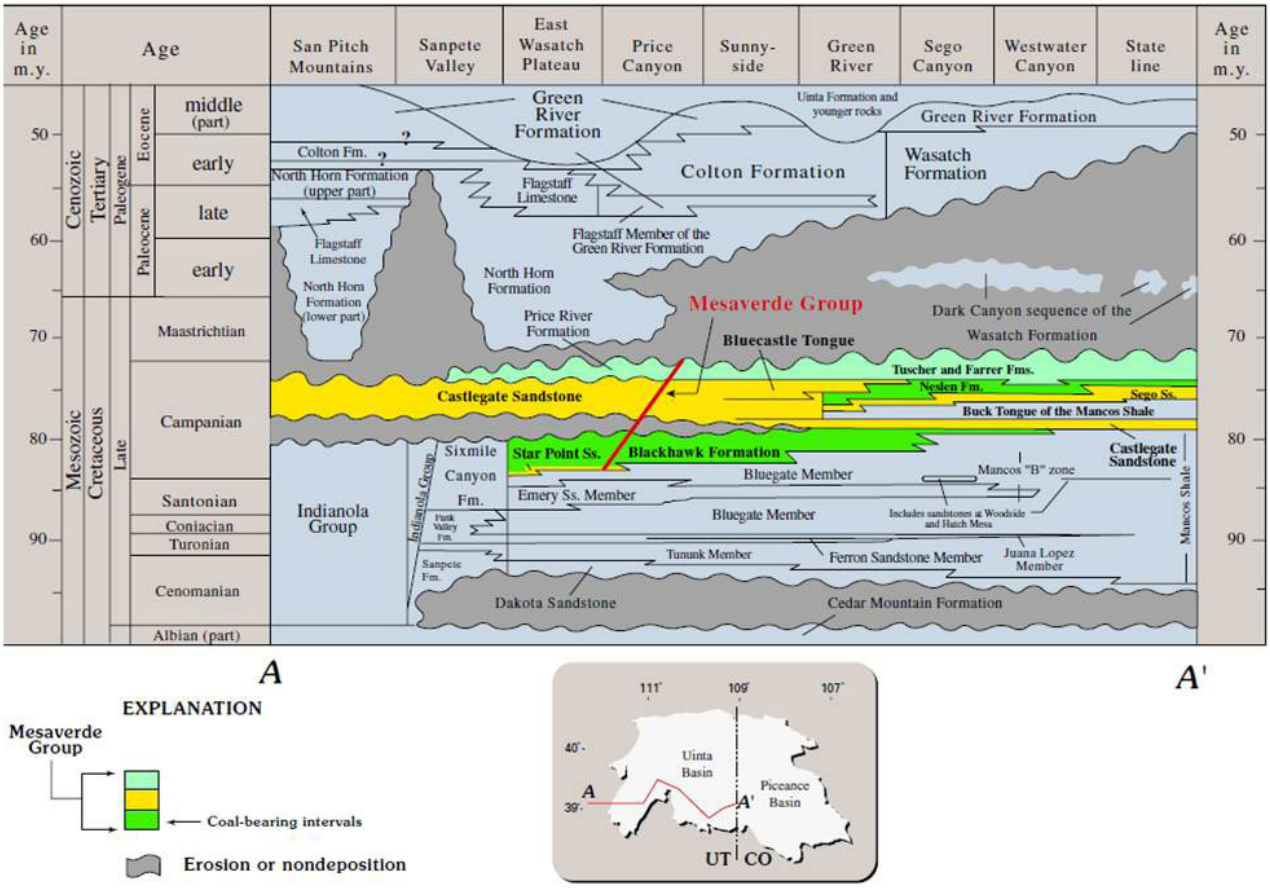

Figure 2-4. West-East chronostratigraphic chart across the Uinta-Piceance basins (Johnson and Roberts, 2003).

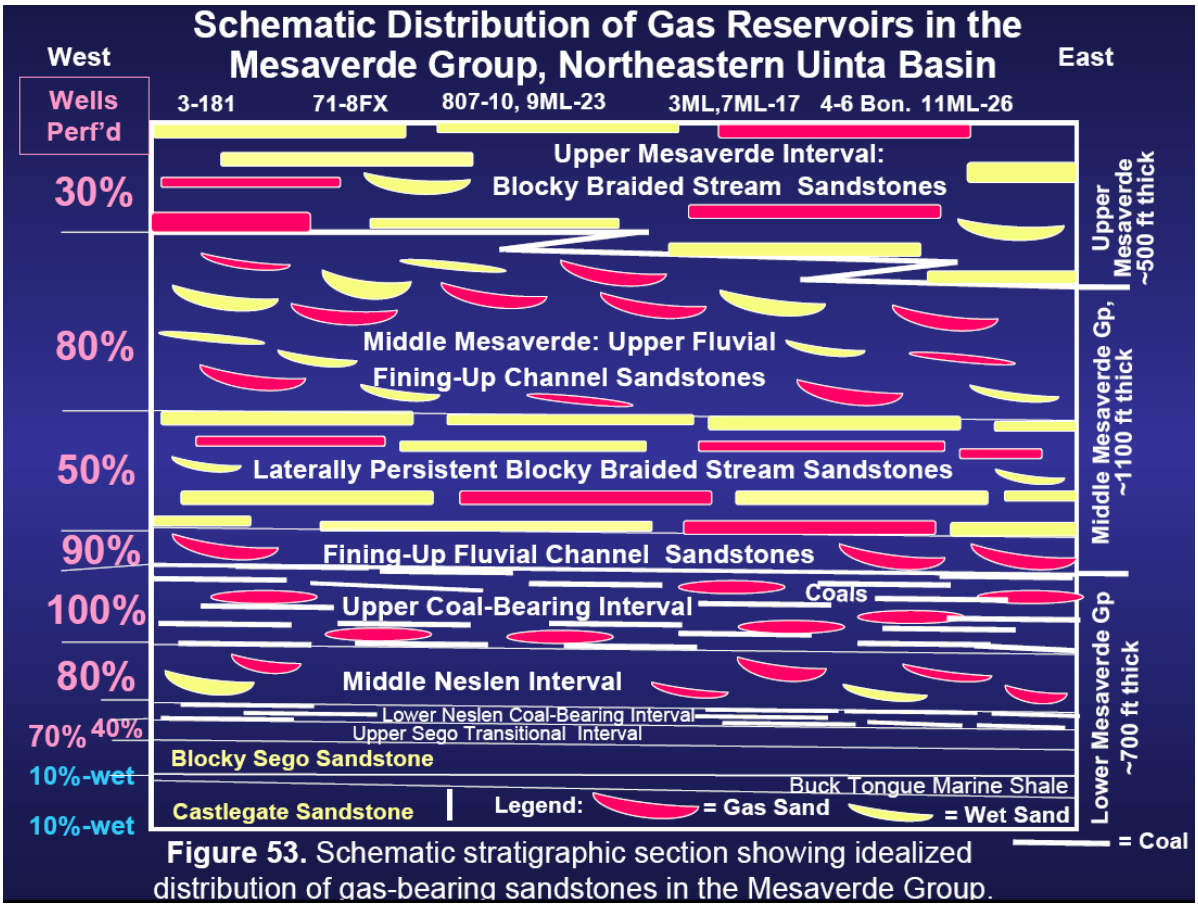

Figure 2-5. Vertical distribution of gas production from eight wells completed in the Mesaverde Group in eastern Uinta Basin. Informal designations: upper Mesaverde is mostly Tuscher Formation, middle Mesaverde is mostly Farrer Formation and Bluecastle Tongue of the Castlegate Sandstone, lower Mesaverde is mostly Neslen, Sego and Castlegate Formations. From Longman and Koepsell (2005).

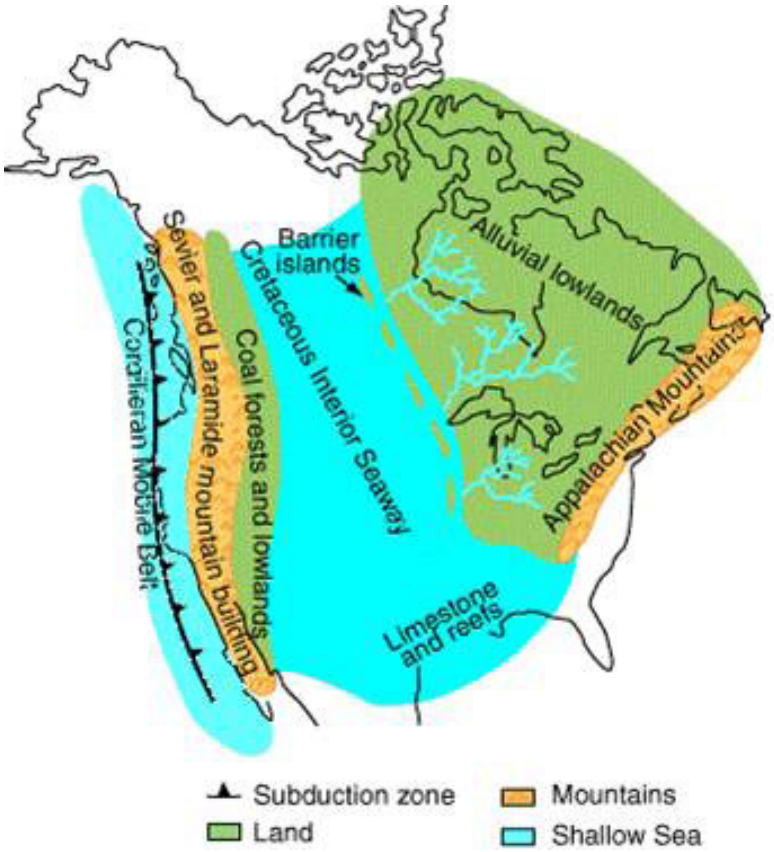

Figure 2-6. Paleogeography of North America during the mid-Cretaceous (about 100 Ma) (from Wicander and Monoroe, 1989).

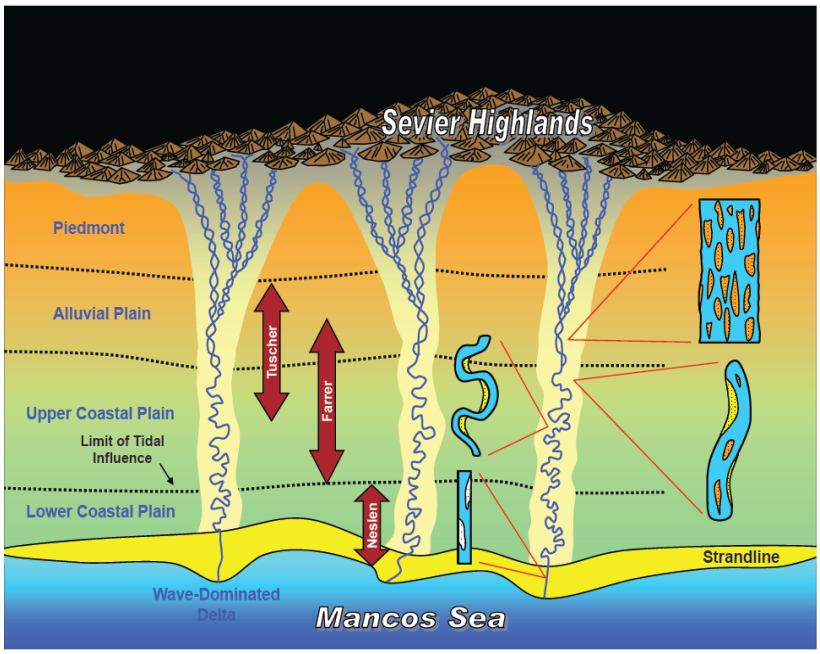

Figure 2-7. Facies distribution and dispositional environments of the Mesaverde formations (White et al., 2008).

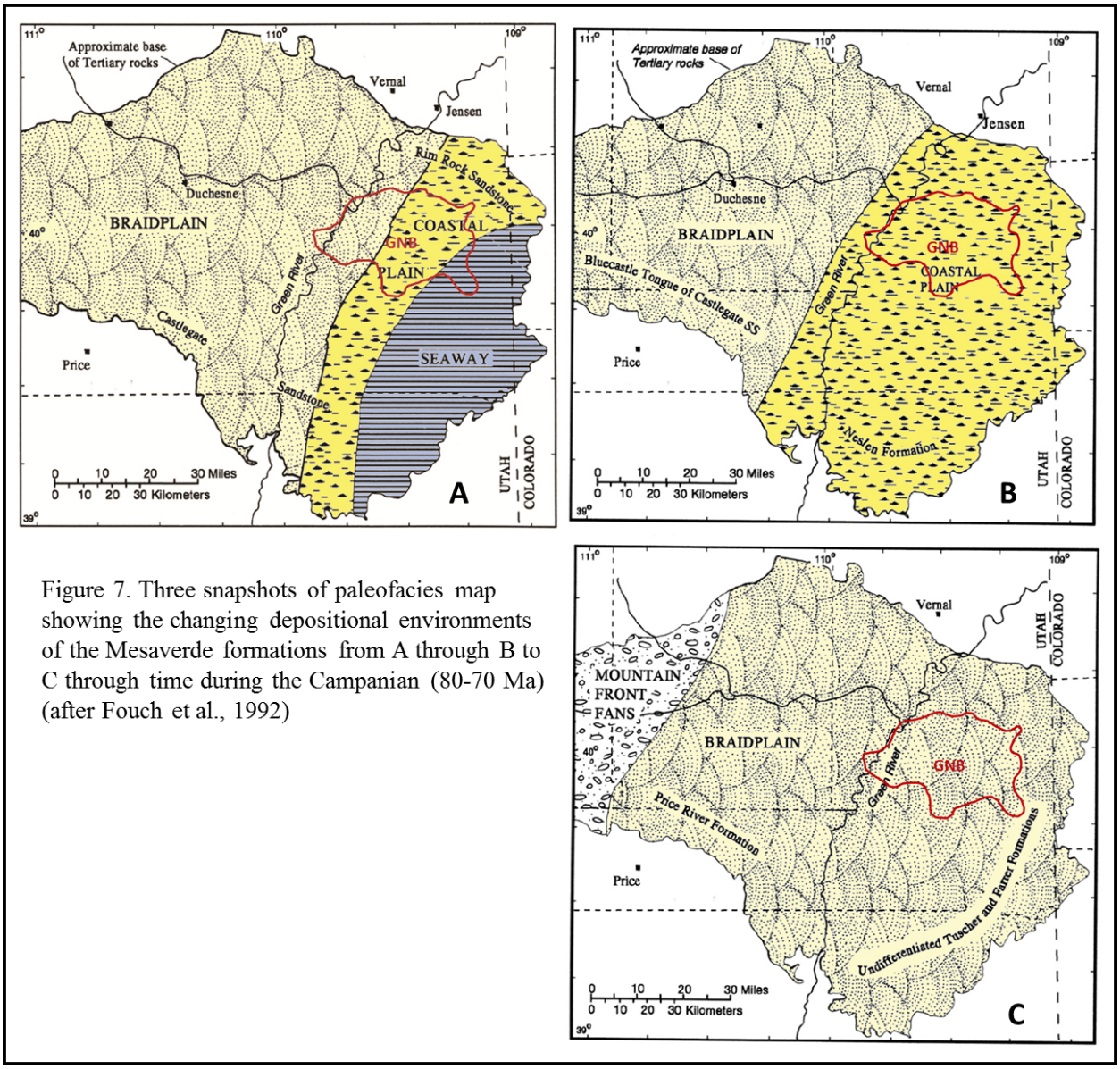

Figure 7. Three snapshots of paleofacies map showing the changing depositional environments of the Mesaverde formations from A through B to C through time during the Campanian (80-70 Ma) (after Fouch et al., 1992)

Figure 2-8. Three snapshots of the paleofacies map showing the changing depositional environments of the Mesaverde formations from A through B to C through time during Campanian (80-70 Ma) (after Fouch et al., 1992).

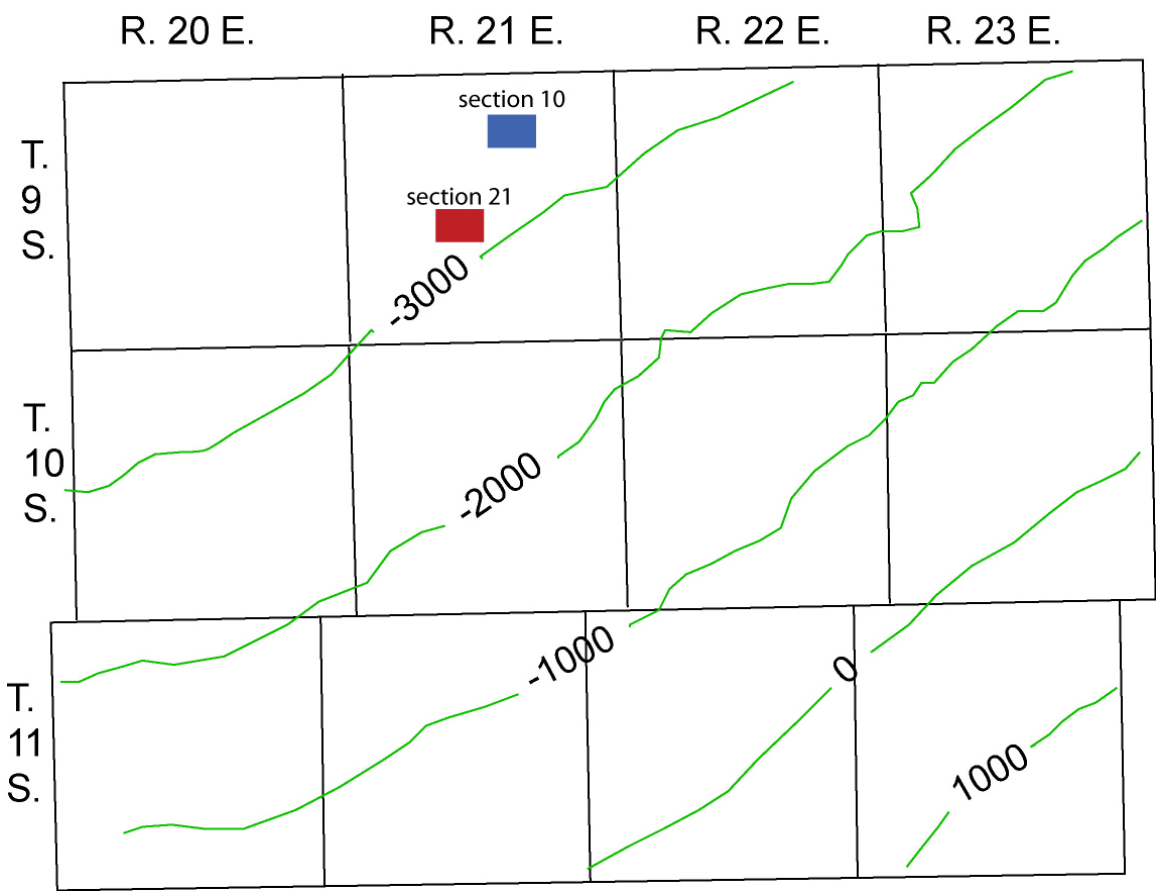

Figure 2-9. Structure on top of the Dark Canyon Conglomerate; contour interval 1000 feet and datum is mean sea level. Modified from Stancel and others (2008). Section 10, T. 9 S., R. 21 E. is the original area of detailed study and modeling; section 21 was later selected for detailed study and modeling.

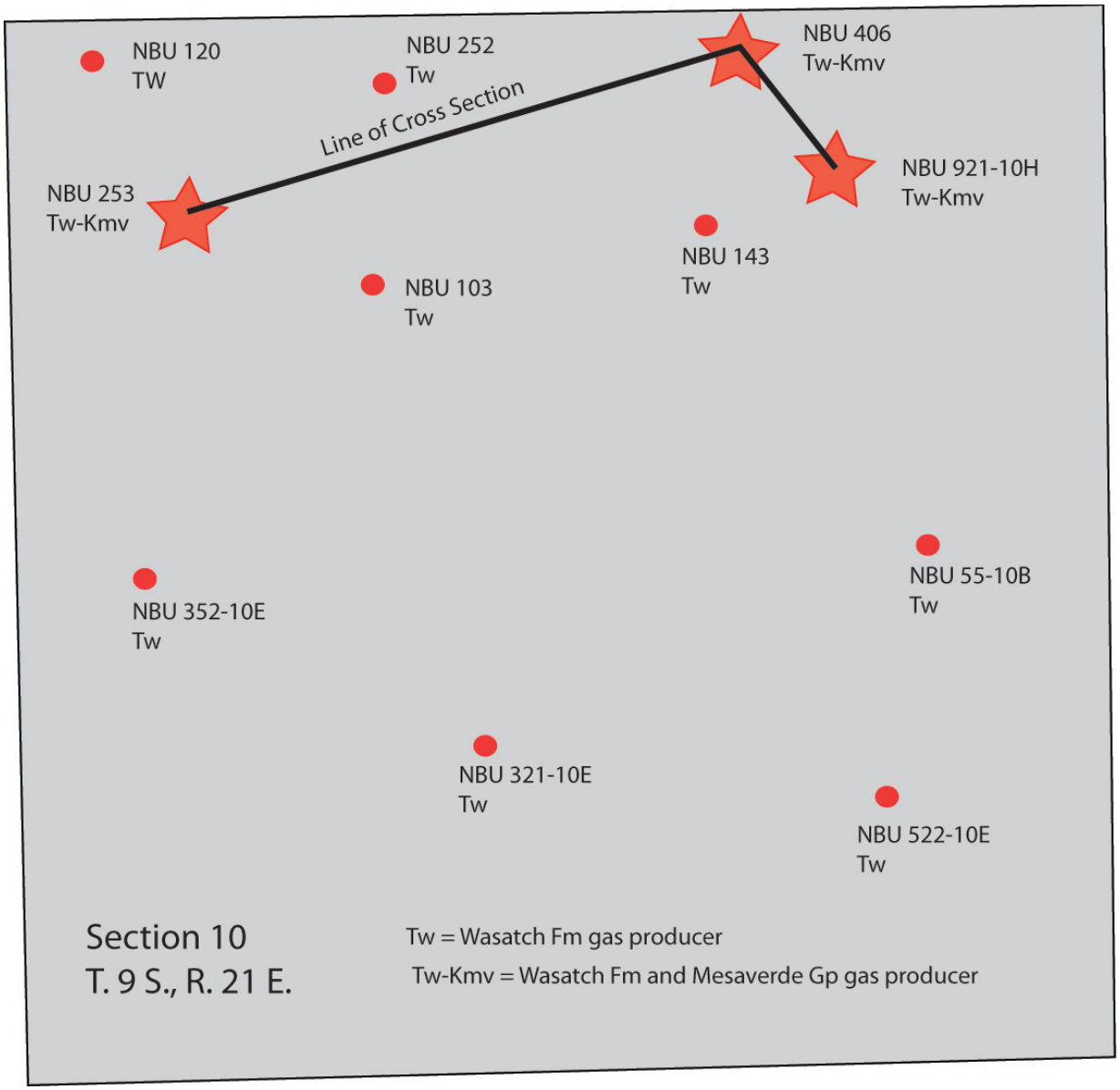

Figure 2-10. Wells in section 10, T. 9 S., R. 21 E., the area of detailed study and modeling. Wells producing gas from the Tertiary Wasatch Formation (Tw) only are shown as red circles, deeper wells that produce gas from both the Mesaverde Group and Wasatch (Tw-Kmv) are shown as red stars. The line connecting the three Mesaverde wells represents the location of the cross section in Figure 2-11.

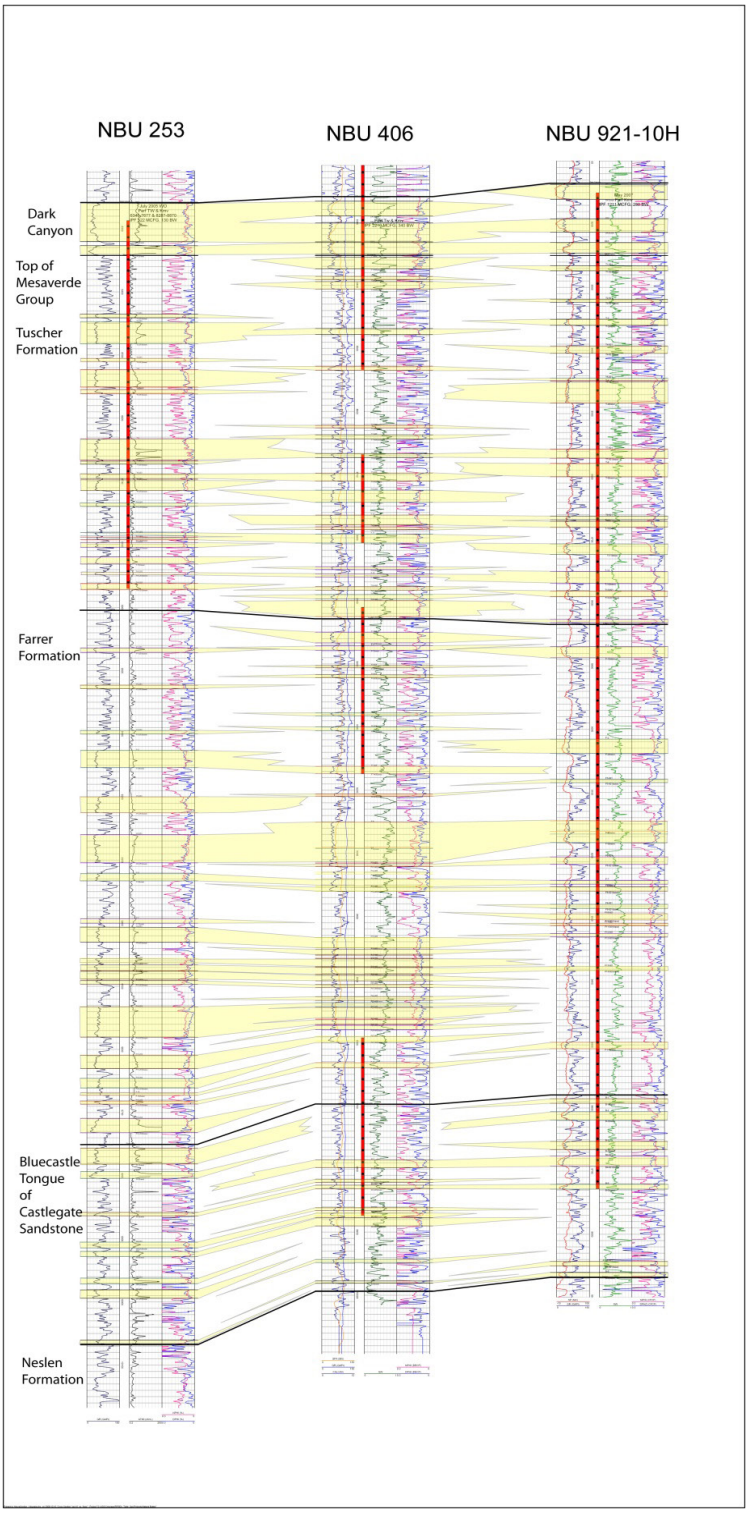

Figure 2-11. Cross-section of the Mesaverde Group in section 10, T. 9 S., R. 21 E., showing the discontinuous nature of the sand bodies. NBU 253 is the only well that penetrated deeper than the Neslen Formation. See figure 6 for location of cross-section.

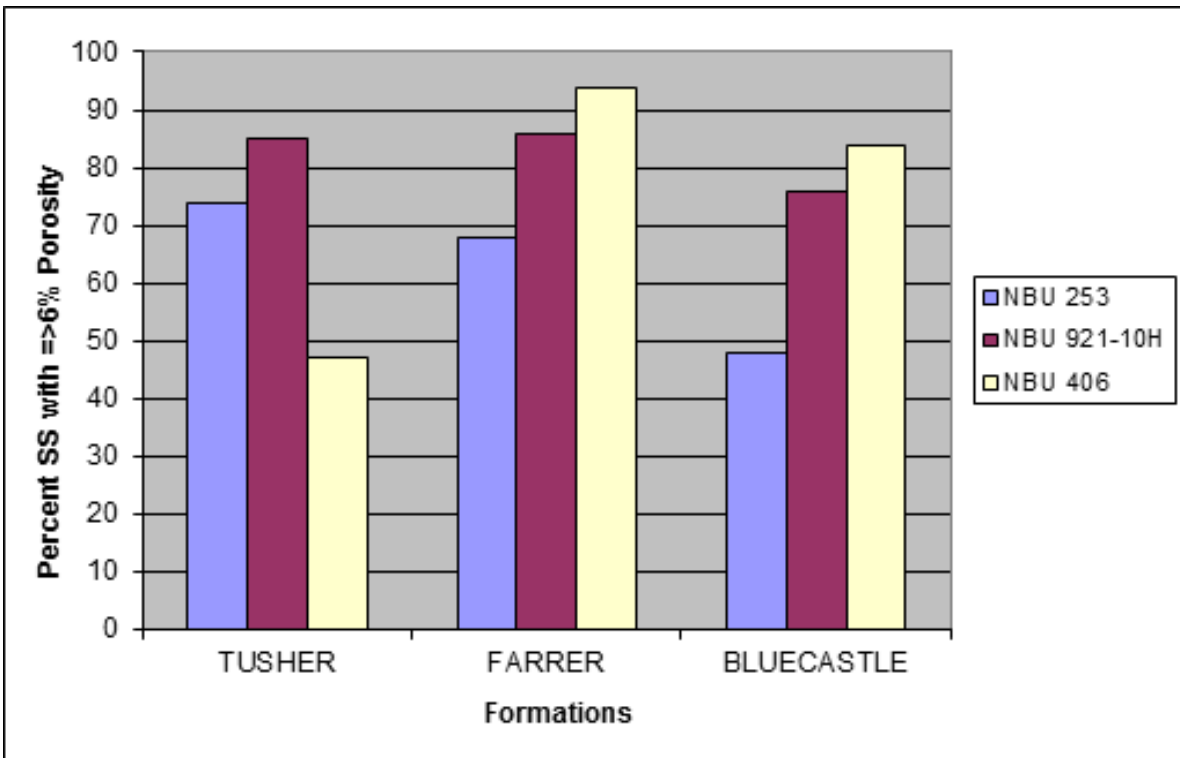

Figure 2-12. Percentage of sandstone beds with 6% or more density/neutron porosity in wells drilled in section 10, T. 9 S., R. 21 E.

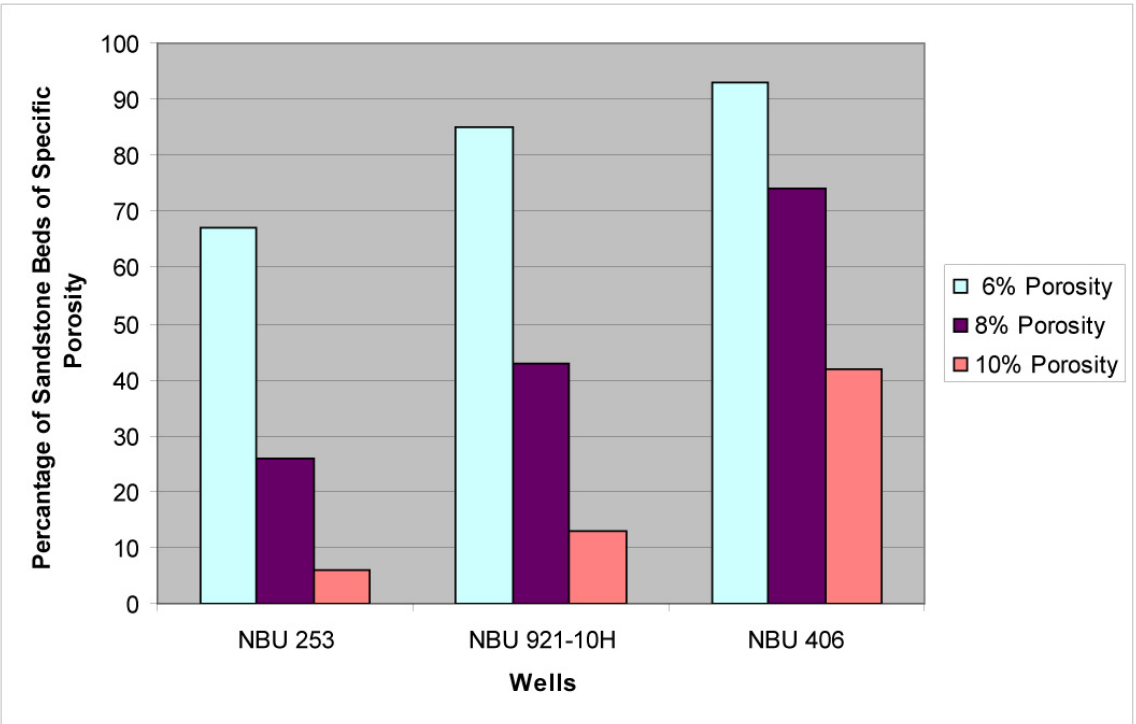

Figure 2-13. Percentage of sandstone beds with 6 to <8%, 8 to <10%, and 10% or more porosity in wells drilled in section 10, T. 9 S., R. 21 E.

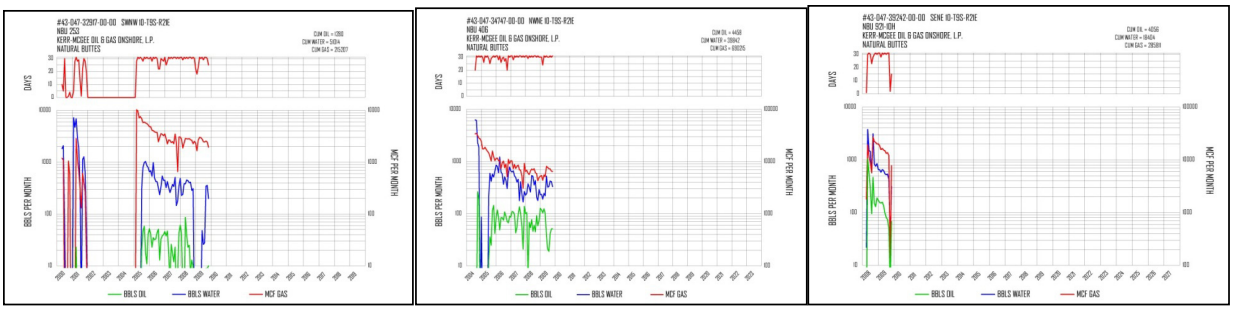

Figure 2-14. Decline curves for the three wells in Tract 21.

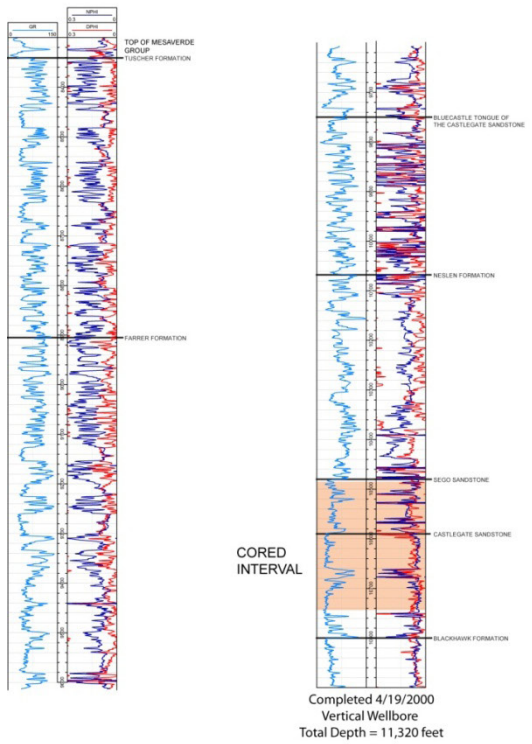

Figure 2-15. Geophysical well log of the NBU 253 well, section 10, T. 9 S., R. 21 E., Greater Natural Buttes field, Uintah County, Utah. The Sego and Castlegate Sandstones of the Mesaverde Group were cored in this well.

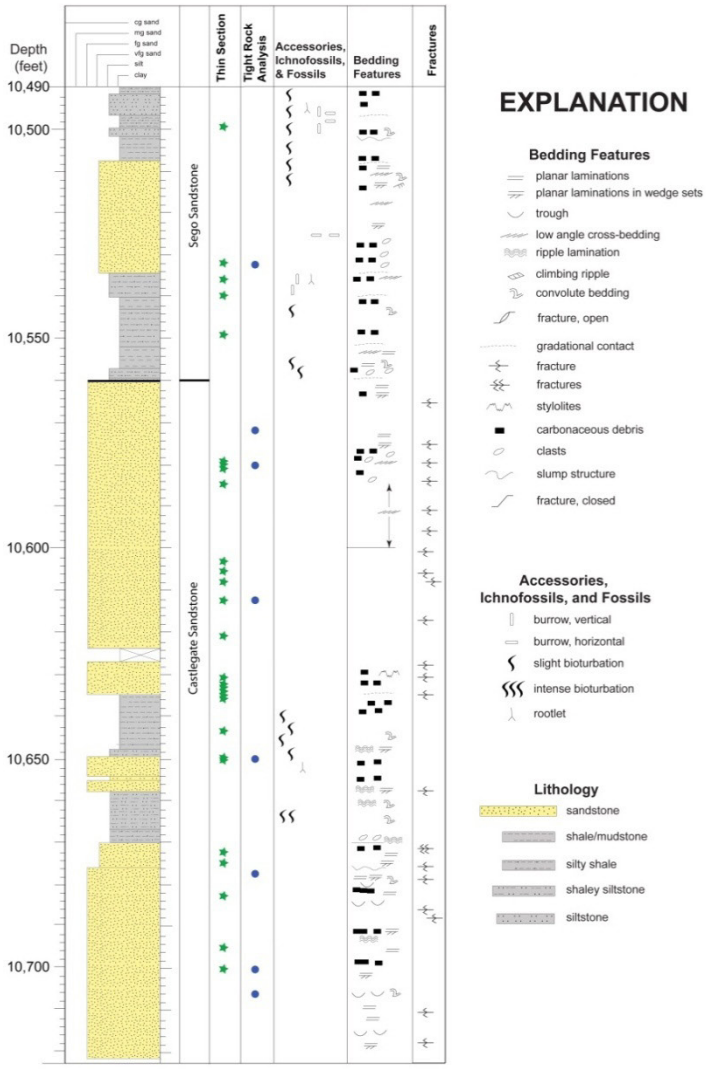

Figure 2-16. Graphical core description of the Sego and Castlegate Sandstones from the NBU 253 well, section 10, T. 9 S., R. 21 E., Greater Natural Buttes field, Uintah County, Utah.

Bioturbated carbonaceous shale; dark red due to high iron content (10,533 feet).

Bioturbated silty sandstone with 3.9% porosity and 0.007 mD of permeability (10,650.5 feet).

Massive, fine-grained sandstone with 5.7% porosity and 0.042 mD of permeability (10,612 feet).

Fine-grained sandstone with horizontal laminations with 5.4% porosity and 0.007 mD of permeability (10,677 feet).

Fine-grained sandstone with cross-bedding. Sandstone has 5.7% porosity and 0.068 mD of permeability (10,572 feet).

Fine-grained sandstone with rip-up clasts of red mudstone and carbonaceous shale (10,633 feet).

Figure 2-17. Examples of lithology and depositional features identified in the NBU 253 core, section 10, T. 9 S., R. 21 E., Uintah County, Utah. Top of each photograph is oriented towards the top of the core.

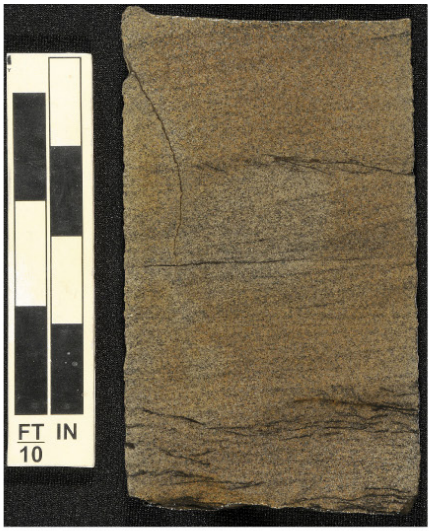

Open fracture in homogenous, fine-grained sandstone with slight iron(?) staining. Sandstone has 2.06% porosity (10,532 feet).

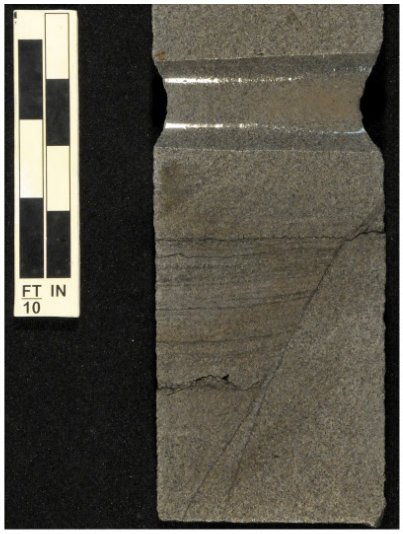

Vertical closed fracture off setting laminated sandstone on left with massive sandstone on the right. Fracture is offset at top by thin, carbonaceous laminae (10,631 feet).

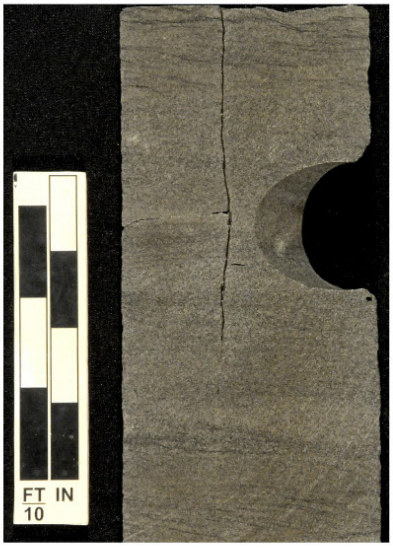

Open, vertical fracture in sandstone. No discernable mineralization in fracture (10,590 feet).

Fine-grained sandstone with high-angle cross-bedding and vertical natural fractures. Fractures are offset and slightly open with no discernable mineral fill (10,718 feet).

Figure 2-18. Examples of fractures found in the NBU 253 well, section 10, T. 9 S., R. 21 E., Uintah County, Utah. Top of each photograph is oriented towards the top of the core.

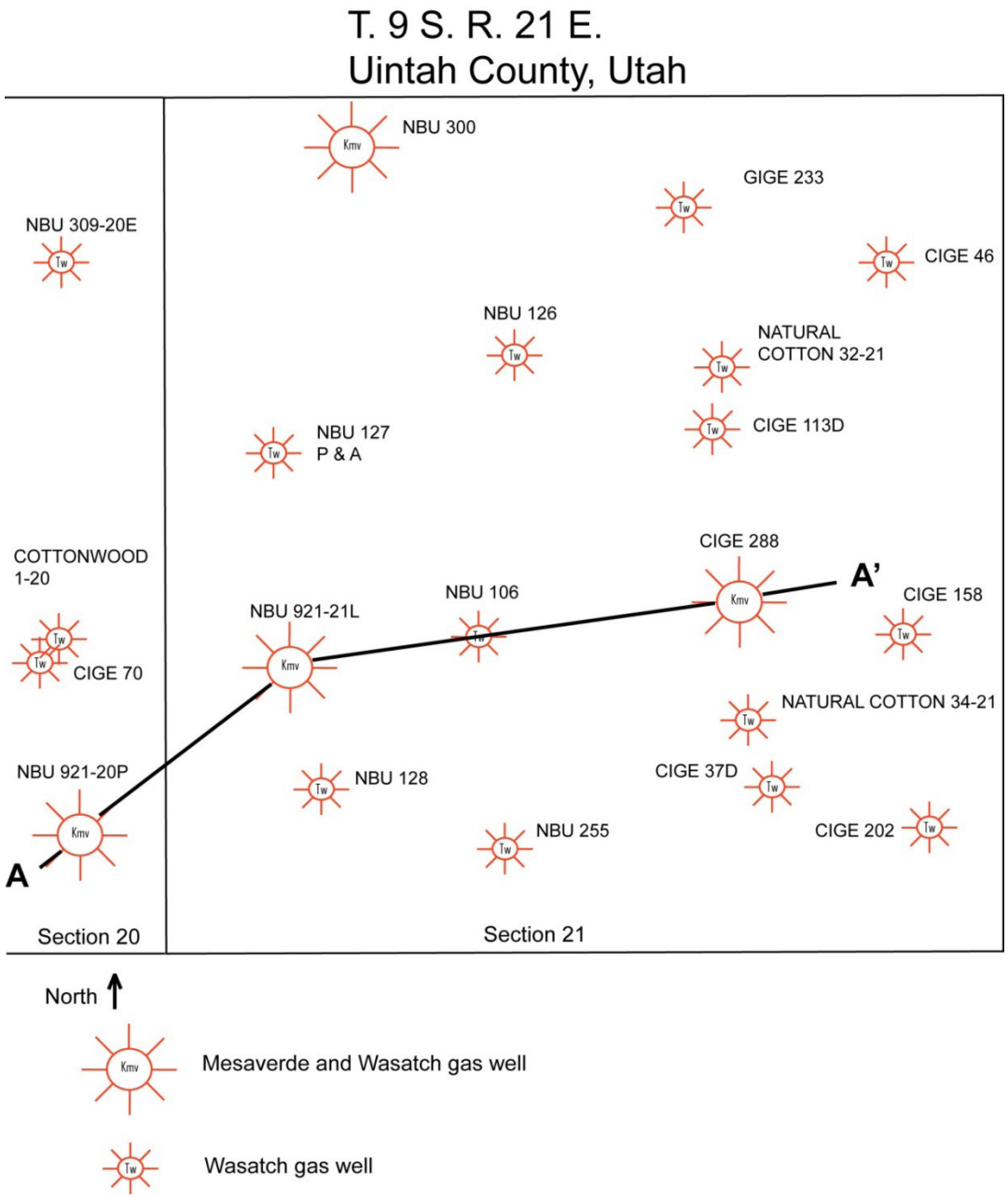

Figure 2-19. Wells in section 21 and eastern ¼ of section 20, T. 9 S., R. 21 E. Wells producing gas from the Tertiary Wasatch Formation that did not penetrate the Mesaverde Group are shown as small well symbols. The larger well symbols are wells that penetrate the Mesaverde Group are shown as small well symbols. The larger well symbols are wells that penetrate the Mesaverde and produce from both the Mesaverde and Wasatch. The NBU 127 well produced from the Wasatch until 1993 and has been plugged and abandoned. The line connecting the three Mesaverde wells represents the location of the cross section in Figure 2-20.

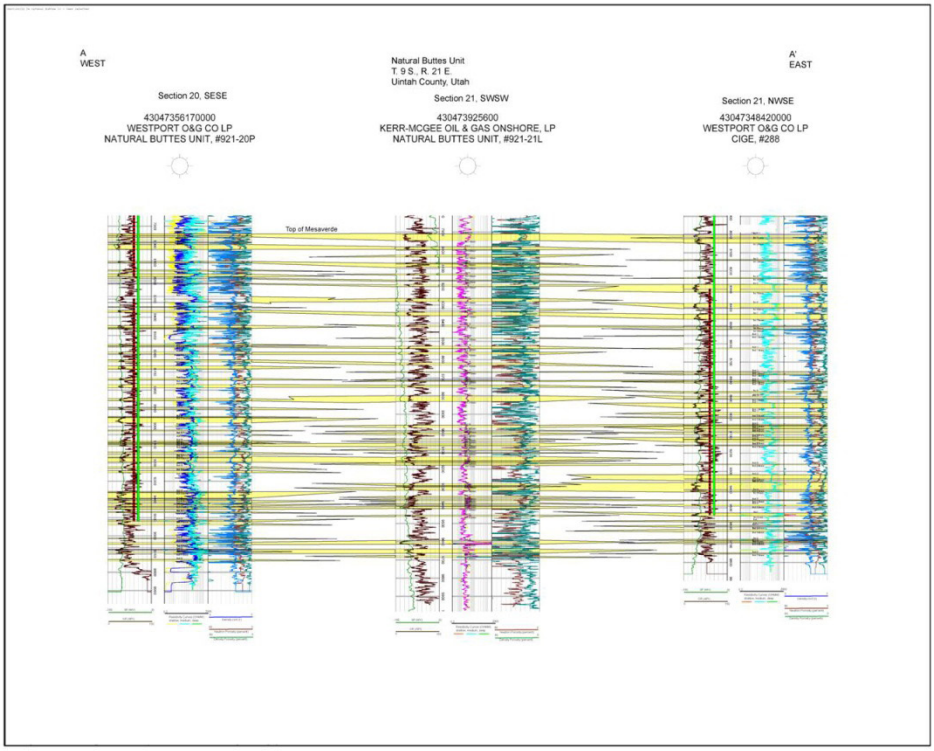

Figure 2-20. Cross section A to A' of the Mesaverde Group in section 20 and section 21, T. 9 S., R. 21 E., showing discontinuous nature of the sand bodies (shown in yellow). Cross section not to scale. See figure 14 for location of cross section and well spacing.

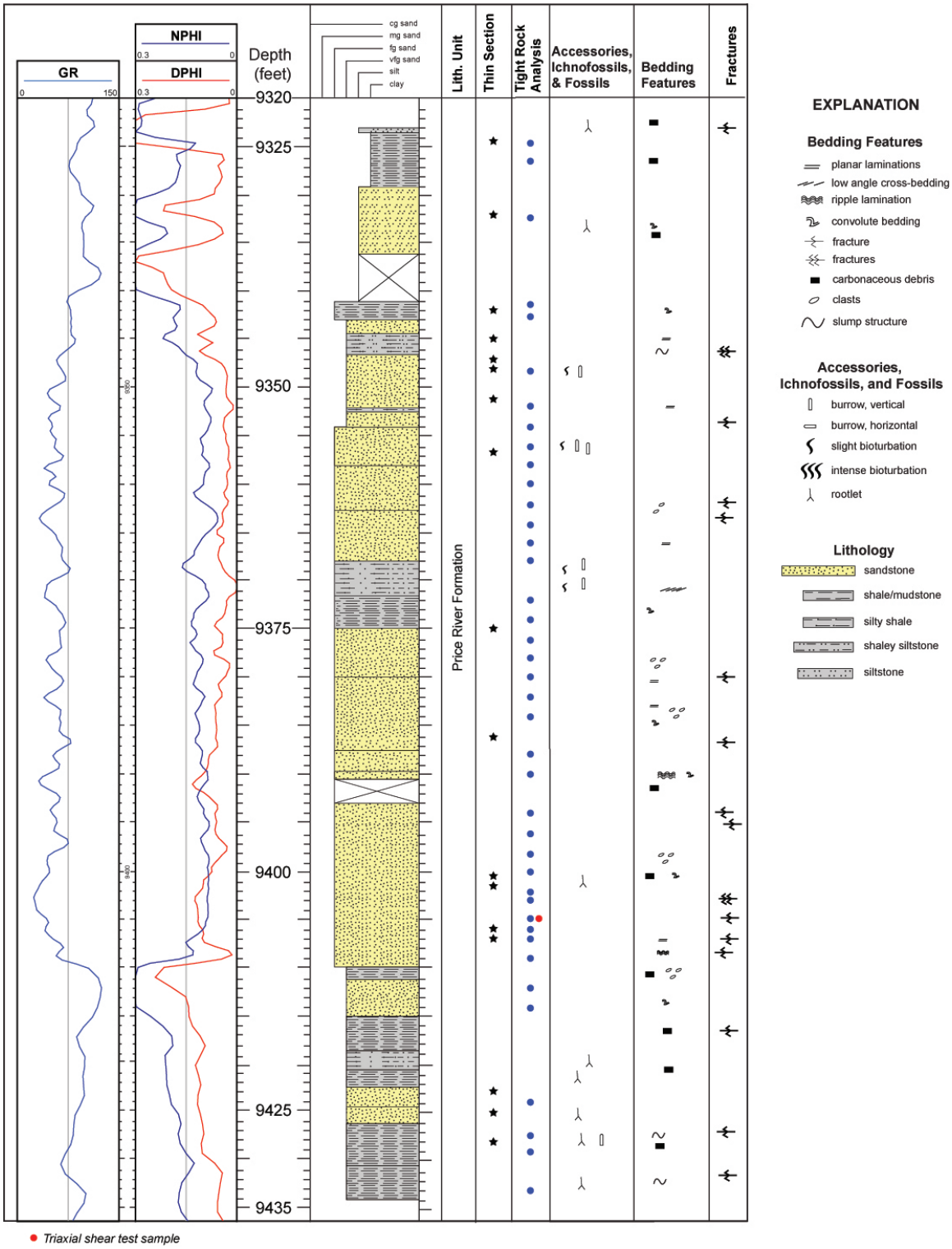

Figure 2-21. Graphical core description of the NBU 921-21L well, section 21, T. 9 S., R. 21 E., Greater Natural Buttes field, Uintah County, Utah.

Open, vertical fracture in carbonaceous mudstone (9324 feet).

Sub-vertical, mineral-filled fracture in very fine grain sandstone with soft-sediment deformation (9403 feet).

Calcite filled, sub-vertical fractures cross cutting burrowed, very fine grain sandstone (9348 feet).

Multiple, vertical, mineral-filled fractures in very fine grain sandstone (9401 feet).

Figure 2-22. Examples of fractures found in the NBU 921-21L well, section 21, T. 9 S., R. 21 E., Uintah County, Utah. Top of each photograph is oriented towards the top of the core.

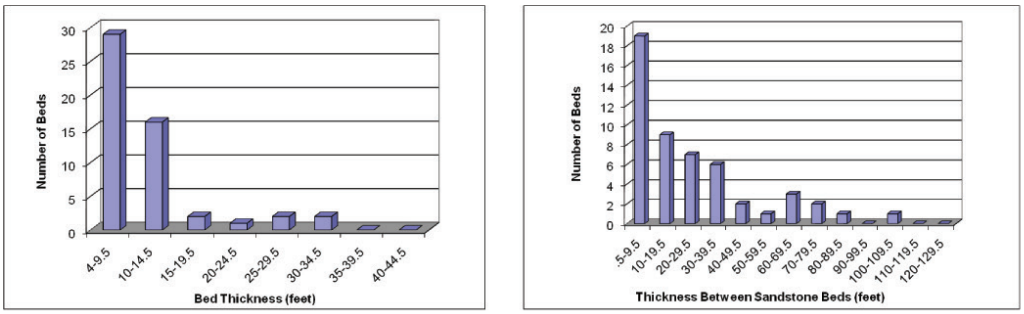

NBU 921-20P

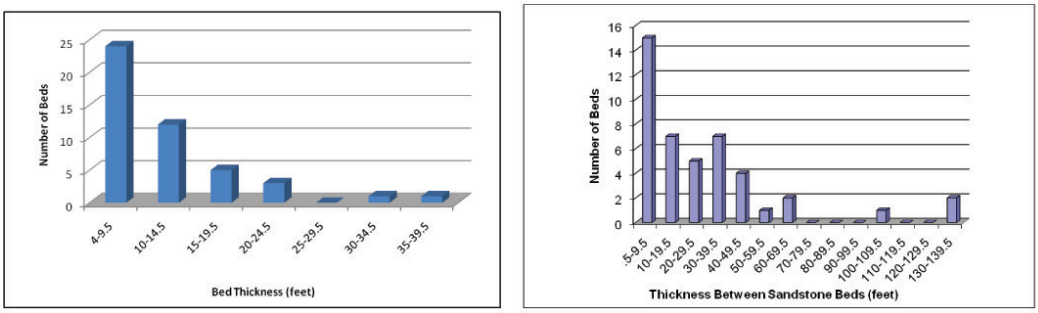

NBU 921-21L

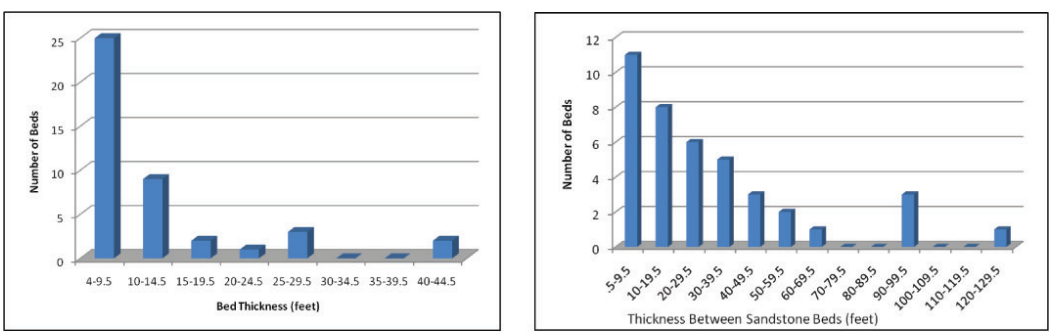

CIGE 288

Figure 2-23. Graphs showing bed thickness and distance between beds in wells penetrating the Mesaverde Group in the Tract 21 site. See Figure 2-19 for well locations.

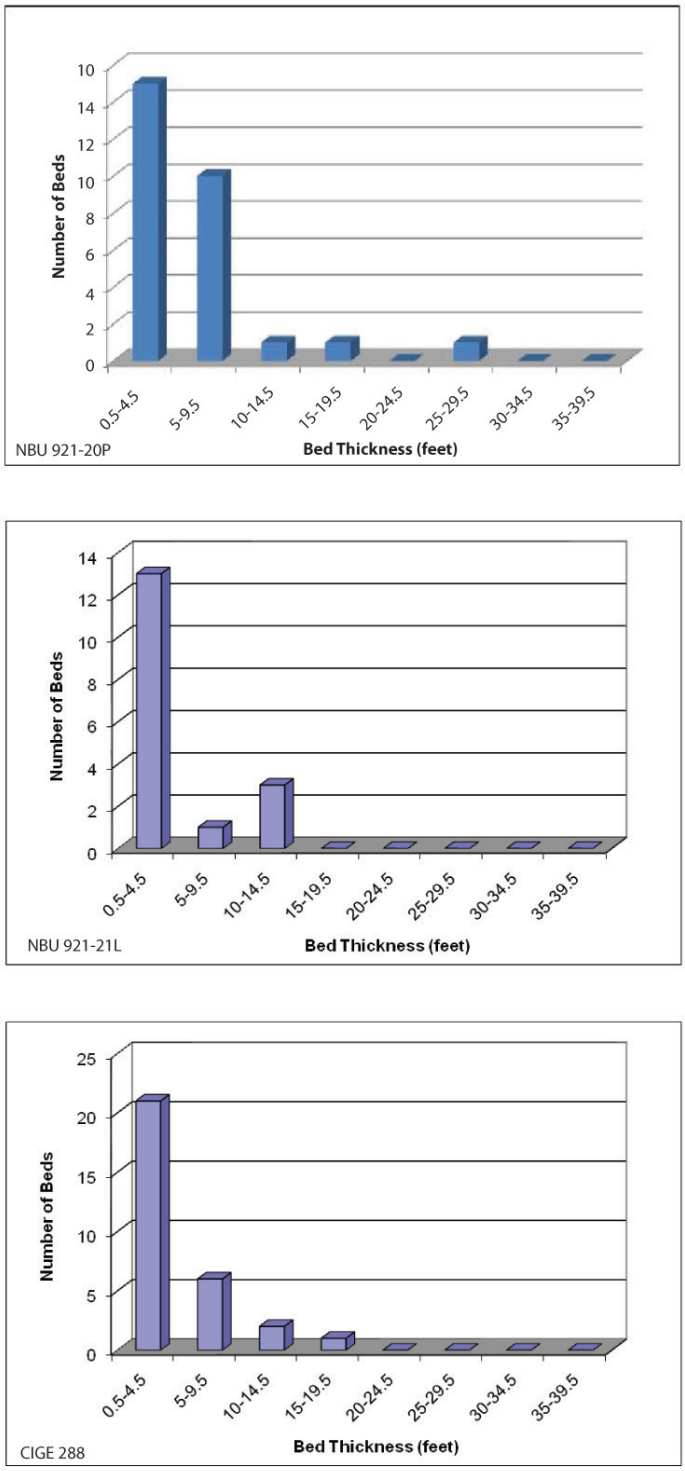

Figure 2-24. Graphs showing the bed thickness with 10% or more density porosity; most are less than 5 feet thick in wells penetrating the Mesaverde Group in the Tract 21 site. See figure 14 for well locations.

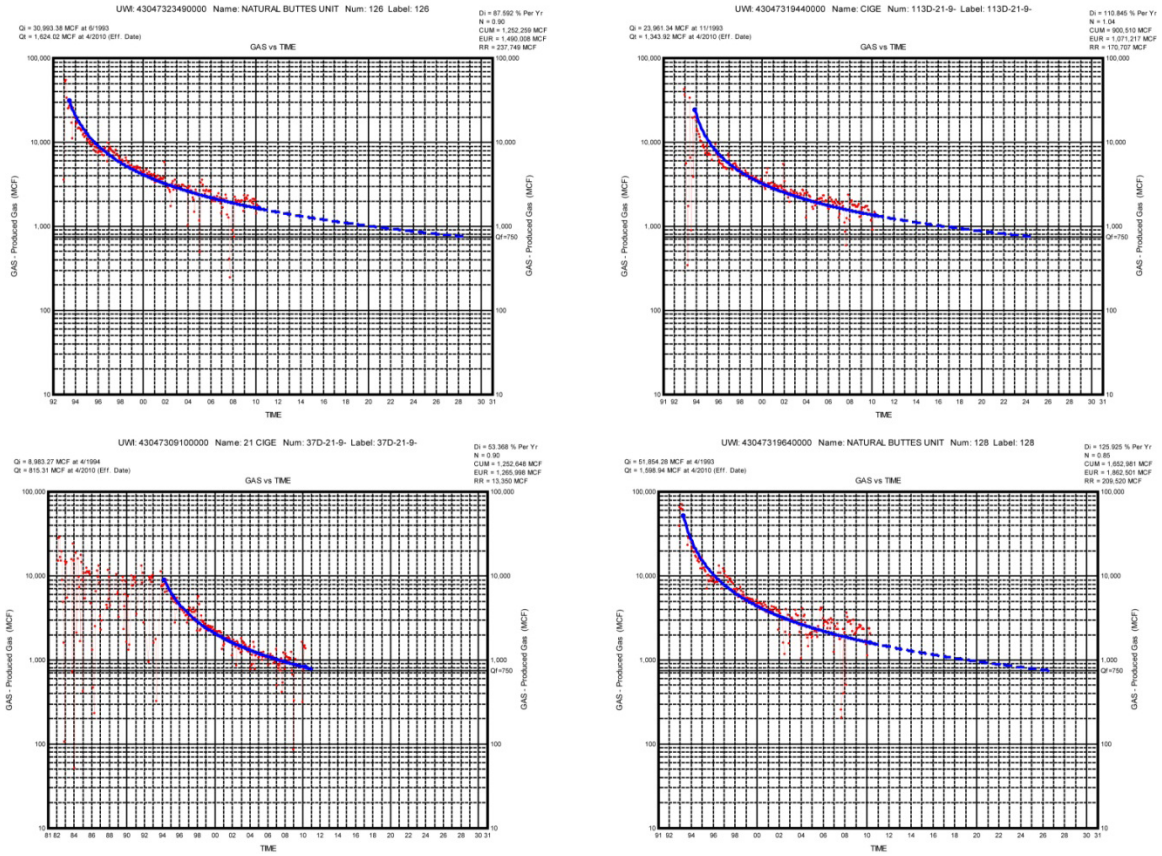

Figure 2-25. Production decline curves for four wells from section 21, T. 9 S., R. 21 E., that are producing from the Wasatch Formation. These wells have the longest production history of the Wasatch producers in the section. Estimated ultimate recovery is calculated using PETRA™ with a best "fit" hyperbolic curve and an economic limit of 750 MCFG/year for each well. The EUR is 1.1 to 1.9 BCFG/well. The red dots are production values and the blue dashed line is the decline curve.

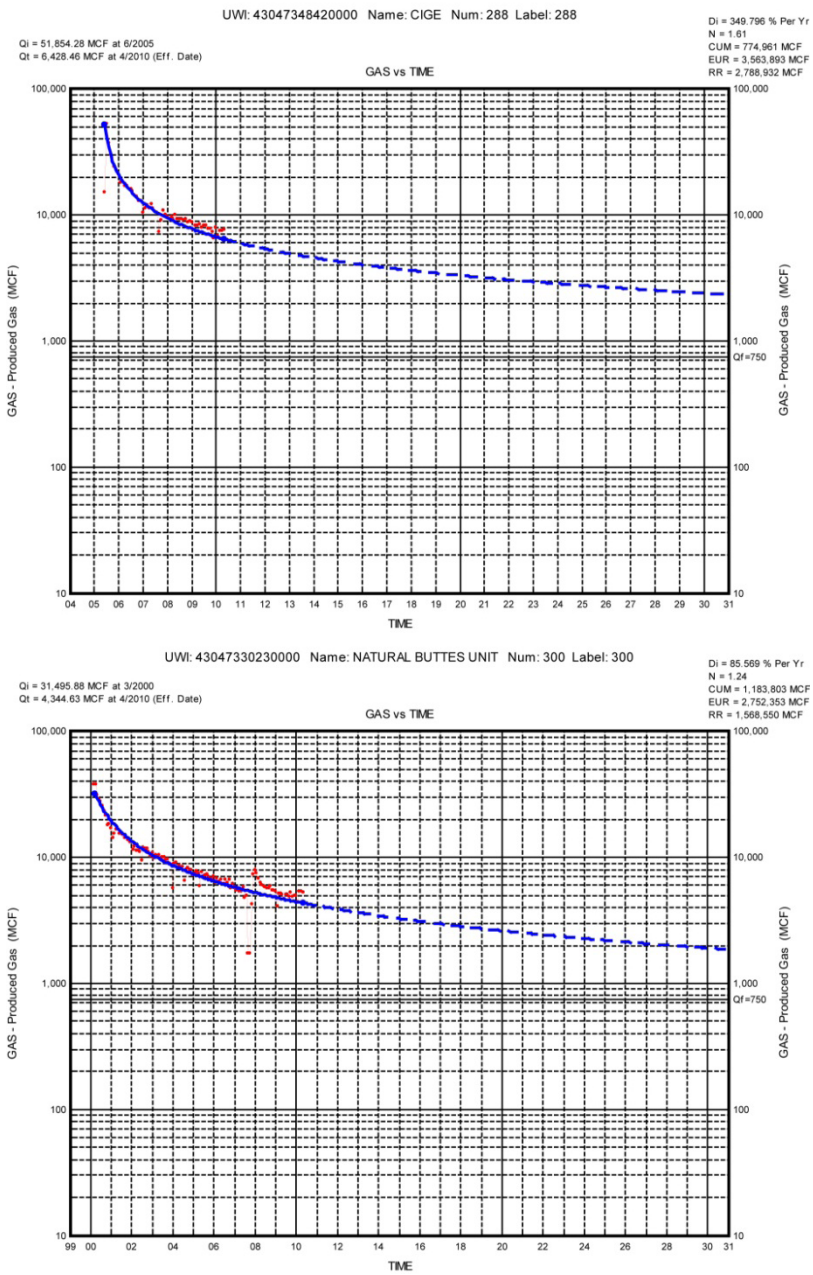

Figure 2-26. Production decline curves for the CIGE 288 and NBU 300 wells, both with commingled production from the Wasatch Formation and Mesaverde Group. Estimated ultimate recovery is calculated using PETRA™ with a best "fit" hyperbolic curve and an economic limit of 750 MCFG/year for each well. The EUR for the CIGE well is 3.6 BCFG and the EUR for the NBU 300 well is 2.8 BCFG. The red dotted line is production and the blue dashed line is the decline curve.

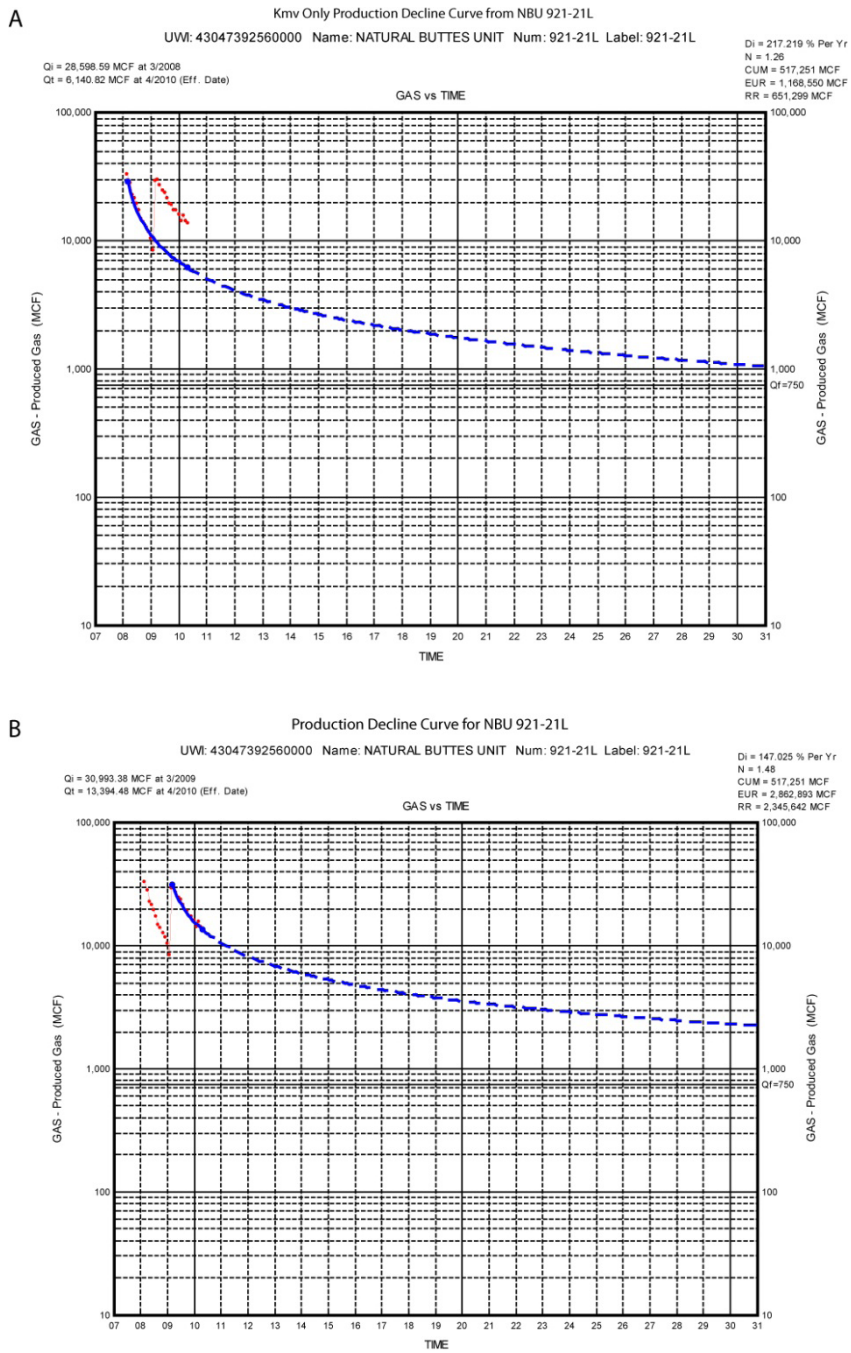

Figure 2-27. Production decline curve for NBU 921-21L well. Estimated ultimate recovery is calculated using PETRA™ with a best "fit" hyperbolic curve and an economic limit of 750 MCFG/year. A is EUR calculated from the first decline in production when the well was producing solely from the Mesaverde Group. Calculated EUR for the Mesaverde is 1.2 BCFG. B shows the decline in production after the well was recompleted with production commingled from the Wasatch Formation and Mesaverde. The calculated EUR for the Wasatch – Mesaverde commingled production is 2.9 BCFG. The red dotted line is production and the blue dashed line is the decline curve.

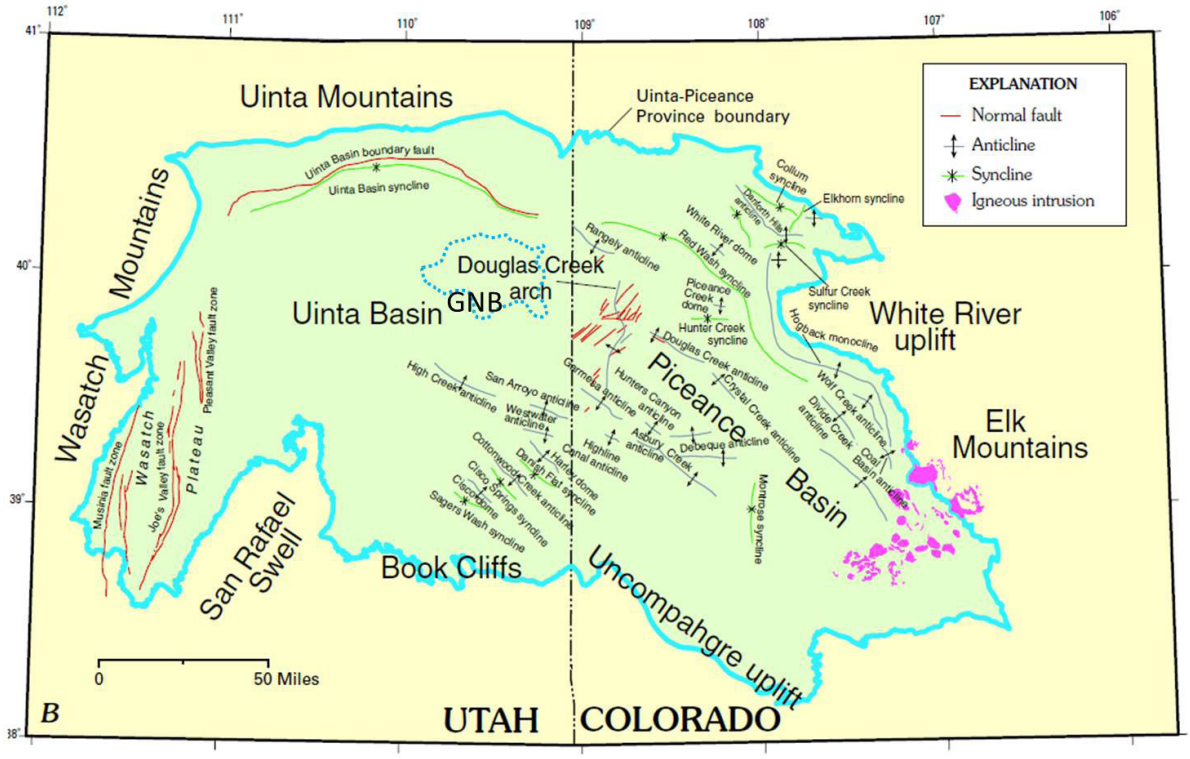

Figure 2-28. Regional structural map of the Uinta-Piceance basins (Johnson and Roberts, 2003).

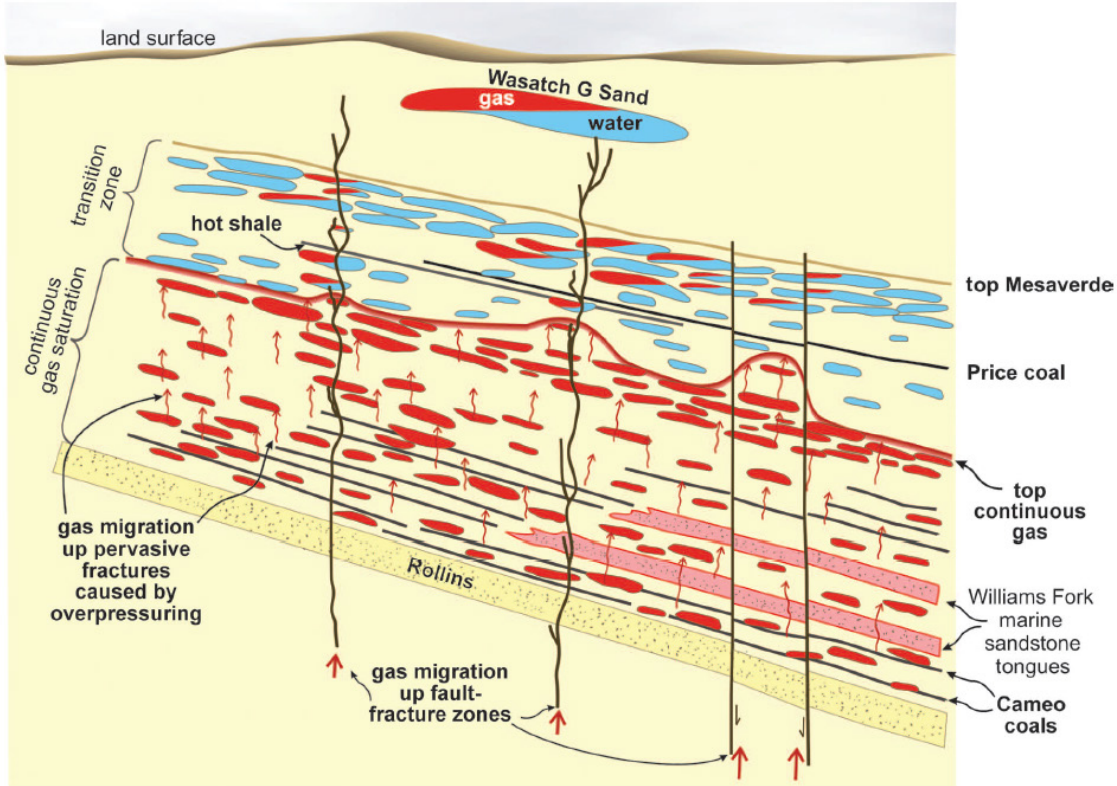

Figure 2-29. Gas migration model in the Mesaverde sediments, highlighting the importance of faults and fractures and the generation of fractures in the rocks by gas generation and associated overpressures (Cumella and Scheevel, 2008).

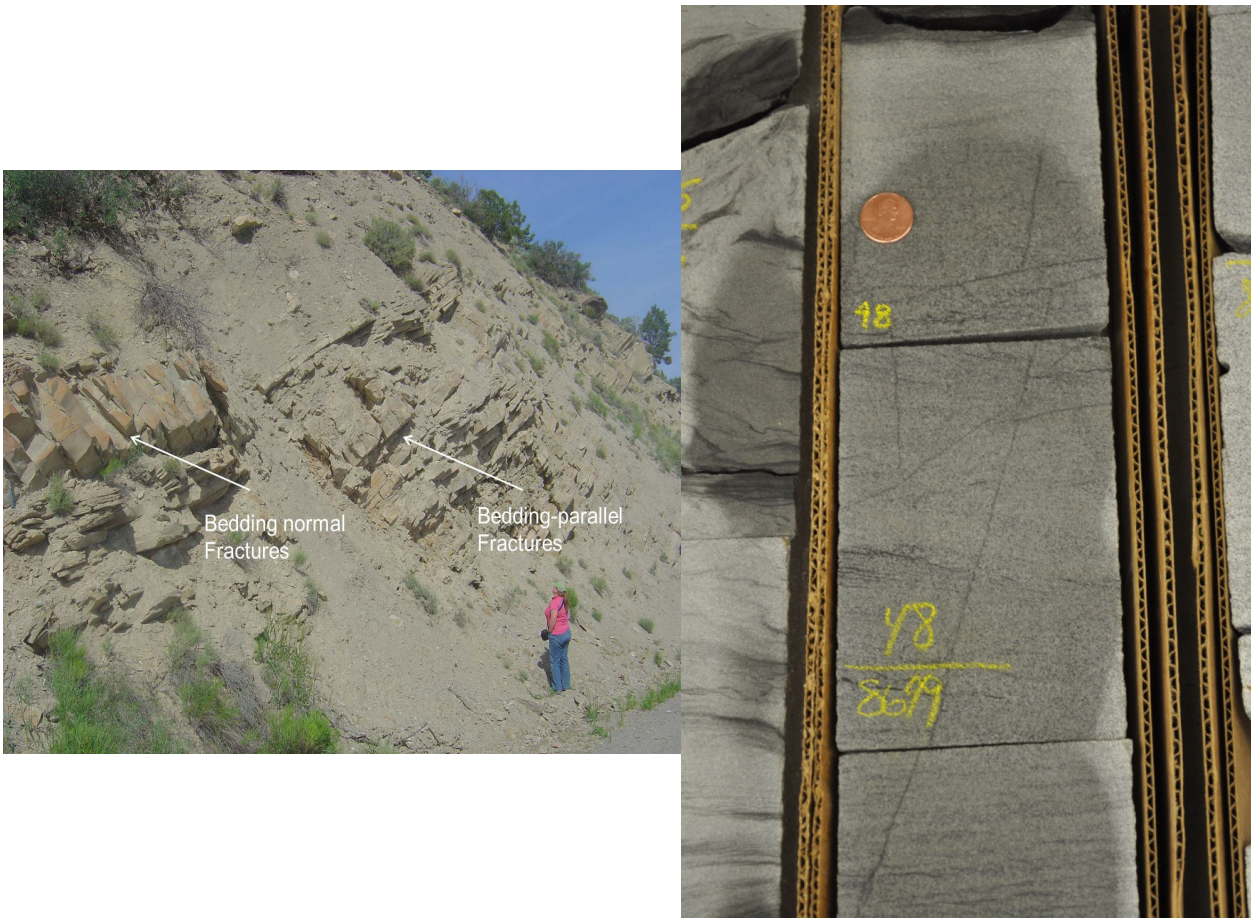

Figure 2-30. (A) Bedding parallel and bedding perpendicular joints in a tilted section of the Mesaverde sandstone, Douglas Creek Arch. (B) Fractures in a core of Mesaverde sandstone, Natural Buttes Well #85433, Anadarko (photos by Rasoul Sorkhabi).

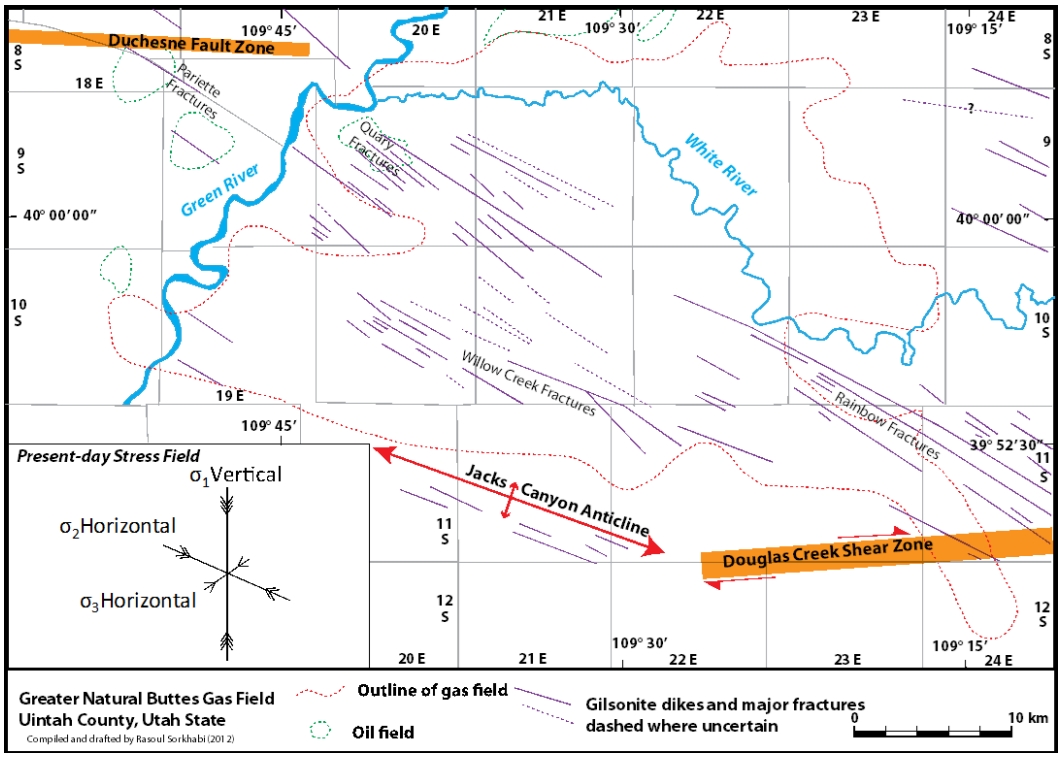

Figure 2-31. Structural map of the Greater Natural Buttes (compiled from Fouch et al., 1992; Osmond et al., 1992; Verbeek and Grout, 1992; Bader, 2009).

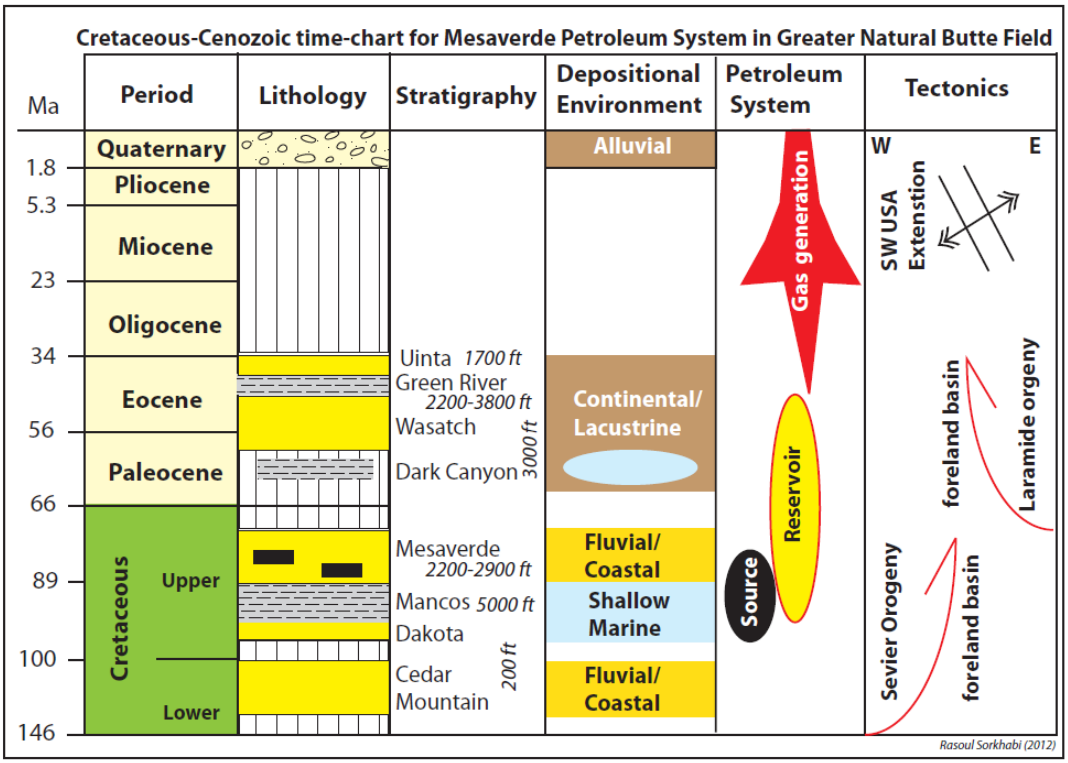

Figure 2-32. Cretaceous-Cenozoic event-chart for the Mesaverde petroleum system in the Greater Natural Buttes Field.

Natural Fracture Characterization

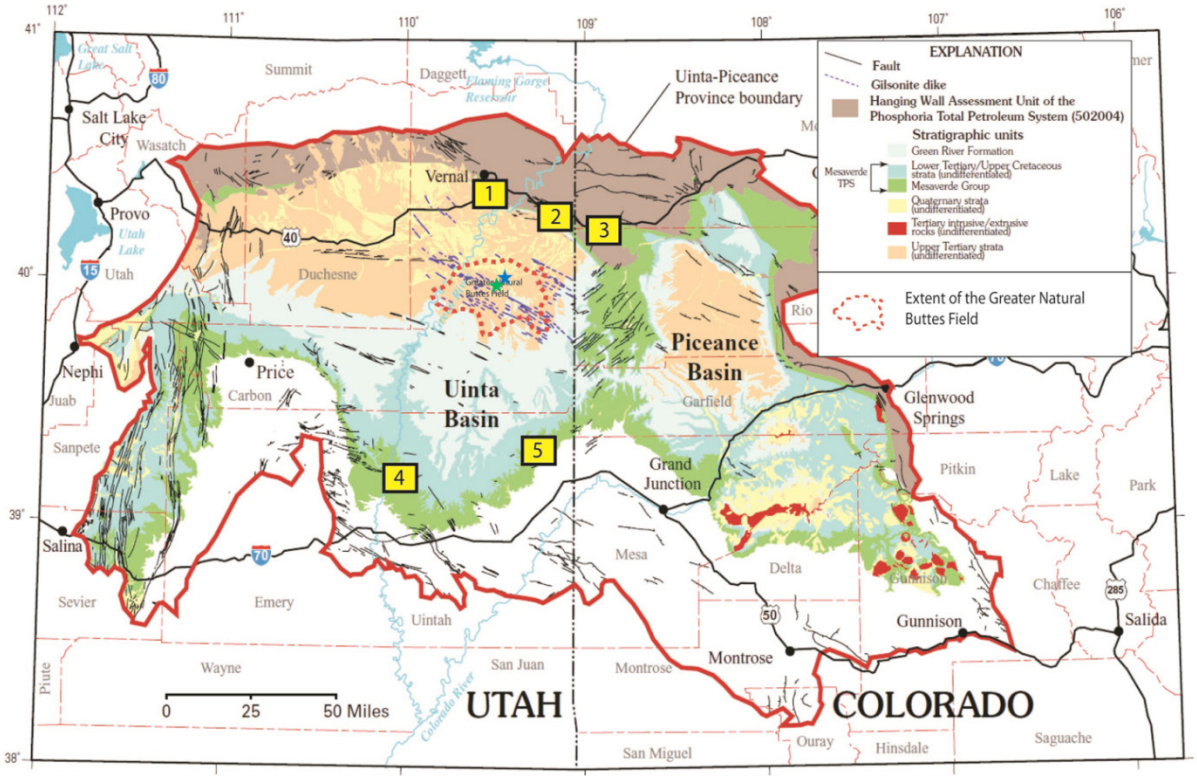

Figure 3-1. Location of the Greater Natural Buttes Gas Field along with the geologic map showing the outcrop exposures of the stratigraphic units within the Uinta Basin. The extent of the Mesaverde Total Petroleum System of the Uinta and Piceance Basins, Utah and Colorado is denoted by the red line. Major fault trends are indicated by the by the black lines. Blue lines indicate gilsonite dike trends. The green represents where Mesaverde Group outcrops and also delineates the extent of the Mesaverde Group TPS. Yellow squares indicate visited field localities where fracture data were collected. The white shading within the red line represents the Mancos Shale. The blue star represents the location of the NBU 253 and the green star is the location of the NBU 921-21L. Figure modified from Johnson and Roberts (2003).

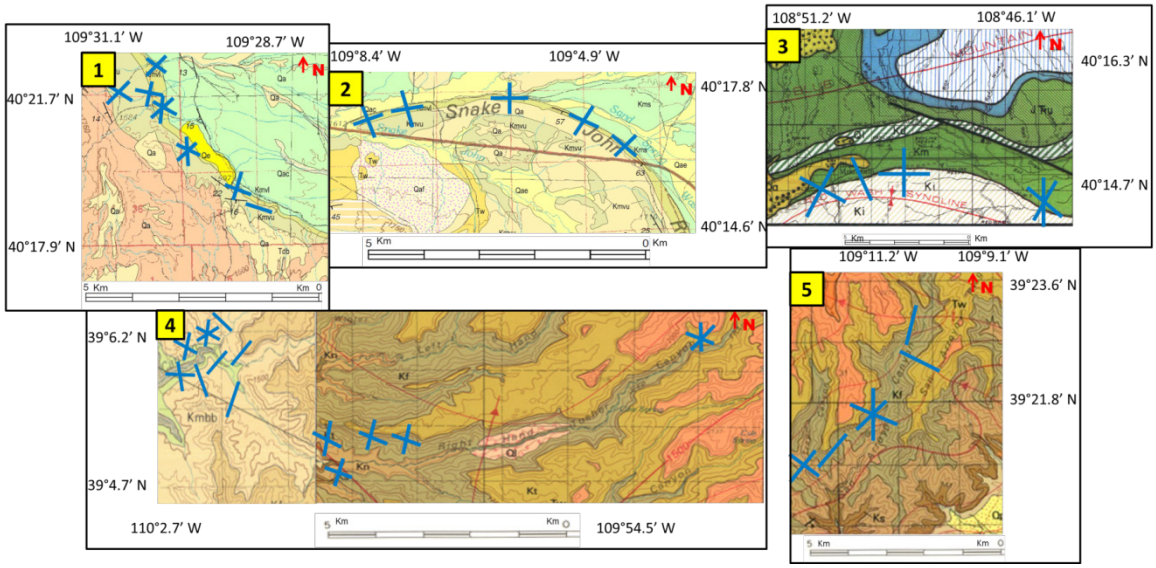

Figure 3-2. Azimuthal distribution of fracture sets at each field locality shown in Figure 3-1. Blue lines indicate orientation of fracture sets. Fracture set orientations are overlain onto the geologic maps of the corresponding area. Locailty 1 (Asphalt Ridge) shows orientation data from 11 scanlines overlain on the Sprinkel (2007) geologic map. Locality 2 (Snake John Reef) shows orientation data from 11 scanlines overlain on the Sprinkel (2007) geologic map. Locality 3 ("Blue Mountain Ridge") shows orientation data from 7 scanlines overlain on the Miller (1977) geologic map. Locality 4 (Tusher Canyon) shows data from 7 scanlines overlain on the Gualtieri (1988) geologic map. Locality 5 (San Arroyo Canyon) shows data from 17 scanlines on the geologic maps from Witkind (1988) and Gualtieri (1988). Bedding dips at Locality (4) and (5) are nearly flat. Red lines in (4) and (5) are structure contours drawn on top of the Castlegate Sandstone. Kmvl = lower Mesaverde Group. Kmvu = upper Mesaverde Group. Kms = Mancos Shale. Ki = Iles Formation of the Mesaverde Group. Kt = Tuscher Formation of the Mesaverde Group. Kn= Neslen Formation of the Mesaverde Group. Kmbb = Buck Tongue of the Mancos Shale.

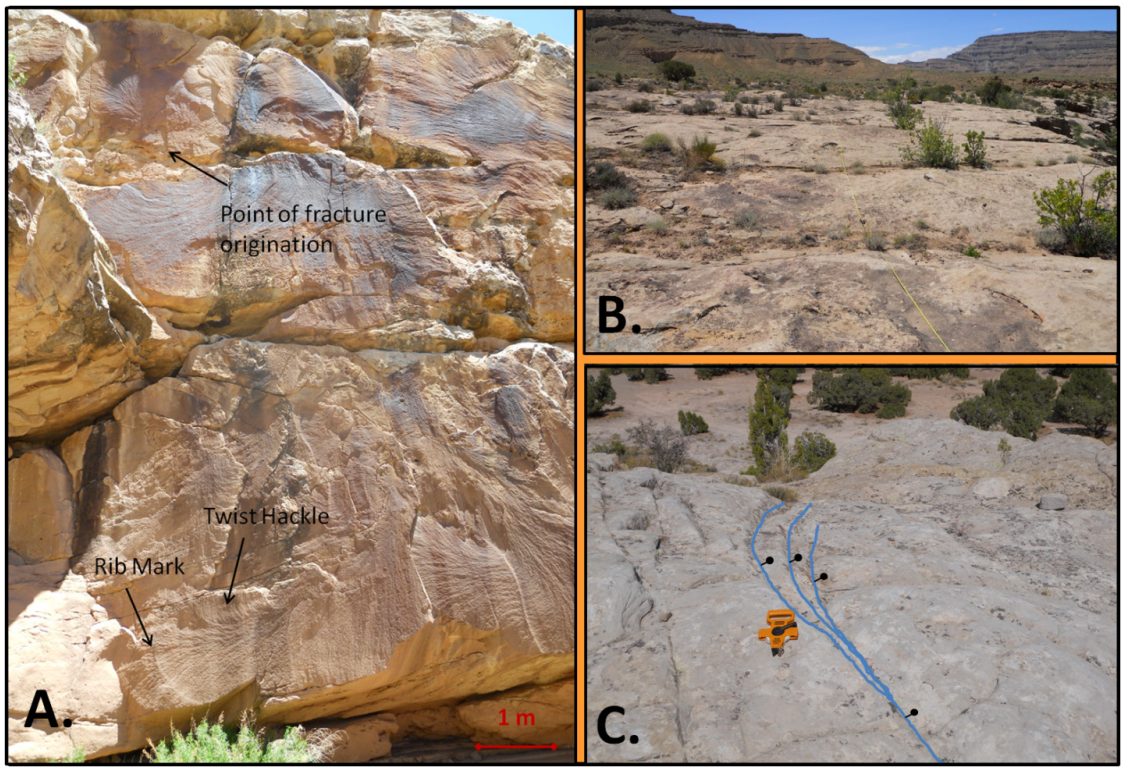

Figure 3-3. A. Photograph of plumose structures on vertical fracture surfaces within the Castlegate Sandstone at Tusher Canyon. B. Photograph of pavement surface on a bedding plane above the exposure in A. with a N-S-striking fracture set of the Castlegate Sandstone at Tusher Canyon. B. Photograph of pavement surface on a bedding plane above the exposure in A. with a N-S-striking fracture set of the Castlegate Sandstone. View is to the WNW. C. Photograph of a rare horsetail splay with interpreted shearing at Asphalt Ridge.

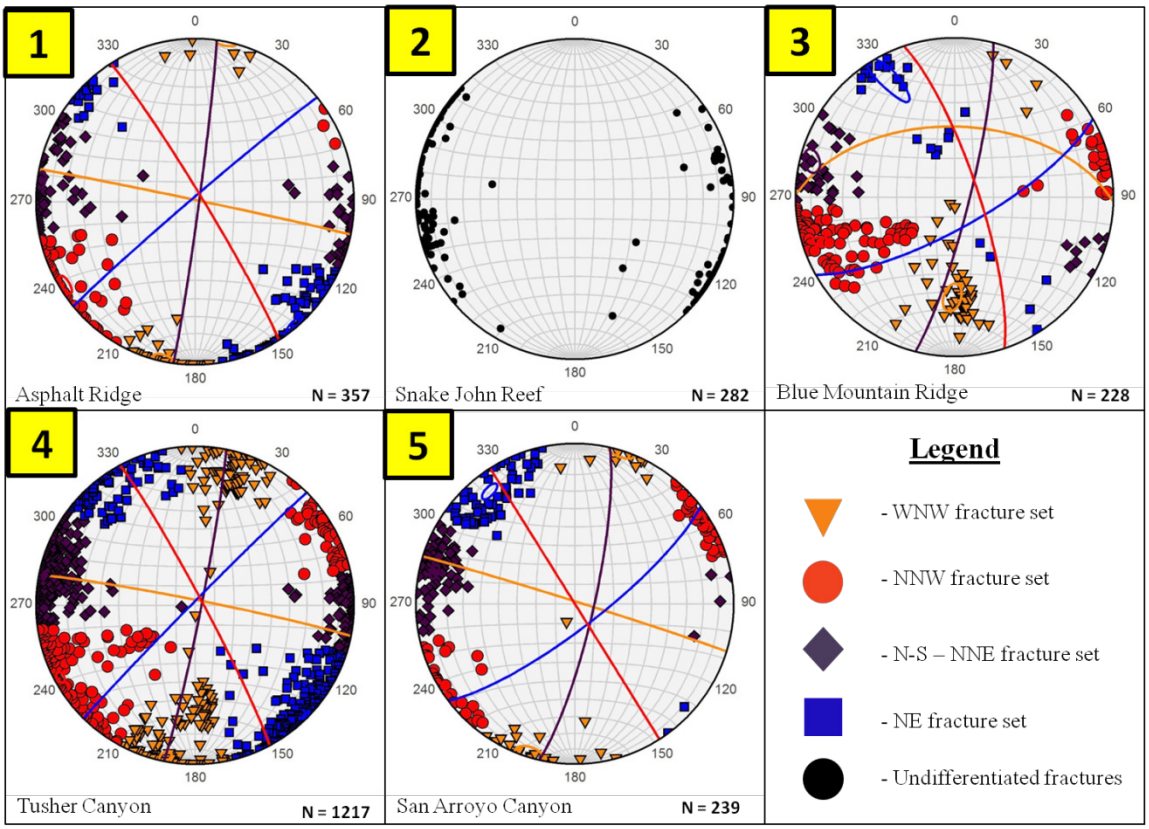

Figure 3-4. Stereonets showing poles to planes of all measured fractures from each locality [Figure 3-1]. Colored symbols are used to discriminate the orientations of distinct fracture sets. Colored lines represent eigenvectors to the fracture set associated with the color.

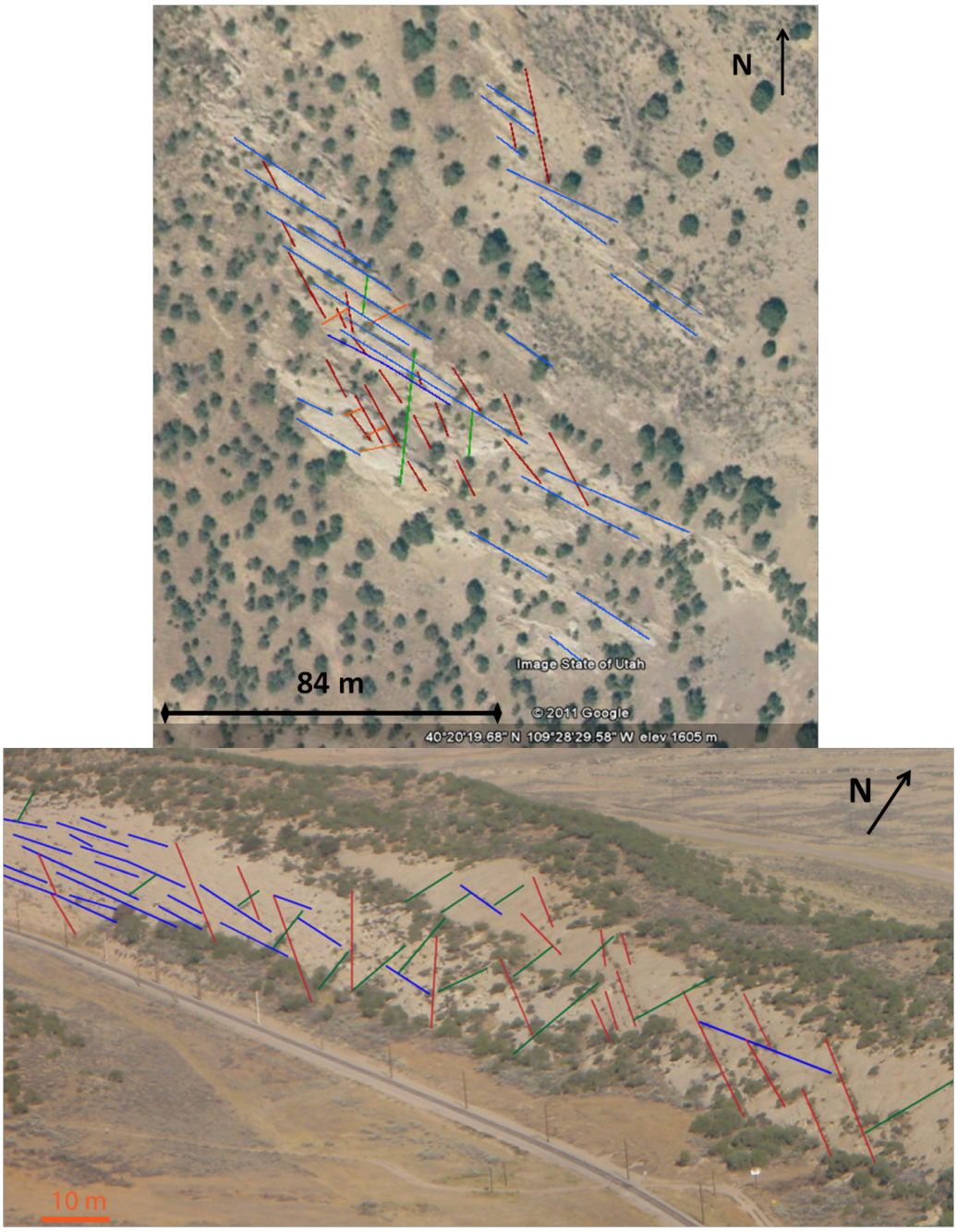

Figure 3-5. Mapped fracture sets on a Google Earth image of Asphalt Ridge (Locailty 1) (top) and a low – angle oblique air photo of "Blue Mountain Ridge" (Locality 3) (bottom) of outcrops of upper Mesaverde Group. Red = NNW fracture set. Blue = WNW-striking fracture set. Green = N-S-striking set. Orange = NE-striking set.

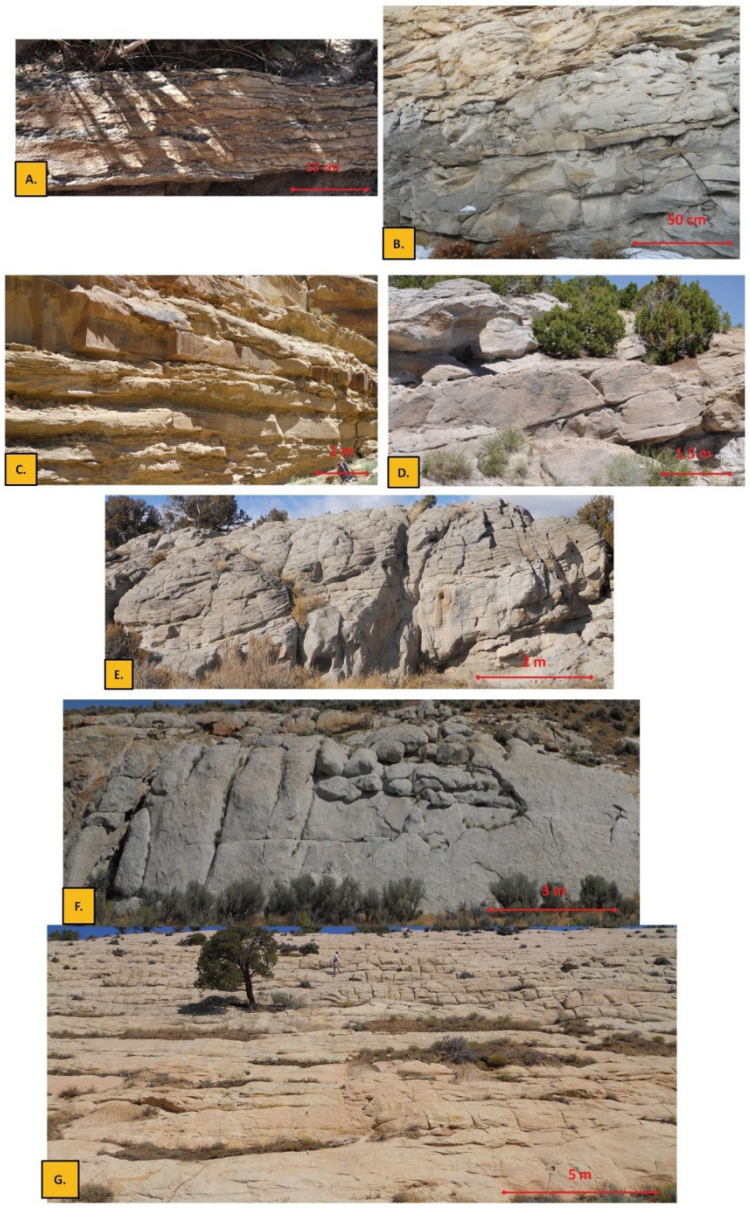

Figure 3-6. Photographs of the seven sampled lithofacies. The lithofacies are described in Table 3-2. Photo A is showing thinly bedded, very fine-grained sandstone interbedded with mudstones. Photo B shows medium bedded laterally discontinuous, lenticular medium- grained sandstone. Gold lines are delineating several lenticular sand bodies of classified within Lithofacies 2. Photo C shows medium bedded, continuous, fine-grained sandstones. Arrows are pointing to multiple medium bedded, continuous sandstones that define Lithofacies 3 within the photo. Photo D shows a thick discontinuous, lenticular, fine-grained sandstone. Gold lines delineate the geometry of the sandstone unit. Photo E shows a thick, tan, laterally discontinuous, upward-fining, medium-grained sandstone atop of a thick, laterally discontinuous, fine-grained sandstone. These two sandstone units are behaving as a single mechanical unit. Photo F is a dip-slope of a thickly- bedded, tan, laterally continuous, cross-bedded, coarse-grained sandstone. Photo G shows a bedding plane exposure of a massively bedded, tan, laterally continuous, medium-grained sandstone.

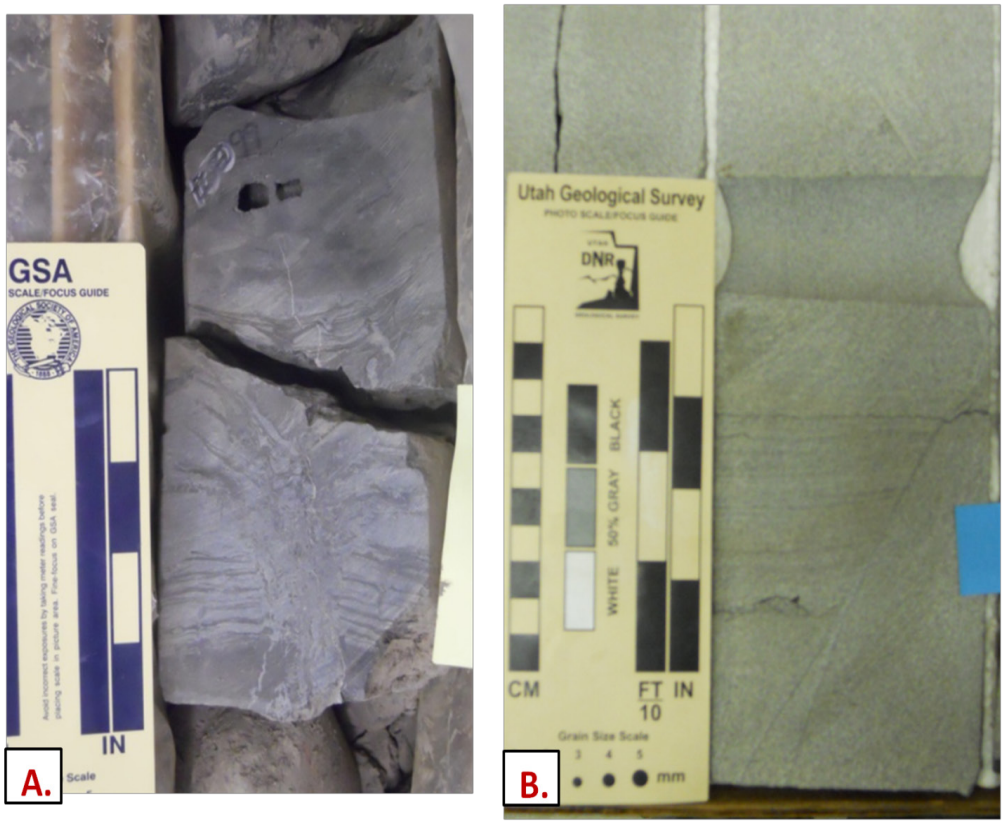

Figure 3-7. (A.) Multiple calcite filled fractures penetrating a fluid escape structure within core from well NBU 921 – 21L at 3,250 meters depth. (B.) Shear fracture terminating into a mud parting and splaying out near the bottom of the core off setting finely laminated sandstone (on left) against a more massive sandstone (on right) at 3,231 meters depth. Amount of offset is unknown. Top of the photos corresponds to the up-direction of the cores.

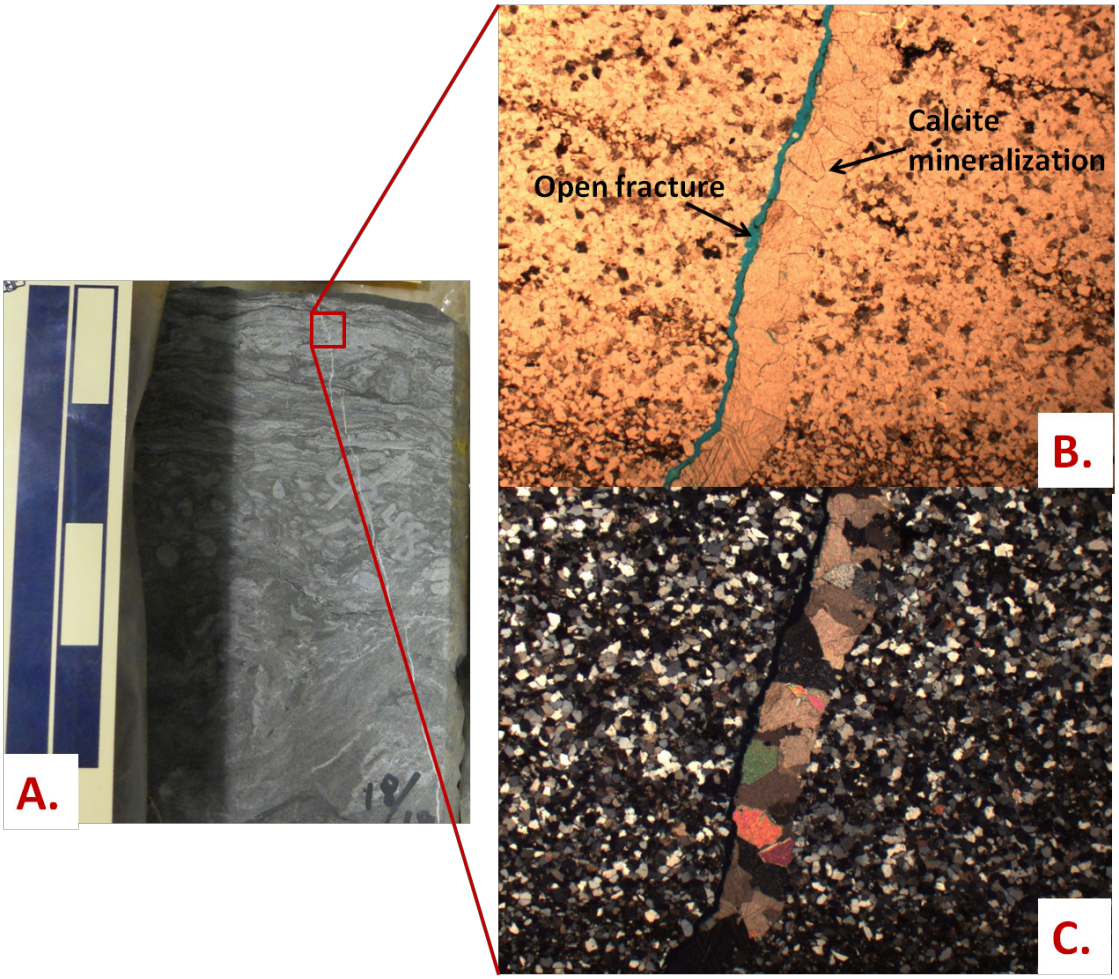

Figure 3-8. Left photograph is of core from well NBU 921 – 21L from the Price River Formation at 2349 meters deep with an extensional fracture with coarse calcite mineralization with an open, unfilled fracture penetrating the edge of the calcite mineralized fracture. Photomicrographs are taken in plane polarized light (B.) and cross polarized light (C.) with 2.5x magnification. Blue epoxy fills void space.

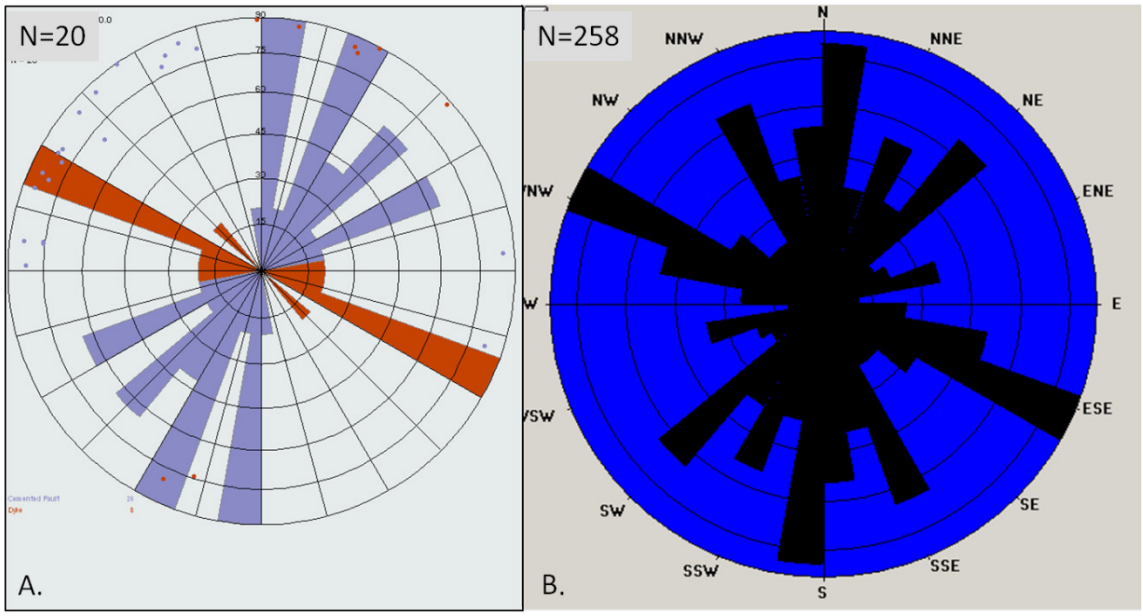

Figure 3-9. Rose diagrams comparing fracture orientations from the subsurface and outcrop. A) Rose diagram orientations of natural fractures from well NBU 920-36M. Red indicates open fractures and blue indicates partially open fractures. Analyses performed by Exterra. B) Rose diagram of orientations of regional fractures measured at the Asphalt Ridge locality (~45 kilometers to the north).

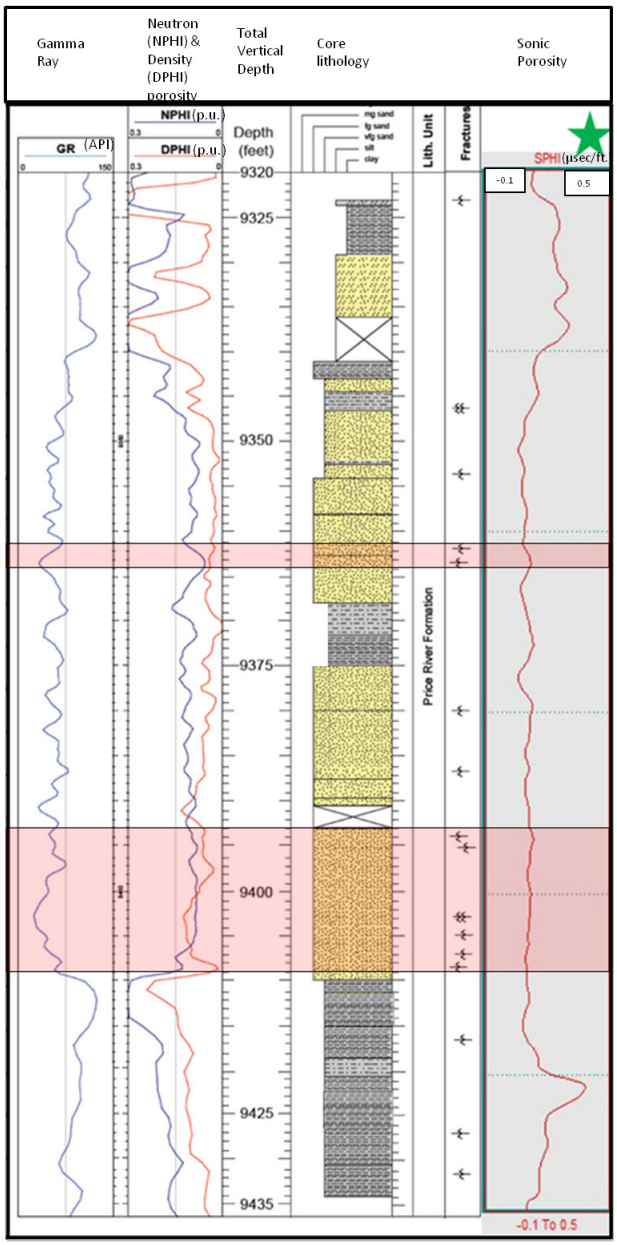

Figure 3-10. Fracture stratigraphy of well NBU 921-21L core compared with wireline log curves. The lithologic logs for each core is matched with the gamma-ray (GR), neutron porosity (NPHI), density porosity (DPHI), and sonic porosity (SPHI) along with fracture occurrences. Fractures generally occur in low porosity values sandstones. The porosity curves indicate very low porosity where fractures are present. Red boxes indicate lowest porosity zones of sandstone with fractures present. Fracture symbols with multiple vertical wavey lines indicate the presence of more than one fracture at the noted depth. Green star indicates the location of the well on Figure 2. Lithologic core description was modified from Carney et al, 2011.

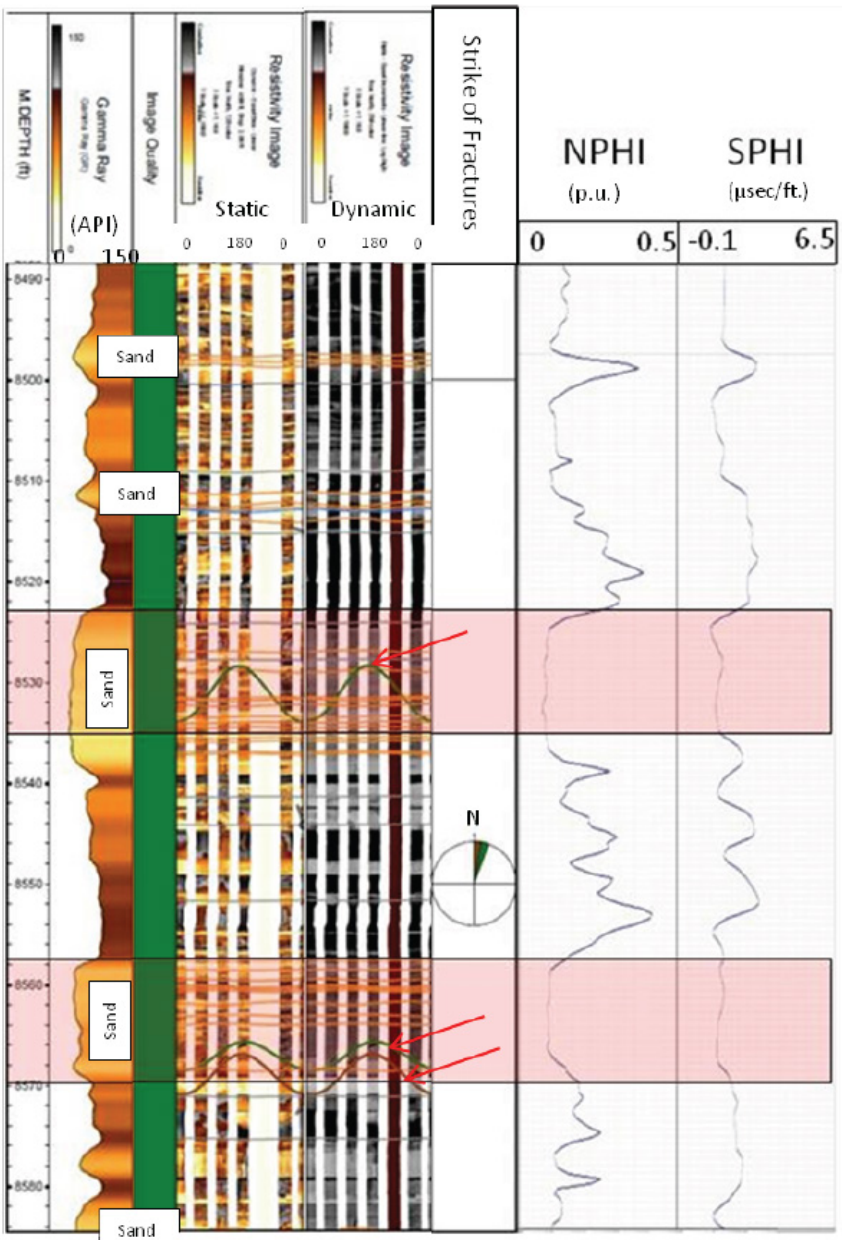

Figure 3-11. The figure displays the gamma ray (GR), static and dynamic resistivity image logs, sonic porosity (SPHI) and neutron porosity (NPHI) logs for well NBU 921-21L from 2587 – 2616 meters depth. The static and dynamic resistivity image logs of the well bore has interpreted bedding planes and fracture planes drawn on the images. Three fractures, denoted by the red arrows, have been interpreted (green = closed, brown = partially open). The fractures have been plotted on the Rose diagram showing their orientation. Gamma Ray track has interpreted sandstone units denoted on it. Green image quality represents high quality image logs were acquired over these depths. Orange, blue, and gray lines on the resistivity images are interpreted bedding features. Image log analysis was done by Exterra. Shaded boxes are highlighting fractured, low porosity sandstone lithofacies. Based on sandstone log thickness the two sandstones within the shaded boxes are comparable to lithofacies 5 & 6 that have been sampled in outcrop.

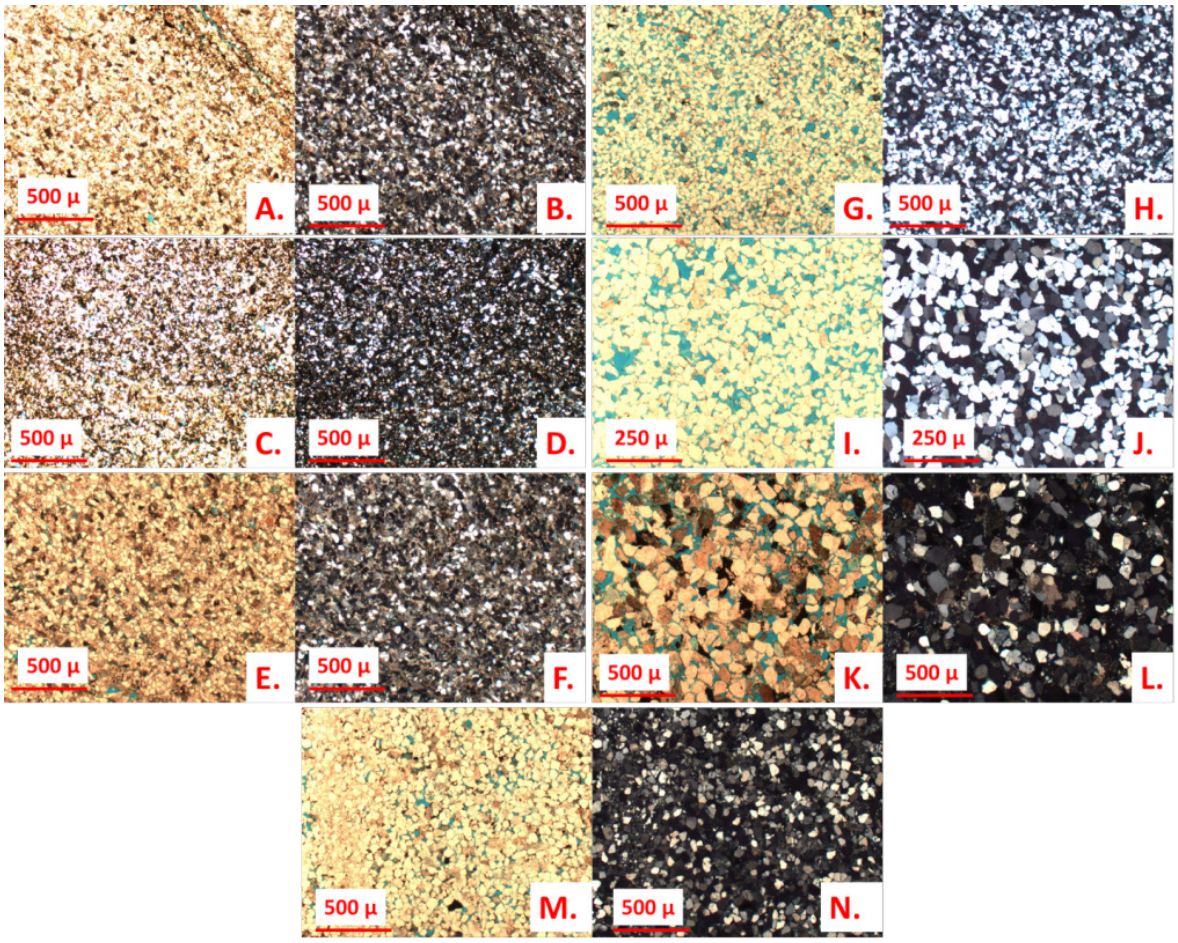

Figure 3-12. Photomicrographs of typical thin sections samples from lithofacies 1 – 7 sampled in outcrop taken in plane polarized light (left) and cross-polarized light (right). Blue epoxy fills the void space in the thin sections. A & B) Thin sections of lithofacies 1 is a poorly sorted, sub-angular to sub-rounded, fine-grained carbonate cemented lithic arenite. C & D) Thin sections of lithofacies 2 is a poorly sorted, sub-angular to sub- rounded, fine-grained carbonate cemented lithic arenite. E & F) Thin sections of lithofacies 3 shows a poorly sorted, sub-angular to sub-rounded, fine-grained carbonate cemented lithic arenite. G& H) Thin sections of lithofacies 4 is a poorly sorted, angular to sub-rounded, medium grained lithic arenite with sparse clay cement. I & J) Thin sections of lithofacies 5 is a poorly sorted, sub-angular to sub-rounded, medium-grained, quartz arenite with cemented grains by pressure solution and sparse clay cement. K & L) Thin sections of lithofacies 6 is a poorly sorted, angular to sub-rounded, coarse-grained lithic arenite with cemented grains by pressure solution and sparse clay cement. M & N). Thin sections of lithofacies 7 is a poorly sorted, sub-angular to sub-rounded, fine-grained, quartz arenite with cemented partially by pressure solution, clay and syntaxial quartz overgrowths. Note the coarser grain size of Lithofacies 6.

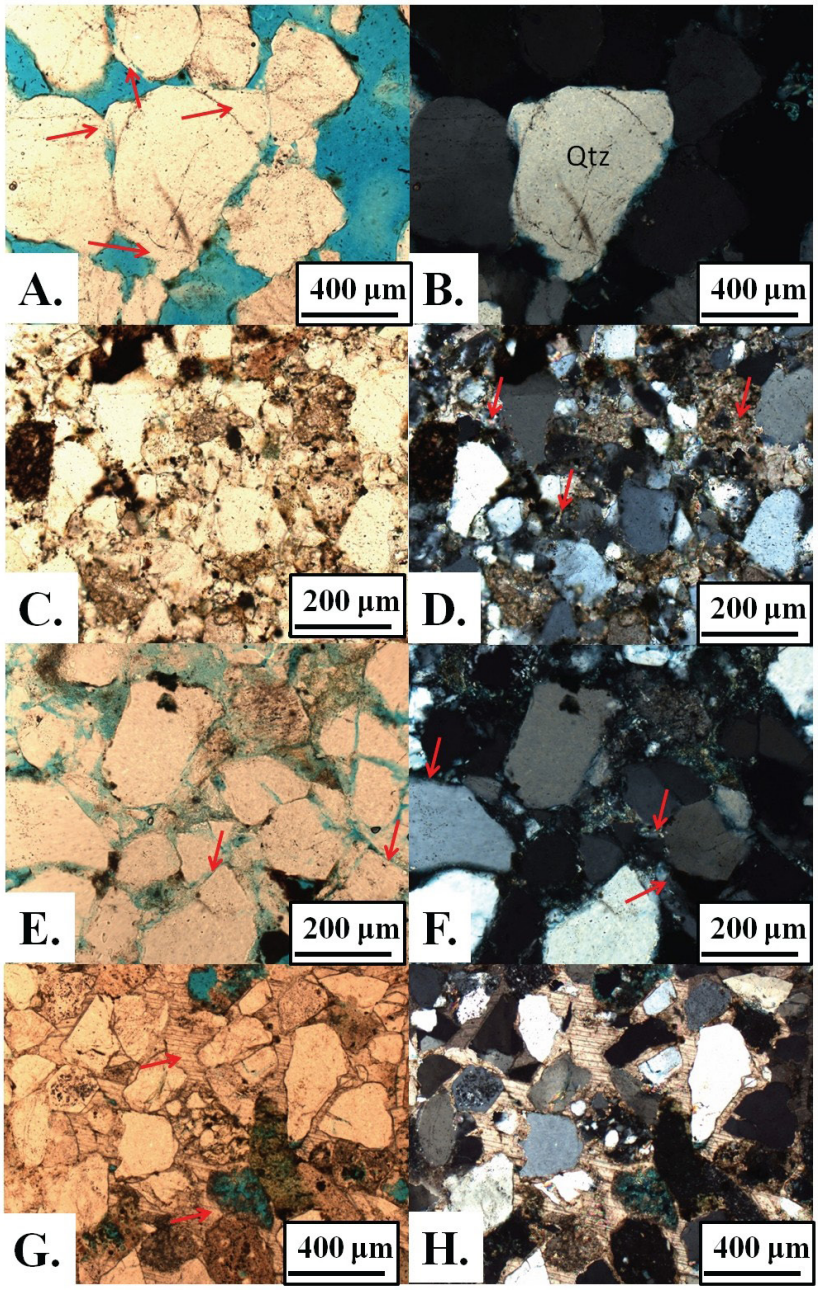

Figure 3-13. Photomicrograph of outcrop samples with the left photos being in plane polarized light and the right photos are in cross polarized light. A & B) Medium-grained, moderately soted, quartz arenite with quartz cement. Arrows point to the quartz overgrowth that are cementing grains to each other. C & D) Fine-grained, poorly sorted, sub-angular to sub-rounded, lithic arenite with fine-crystalline calcite cement. Arrows point to examples of fine-crystalline calcite cement. E & F) Fine-grained , poorly sorted, sub-angular, quartz arenite with clay mineral cement. Arrows point to clay minerals cementing quartz and lithic grains. G & H) Medium-grained, poorly sorted, sub-angular, quartz arenite with poikilotopic calcite cement. Arrows point to examples of poikilotopic calcite cement within the sample. Blue epoxy fills the void space within the thin section.

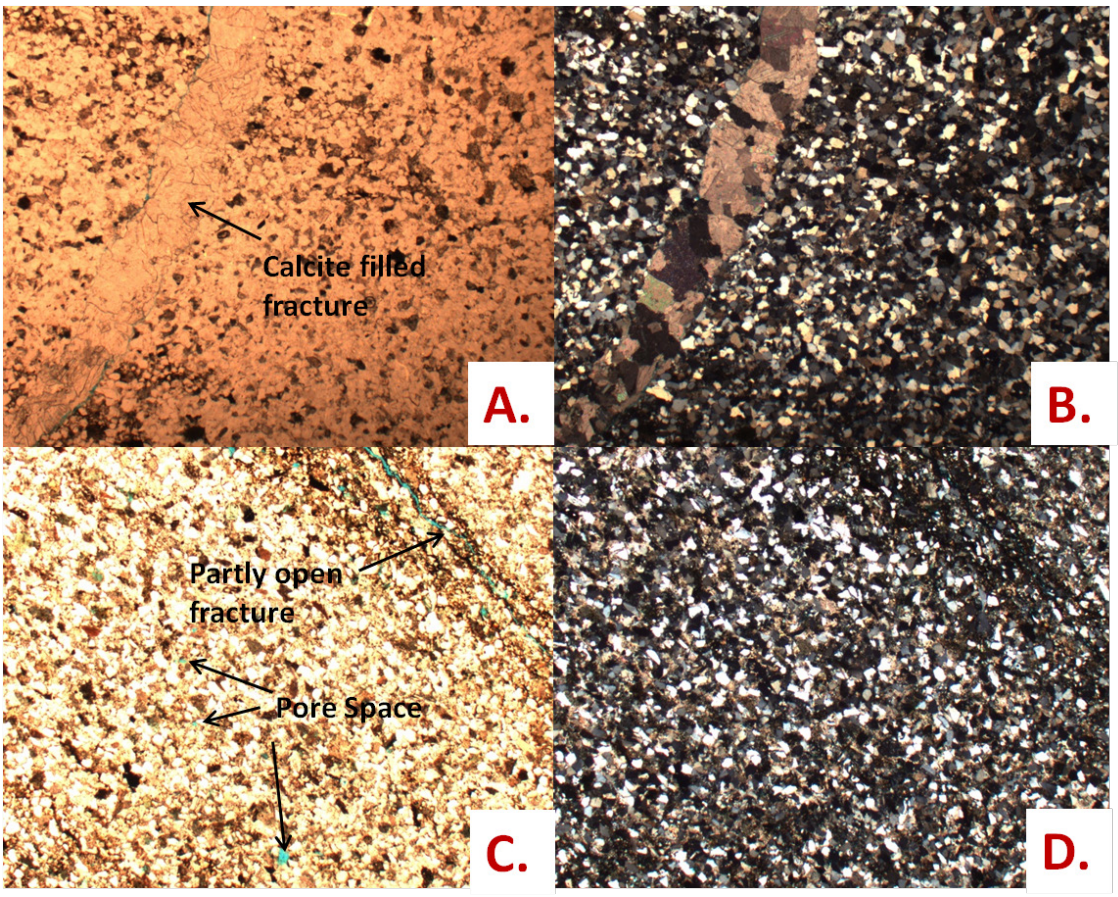

Figure 3-14. Photomicrographs of outcrop (photo C & D) and core (photo A &B) samples taken at 2.5x magnification with the left photos being in plane polarized light and the right photos are in cross polarized light. Photos A & B taken of a calcite mineralized fracture within a very fine grained lithic arenite. Photos C & D are taken of an open, unfilled fracture from outcrop in a fine-grained lithic arenite. Note the lack of pore space.

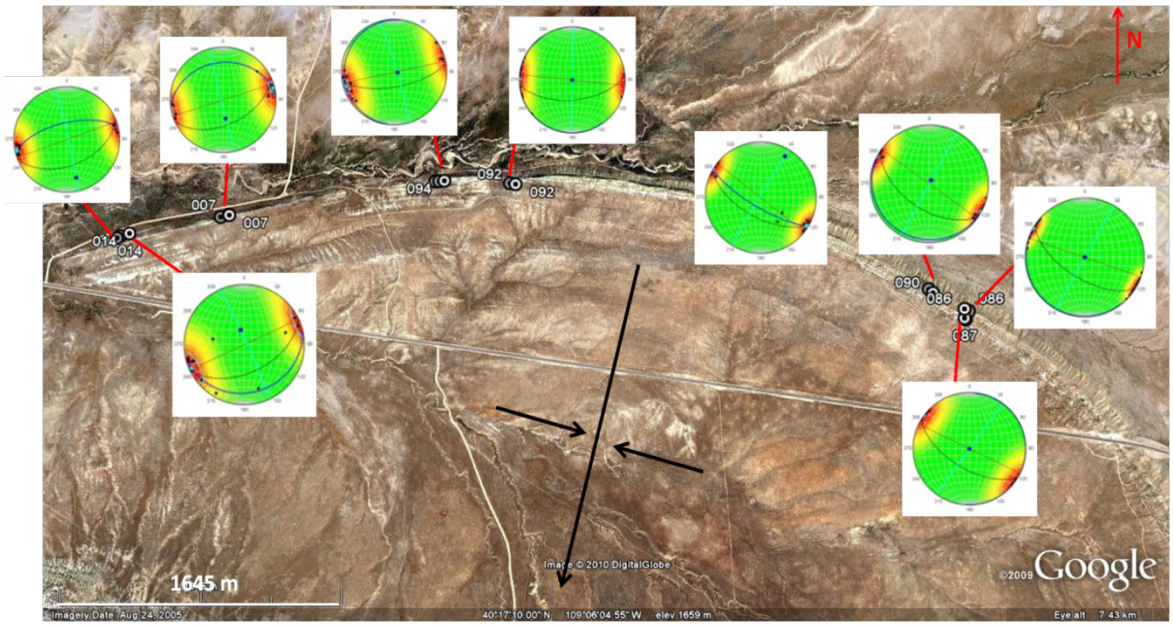

Figure 3-15. Contoured stereonets of poles to planes of joints from each scanline at Snake John Reef (Locality 2) overlain on a Google Earth image. Solid Black line is the orientation of the bedding plane. Brown line is the orientation of the scanline. Light blue is the great circle of the maximum eigenvector. Light blue dot is the pole to the plane of the maximum eigenvector. Light blue cones is the cone of confidence of the maximum eigenvector.

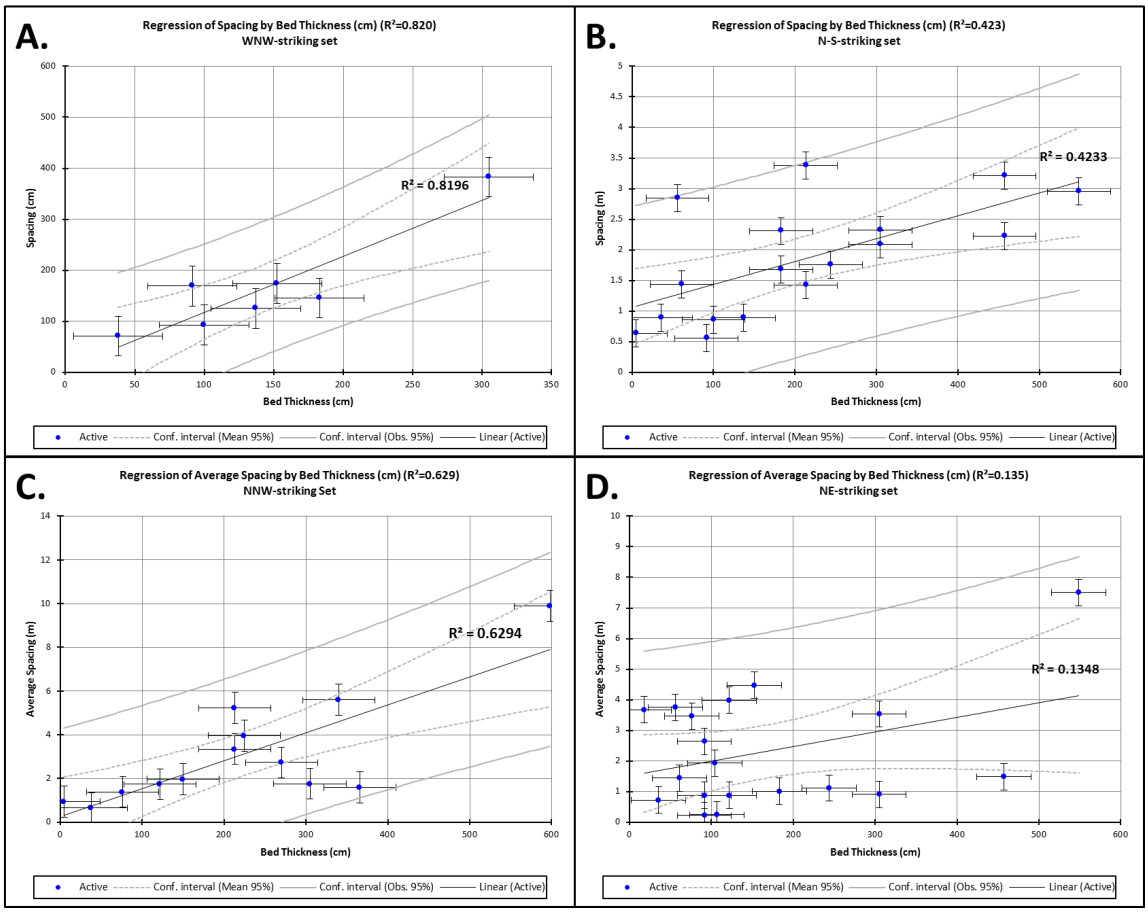

Figure 3-16. Plots of bed thickness versus fracture spacing for the four regional fracture sets identified in the basin. Plots show that there is a relationship between fracture spacing and bed thickness. A) Simple linear regression of the WNW fracture set. B) Simple linear regression of the WNW fracture set. B) Simple linear regression of the N-S fracture set. C) Simple linear regression of the NNW fracture set. D) Simple linear regression of the NE fracture set. Highest R- squared value was calculated for the WNW fracture set (0.82) and the lowest value was calculated for the NE set (0.13).

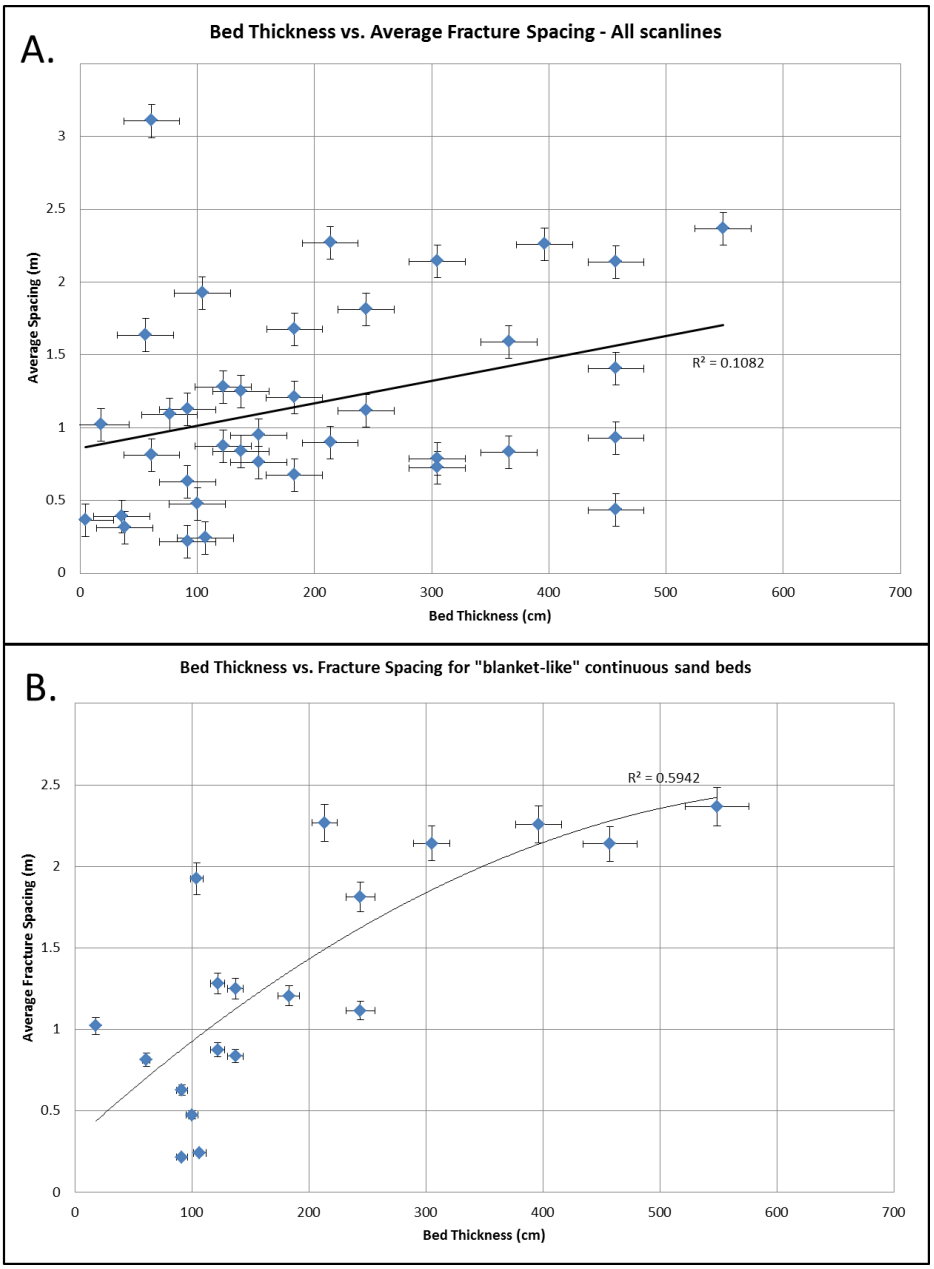

Figure 3-17. Crossplots of bed thickness versus fracture spacing. A) Simple linear regression for all scanline stations. B) A non-linear fit yields the best fit for stations with continuous sandstone beds. One outlier was removed.

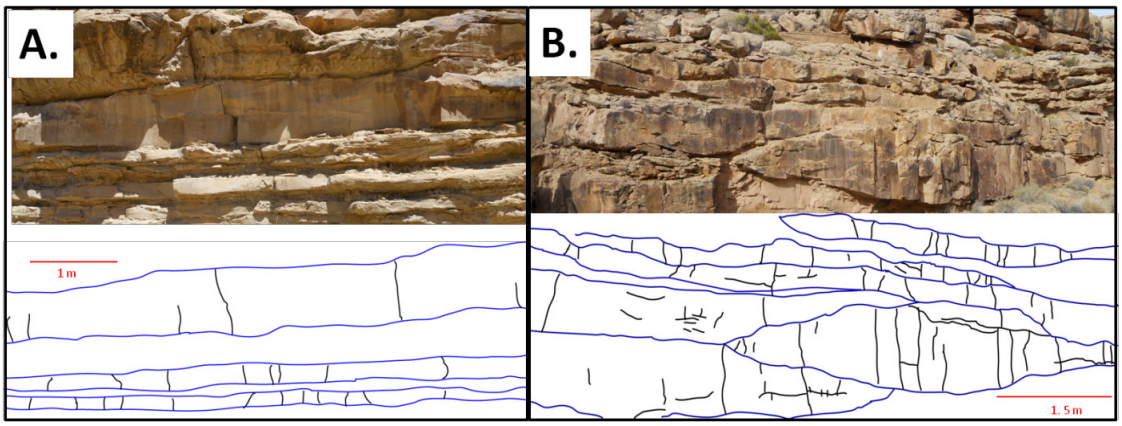

Figure 3-18. A. Photo and interpretative drawing illustrates typical bed thickness control on fracture distribution with thick sandstone bed above with relatively low fracture density and thinner sandstone beds below with higher fracture density. B. Interpretive drawing show the terminations of fractures along the boundaries of the lenticular sandstones within the Castlegate Sandstone. Fracture densities are similar in both thin and thick discontinuous, lenticular sandstone units.

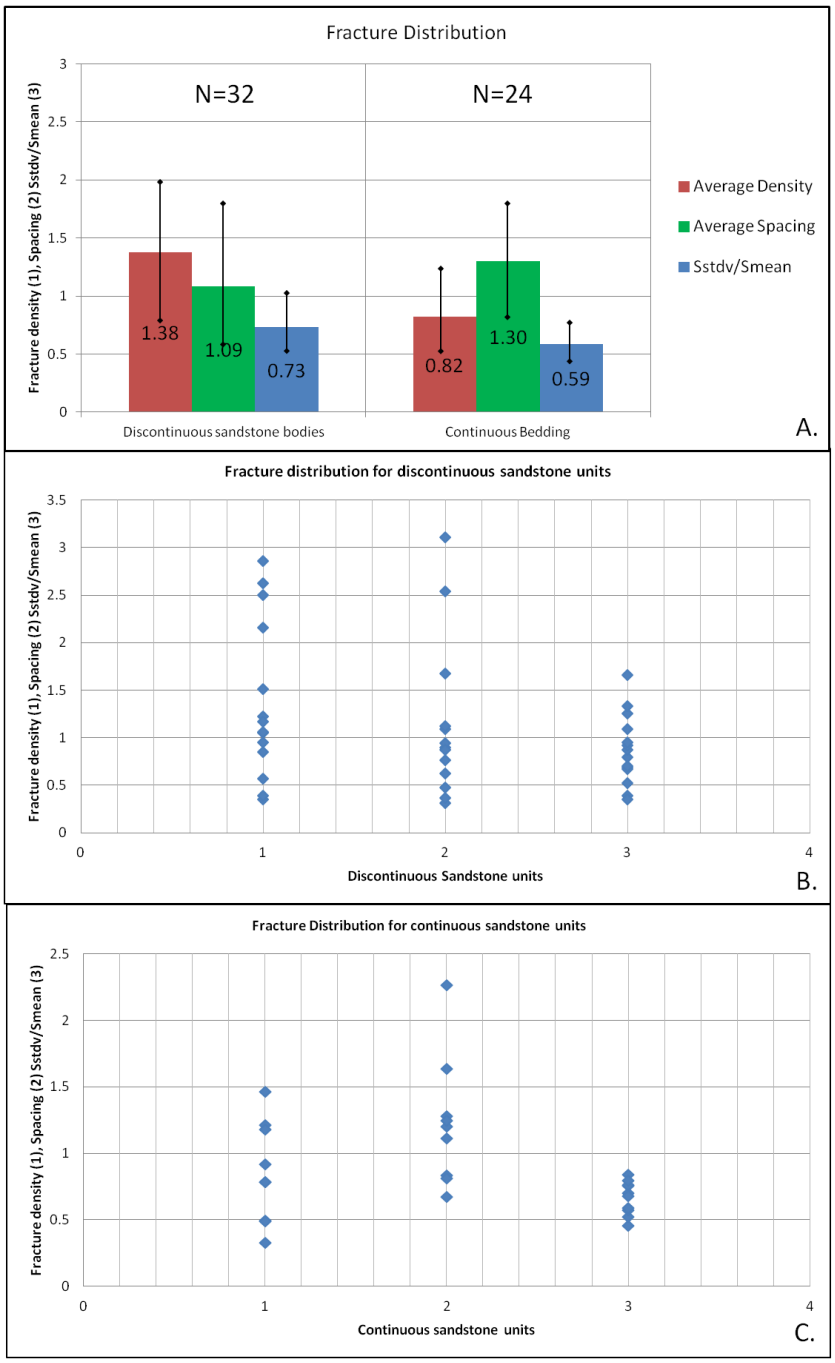

Figure 3-19. A) Histograms of average fracture distribution data comparing discontinuous sandstone bodies and continuous blanket-like sandstone beds sampled. B) Raw data plotted for discontinuous sandstone bodies taken at each scanline station. On the x-axis: 1= fracture density, 2 = fracture spacing, 3 = Sstdv/Smean. C) Raw data plotted for continuous sandstone bodies taken at each scanline station. On the x-axis: 1 = fracture density, 2 = fracture spacing, 3 = Sstdv/Smean.

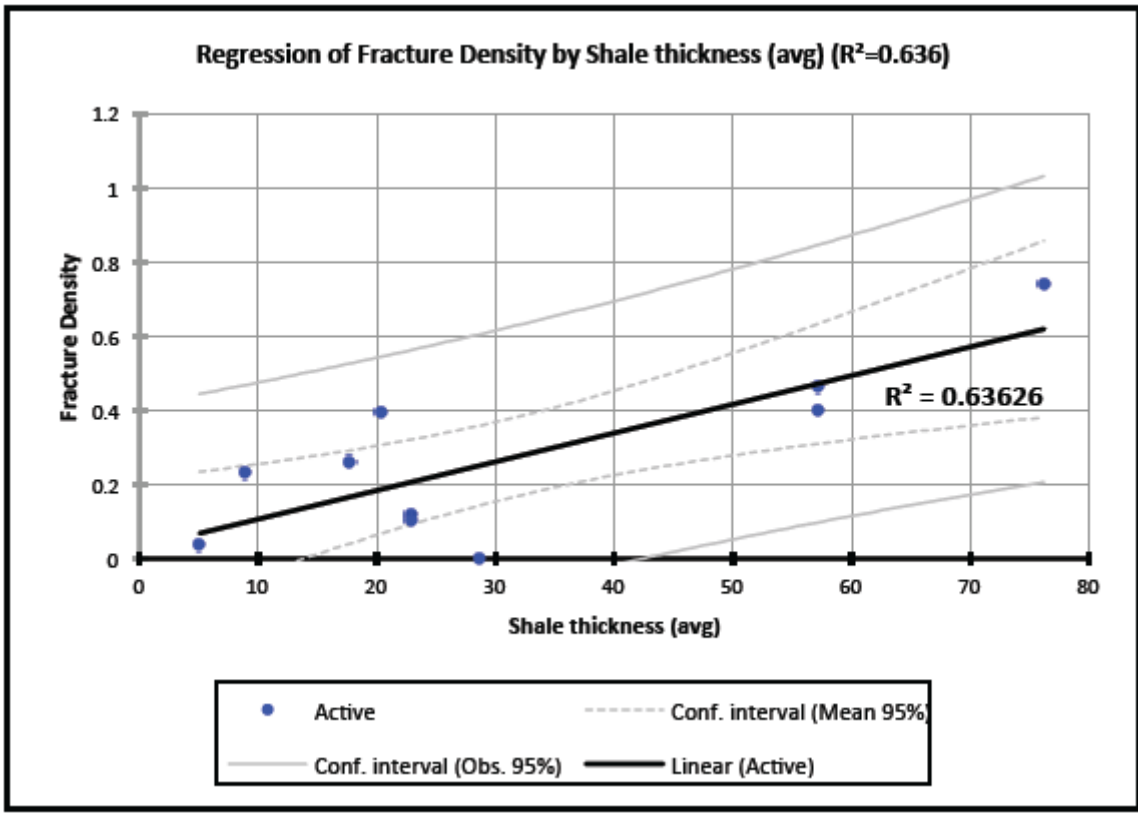

Figure 3-20. Cross plot of fracture density of through-going fractures (y-axis) and thickness of shale that bounds the mechanical unit (x-axis) the scanline was taken in.

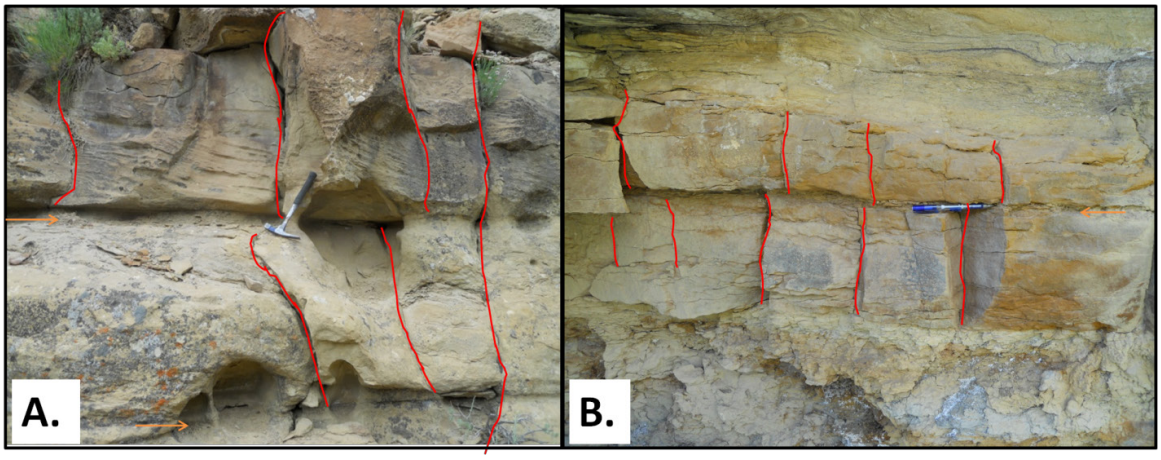

Figure 3-21. A & B. Photographs are taken of a vertical face. Photographs of sandstone bed with mudstone/ shale partings where fractures are terminating. Off the photos, to the right and left, the beds acts as single mechanical units but in the photos the thin mudstone/shaley partings act as mechanical barriers and terminate fractures.

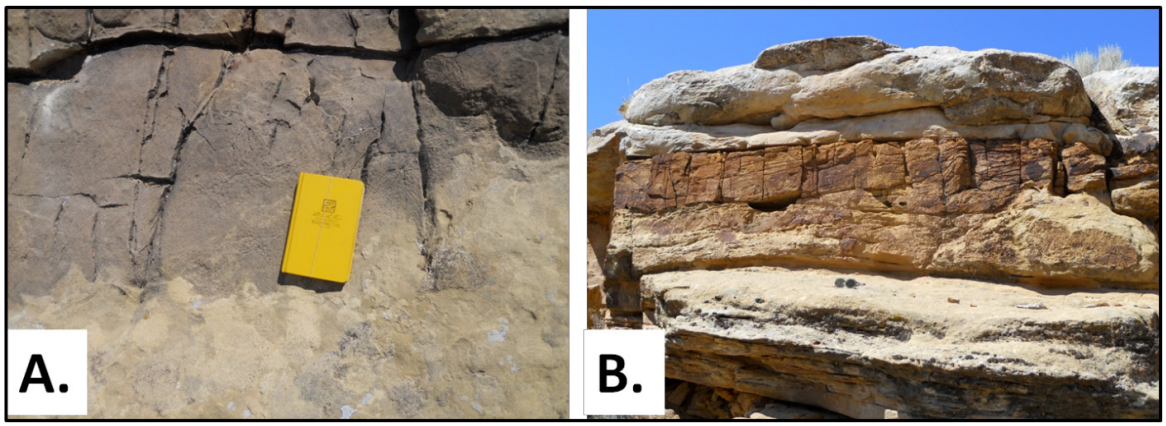

Figure 3-22. A. Photo of a bedding plane of a well indurated, carbonate cemented sandstone with locally high fracture density (top) overlying a tan, friable sandstone stratigraphically above it with a low fracture density. B. Well indurated, tabular carbonate cemented litharenite with high fracture density between two cross-bedded, clay cemented, friable quartz arenites with very few fractures.

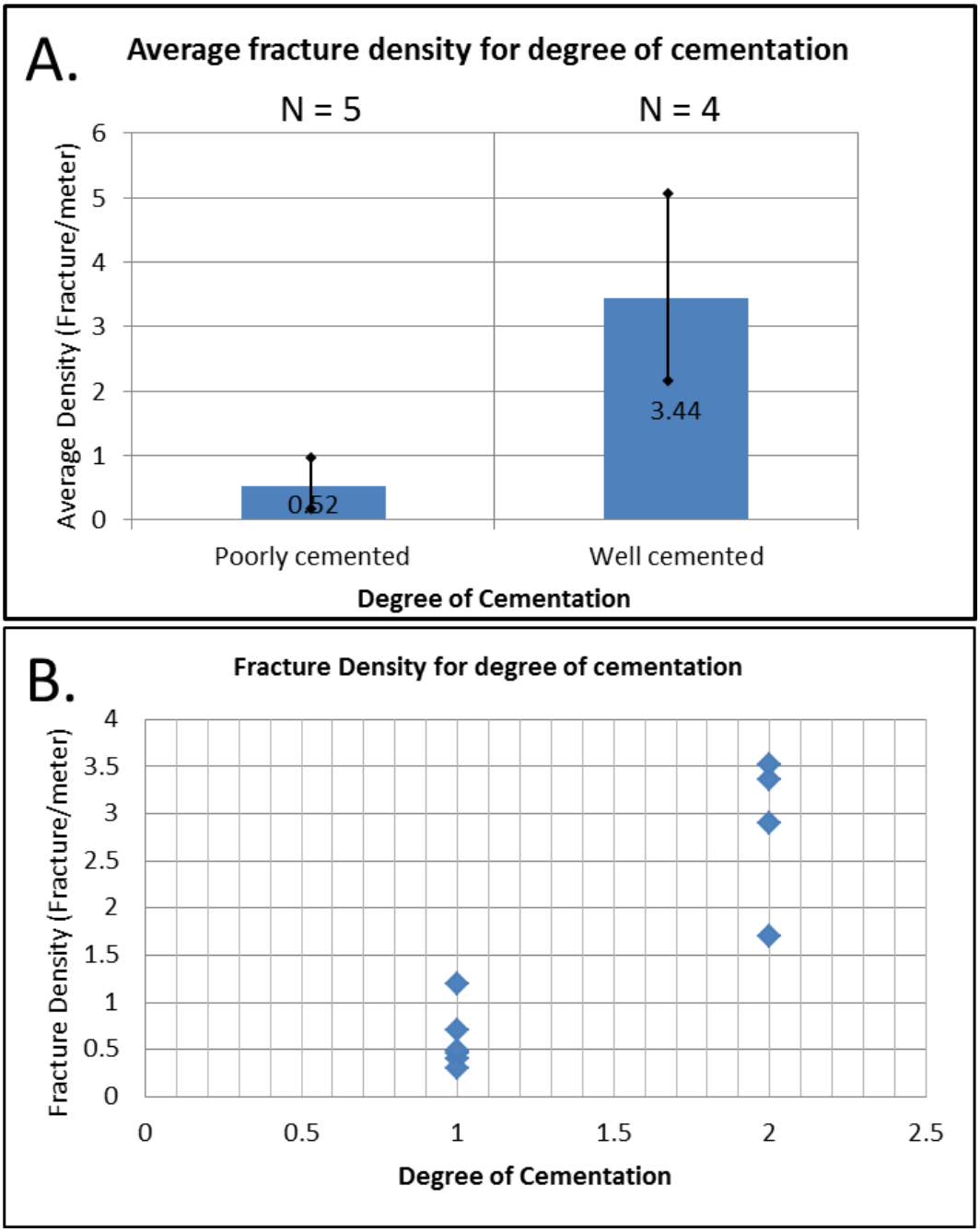

Figure 3-23. A) Histogram of average fracture density for poorly and well-cemented samples of similar bed thicknesses from 90 cm – 105 cm thick. B) Plot of raw data taken for poorly cemented (x-axis – value of 1) samples and well cemented samples (x-axis – value of 2) for sandstone units between 90 and 105 cm thick.

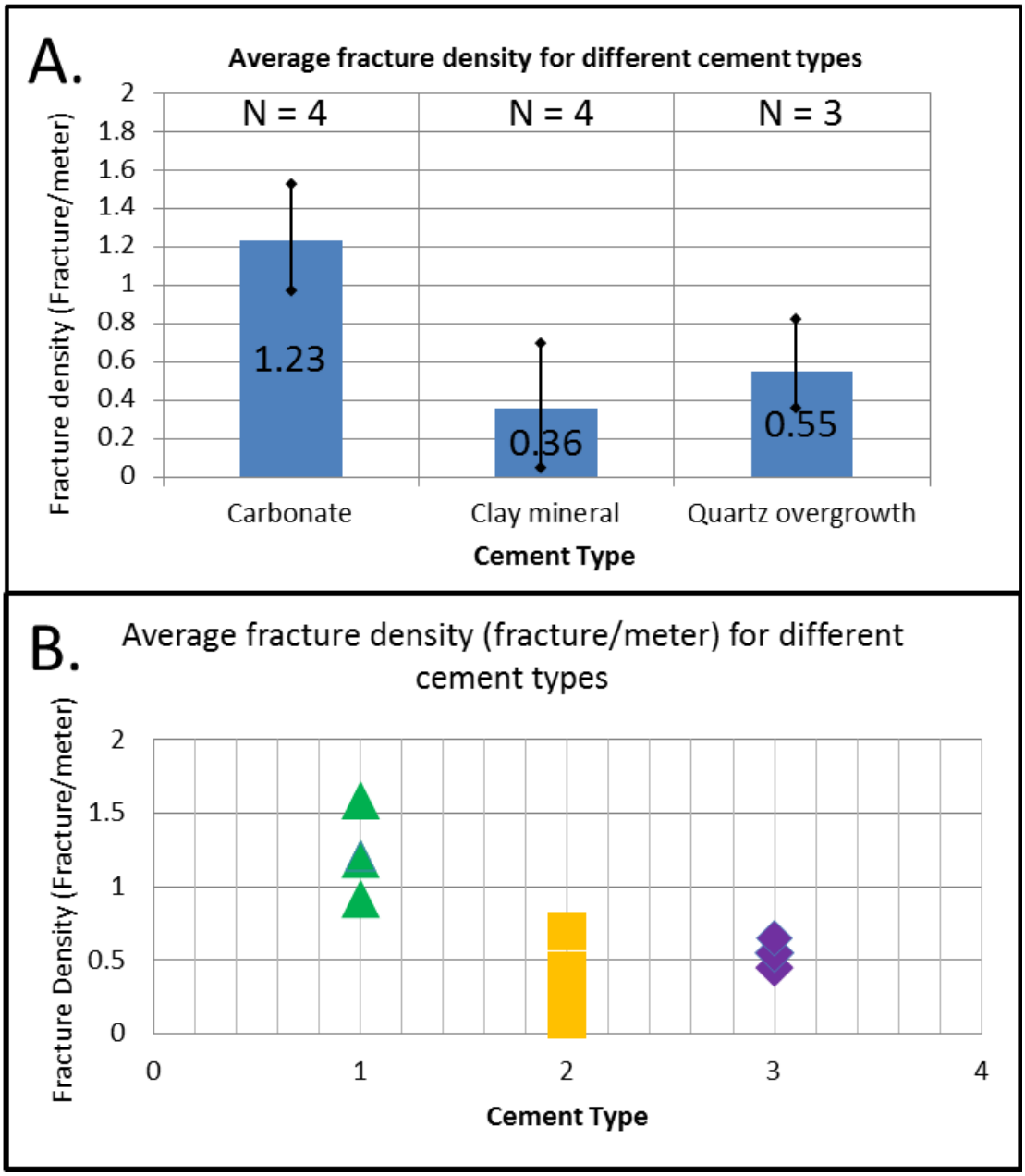

Figure 3-24. A) Histogram of average fracture densities for different cement types identified in thin sections. Fracture densities are from continuous sandstone beds with thicknesses from 305 cm – 550 cm thick. B) Cross plot of raw data with cement type versus fracture density. Green triangles (x-axis – value of 1) = carbonate cement, yellow squares (x-axis – value of 2) = clay mineral cement and purple diamonds (x-axis – value of 3) = quartz overgrowth.

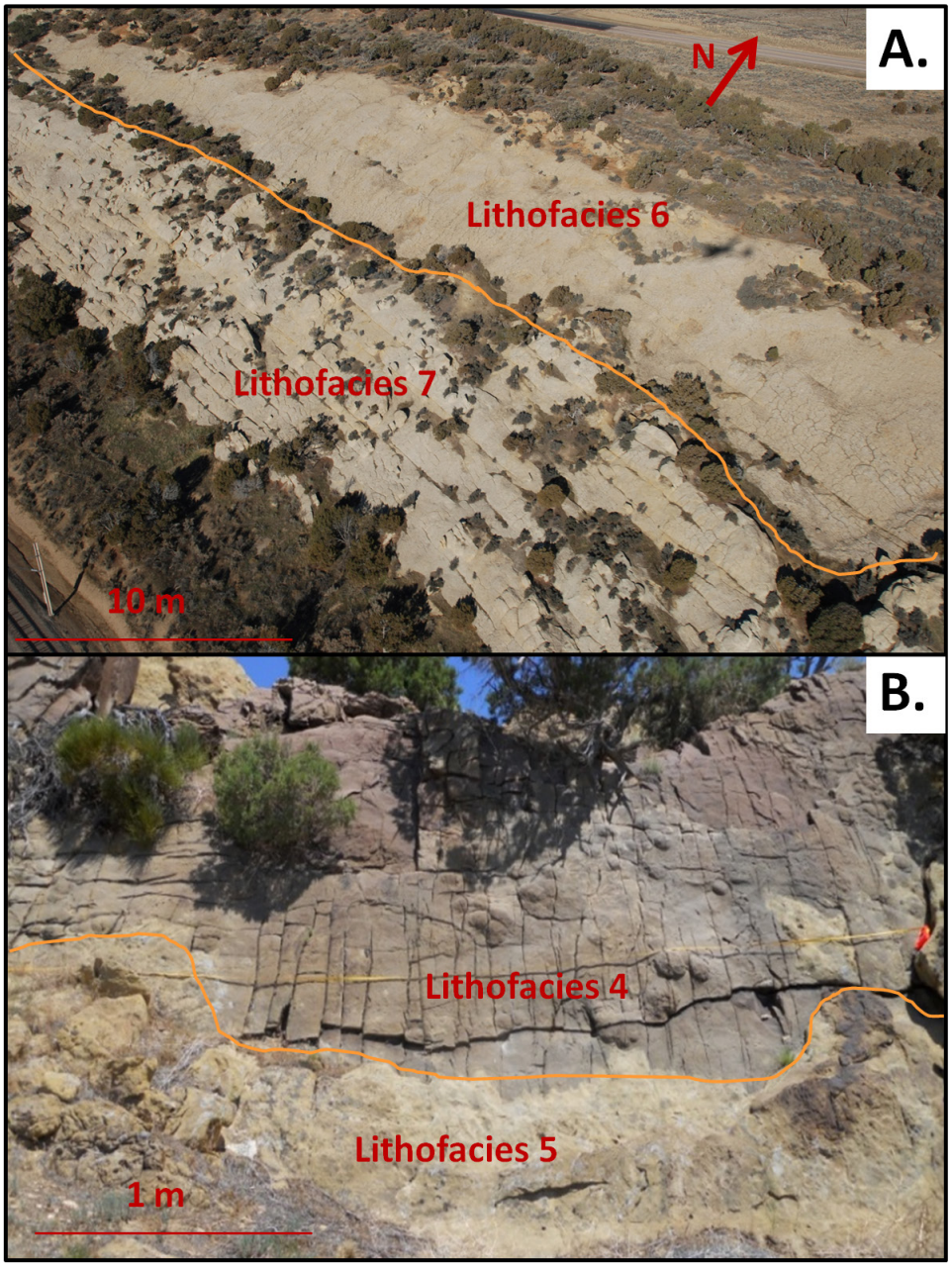

Figure 3-25. Photographs exhibiting fracture character in different lithofacies sampled. A. Low – altitude oblique aerial photograph of a pavement surface of lithofacies 6 & 7. Lithofacies 7 has a much higher fracture density than lithofacies 6. B. Photograph of a dip slope at Snake John Reef of lithofacies 3 and 5. In this photograph, Lithofacies 4 has a much higher fracture density than lithofacies 5.

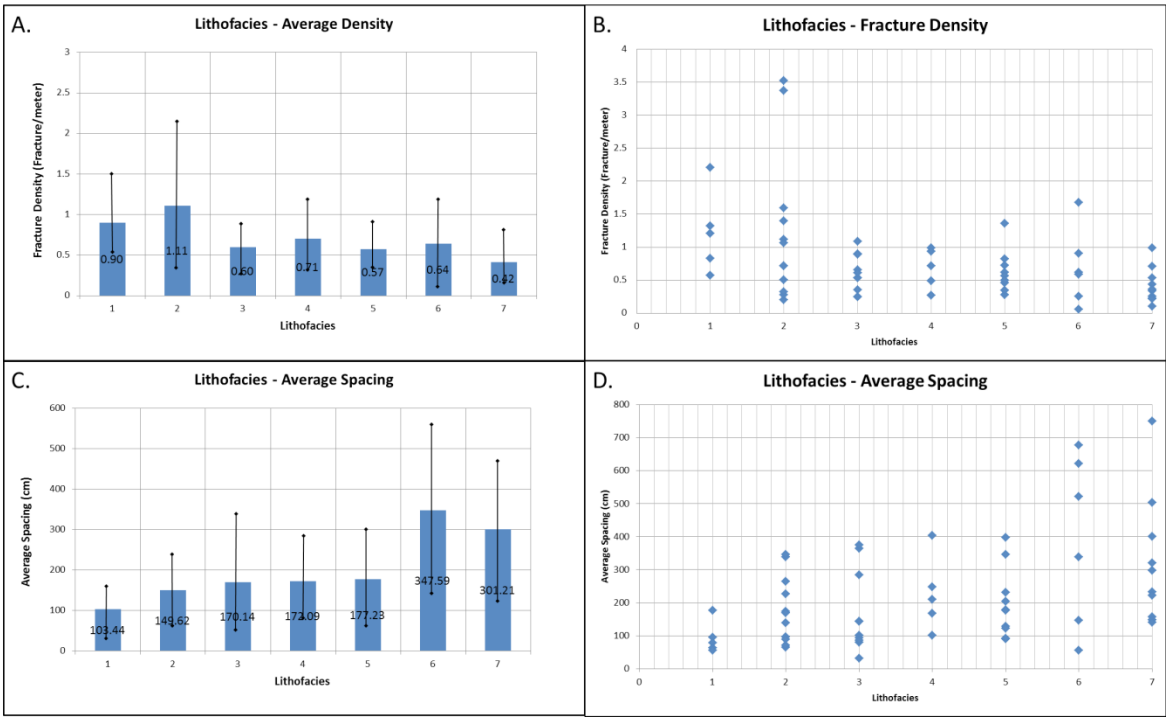

Figure 3-26. A & C) Histogram of the average fracture spacing and average fracture density for each lithofacies. B & D) Plot of raw data for each scanline station of fracture spacing and fracture density versus lithofacies type.

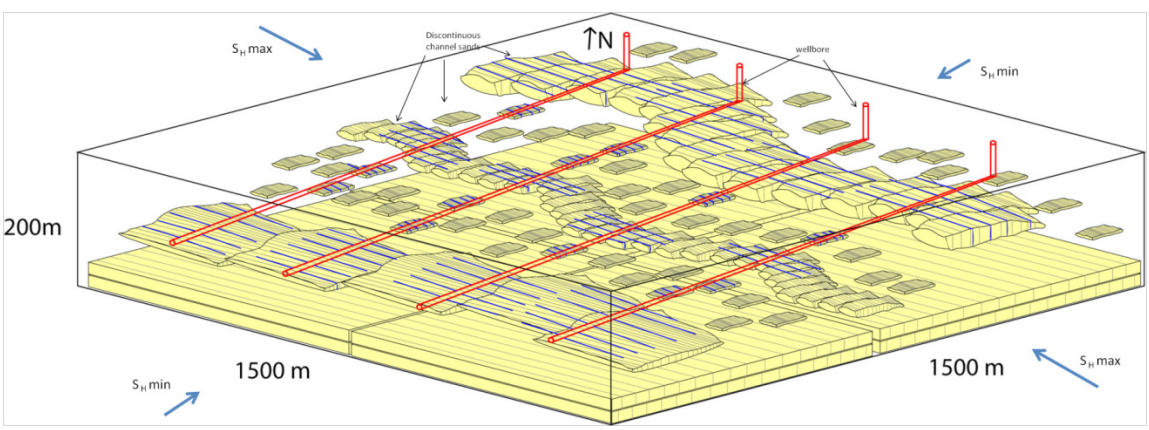

Figure 3-27. Schematic 3D box diagram showing different sandstone reservoirs present within the GNB field. Sandstone reservoirs of five different lithofacies sampled are represented with their characteristic fracture patterns controlled by bed thicknesses, sandstone architecture/geometry, and type of cement. Sandstones are assumed to be well-cemented with low porosity. The dominant fracture set depicted is the WNW fracture set. Lithofacies 7 is the tabular, continuous sandstone beds along the bottom of the figure with a more regular fracture spacing and Lithofacies 2-5 are shown stratigraphically higher (above) being more discontinuous in nature with higher fracture density. Productive wells are shown penetrating into lithofacies 3,4 & 5 with schematic hydraulic fractures shown in blue. The gray lines are the dominant wnw-striking fracture set.

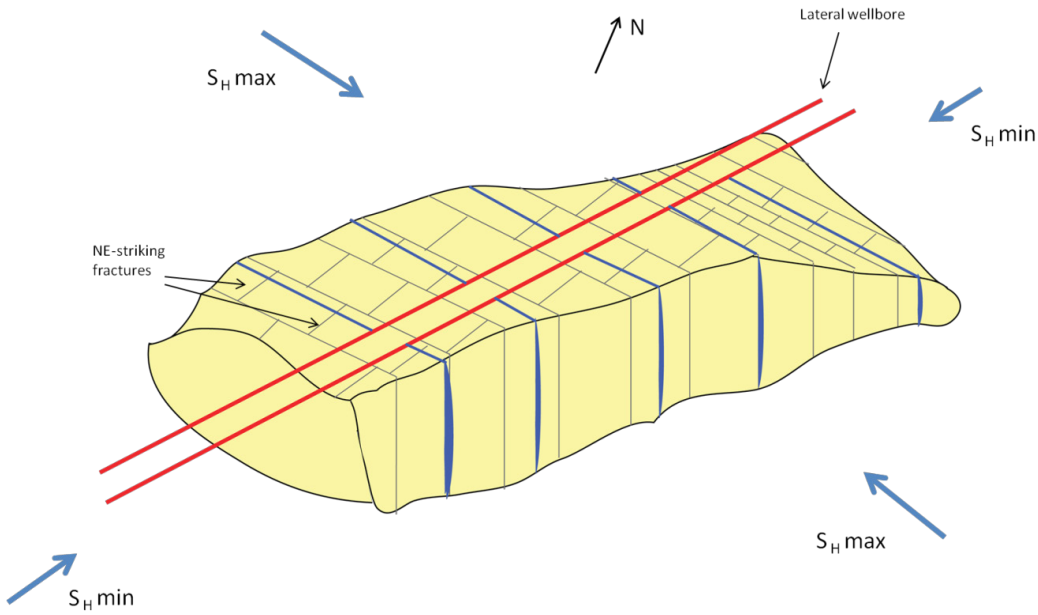

Figure 3-28. Schematic illustration of a lateral wellbore penetrating through lithofacies 4. Hydraulic fractures (blue lines) are shown to intersect the WNW-striking fracture set and the NE fracture set connecting the two fracture sets and potentially connecting the two fracture sets and potentially connecting the fracture systems allowing for increased drainage of the reservoir.

Creation of Discrete Fracture Networks and Validation

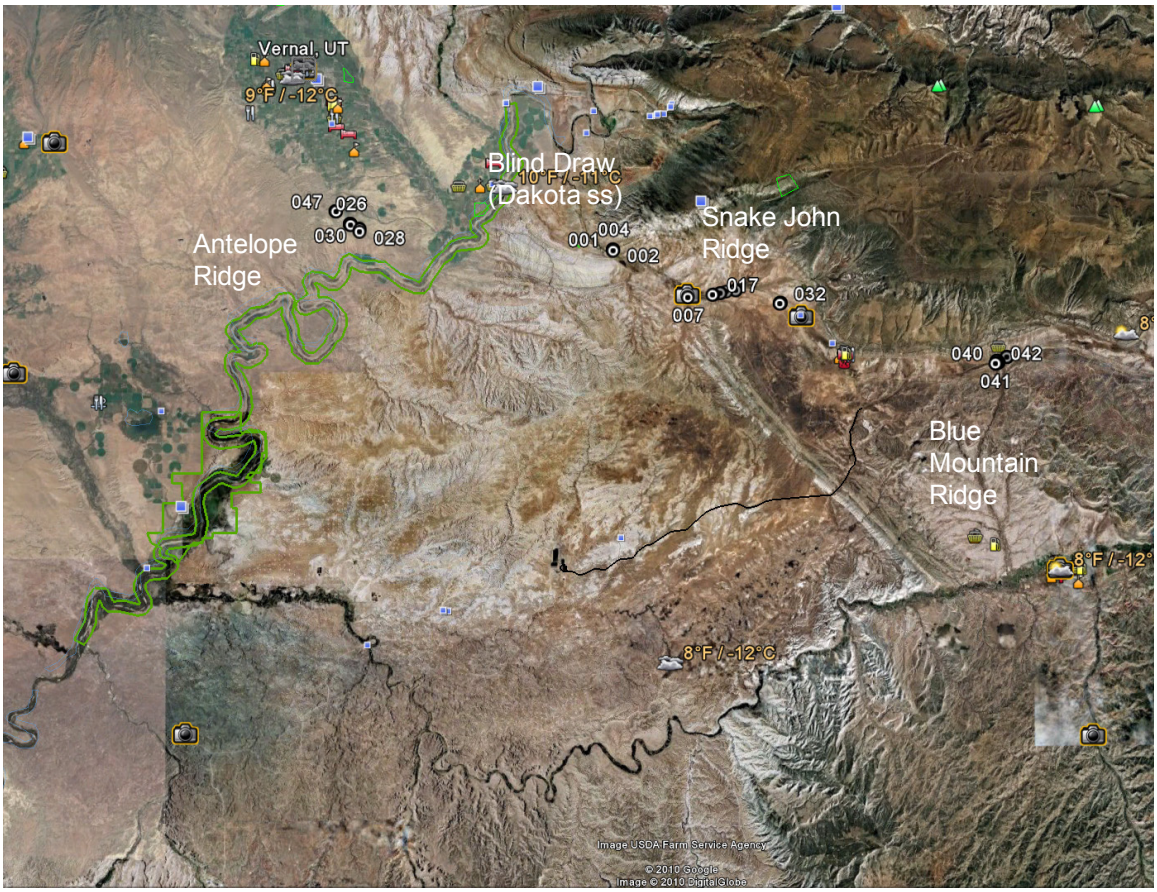

Figure 4-1. Primary outcrop locations for GCM development and fracture data acquisition. GPS station numbers are indicated by numbers.

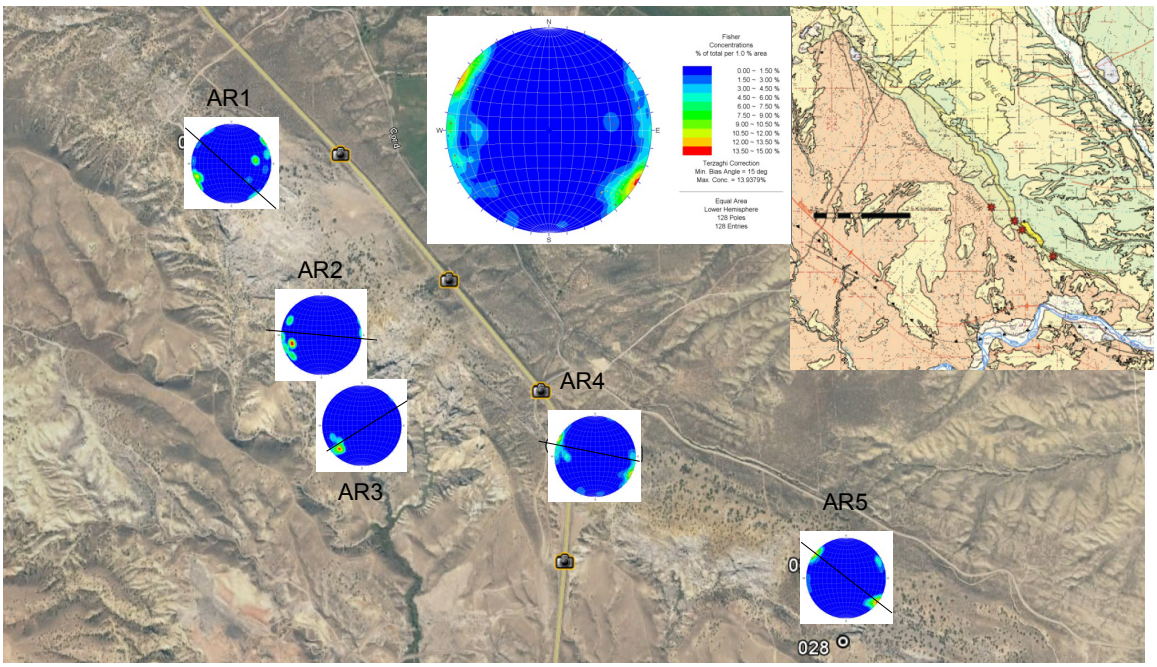

Figure 4-2. Photo of Antelope Ridge scanline site, including stereoplots of fractures measured at each of the five scanlines. The black line in each small stereoplot shows the trend of the scanline used to acquire the data.

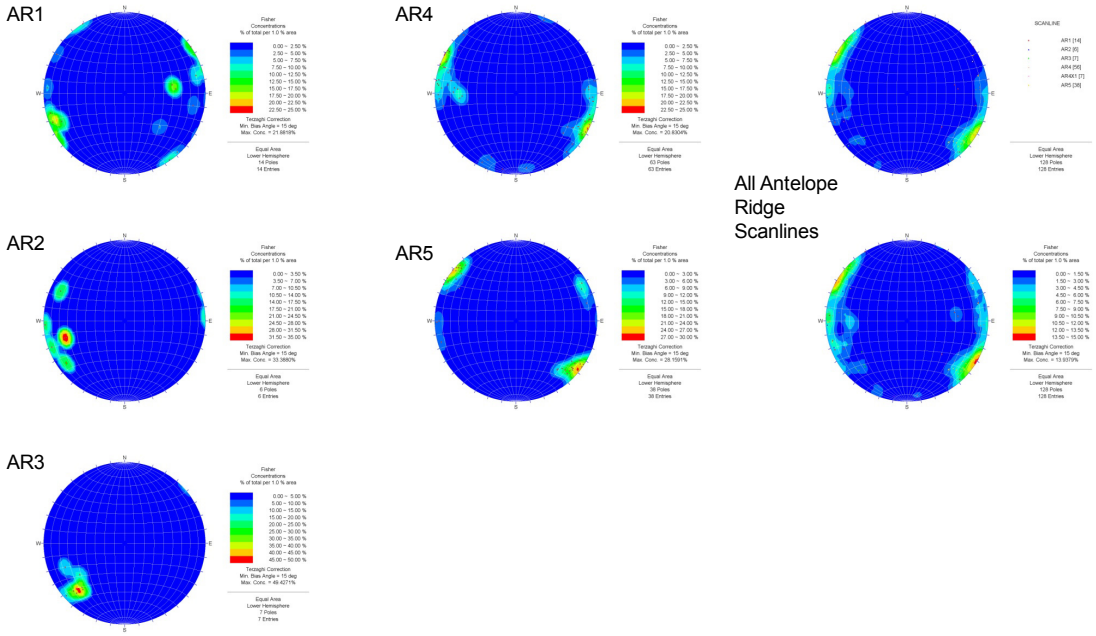

Figure 4-3. Stereoplot for all Antelope Ridge scanlines.

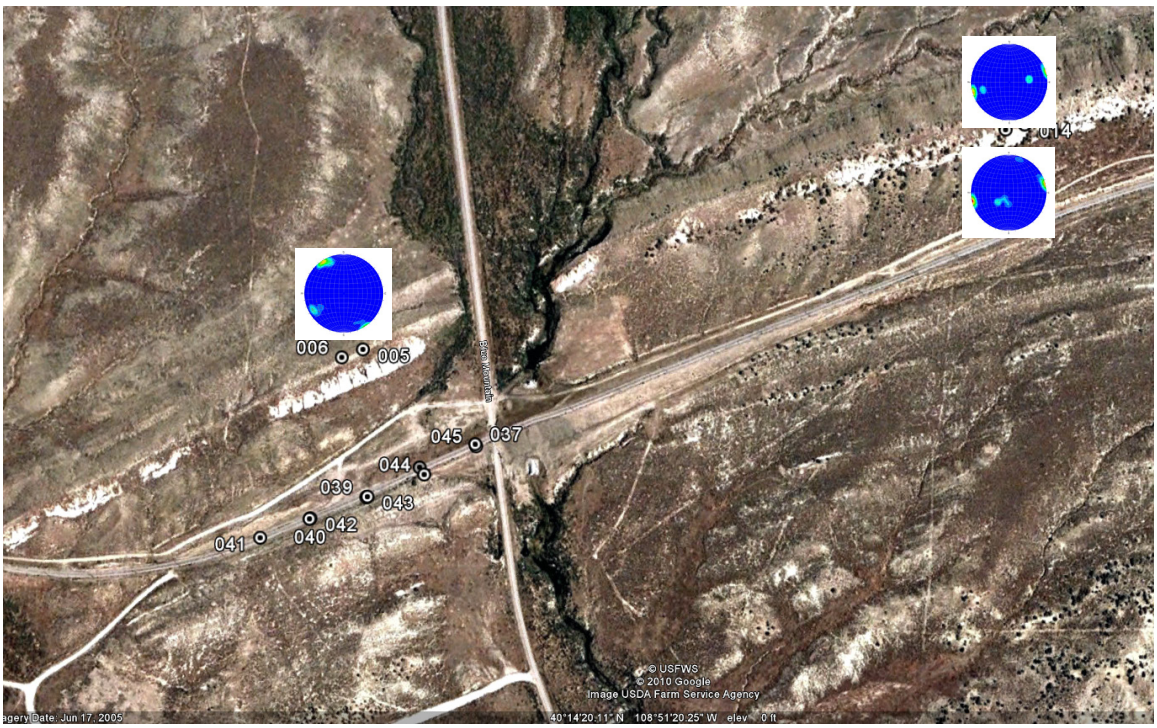

Figure 4-4. Blue Mountain outcrop area scanline locations. Numbers indicate GPS locations.

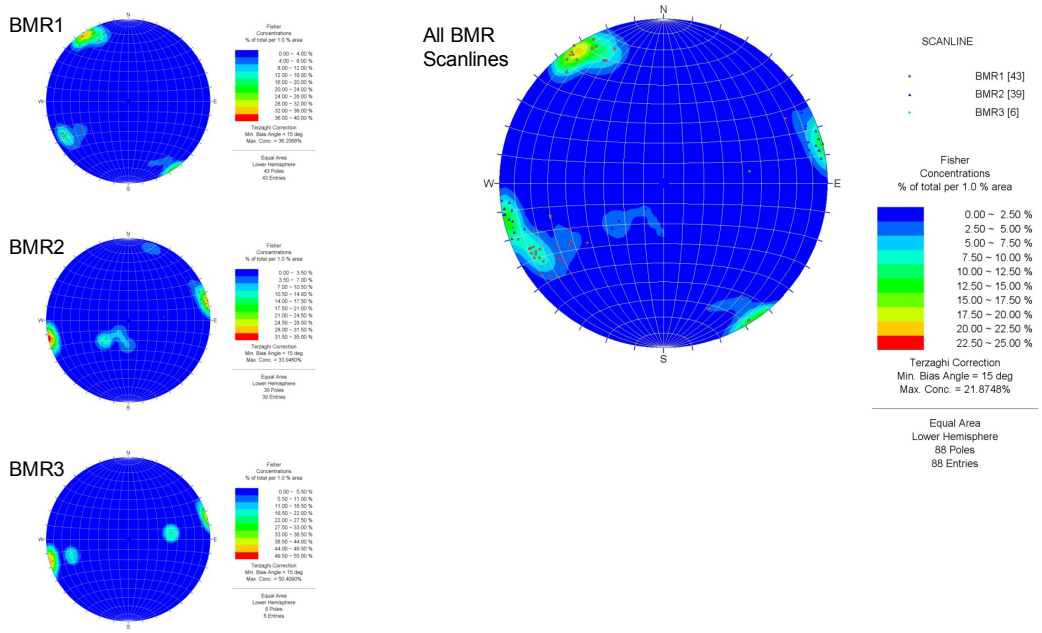

Figure 4-5. Stereoplots for the Blue Mountain scanline site.

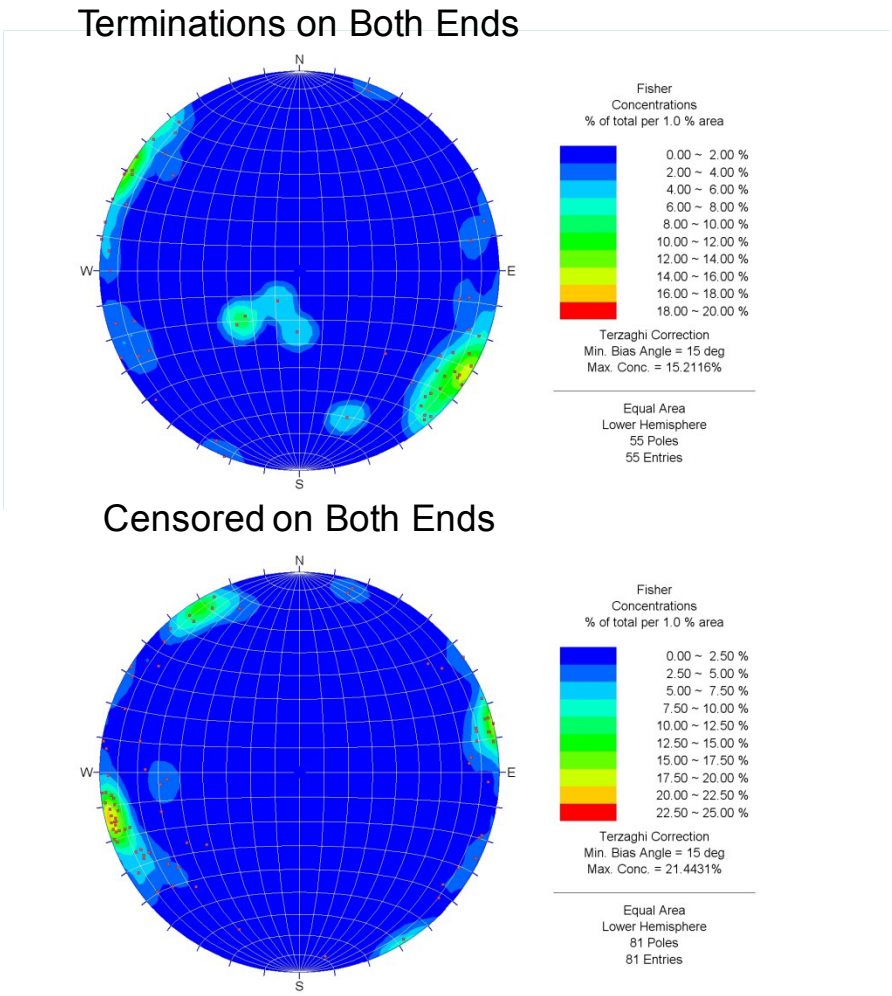

Figure 4-6. Relation of fracture orientation and termination style.

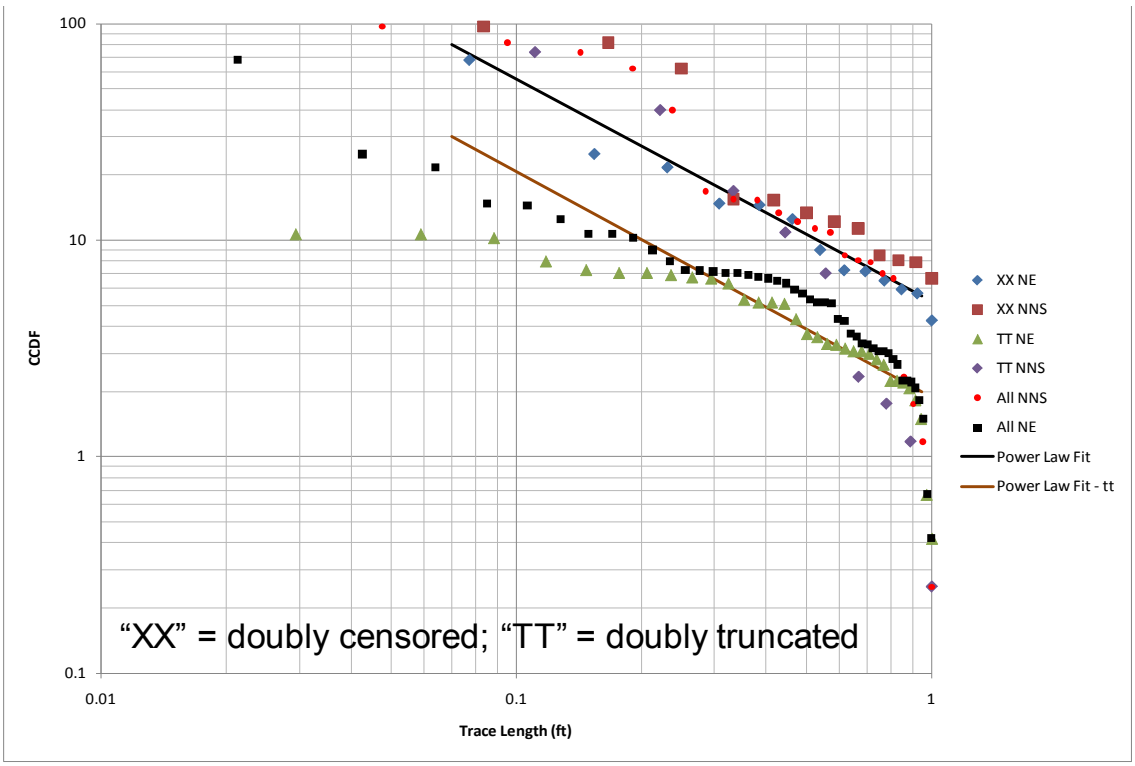

Figure 4-7. CCN plot for doubly censored and doubly truncated fractures from all outcrops.

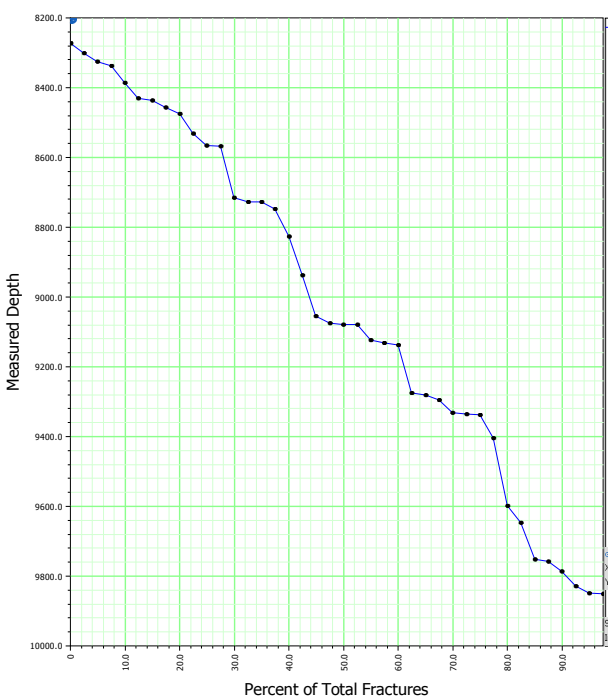

Interval ID	Starting MD	Ending MD	P10
1	8294.1	8336.2	0.047
2	8430.3	8474.3	0.065
3	8564.4	8568.4	0.284
4	8714.6	8742.6	0.104
5	9057.0	9083.0	0.121
6	9123.0	9137.0	0.135
7	9277.2	9293.2	0.127
8	9329.3	9337.3	0.218
9	9747.7	9843.8	0.049

Figure 4-8. CFI plot for NBU921_21L, along with intervals of mechanical layering and their P10 values.

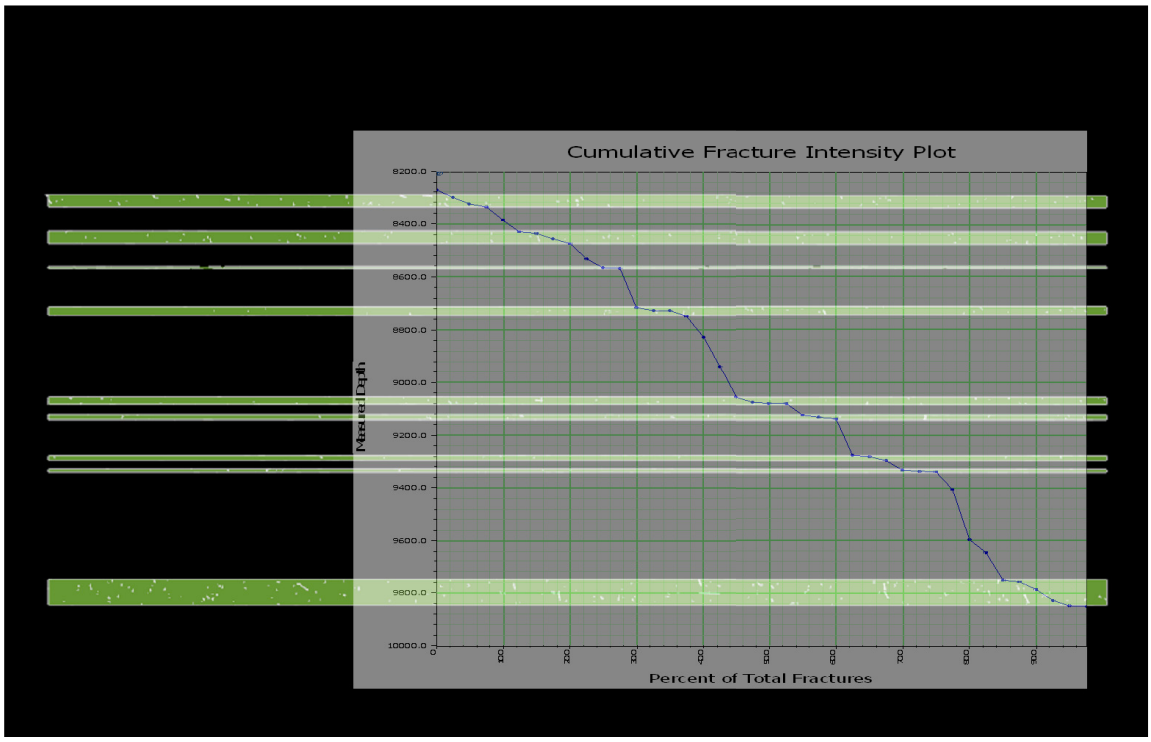

Figure 4-9. Visualization of mechanical layers derived from the CFI plot shown in Figure 4-8.

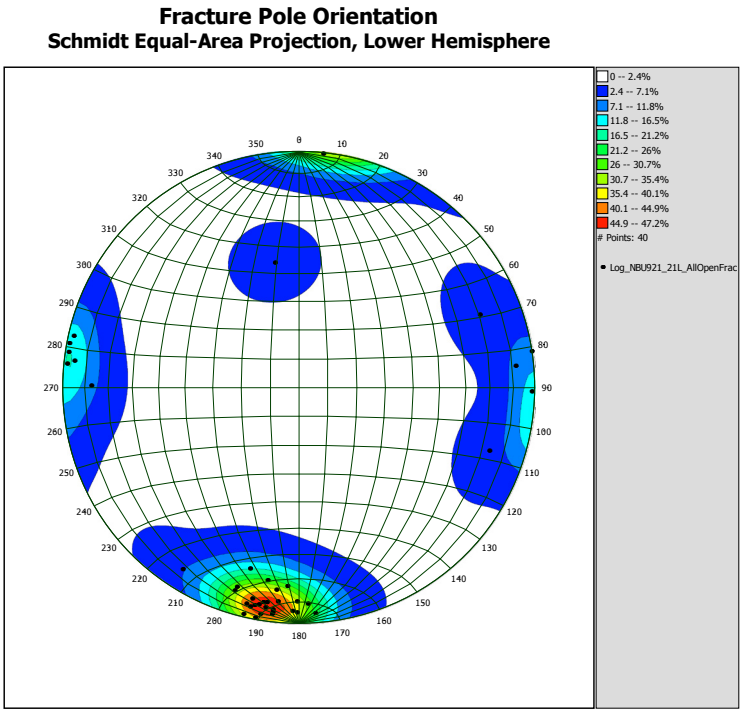

Figure 4-10. Stereoplot of open fractures for NBU21_21L.

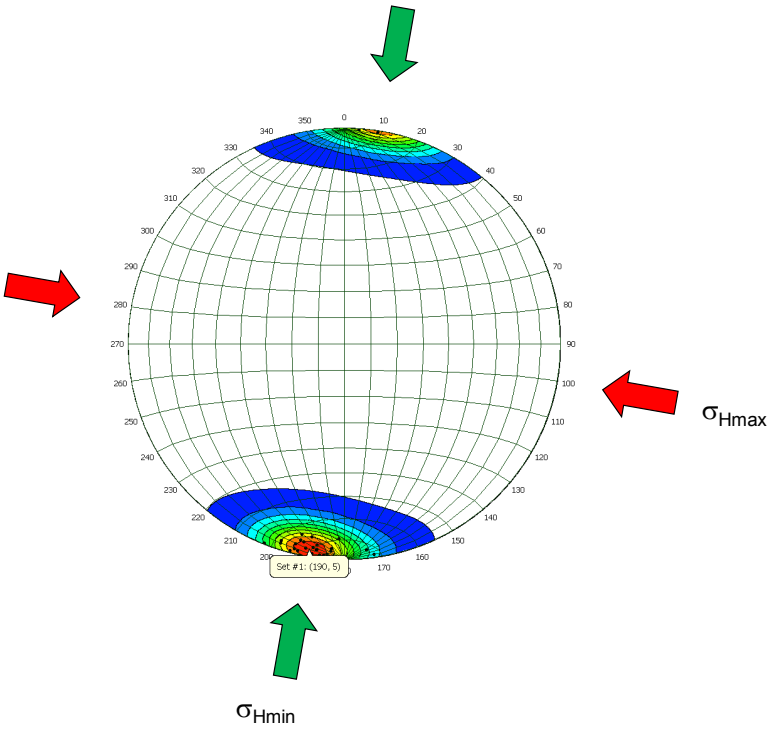

Figure 4-11. Orientation of induced hydrofractures in NBU21_21L data.

	Fisher distribution	Bivariate Normal distribution	Bivariate Bingham distribution	Elliptical Fisher distribution
"Set #1"				
Fracture Count	12	12	12	39
Relative Intensity	30 %	30 %	30 %	97.5 %
Mean Pole	276.380, 1.812	278.983, 1.975	93.624, 1.024	192.250, 6.862
Major Axis	96.380, 88.188	98.983, 88.025	184.721, 46.946	282.253, 0.030
Minor Axis	186.380, 0.000	8.983, 0.000	2.668, 43.036	12.504, 83.138
K1	10.6286	23.5501	-28.2577	4.97839
K2		15.4	-5.12653	3.70958
K12		0.825708		
Kolmogorov-Smirnov	0.303583	0.411111	0.3	0.287538
K_S Probability	25.095 %	4.46169 %	26.3381 %	0.997873 %
"Set #2"				
Fracture Count	28	28	28	1
Relative Intensity	70 %	70 %	70 %	2.5 %
Mean Pole	189.040, 8.242	189.071, 8.186	188.985, 8.230	108.300, 16.200
Major Axis	9.040, 81.758	9.071, 81.814	65.093, 75.480	3.691, 40.964
Minor Axis	279.040, 0.000	279.071, 0.000	280.730, 11.887	214.927, 44.563
K1	88.6652	7.06954	-24.8771	100
K2		5.06647	-19.4639	1
K12		0.13101		
Kolmogorov-Smirnov	0.10086	0.115079	0.34127	0.742442
K_S Probability	96.6151 %	90.5325 %	0.707682 %	64.3364 %
Total Fracture Count	40	40	40	40
Data Pedigree				
Filter	-			
Data Source 1	Log_NBU921_21L_AllOpenFrac			

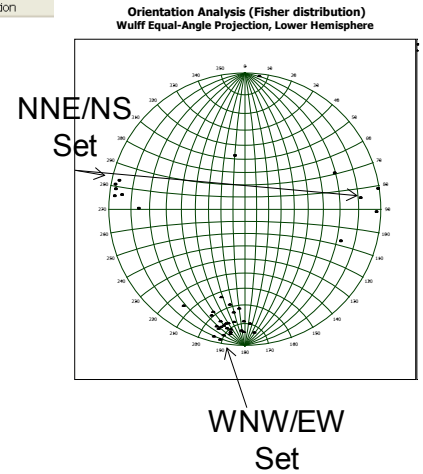

Figure 4-12. ISIS analysis of open fracture data from the NBU21_21L well.

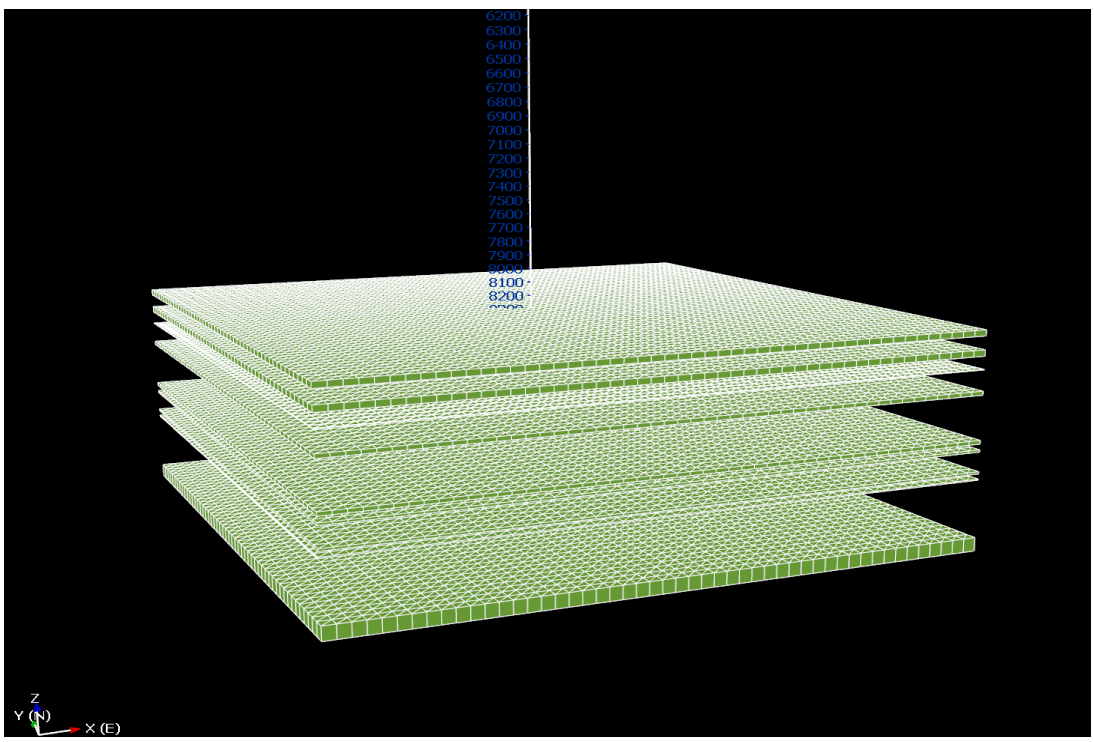

Figure 4-13. Fracture generation grids for Tract 21 model based on CFI plots for NBU21_21L open fracture data.

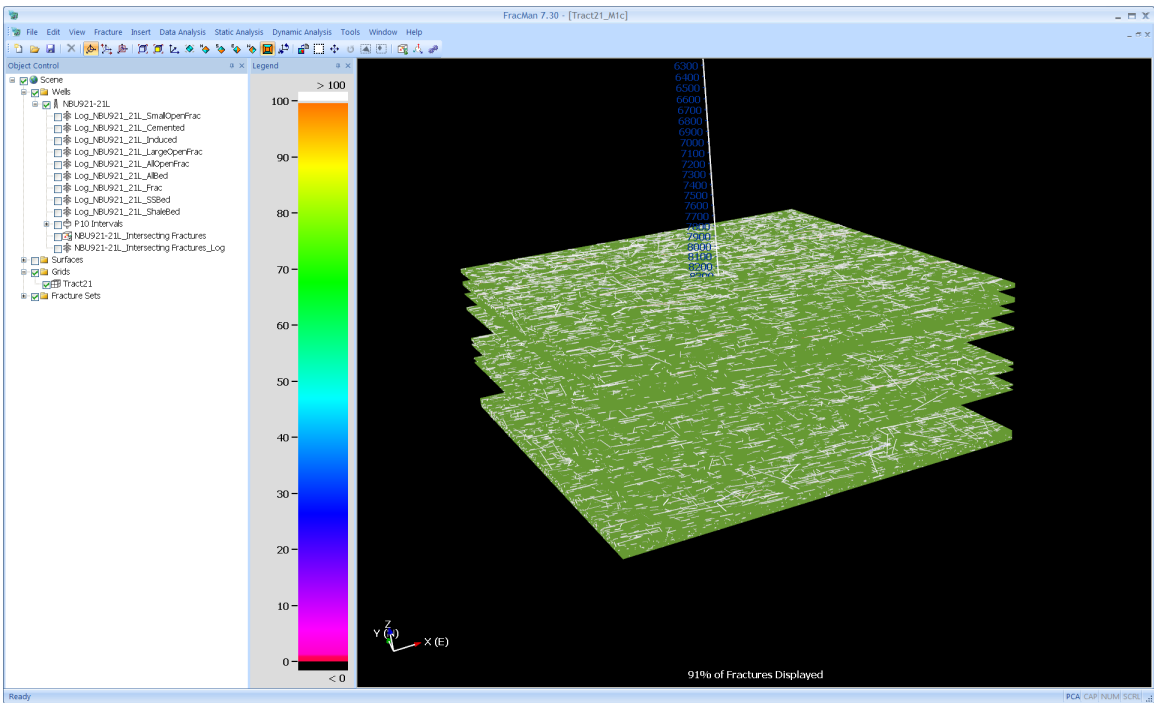

Figure 4-14. Generation of fractures from the fracture generation grids.

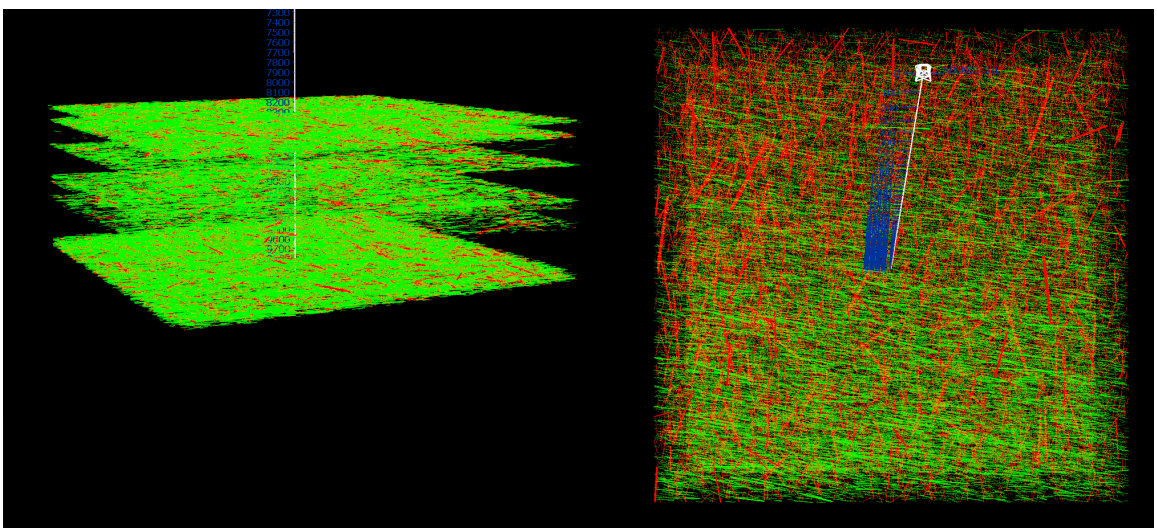

Figure 4-15. Visualization of fractures generated in the preliminary DFN model for Tract 21.

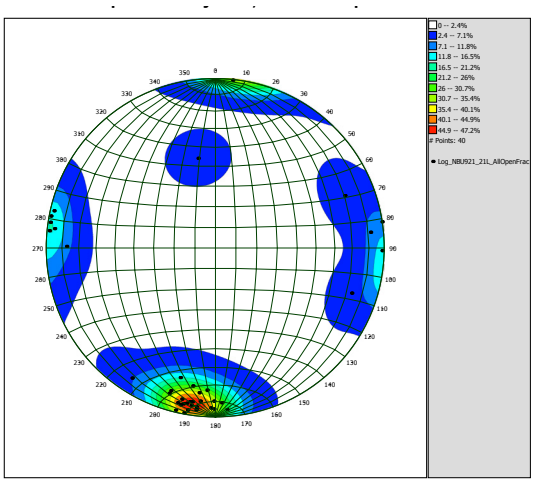

FMI Data

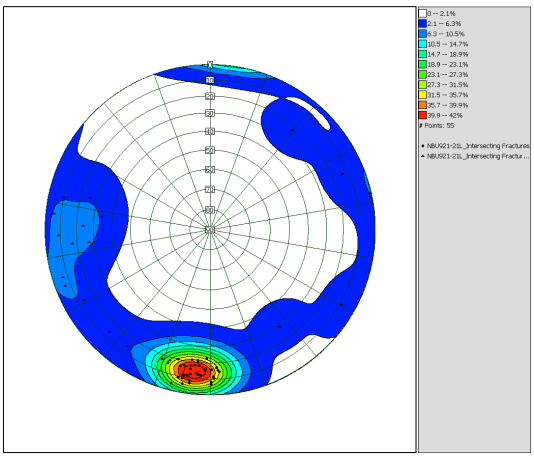

DFN Simulation – Intersecting Fractures

Figure 4-16. Validation of fracture orientations in the Tract 21 DFN model, comparing measured fractures with fractures intersected by well in the DFN model.

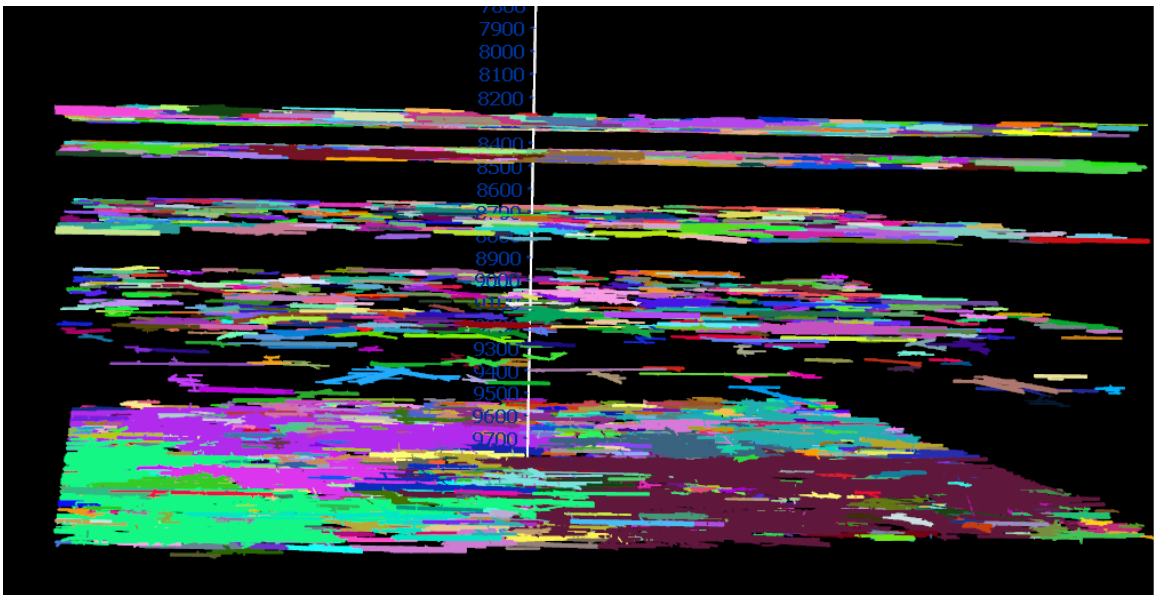

Figure 4-17. Compartmentalization analysis of the preliminary Tract 21 DFN model.

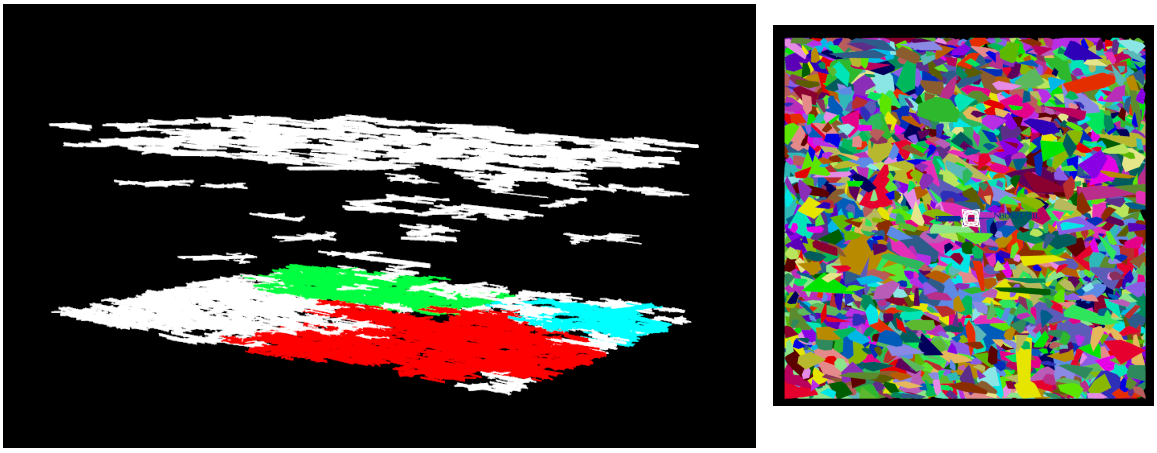

Figure 4-18. Compartment formation in the preliminary Tract 21 DFN model.

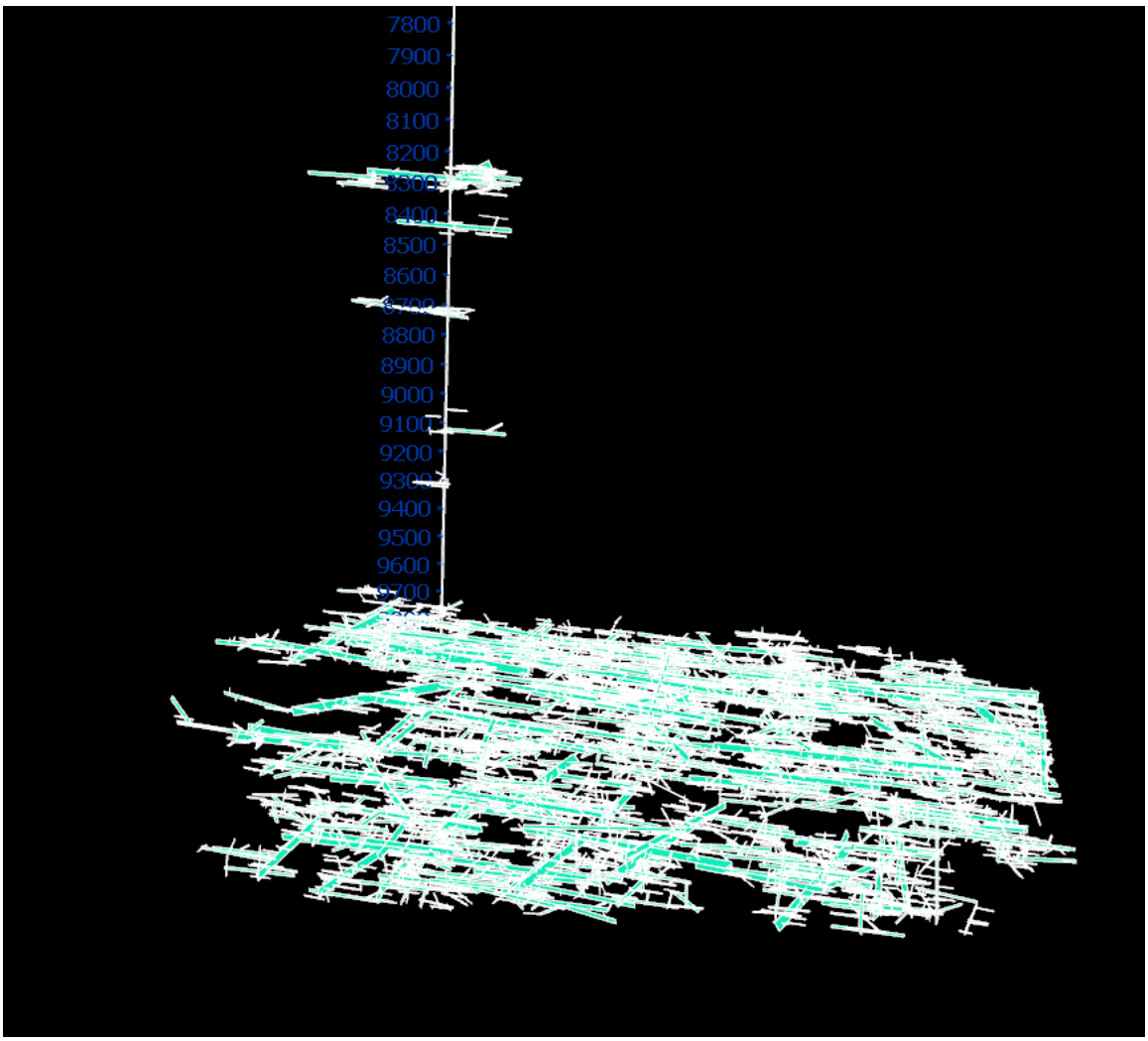

Figure 4-19. Visualization of fractures connected to the wellbore in the preliminary Tract 21 DFN model.

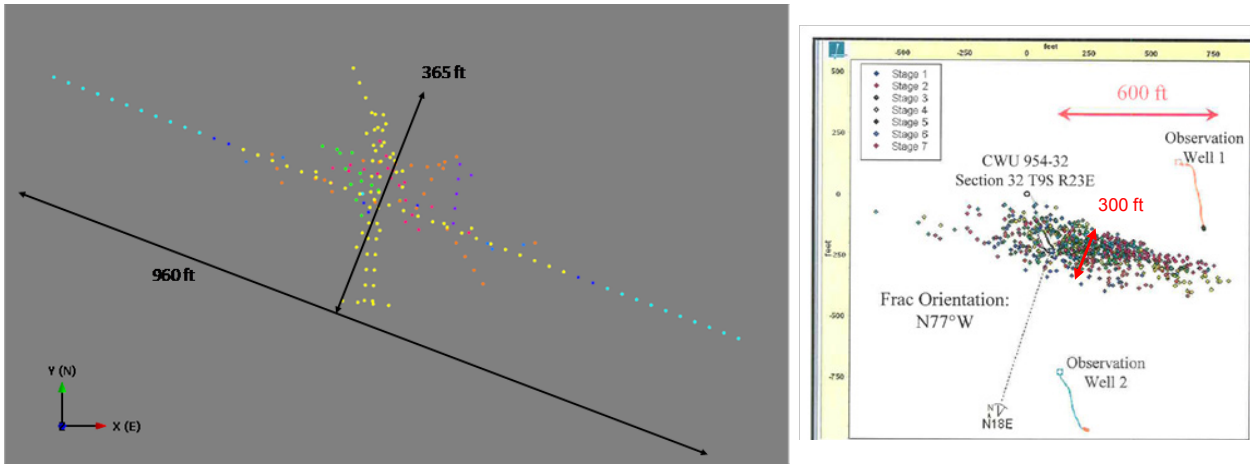

Figure 4-20. Microseismic response from Chapita Wells hydrofracturing and comparison with model results.

Integration of Geomechanics in Reservoir Simulation

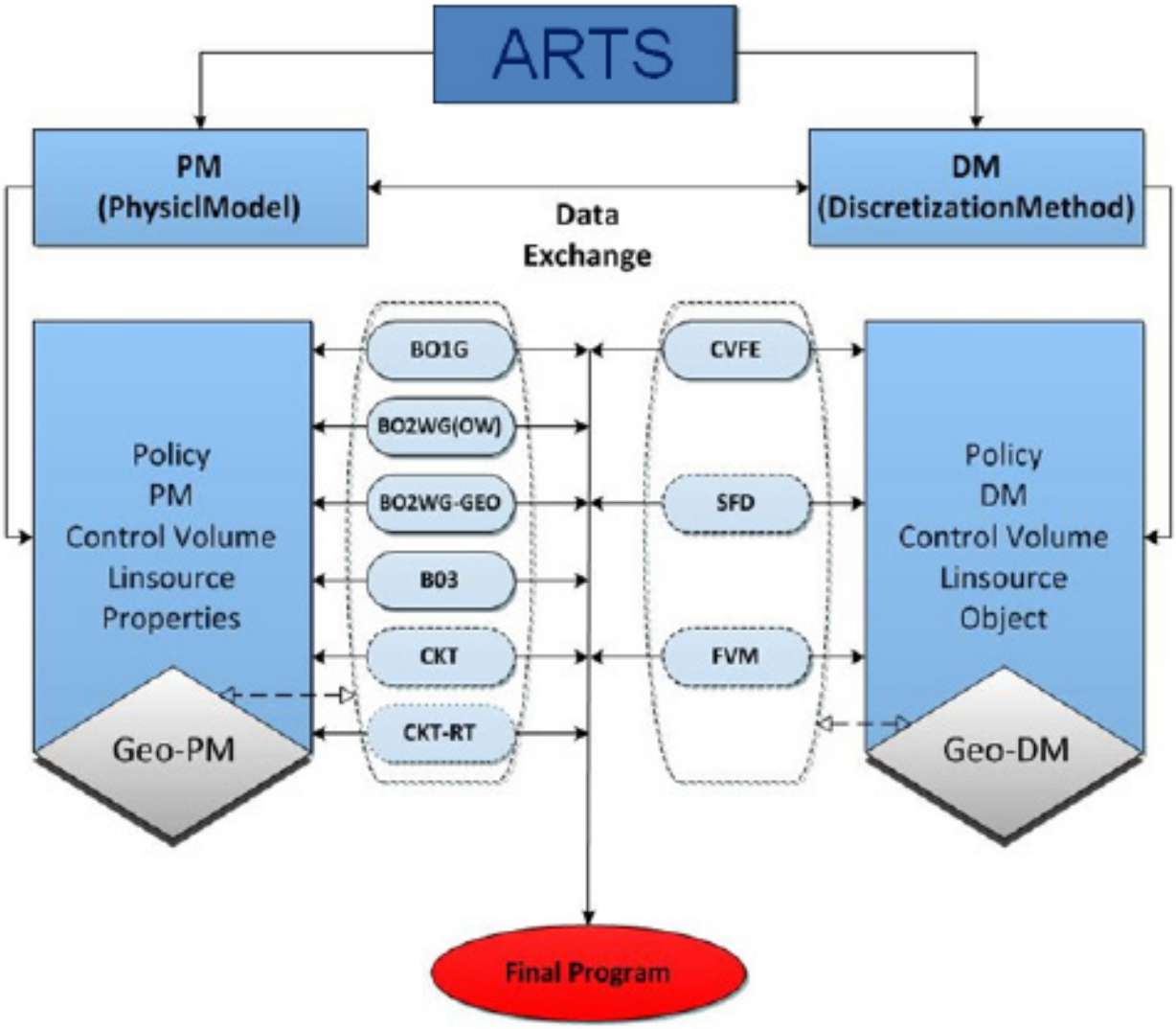

Figure 5-1. The University of Utah reservoir simulator framework – ARTS – Advanced Reactive Transport Models – that couples reservoir geomechanics with flow.

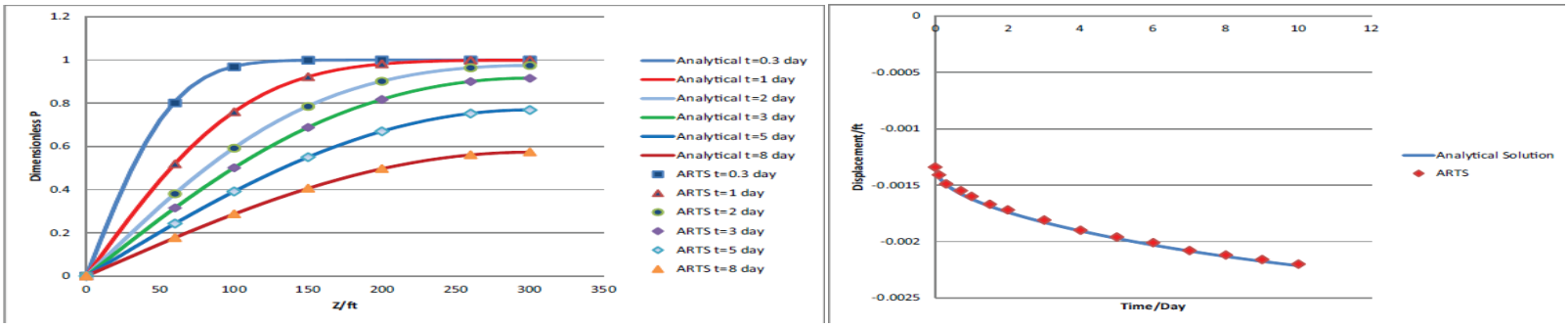

Figure 5-2. Comparison of the analytical and numerical solutions for a one-dimensional compression problem showing that the numerical implementation of the code in ARTS is verified.

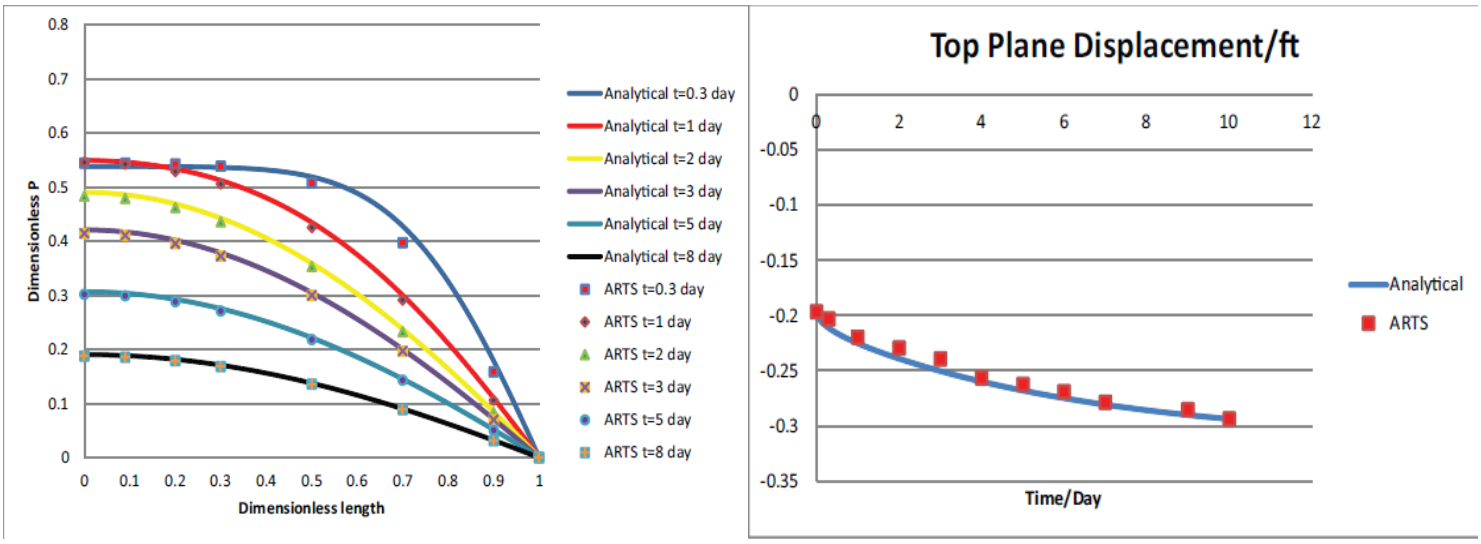

Figure 5-3. Comparison of the analytical and numerical solutions for the two-dimensional compression problem (Mandel problem) showing that the numerical implementation of the code in ARTS is verified.

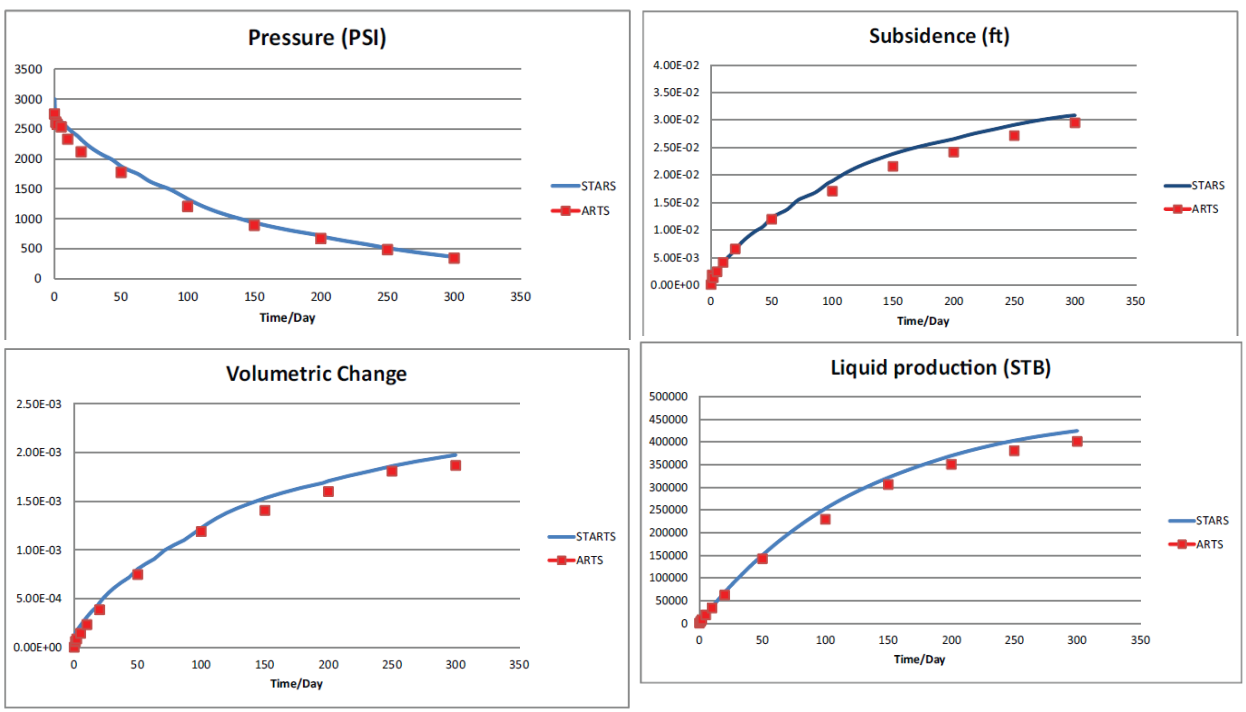

Figure 5-4. Comparison of various simulation output attributes between STARS and ARTS. The agreement is excellent once again validating the implementation of geomechanics in ARTS.

Integrating Hydraulic Fractures and Natural Fractures and Simulation

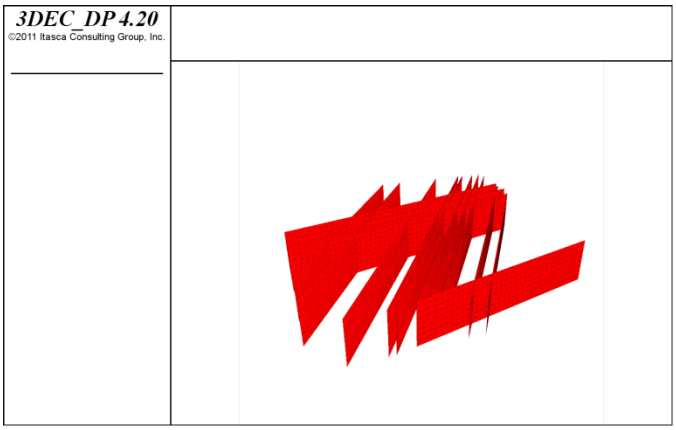

Figure 6-1. The fracture network used in 3-DEC simulations to create hydraulic fractures in the presence of natural fractures.

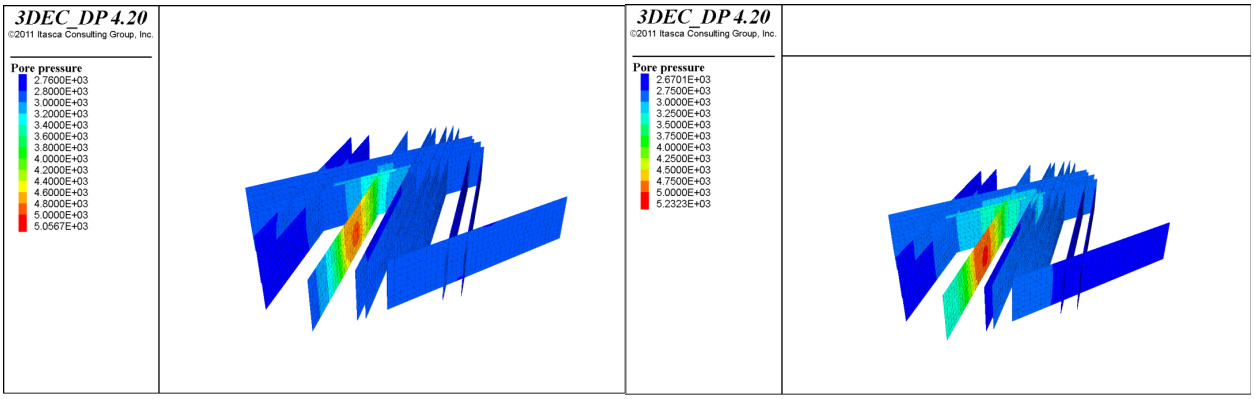

Figure 6-2. Pressures in the fracture system after 866 and 1624 seconds respectively. Injection rate was 50 barrels per minute. Pressures are in psi.

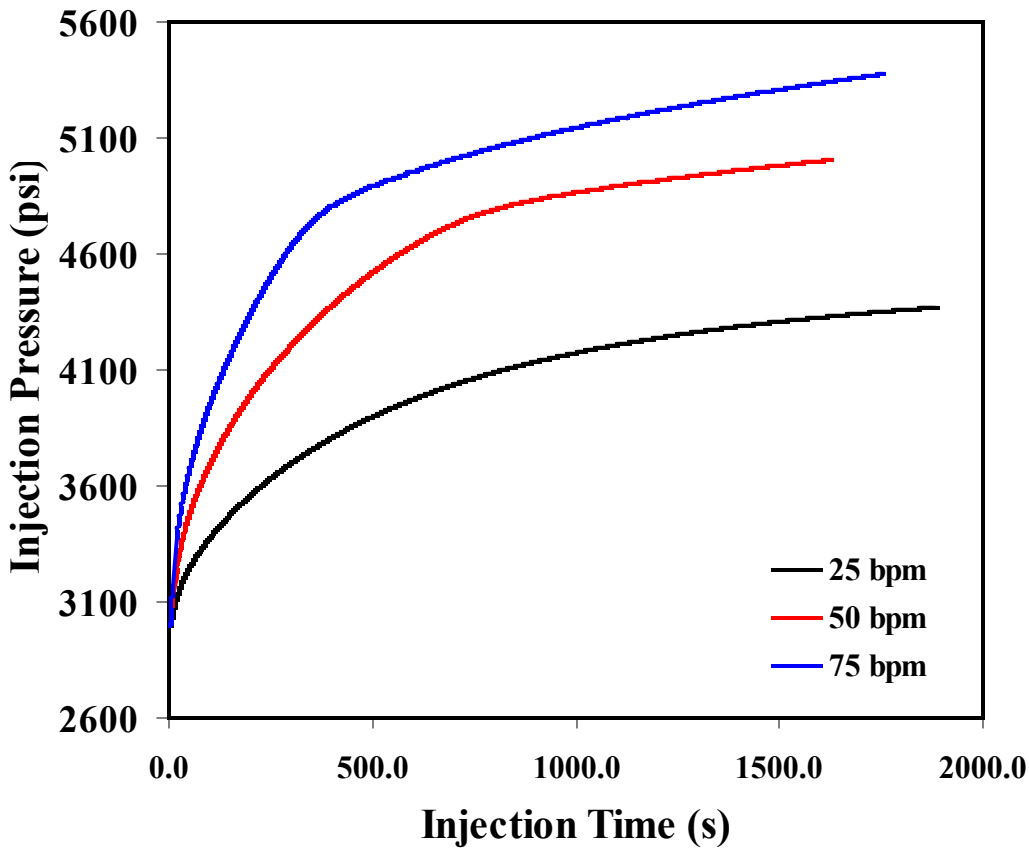

Figure 6-3. Injection pressure increase as a function of injection rate.

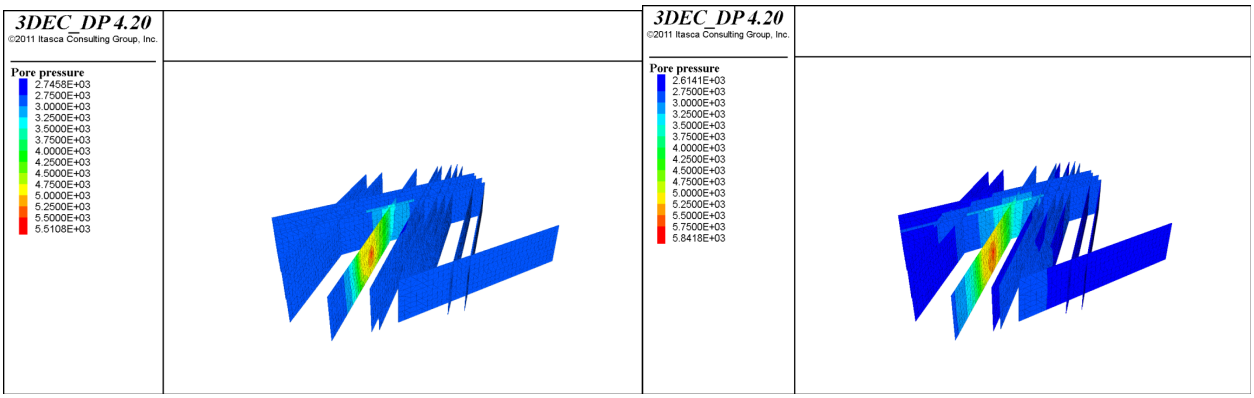

Figure 6-4. Pressure in the fracture system at 2 cp fluid injection at 50 bpm. Left panel shows the pressure at 849 seconds and the right panel at 1931 seconds. Pressures are in psi.

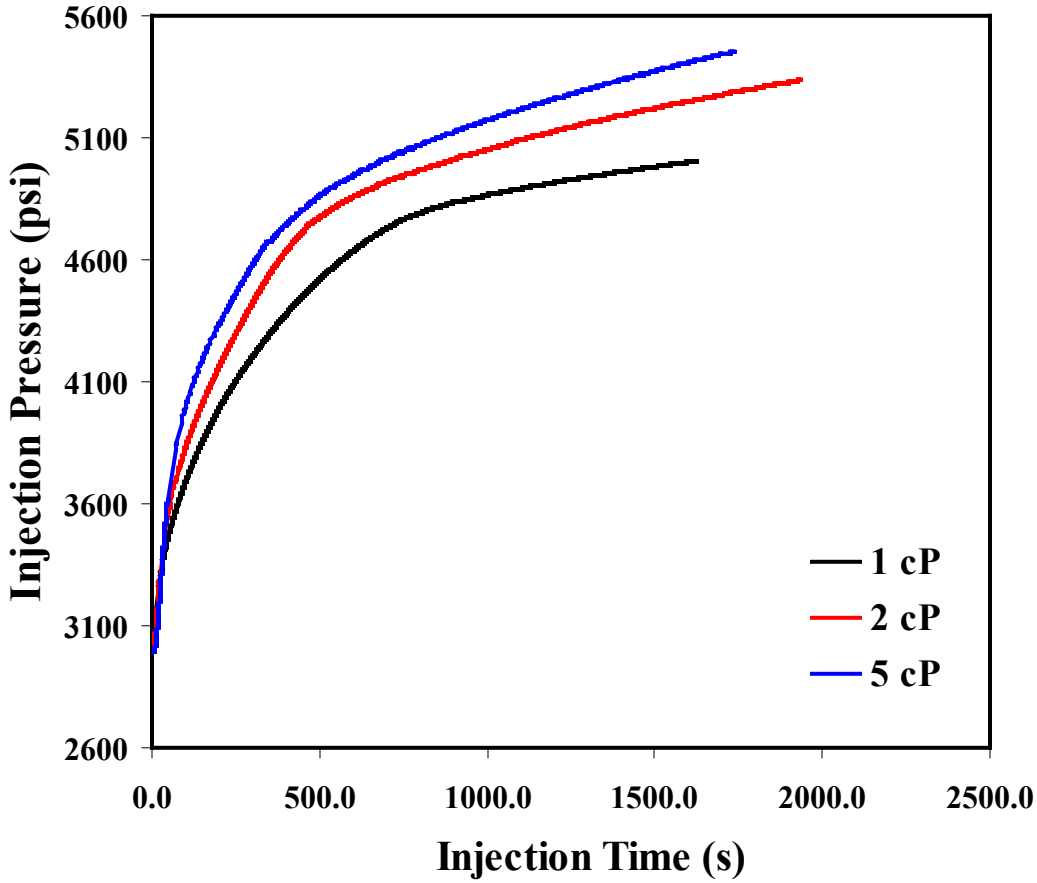

Figure 6-5. Pressure as a function of injection fluid viscosity.

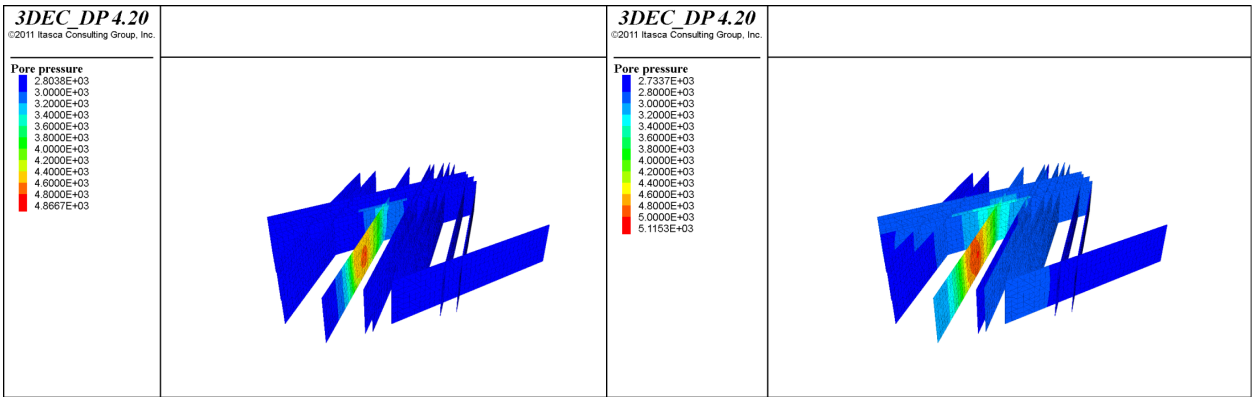

Figure 6-6. Snapshot of fluid pressure in the fracture system after 587 and 1054 seconds of injection at 50 bpm with fluid loss coefficient of 0.001 ft/min1/2.

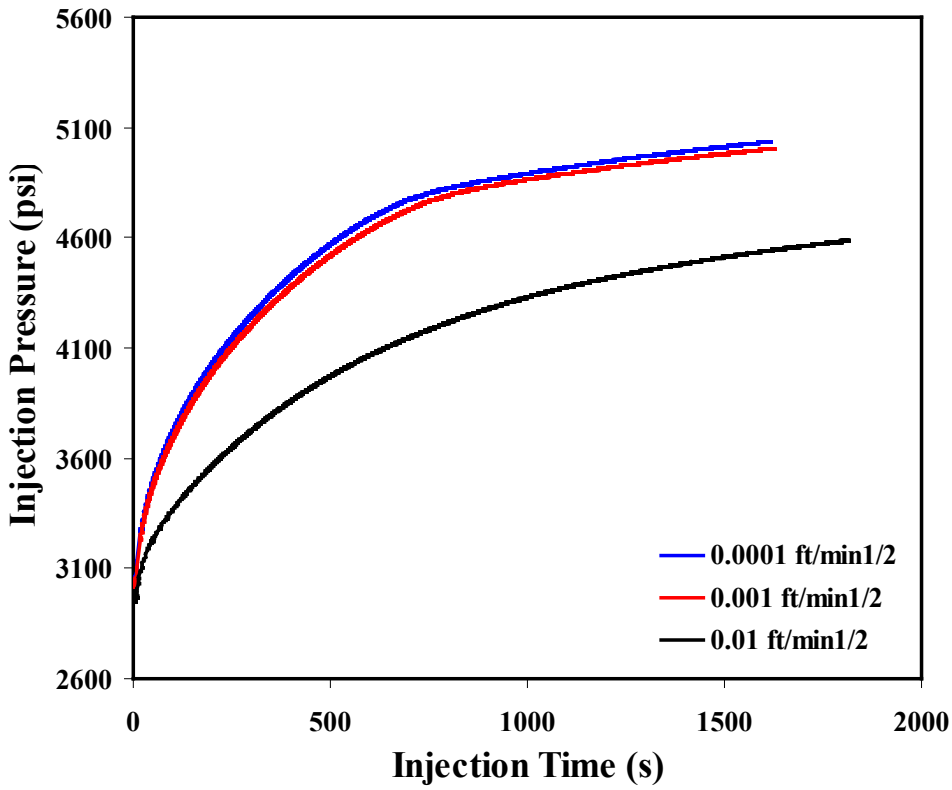

Figure 6-7. Time profile for injection pressure with different leakoff coefficients.

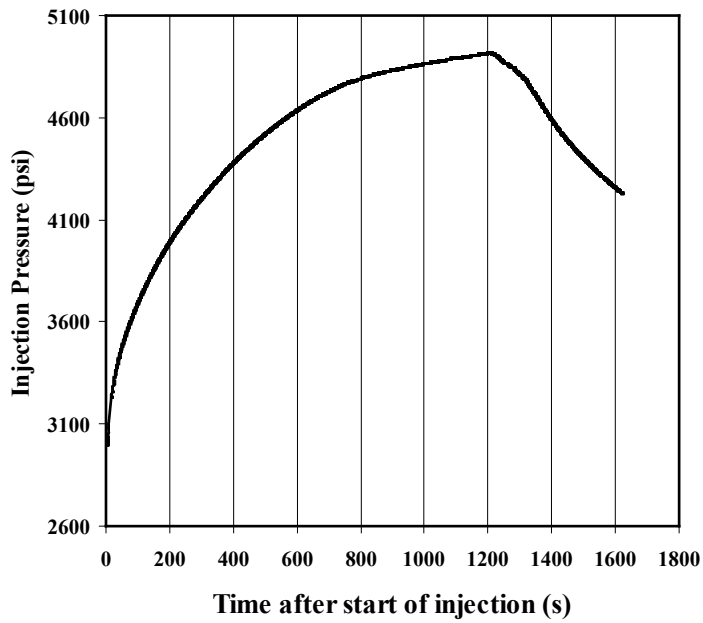

Figure 6-8. Time profile for injection pressure for a 20 min injection, period followed by shut-in. This plot is extremely important. Many interpretations of in-situ behavior are based on shut-in behavior that is predicated by assumptions of a single planar fracture. These numerical simulations allow simulation of closure of complex fracture networks, and representation of the associated pressure decay.

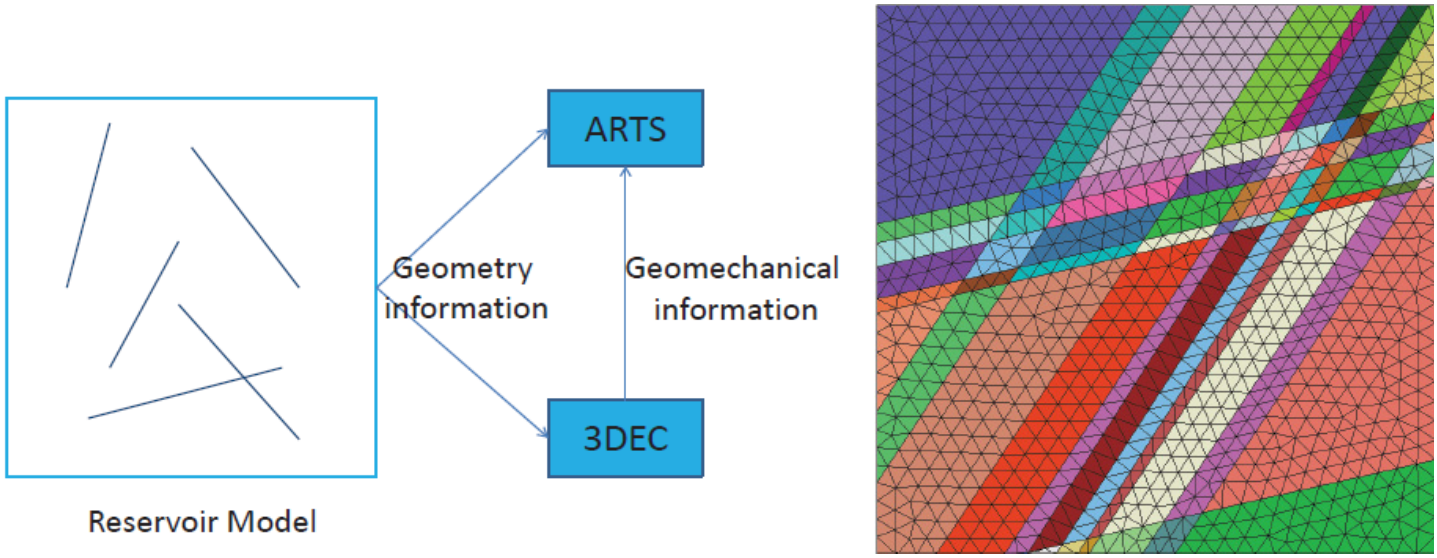

Figure 6-9. The soft coupling scheme used for the implementation of geomechanics in reservoir simulation and the geometry employed (right).

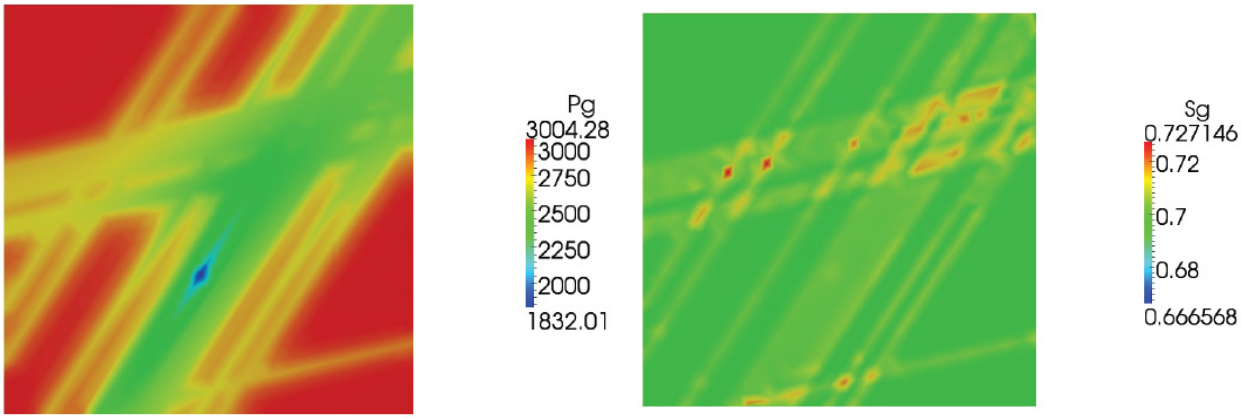

Figure 6-10. Gas pressures and saturations in the fractured reservoir – no geomechanical coupling.

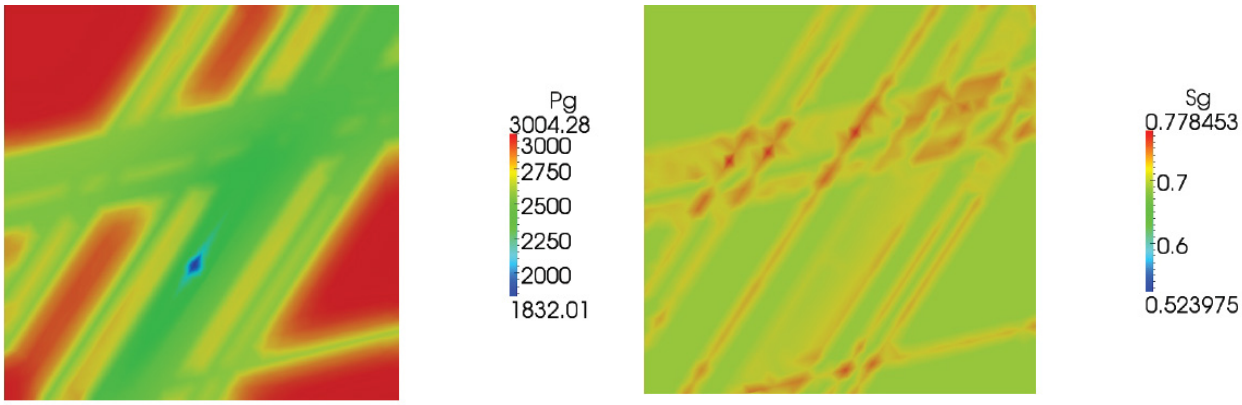

Figure 6-11. Gas pressures and saturations in the fractured reservoir – case 1 simple geomechanical coupling where same geomechanical attributes are expected to affect all features.

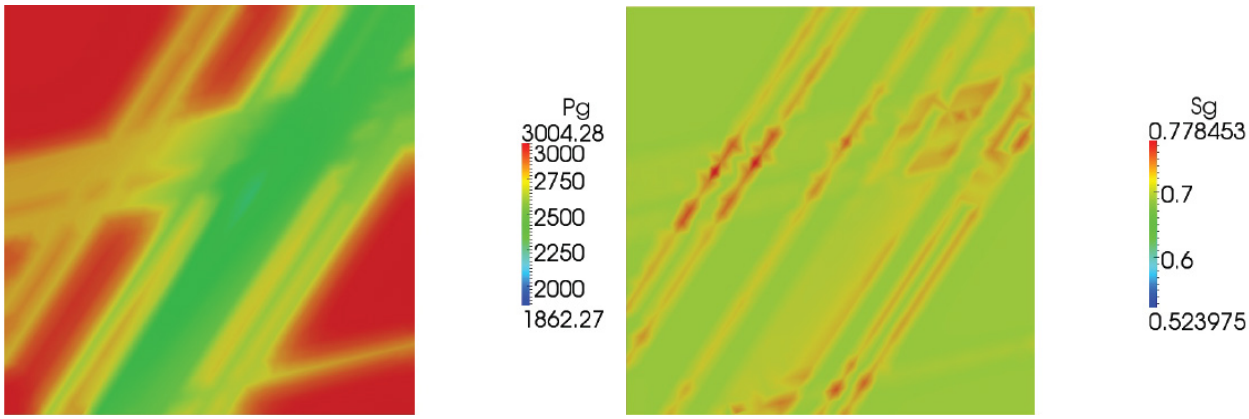

Figure 6-12. Gas pressures and saturations in the fractured reservoir – case 2 complex geomechanical coupling where different geomechanical attributes are expected to affect all features.

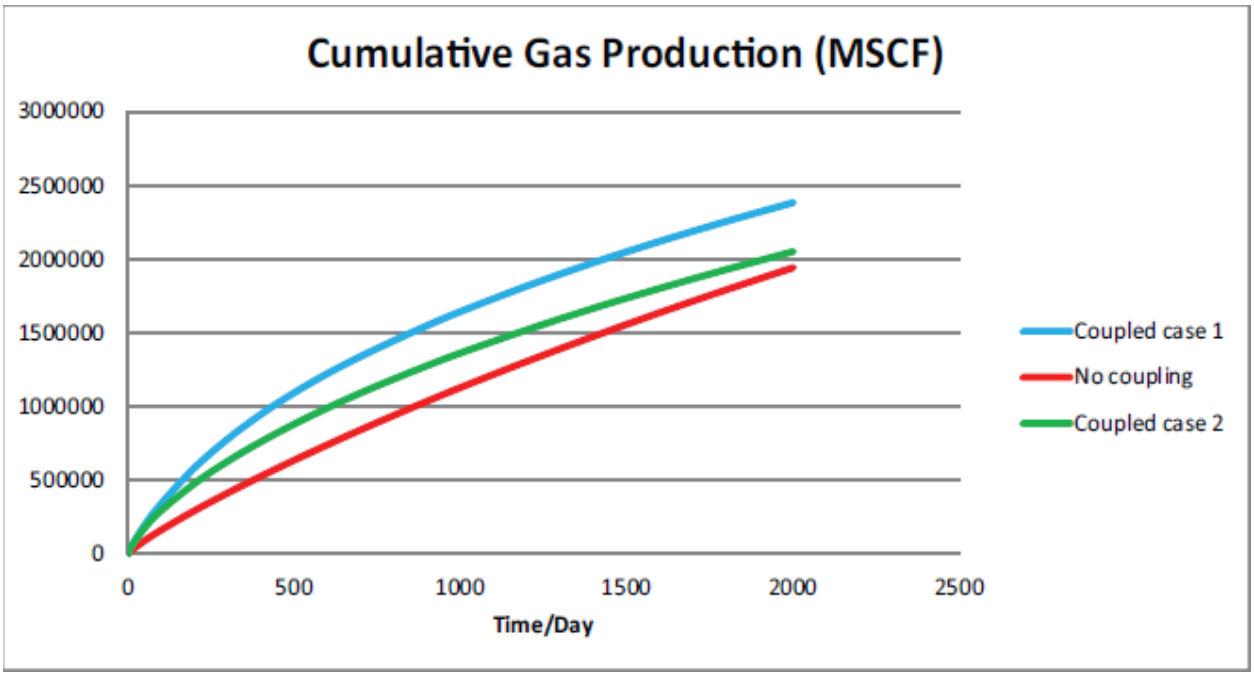

Figure 6-13. Cumulative gas production for the three cases of no geomechanical coupling, simple coupling and complex coupling. All use the soft coupling scheme.

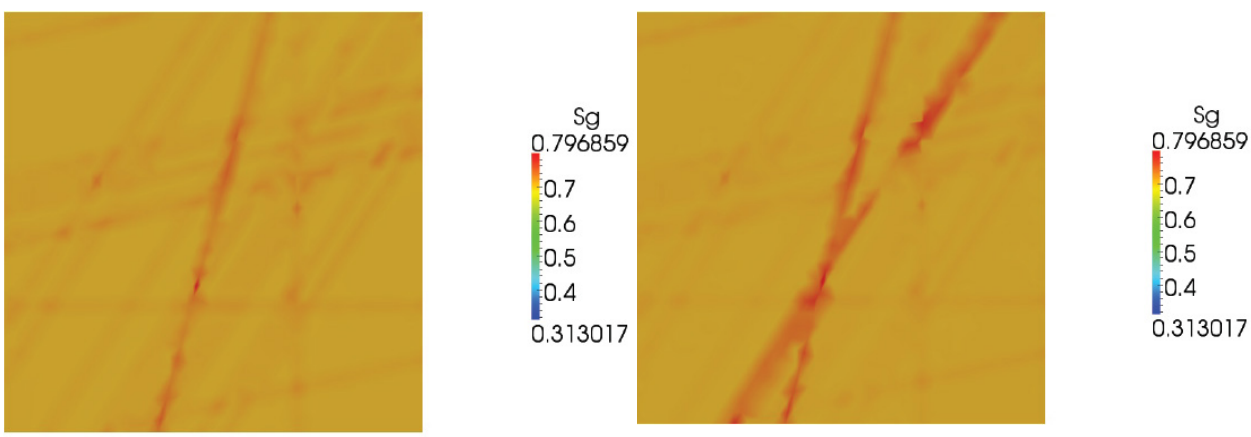

Figure 6-14. Gas saturation profiles with (right) and without (left) the presence of proppant. With the proppant, the drawdown limits permeability reduction.

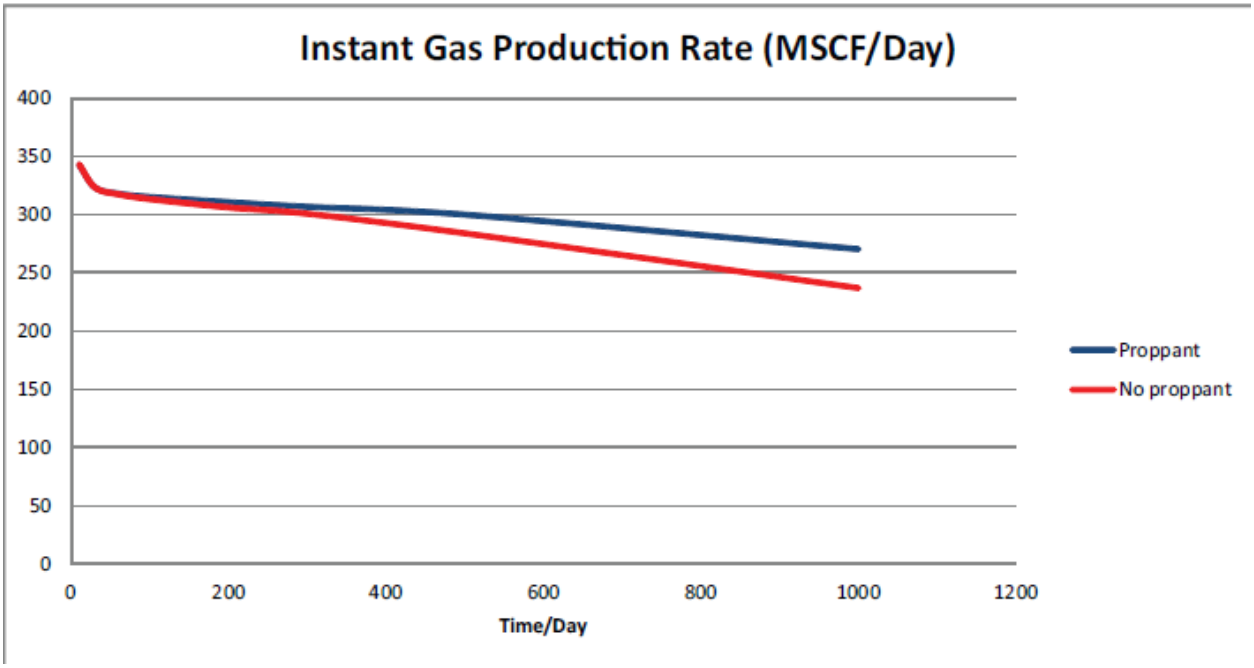

Figure 6-15. Gas production rates with and without proppant.

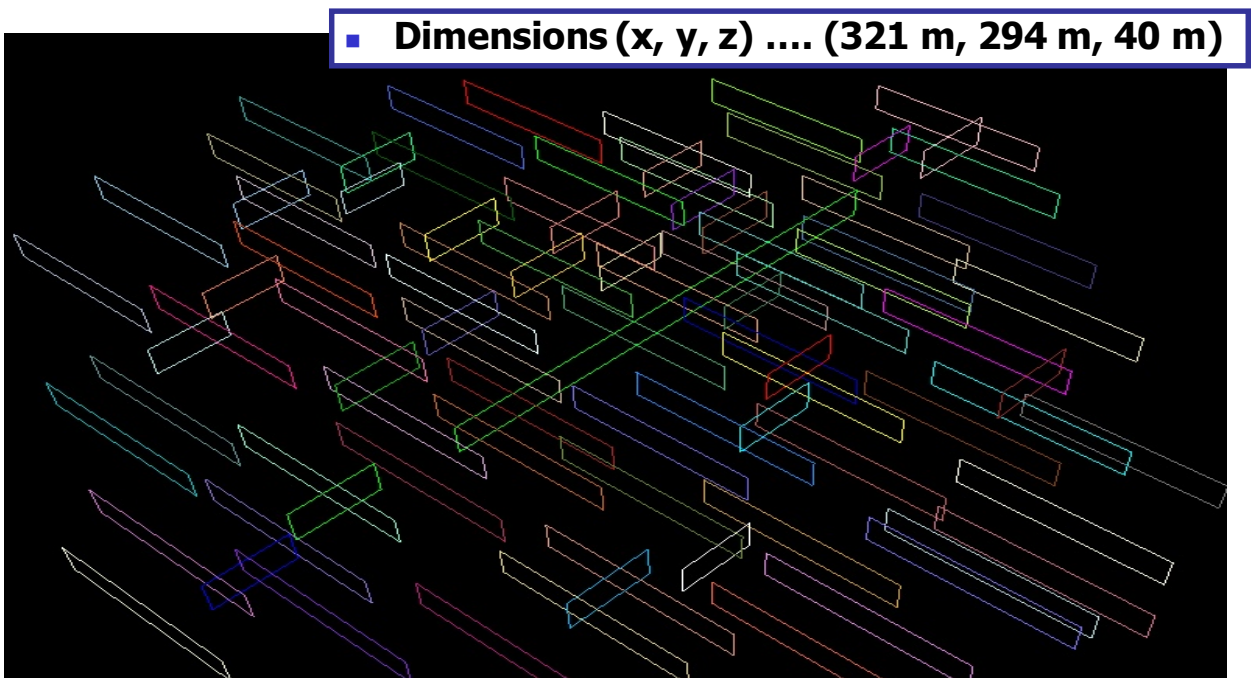

Figure 6-16. A simplified view of a naturally fractured reservoir, subjected to in-situ stresses.

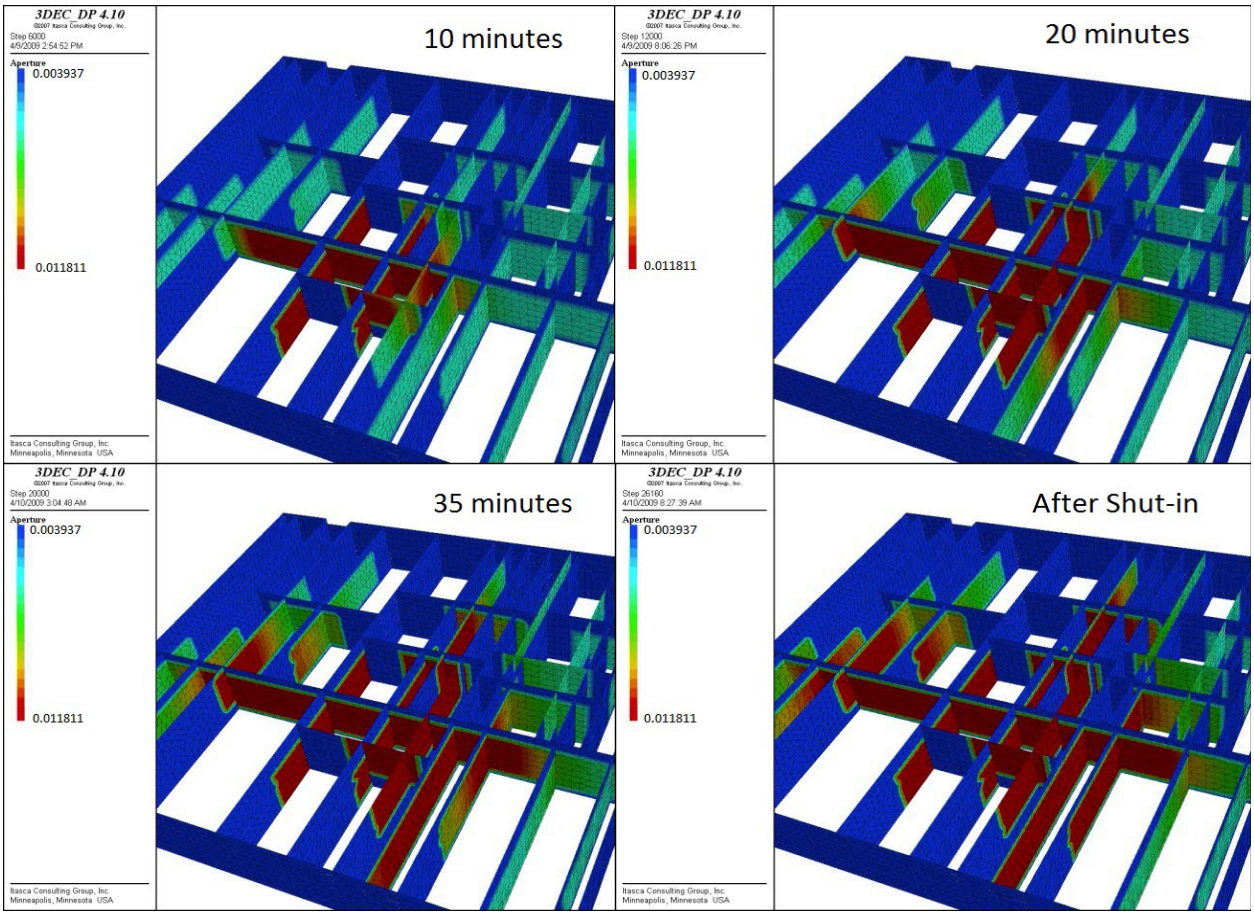

Figure 6-17. This is a cutout from the overall simulation (with dimensions of 1060 feet by 970 feet by 132 feet) showing inflated apertures. All apertures are in inches. All penetration into numerous natural fractures is evident to occur rapidly – and since there is finite initial width it can occur below fracturing pressure. Different panels show the evolution of the complex hydraulic fracture at various times.

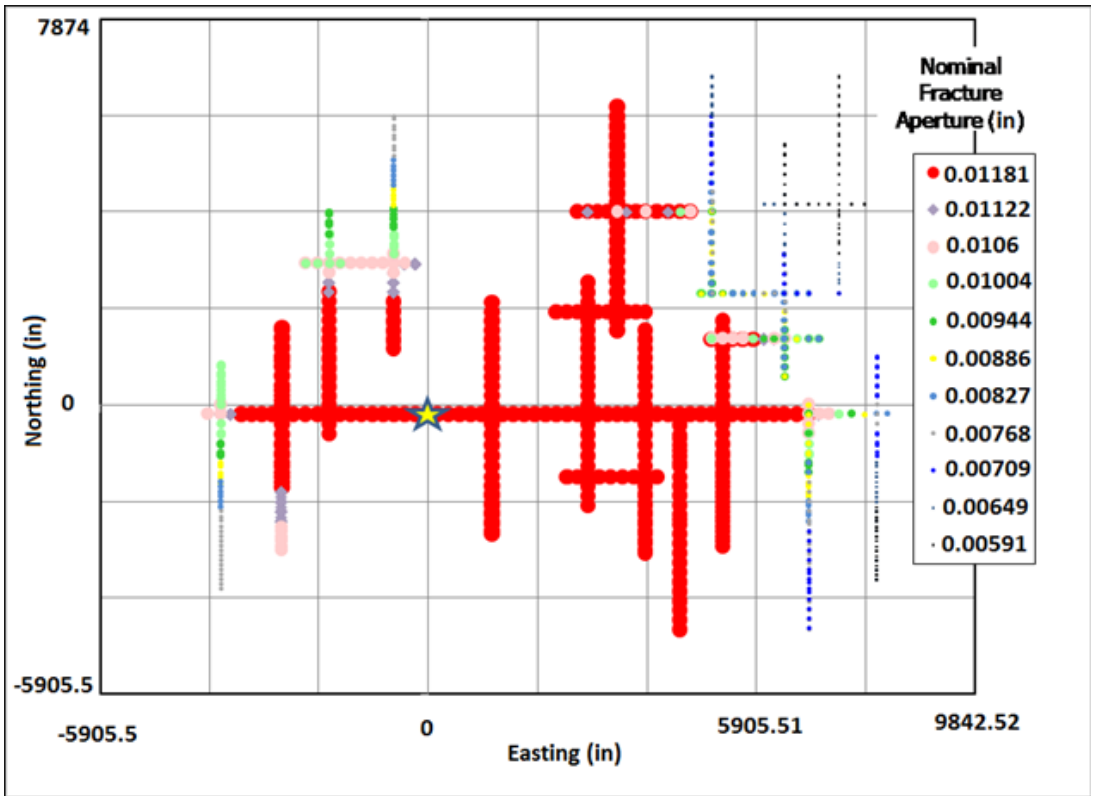

Figure 6-18. End of Job (EOJ) geometries for the hydraulic fracture modeling at 0.254 m3/minute injection rate.

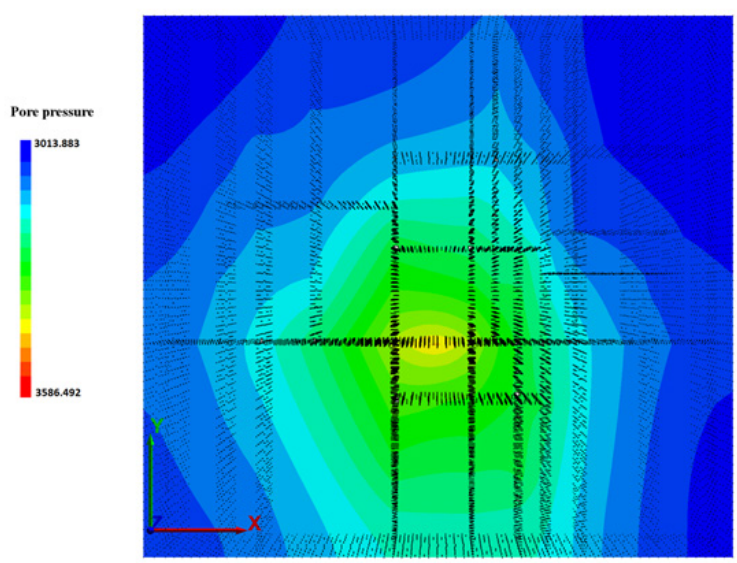

Figure 6-19. Pore pressure (in psi) distribution profile at the end of hydraulic stimulation treatment (plan view) showing influence of the fracture network. In the first quadrant where natural fractures are closely spaced, injection fluid tends to follow the paths of least resistance, and no longer results in a simple elliptical pressure diffusion front as assumed by analytical models.

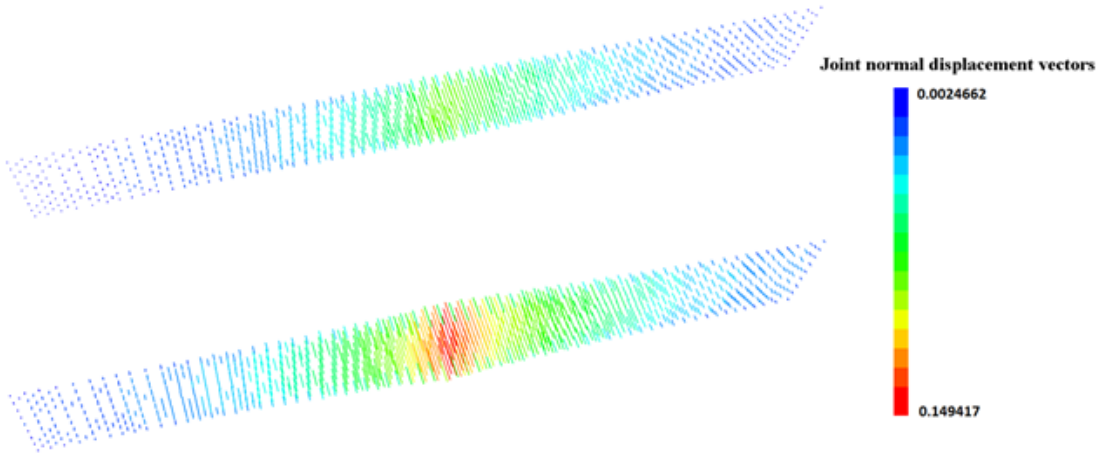

Figure 6-20. Comparison of aperture of the hydraulic fracture at the end of injection treatment using different rates. Joint displacement vectors shown in inches are a proxy for apertures. Doubling the injection rate from 0.264 m3/min (above) to 0.528 m3/min (below) helps increase the hydraulic fracture aperture by ~30%-50% at the well and 2-10 times at the fracture tips. For tight gas and gas shales, this large increase in fracture conductivity may justify the cost of higher hydraulic power.

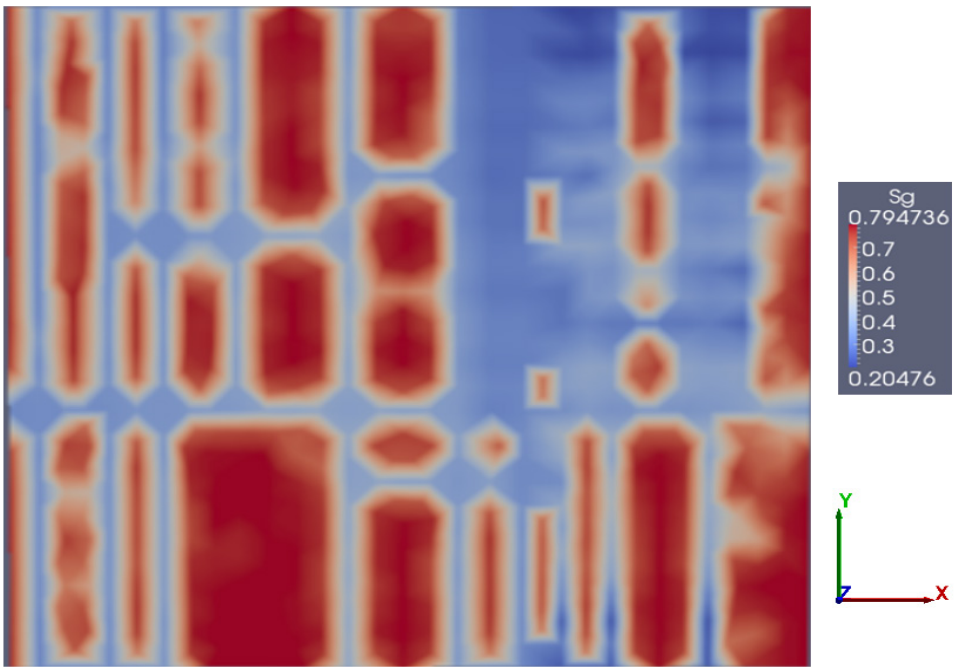

Figure 6-21. Gas saturations after 100 days of multiphase simulations using the University of Utah discrete-fracture network multiphase simulator. It is seen that the areas around the large-aperture fractures are drained effectively, while the remainder of the reservoir with poorly connected large-aperture fractures remains at high gas saturation.

Figure 6-22. Demonstration of the water-block concept in a simpler domain. It is seen that the gas is locked out of the flow system.

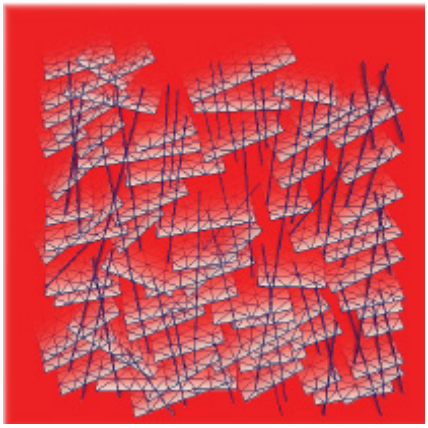

Figure 6-23. The realistic fracture network used to demonstrate the coupling of geomechanics and reservoir flow simulation.

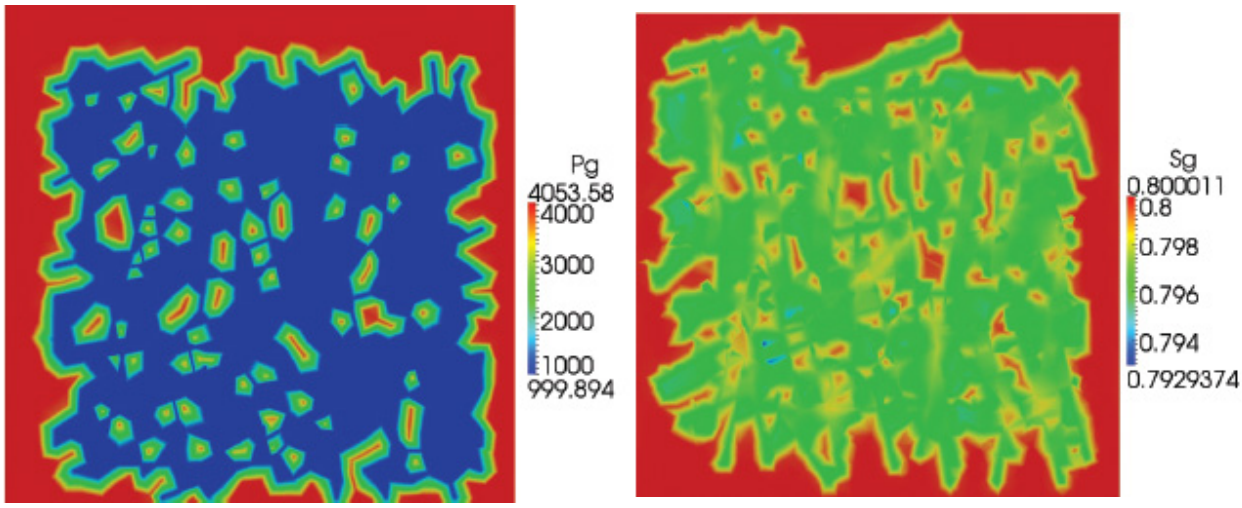

Figure 6-24. Pressures and gas saturations in a simulation where the geomechanics is coupled with flow. The gas saturation variation is minimal since the gas is basically redistributed in the system.

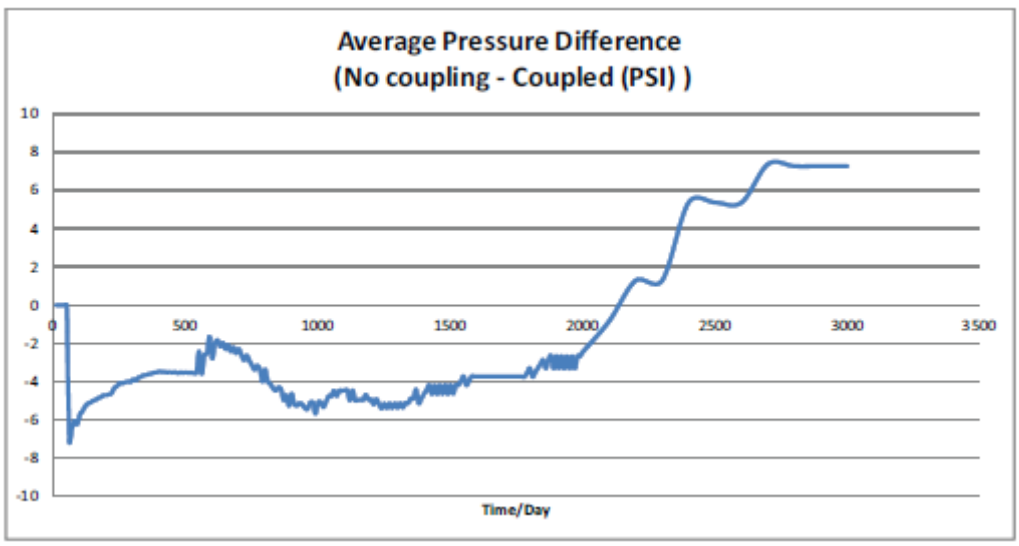

Figure 6-25. Reservoir average pressure difference between coupled and uncoupled geomechanics simulations. The difference in pressure is not significant.

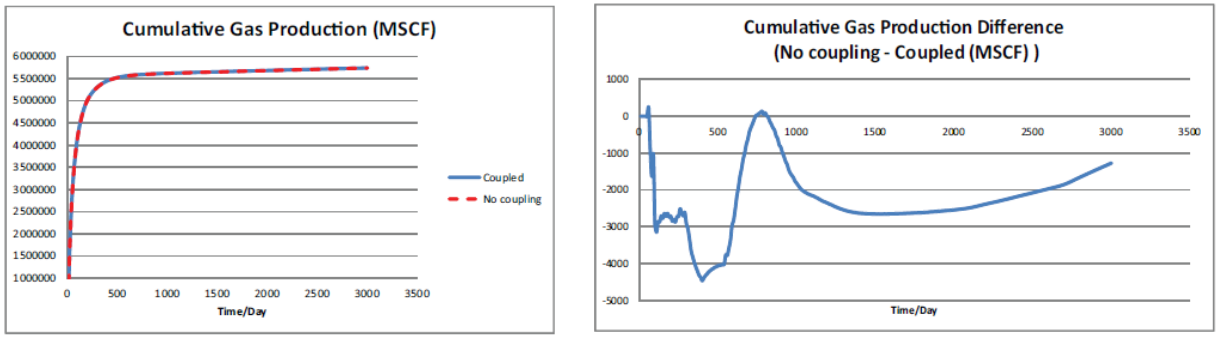

Figure 6-26. This figure shows the difference in cumulative gas production between the coupled and the uncoupled cases in the left panel. The differences are not discernible at this scale. The actual differences on an expanded y-scale are plotted in the right panel. There are some differences, but not significant due to the diffuse nature of the fracture system.

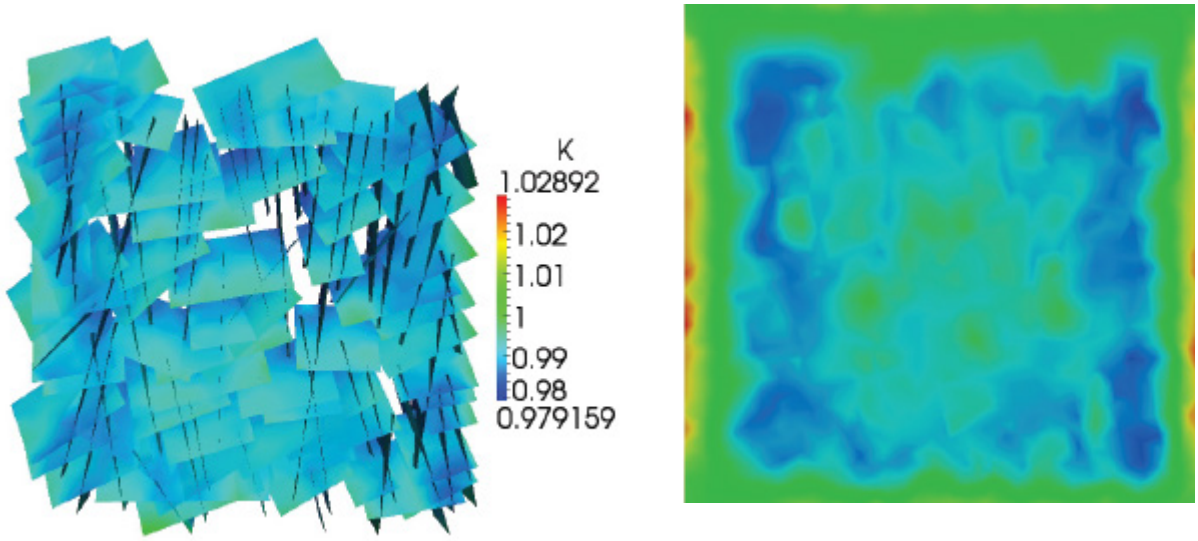

Figure 6-27. The difference between the initial and permeabilities at 2800 days in the fractures (left) and in the matrix (right) are shown in this figure. The differences between the permeabilities are not significant. But the permeability change is uneven dictated by the nature of the fracture system.

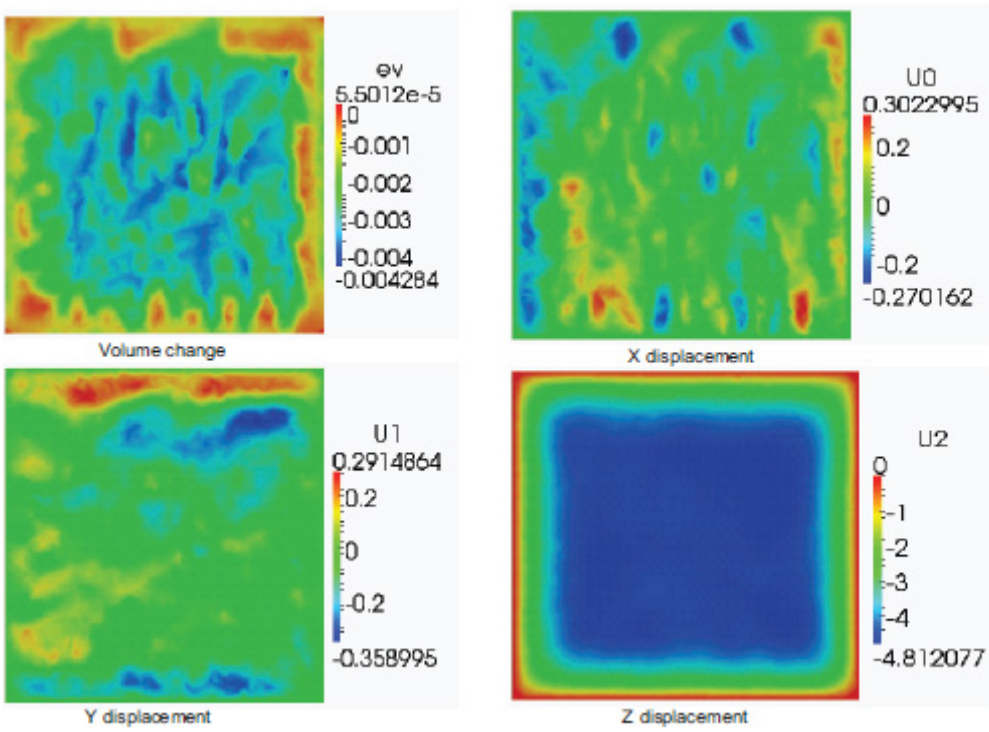

Figure 6-28. Volumetric and displacement changes in the reservoir at 2800 days.